Doctorate Dissertation
博士論文

Measurement of neutrino interactions on water and search for electron anti-neutrino appearance in the T2K experiment
(T2K実験における水標的でのニュートリノ反応の測定と反電子ニュートリノ出現現象の探索)

A Dissertation Submitted for Degree of Doctor of Philosophy
July 2018
平成30年7月博士(理学)申請

Department of Physics, Graduate School of Science,
The University of Tokyo
東京大学大学院理学系研究科物理学専攻

Taichiro Koga
古賀太一朗

Abstract

T2K is a long baseline neutrino oscillation experiment, started from 2009. A muon neutrino beam produced by J-PARC accelerator is measured by the Super-Kamiokande detector to measure probabilities of neutrino oscillations. Main purposes of the T2K are the first observation of CP violation in lepton sector and an investigation of flavor mixing structure. In this thesis, three analyses are performed to achieve a precise neutrino oscillation measurement in the T2K experiment.

The first analysis is measurements of inclusive charged current muon neutrino cross sections with water, plastic, iron and their ratios. The purpose of the measurements is to understand difference of the neutrino-nucleus interactions between the plastic and water target that is one of systematic uncertainties in the T2K. The analysis is performed with a new water target detector, water module, one of the T2K near detectors located at on-axis. Main results of the measurements are $\sigma_{\mathrm{CC}}^{\mathrm{H_2O}} = (0.840 \pm 0.010(\mathrm{stat.})^{+0.10}_{-0.081}(\mathrm{syst.})) \times 10^{-38}$ cm^2/nucleon and $\frac{\sigma_{\mathrm{CC}}^{\mathrm{H_2O}}}{\sigma_{\mathrm{CC}}^{\mathrm{CH}}} = 1.028 \pm 0.016(\mathrm{stat.}) \pm 0.053(\mathrm{syst.})$ for muons whose angle is less than 45 degree and momentum is more than 0.4 GeV with the mean neutrino energy of 1.5 GeV. These are the measurement with the best accuracy in the world. This measurement ensures correctness of the assumed systematic uncertainty of the difference of neutrino interaction between water and plastic target with experimental data for the first time in the world and improves reliability of the oscillation analysis of the T2K.

The second analysis is a validation of the measurement of the T2K near detector, ND280. The ND280 measures neutrino flux and interactions and constrains their uncertainties for the T2K oscillation measurements. In this analysis, observed neutrino event rates at other near detectors located at on-axis, water module and Proton Module, are compared with Monte Carlo prediction with the constraint from the ND280. This is the first trial to cross check the constraint from the near detector based on real data in any long baseline neutrino experiments. The measured event rates of the forward scattered muons at the water module and Proton Module are consistent with the prediction with a p-value of 0.303. This ensures the correctness of the ND280 measurement. On the other hand, the measured event rates of large angle muons and protons, which are not included in the ND280 measurement, are not consistent with the prediction with a p-value of 4×10^{-4}. It indicates the over prediction of the number of emitted protons and gives a significant hint to improve a modeling of the neutrino interactions.

The third analysis is a measurement of the neutrino oscillations with doubled statistics compared with the last T2K analysis performed in 2016. The accumulated number of protons used for the analysis is 1.49×10^{21} with neutrino beam and 1.12×10^{21} with anti neutrino beam. Four types of the neutrino oscillations, $\nu_\mu \rightarrow \nu_\mu$, $\nu_\mu \rightarrow \nu_e$, $\overline{\nu}_\mu \rightarrow \overline{\nu}_\mu$ and $\overline{\nu}_\mu \rightarrow \overline{\nu}_e$, are measured by the Super-Kamiokande. The four oscillations are jointly fitted to extract the parameters of the unitary matrix in the standard three flavor mixing model (PMNS matrix): δ_{CP}, θ_{23}, Δm^2_{32} and θ_{13} as well as the mass hierarchy. The measured values with 1σ uncertainties are $\delta_{CP} = -1.72^{+0.58}_{-0.61}$($[-2.739, -0.6078]$ with 2σ intervals), $\sin^2\theta_{23} = 0.544^{+0.046}_{-0.029}$, $\Delta m^2_{32} = (2.450^{+0.065}_{-0.068}) \times 10^{-3}$ eV^2 and $\sin^2 2\theta_{13} = 0.0871^{+0.0043}_{-0.0045}$ with the normal hierarchy assumption and constraint from solar and reactor neutrino experiments. The δ_{CP}, θ_{23} and Δm^2_{32} are measured with the best accuracy in the world. $\delta_{CP} = 0$, corresponding to CP conservation, is excluded with a significance of 2σ for the first time in the world. Normal hierarchy is more preferred than inverted hierarchy with a Bayes factor of 10.49 with the reactor constraint. These results are consistent with other neutrino oscillation experiments. In addition, a search for $\overline{\nu}_\mu \rightarrow \overline{\nu}_e$ oscillation is performed with the best sensitivity in the world. $\overline{\nu}_\mu \rightarrow \overline{\nu}_e$ oscillation is not observed so far although it is predicted by the standard oscillation framework. Two hypothesis are tested in this analysis. One hypothesis assumes a probability of $\overline{\nu}_\mu \to \overline{\nu}_e$ is zero and the other assumes the probability is the same as the prediction from the PMNS matrix parameters. P-value of the former (latter) hypothesis is calculated to be 0.219 (0.213) based on information of only the total number of observed event. With additional information of lepton kinematics, the p-value of the former (latter) hypothesis is calculated to be 0.233 (0.087). Both of the hypotheses are not excluded.

Acknowledgements

First of all, I would like to express my special thanks of gratitude to my supervisor, Masashi Yokoyama for his great support and encouragements throughout my research life. He gave me beautiful experiences to learn fun of fundamental research and foundations of an experimental physicist. Every day of interesting discussion and enjoyable conversation with him are the most valuable treasures in my life.

I would like to thank all of T2K collaborators for their great supports of my research, including following people: Tsuyoshi Nakaya, Atsuko Ichikawa and Akihiro Minamino. I really appreciate Nakaya-san for his great support since I was in Kyoto University. I am always surprised his sharp advices to the point with his extensive experiences. I also appreciate Ichikawa-san who helps my research at J-PARC greatly. I have respected her interesting and flexible ideas of physics and a way of thinking as a physicist. I am also grateful to Minamino-san who has been working together directly through WAGASCI experiment for a long time. I appreciate him for trusting me with every important job of water module detector with his enormous support and patient. It was quite interesting and invaluable experience for me to learn a lot of things.

I would like to thank all of WAGASCI collaborators related to the water module detector: Michel Gonin, Thomasz Mueller, Oliver Drapier, Alain Bonnemaison, Oscar Ferreria, Remi Cornat, Frank Gastaldi, Benjamin Quilain, Mattieu Liccardi, Tatiana Ovsjannikova, Etam Noah, Yoshihiro Seiya and Kazuhiro Yamamoto. I also would like to thank all members of KEK neutrino group, Daiichi-tekkou company, Nichirei-seiki company and Suzuno-giken company. I could not construct the nice detector without all of your helps.

I would like to thank all persons who help my physics analysis: Yoshinari Hayato, Mark Hartz, Laula Zambelli, Son Cao, Kendall Mahn, Callum Wilkinson, Mark Scott, Christophe Bronner, Claudio Giganti, Simon Bienstock, Andy Chappell, Artur Sztuc and Francis Bench. I could not finalize my physics analyses described in this thesis without all of your supports.

I would like to thank members working together at J-PARC: Kikawa-san, Suzuki-san, Shota-san, Hiraki-san, Hayashino-kun, Nakamura-kun, Yoshida-kun, Wakamatsu-kun, Kin-kun, Harada-kun, Ashida-kun, Hiramoto-san, Nakanishi-san and Uno-kun. My quality of life at Tokai was very good thanks to you.

I would like to show my appreciation to the members in my laboratory: Aihara-san, Onuki-san, Denis, Watson, Iwamoto-kun, Mineo-san, Clement, Kanazawa-san, Shimizu-san, Suda-san, Sasaki-kun, Jin-kun, Chikuma-kun, Hosomi-kun, Nikura-san, Wan-kun, Arehandra, Lou-kun, Tamura-kun, Ose-kun, Fujita-kun, Ishii-kun, Matsushita-kun and Kono-san. I could enjoy my 5.5 years life at the University of Tokyo thanks to all of you.

Finally, I want to express my deepest appreciation to my family: Keiichi Koga, Junko Koga, Lisa Koga, Noriko Toyomura, Shoko Tanabe and Mie Koga, for their bringing up, encouragements and lots of love to me up to now.

Contents

Chapter 1

Introduction

Particle physics is one of the branches of physics to investigate a fundamental theory to explain the origin and behavior of elementary particles which compose our universe with no substructure. The most successful theory in this branch is the standard model (SM) which was born in 1970s and has explained almost all experimental results. However, there are remained experimental mysteries which are not described by the SM as follows:

- The SM assumes masses of the neutrinos to be zero but they are not zero in reality.
- The origin of matter-antimatter asymmetry in the universe is not known.
- Dark matter and dark energy are not explained by the SM.
- Gravity is not included in the SM.

In addition, the SM itself is not theoretically beautiful in several points of views as follows:

- The SM contains many elementary fermion particles but their origin is not known. It also contains three types of interactions and they are not unified.
- The SM contains free parameters but their origin is not known: masses of the particles, the number of generation, coupling constant of the interactions and flavor mixing of the particles.

In order to develop new theory beyond the SM answering these questions, there have been many theoretical and experimental approaches. Physics of neutrino is one of them. Neutrino is a neutral lepton and one of the fundamental particles in the SM. In 1998, a property of neutrinos to change their flavor while flying (neutrino oscillation) was observed through a measurement of atmospheric neutrinos by Super-Kamiokande collaboration [1]. The observation requires to modify the SM because an existence of the neutrino oscillation indicates the non zero masses of the neutrinos with a mixing of their flavor and mass eigenstates. In addition, the observation of neutrino oscillation indicates a possibility of CP violation in the lepton sector through the flavor mixing. It is possible to explain the matter-antimatter asymmetry with large CP violation in the lepton sector and leptogenesis scenario [2] , although the CP violation in the lepton sector is not experimentally measured so far. It is interesting to measure the CP violation and check if there is additional CP violation from a new physics behind the flavor mixing.

In addition, we have a question about modeling of the flavor mixing in the lepton sector. In the current understanding, the flavor mixing of the neutrino is explained that the three flavor and three mass eigenstates are mixed through a 3×3 unitary matrix. The matrix is parametrized by four parameters named δ_{CP}, θ_{13}, θ_{12} and θ_{23} based on [3] (Pontecorvo-Maki-Nakagawa-Sakata

(PMNS) matrix). In order to validate if this standard three flavor mixing model is correct or not, consistency checks between theoretical predictions with the model and experimental measurements are needed through many experiments with several points of views. However, due to difficulty of the neutrino detection, enough number of consistency checks have not been performed in the lepton sector compared with that in the quark sector, which has been checked with many measurements of the unitary matrix elements [4]. At present, the flavor mixing structure in the lepton sector can be measured only through the measurement of the neutrino oscillation. A precise understanding of the neutrino oscillation is important to observe the CP violation in the lepton sector and to validate the three flavor mixing model.

In this thesis, three analyses are performed to achieve a precise neutrino oscillation measurement in T2K experiment, one of long baseline accelerator neutrino experiments. The first analysis is measurements of charged current muon neutrino cross section with water, plastic, iron and their ratios as described in Section 6. Difference of the neutrino-nucleus interaction between the plastic and water targets is one of systematic uncertainties in the T2K. In order to understand the difference experimentally, this analysis is performed with a new water target neutrino detector called “water module” located at on-axis, as described in Section 5.

The second analysis is a validation of the T2K near detector measurement as described in Section 7. The near detector, ND280, is located 280 m downstream of a target for the neutrino beam production. It measures neutrino beam flux and neutrino-nucleus interaction and constrains their uncertainties reduced from 15% to 3%. The constraint is propagated to the T2K far detector for the oscillation measurement. However, it is impossible to check if the constraint is correct or not at the far detector directly because not only the flux and interactions but also the neutrino oscillations affect the neutrino events at the far detector. In this analysis, to cross check the constraint from the ND280 measurement, observed neutrino event rate at the other near detectors located at on-axis, water module and Proton Module, is compared with the Monte Carlo prediction with the constraint from the ND280. Because there is no effect of the neutrino oscillations at the water module and Proton Module located 280 m downstream from the target, the constraint of the flux and interactions are validated. This is the first trial to cross check the near detector measurement based on real data directly in any long baseline accelerator oscillation experiments. In addition, the on-axis detectors are sensitive to protons and muons with large scattered angle, which are not measured by the ND280. By measuring them and comparing them with the prediction with the constraint from the ND280, modeling of the neutrino interactions is validated.

The third analysis is a measurement of the neutrino oscillations as described in Section 8. The analysis is performed with twice larger statistics than the last analysis performed by T2K in 2016, with 1.5 times accumulated neutrino beam statistics and enlarged fiducial volume of the T2K far detector, Super-Kamiokande, by improvement of Cherenkov ring reconstruction algorithm. Four types of the neutrino oscillations, $\nu_\mu \to \nu_\mu$, $\nu_\mu \to \nu_e$, $\overline{\nu}_\mu \to \overline{\nu}_\mu$ and $\overline{\nu}_\mu \to \overline{\nu}_e$, are measured by the T2K far detector. They are jointly fitted to extract the parameters of the PMNS matrix: δ_{CP}, θ_{23}, Δm^2_{32} and θ_{13} as well as mass hierarchy which is order of mass eigenstate values of neutrinos. The main interest of this analysis is the observation of the CP violation in the lepton sector through a comparison of $\nu_\mu \to \nu_e$ and $\overline{\nu}_\mu \to \overline{\nu}_e$. The analysis aims to exclude the CP conservation low ($\delta_{CP} = 0$) in the lepton sector with a significance of more than 2σ. The parameters of θ_{23} and Δ^2_{23} are measured with the best accuracy in the world and they are compared with other oscillation experiments. In addition, a search for $\overline{\nu}_\mu \to \overline{\nu}_e$ oscillation is performed with the best sensitivity in the world. $\overline{\nu}_\mu \to \overline{\nu}_e$ oscillation is not observed so far although it is predicted by the standard oscillation framework. Observation of $\overline{\nu}_\mu \to \overline{\nu}_e$ is one of milestones for the validation of the standard oscillation framework and an exciting challenge to search for a new physics beyond the SM.

Chapter 2

Physics of neutrino oscillation

2.1 Discovery of neutrino

Neutrino is a neutral spin $\frac{1}{2}$ particle which is one of the elementary particles of the SM. Existence of neutrino was predicted by Pauli in his letter in 1930 for the first time. He introduced a neutral spin $\frac{1}{2}$ particle for describing broad energy spectrum of electrons produced in beta decay ($n \to p + e^-(+\overline{\nu}_e)$), which seemed to violate the energy conservation law by assuming only neutron, proton and electron. Because the probability of neutrino interactions with materials is extremely small as predicted by Fermi, a strong source of neutrino was needed for their detection. It was observed about 25 years later by Reines and Cowan in 1956 by using a reactor and detecting inverse beta decays ($p + \overline{\nu}_e \to n + e^+$) on a $\mathrm{CdCl_2}$ loaded water target[5]. After the observation, property of the neutrinos has been investigated from various points of view. In 1955-1960, Ray Davis distinguish the neutrino and anti neutrino by measuring the interaction rate of inverse beta decay on $\mathrm{CCl_4}$ target ($\nu + \mathrm{Cl}^2 \to \mathrm{Ar}^{37} + \mathrm{e}^-$)[6]. He confirmed that the inverse beta decay does not occur with the anti neutrinos from reactor, although it should occur if the neutrino and anti neutrino are the same particles. In 1962, it was shown that the electron neutrino and muon neutrino are not the same particle by measuring secondary particles produced with interactions of muon neutrinos [7]. The muon neutrino is produced by accelerator through decays of pions. The number of flavor of the standard neutrinos was determined to be three, by measuring decay width of Z boson by collider experiments, at LEP [8].

2.2 Discovery of neutrino oscillation

In 1969, Ray Davis started to measure the neutrino emitted by fusion reactions in the Sun by using the $\mathrm{CCl_4}$ target. The number of observed neutrino is three times smaller than a prediction by the standard solar model [9]. At that time, not so many people considered that the deviation is coming from the unknown property of the neutrino because the modeling of the Sun itself was not considered to be reliable. However, in 1980s, similar results were reported by several solar neutrino experiments: $^{71}\mathrm{Ga}$ target experiments, SAGE [10] and GALLEX [11], and water Cherencov detector, Kamiokande [12]. The different experiments with different targets, which have different threshold of the accessible neutrino energy, showed different amount of the discrepancy from the prediction as shown in Fig. 2.1 [13]. These energy dependent deviations could not be explained by simple modification of the solar model. There was a theory to explain the deviations by assuming a property of neutrinos to change their flavor while flying through mixing of the flavor and mass eigenstates (neutrino oscillation) [14] but experimental evidence was not enough to be confident.

In 1988, the Kamiokande experiment measured atmospheric neutrino [15] emitted by decay of pions and muons produced with interactions of primary cosmic protons and atmosphere. The number of observed muon neutrino event is about 40% smaller than a theoretical prediction, although the number of electron neutrino event is consistent with the prediction. Because the number of neutrino event, 277, is not so large and a few experiments with calorimeter, Frejus [16] and Nusex [17], reported different results from the Kamiokande, the deviation is not clear. However, another calorimeter experiment, Soudan 2 [18], reported a consistent result with the Kamiokande in 1994.

This atmospheric neutrino anomaly is finally solved in 1998 by Super-Kamiokande(SK) experiment [1] with the first observation of the neutrino oscillation. The SK measures zenith angle of atmospheric electron neutrinos and muon neutrinos, which corresponds to the flight length of the neutrinos as shown in Fig. 2.2. An assumption of the neutrino oscillation explains the atmospheric neutrino data.

The solar neutrino problem was finally solved with the SNO experiment, which measured sum of the three flavor neutrinos coming from the Sun by using a deuterium target in 2002 [20]. The sum of all neutrinos with different flavors were conserved and consistent with the theoretical prediction with the modeling of the Sun. The neutrino oscillation was also observed through the measurement of the reactor neutrino by KAMLAND experiment [19] in 2003. The result is consistent with the solar neutrino experiments and the main region of oscillation parameters to describe the solar neutrino oscillation is determined by this measurement. The existence of the neutrino oscillation gave us great impact because it requires to modify the SM which assumes no neutrino oscillations.

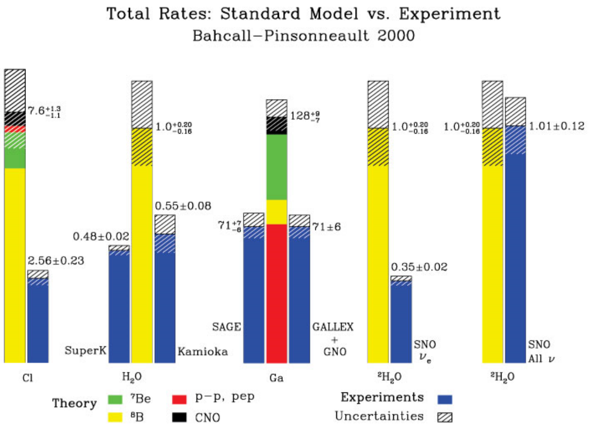

Figure 2.1: Event rate of the solar neutrinos predicted by theory and observed by experiments with several kinds of the target.[13]

2.3 Measurement of neutrino oscillation

Neutrino oscillation is a phenomenon of neutrinos to change their flavor while flying. In the current understanding, properties of the neutrino oscillation are described by mixture of the three flavor eigenstates and three mass eigenstates. To simplify, neutrino oscillation with two generations is introduced here at first. With the two generations, the mixture of the eigenstates is represented by 2 × 2 unitary matrix U as follows:

$$|\nu_\alpha\rangle = \sum_i U_{\alpha i} |\nu_i\rangle \tag{2.1}$$

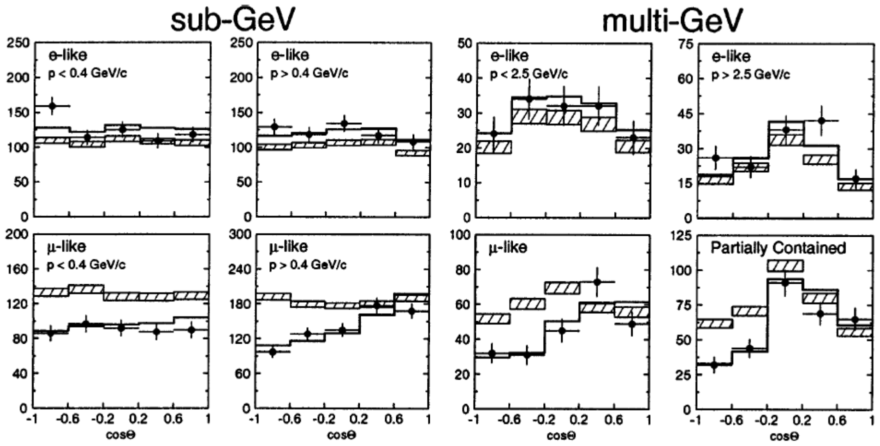

Figure 2.2: Zenith angle distributions of the muon like and electron like events for sub-GeV and multi-GeV data sets by Super-Kamiokande. [1] Upward-going particles have cosΘ < 0 and downward-going particles have cosΘ > 0. p is the momentum of lepton. The hatched region shows the expectation by Monte Carlo simulation for no oscillations normalized to the data live time with statistical errors. The bold line is the best-fit expectation for $\nu_\mu \leftrightarrow \nu_\tau$ oscillations with the overall flux normalization.

$$U = \left(\begin{array}{cc} \cos\theta & \sin\theta \\ -\sin\theta & \cos\theta \end{array} \right)$$

where $|\nu_\alpha\rangle$ $(\alpha = e, \mu)$ is the eigenstate of weak interaction corresponding the flavor and $|\nu_i\rangle$ $(i = 1, 2)$ is the eigenstate of mass with an eigenstate value of m_i. When a neutrino is produced by the weak interaction, state of the neutrino should be one of the eigenstates of the weak interaction. Here, it is assumed to be $|\nu_\mu\rangle$:

$$|\nu(t=0)\rangle \;\; = \;\; |\nu_\mu\rangle \tag{2.2}$$

Time evolution of the state in vacuum is written as follows by Schrödinger equation:

$$\begin{aligned} |\nu(t)\rangle &= e^{-iHt}\,|\nu(t=0)\rangle & (2.3)\\ &= e^{-iHt}\,|\nu_\mu\rangle & (2.4)\\ &= -\sin\theta\; e^{-i(p+\frac{1}{2E}m_1^2)t}\,|\nu_1\rangle + \cos\theta\; e^{-i(p+\frac{1}{2E}m_2^2)t}\,|\nu_2\rangle & (2.5) \end{aligned}$$

where p is neutrino momentum, E is neutrino energy and $m_i << p$ is assumed. Probabilities of the neutrino oscillations are written as follows:

$$\begin{aligned} P(\nu_\mu \to \nu_\mu)(t) &= |\langle\nu_\mu\,|\nu(t)\rangle\,|^2 & (2.6)\\ &= |\sin^2\theta\; e^{-i(p+\frac{1}{2E}m_1^2)t} + \cos^2\theta\; e^{-i(p+\frac{1}{2E}m_2^2)t}|^2 & (2.7)\\ &= 1 - \sin^2 2\theta\;\sin^2(\frac{\Delta m_{21}^2}{4E}L) & (2.8)\\ P(\nu_\mu \to \nu_e)(t) &= |\langle\nu_e\,|\nu(t)\rangle\,|^2 & (2.9)\\ &= \sin^2 2\theta\;\sin^2(\frac{\Delta m_{21}^2}{4E}L) & (2.10) \end{aligned}$$

where $\Delta m_{21}^2 = m_2^2 - m_1^2$ and $L = ct$ is a flight distance. The neutrino oscillations exist when θ is not zero and Δm_{21}^2 is not zero. The probability of oscillations are maximized with $\frac{\Delta m_{21}^2}{4E}L = 1$.

In a neutrino oscillation experiment, L is fixed to maximize the probabilities. Amplitude of the probabilities depends on θ and oscillation period depends on Δm^2_{21} as shown in Fig. 2.3. By measuring the oscillation probabilities as a function of the neutrino energy, the parameters of θ and Δm^2_{21} can be measured.

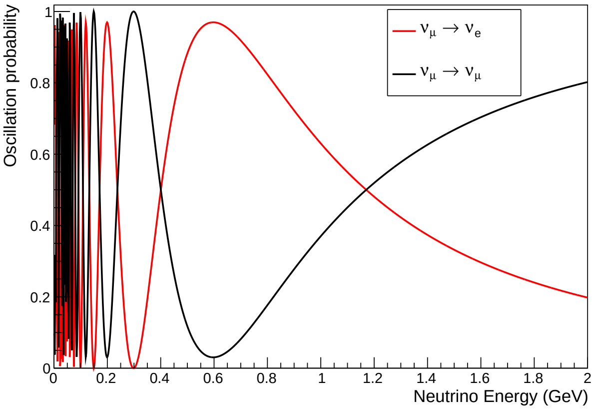

Figure 2.3: Oscillation probabilities with two generations as a function of neutrino energy calculated by Eq. 2.6. L=300 km, Δm^2_{21}=0.0025 eV, θ =40 degrees are assumed.

These equations with the two generations are expanded to three generations as follows:

$$|\nu_\alpha\rangle = \sum_i U_{\alpha i}\,|\nu_i\rangle \tag{2.11}$$

where $\alpha = e, \mu, \tau$ and i=1,2,3. $U_{\alpha i}$ is an element of 3×3 unitary matrix. This is the standard three flavor mixing model. The matrix is called Pontecorvo-Maki-Nakagawa-Sakata (PMNS) matrix [3], parametrized as follows:

$$\begin{aligned} U &= \begin{pmatrix} 1 & 0 & 0 \\ 0 & c_{23} & s_{23} \\ 0 & -s_{23} & c_{23} \end{pmatrix} \begin{pmatrix} c_{13} & 0 & s_{13}e^{-i\delta_{CP}} \\ 0 & 1 & 0 \\ -s_{13}e^{i\delta_{CP}} & 0 & c_{13} \end{pmatrix} \begin{pmatrix} c_{12} & s_{12} & 0 \\ -s_{12} & c_{12} & 0 \\ 0 & 0 & 1 \end{pmatrix} \\ &= \begin{pmatrix} c_{12}c_{13} & s_{12}c_{13} & s_{13}e^{-i\delta_{CP}} \\ -s_{12}c_{23} - c_{12}s_{13}s_{23}e^{i\delta_{CP}} & c_{12}c_{23} - s_{12}s_{23}s_{13}e^{i\delta_{CP}} & c_{13}s_{23} \\ s_{12}s_{23} - c_{12}s_{13}c_{23}e^{i\delta_{CP}} & -c_{12}s_{23} - s_{12}s_{23}s_{13}e^{i\delta_{CP}} & c_{13}c_{23} \end{pmatrix} \end{aligned} \tag{2.12}$$

where $c_{ij}(s_{ij})$ mean $\cos\theta_{ij}$ $(\sin\theta_{ij})$. θ_{ij} are mixing angles and δ_{CP} is a CP phase. The probability of the neutrino oscillation after traveling the distance L in vacuum is calculated as follows:

$$\begin{aligned} P(\nu_\alpha \to \nu_\beta) = \delta_{\alpha\beta} \quad &- \quad 4\sum_{i>j} \mathrm{Re}(\mathrm{U}^*_{\alpha\mathrm{i}}\mathrm{U}_{\beta\mathrm{i}}\mathrm{U}_{\alpha\mathrm{j}}\mathrm{U}^*_{\beta\mathrm{j}})\sin^2\left(\frac{\Delta \mathrm{m}^2_{\mathrm{ij}}\mathrm{L}}{4\mathrm{E}}\right) \\ &- \quad 2\sum_{i>j} \mathrm{Im}(\mathrm{U}^*_{\alpha\mathrm{i}}\mathrm{U}_{\beta\mathrm{i}}\mathrm{U}_{\alpha\mathrm{j}}\mathrm{U}^*_{\beta\mathrm{j}})\sin\left(\frac{\Delta \mathrm{m}^2_{\mathrm{ij}}\mathrm{L}}{2\mathrm{E}}\right) \end{aligned} \tag{2.13}$$

In case of accelerator neutrino experiments, neutrinos go through matter of earth not vacuum. In that case, the electron neutrinos coherently interact with electron in matter by exchanging

W boson, although the muon and tau neutrinos does not. This effect is called “matter effect” and additional potential V is added to the Schrődinger equation:

$$\begin{aligned} i\frac{d}{dt}\left|\nu(t)\right\rangle &= (H_{\rm vac}+V)\left|\nu(t)\right\rangle \qquad (2.14)\\ V &= \begin{pmatrix} +(-)\sqrt{2}G_F n_e & 0 & 0\\ 0 & 0 & 0\\ 0 & 0 & 0\end{pmatrix} \qquad (2.15)\end{aligned}$$

where G_F is Fermi constant and n_e is electron density in matter. The sign is $+$ for ν_e and $-$ for $\overline{\nu}_e$. Including the matter effect, the oscillation probabilities of $\nu_\mu \to \nu_e$ and $\nu_\mu \to \nu_\mu$ for long base line accelerator neutrino experiments are concretely written as follows [21] [22]:

$$\begin{aligned} P(\nu_\mu\to\nu_e) &= 4c_{13}^2s_{13}^2s_{23}^2\Big(1+\frac{2a}{\Delta m_{31}^2}(1-2s_{13}^2)\Big)\sin^2\Phi_{31}\\ &\quad +8c_{13}^2s_{12}s_{13}s_{23}(c_{12}c_{23}\cos\delta_{CP}-s_{12}s_{13}s_{23})\cos\Phi_{32}\sin\Phi_{31}\sin\Phi_{21}\\ &\quad +(-)8c_{13}^2c_{12}c_{23}s_{12}s_{13}s_{23}\sin\delta_{CP}\sin\Phi_{32}\sin\Phi_{31}\sin\Phi_{21}\\ &\quad +4s_{13}^2c_{13}^2(c_{12}^2c_{23}^2+s_{12}^2s_{23}^2s_{13}^2-2c_{12}c_{23}s_{12}s_{13}\cos\delta_{CP})\sin^2\Phi_{21}\\ &\quad -2c_{13}^2s_{13}^2s_{23}^2\frac{aL}{E}(1-2s_{13}^2)\cos\Phi_{32}\sin\Phi_{31} \qquad (2.16)\\ &\simeq \sin^2 2\theta_{13}\sin^2\theta_{23}\sin^2\Phi_{31}+(-)\propto\sin\delta_{CP}+\text{matter effect} \qquad (2.17)\\ P(\nu_\mu\to\nu_\mu) &= 1-4c_{13}^2s_{23}^2(c_{13}^2c_{23}^2+s_{12}^2s_{13}^2s_{23}^2)\sin^2\Phi_{32}-4c_{12}^2s_{23}^2(s_{12}^2c_{23}^2+c_{12}^2s_{13}^2s_{23}^2)\sin^2\Phi_{31}\\ &\quad +c_{13}^2s_{13}^2s_{23}^2(1-2c_{13}^2s_{23}^2)\frac{8a}{\Delta m_{31}^2}\sin\Phi_{31}(\sin\Phi_{31}-\Phi_{31}\cos(\Phi_{31}))\\ &\quad -8c_{12}c_{13}^2c_{23}s_{12}s_{13}s_{23}^3\cos\delta_{CP}(\sin^2\Phi_{31}-\sin^2\Phi_{32})\\ &\quad -4\Big((c_{12}^2c_{23}^2+s_{12}^2s_{13}^2s_{23}^2)(s_{12}^2c_{23}^2+c_{12}^2s_{13}^2s_{23}^2)-4c_{12}^2c_{23}^2s_{12}^2s_{13}^2s_{23}^2\cos^2\delta_{CP}\\ &\quad +2c_{12}c_{23}s_{12}s_{13}s_{23}(c_{23}^2-s_{13}^2s_{23}^2)(c_{12}^2-s_{12}^2)\cos\delta_{CP}\Big)sin^2\Phi_{21} \qquad (2.18)\\ &\simeq 1-(\cos^4\theta_{13}\sin^2 2\theta_{23}+\sin^2 2\theta_{13}\sin^2\theta_{23})\sin^2\Phi_{32} \qquad (2.19)\end{aligned}$$

$$\Phi_{ij}=\frac{\Delta m_{ij}^2 L}{4E}\simeq 1.267\times\frac{\Delta m_{ij}^2\ (\text{eV}^2)\times\text{L (km)}}{E\ (\text{GeV})} \qquad (2.20)$$

$$a=2\sqrt{2}G_F n_e E\simeq 7.6\times10^{-5}\times E\ (\text{GeV})\times\rho\ (\text{g/cm}^3)\ [\text{eV}^2] \qquad (2.21)$$

The probability of anti neutrino oscillations are represented as the same equations, except for the matter effect and opposite sign of the third term.

Through the measurement of these oscillation probabilities, we can measure the parameters of θ_{13}, θ_{23}, Δm_{32}^2 and δ_{CP}. Figures 2.4 and 2.5 show the oscillation probabilities with various oscillation parameters for example. The $\nu_\mu \to \nu_\mu$ and $\overline{\nu}_\mu \to \overline{\nu}_\mu$ (disappearance) channels are sensitive to the θ_{23} and Δm_{32}^2 as shown in Fig. 2.4. Meanings of the parameters are the same as that with the two generations: amplitude of the probability depends on θ_{23} and oscillation period depends on Δm_{32}^2. On the other hand, the $\nu_\mu \to \nu_e$ and $\overline{\nu}_\mu \to \overline{\nu}_e$ (appearance) channels are sensitive to the θ_{13} and δ_{CP} as shown in Fig. 2.5. Especially, a comparison of $P(\nu_\mu \to \nu_e)$ and $P(\overline{\nu}_\mu \to \overline{\nu}_e)$ is sensitive to the δ_{CP} because the sign of the third term in Eq. 2.16 is opposite. The comparison is important because it is sensitive to any CP violations including effect of a new physics behind the standard three flavor mixing model. In addition, the appearance channels are sensitive to the order of mass eigenstates (mass hierarchy) because the matter effect term in Eq. 2.16 depends on the mass hierarchy as shown in Fig. 2.5. The case of $m_1 < m_3$ is called normal hierarchy (NH) and $m_1 > m_3$ is called inverted hierarchy(IH). We can measure other parameters not covered by the accelerator neutrino experiments through the measurements of different types of the neutrino oscillation in the same way basically.

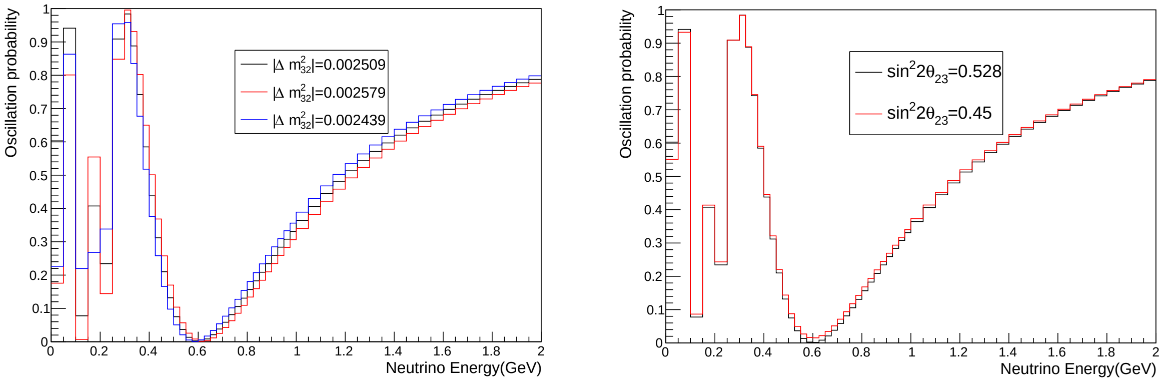

$\nu_\mu \rightarrow \nu_\mu$ (Δm^2_{32}) $\nu_\mu \rightarrow \nu_\mu$ (θ_{23})

Figure 2.4: Probabilities of $\nu_\mu \rightarrow \nu_\mu$ oscillation with various oscillation parameters. The Δm^2_{32}(left) and θ_{23}(right) are varied with 1σ uncertainty. The other oscillation parameters are fixed near the best fit values shown in Table 2.1. L=295 km is assumed.

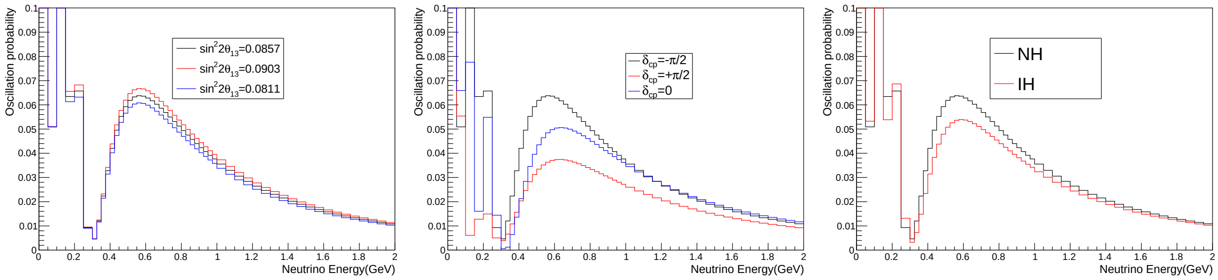

$\nu_\mu \rightarrow \nu_e$ (θ_{13}) $\nu_\mu \rightarrow \nu_e$ (δ_{CP}) $\nu_\mu \rightarrow \nu_e$ (mass hierarchy)

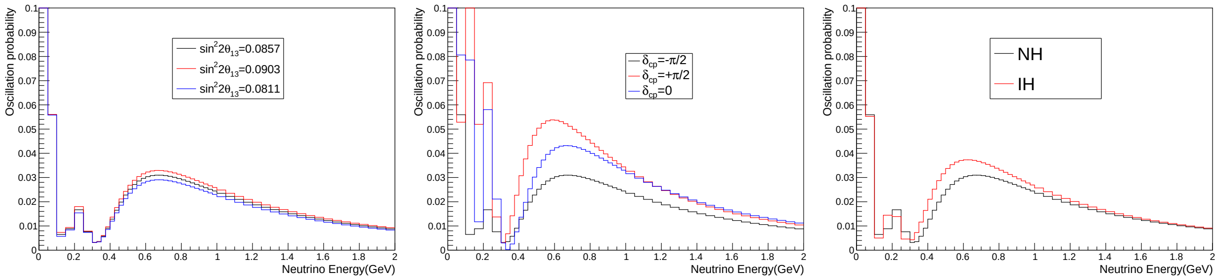

$\overline{\nu}_\mu \rightarrow \overline{\nu}_e$ (θ_{13}) $\overline{\nu}_\mu \rightarrow \overline{\nu}_e$ (δ_{CP}) $\overline{\nu}_\mu \rightarrow \overline{\nu}_e$ (mass hierarchy)

Figure 2.5: Probabilities of $\nu_\mu \rightarrow \nu_e$ (top) and $\overline{\nu}_\mu \rightarrow \overline{\nu}_e$ oscillations (bottom) with various oscillation parameters. The Δm^2_{32}(left) and θ_{23}(right) are varied with 1σ uncertainty. The other oscillation parameters are fixed near the best fit values shown in Table 2.1. L=295 km is assumed.

We are not sure if the standard three flavor mixing model represented by Eq. 2.11 completely describes the neutrino flavor mixing structure. In order to validate the standard three flavor mixing model, each parameter of the PMNS matrix and Δm^2 have been measured by several neutrino oscillation experiments. The measured best fit values of the parameters are summarized in Table 2.1 [4]. θ_{12} and Δm^2_{21} have been measured by solar neutrino [23] and KamLAND [24] experiments. θ_{23} and $|\Delta m^2_{32}|$ are measured by atmospheric neutrino measurements, Super-Kamiokande [25], IceCube [26] etc. and accelerator measurements, MINOS [27], T2K [28] and NOνA [29]. θ_{13} is measured by reactor experiments, Daya Bay [30], Double Chooz [31], RENO [32] and T2K. δ_{CP} is partially limited by combination of reactor and accelerator experiments, although $\delta_{CP} = 0$ is not excluded. The measured parameters are compared between these experiments for the validation as shown in Figs. 2.6–2.9. There is not significant tensions between the experiments at present.

Table 2.1: Summary of the measured parameters of the PMNS matrix and Δm^2 [4]. Normal hierarchy is assumed and inverted hierarchy is assumed in parentheses.

Parameters	Best fit	3σ
$\sin^2\theta_{12}$	0.297	0.250-0.354
$\sin^2\theta_{23}$	0.425(0.589)	0.381-0.615(0.384-0.636)
$\sin^2\theta_{13}$	0.0215(0.0216)	0.0190-0.0240(0.0190-0.0242)
δ_{CP}/π	1.38(1.31)	-
$\Delta m^2_{21}[10^{-5}\ \mathrm{eV}^2]$	7.37	6.93-7.96
$\Delta m^2_{32(31)}[10^{-3}\ \mathrm{eV}^2]$	2.56(2.54)	2.45-2.69(2.42-2.66)

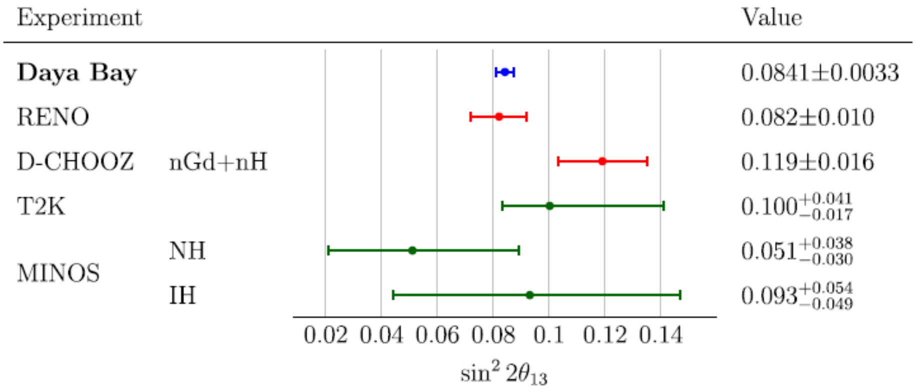

Figure 2.6: Measured values of the θ_{13} with several reactor and accelerator experiments [34].

2.4 Remained questions of neutrino oscillation

Inspite of these effort, there are a few outstanding issues related to the neutrino oscillations. Topics related to this thesis are picked up as follows.

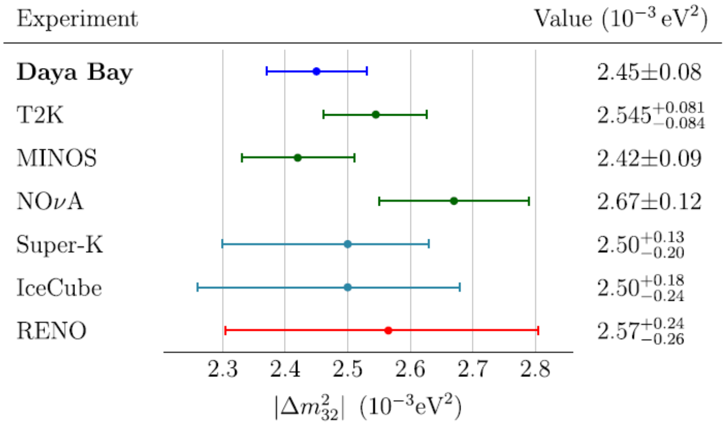

Figure 2.7: Measured values of $|\Delta m^2_{32}|$ with several reactor, atmospheric and accelerator experiments [34].

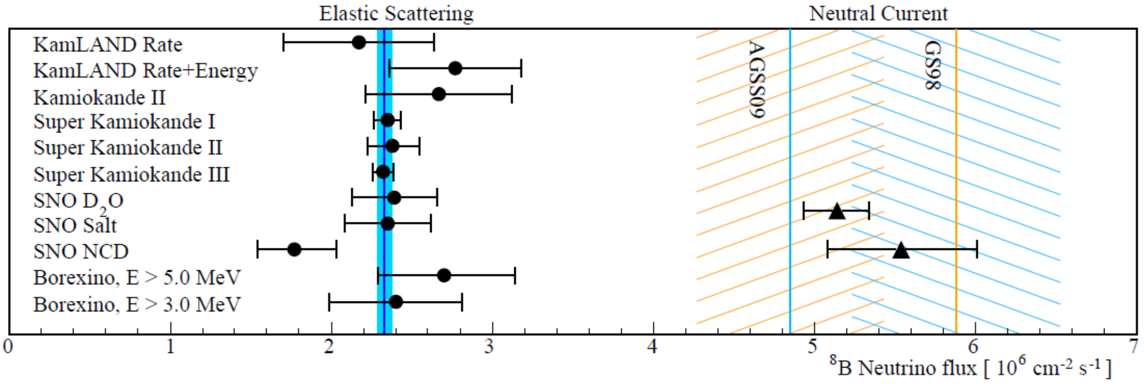

Figure 2.8: Solar neutrino flux emitted from ^8B measured with several experiments [23].

2.4.1 Observation of CP violation in lepton sector

CP violation can be a key to explain the matter-antimatter asymmetry in the universe. The CP violation in the quark sector was observed in 1964 [33] and the size of the violation was too small to explain the matter-antimatter asymmetry in the universe. On the other hand, there is no measurement of the CP violation in the lepton sector so far and it is possible to explain the matter-antimatter asymmetry with large CP violation in the lepton sector with the leptogenesis scenario [2]. In the PMNS parametrized in Eq. 2.12, the magnitude of the CP violation in $\nu_l \to \nu_{l'} (l \neq l')$ is determined by invariant J_{CP}, associated with the δ_{CP} [35]:

$$\begin{aligned} J_{\mathrm{CP}} &= \mathrm{Im}(\mathrm{U}_{\mu 3}\mathrm{U}^*_{\mathrm{e}3}\mathrm{U}_{\mathrm{e}2}\mathrm{U}^*_{\mu 2}) && (2.22) \\ &= \frac{1}{8}\cos\theta_{13}\sin 2\theta_{12}\sin 2\theta_{23}\sin 2\theta_{13}\sin\delta_{CP} && (2.23) \end{aligned}$$

Because the values of θ_{13}, θ_{12} and θ_{23} are known experimentally, δ_{CP} determines the magnitude of the CP violation in the lepton sector. At present, δ_{CP} can be measured only through the accelerator neutrino experiments by comparing the neutrino appearance and anti neutrino ap-

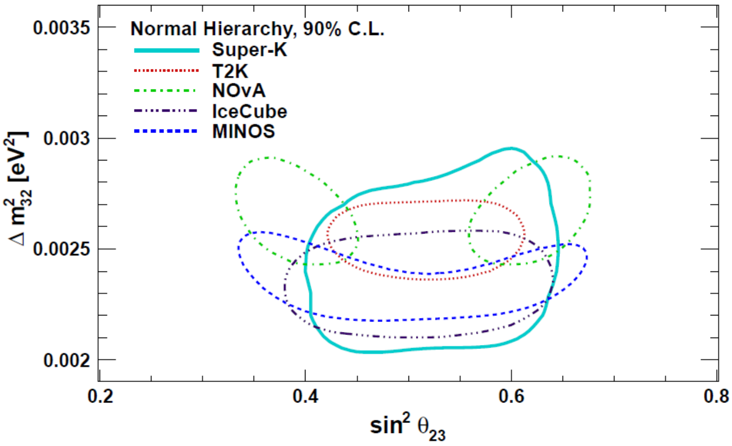

Figure 2.9: Measured values of $\sin^2\theta_{23}$ vs $|\Delta m^2_{32}|$ with several accelerator and atmospheric experiments assuming normal hierarchy [4].

pearance. The comparison is important because it is sensitive to any CP violations including effect of a new physics behind the standard three flavor mixing model.

2.4.2 Large value of mixing parameters

The mixing parameters of the PMNS matrix ($\theta_{12} = 33 \pm 1$, $\theta_{23} = 46 \pm 3$ and $\theta_{13} = 8.9 \pm 0.4$ degrees) are large compared with the flavor mixing in the quark sector ($\theta_{12}^{CKM} = 13.04 \pm 0.05$, $\theta_{23}^{CKM} = 2.38 \pm 0.06$ and $\theta_{13}^{CKM} = 0.201 \pm 0.011$ degrees) [4]. Especially, the measured value of θ_{23} is near 45 degrees corresponding to maximal $\nu_\mu \to \nu_\mu$ oscillation and it is interesting that if θ_{23} is exactly 45 degrees or not. There are theoretical models to derive $\theta_{23} = 45$ degrees and large mixing angles. An example is a flavor symmetry which drives Tri-bimaximal mixing [36], although the simplest Tri-bimaximal mixing is not consistent with the measured value of θ_{13} and correction of the model is needed. More precise measurements of the mixing parameters including δ_{CP} are needed to identify the correct model.

2.4.3 Determination of mass hierarchy

We are not sure if the mass hierarchy is normal or inverted. It is important to determine the mass hierarchy because the masses are essential parameters of the SM. If the mass hierarchy is determined, limit of each neutrino mass is more constrained than the current limit because the sum of the neutrino masses are constrained by cosmology and astrophysics. In addition, the mass hierarchy is related to the origin of the neutrino masses. The neutrino masses can be simply introduced by assuming additional right handed particles in the SM and two types of the particles are possible: Dirac particles and Majorana particles. If the Majorana particle and inverted hierarchy are assumed, the predicted lower limit of effective mass ($m_{\beta\beta}$) of neutrino less double beta decay is near the current experiment limit by KamLAND-Zen experiment [37].

2.4.4 Observation of each type of neutrino oscillation

The standard three flavor mixing model predicts that three kinds of neutrinos oscillate each other. Including the anti neutrino oscillations, there are $3 \times 3 + 3 \times 3 = 18$ types of the neutrino oscillations. Observation of each type of oscillation is important to validate the three flavor mixing model, however, only a few of them are observed independently as listed in Table 2.2 [1]. It is important to observe each type of oscillation to validate the standard oscillation framework.

Table 2.2: Status of search for each type of neutrino oscillation. The oscillations observed with a significance of 3σ separated from the other types of oscillations are filled with a circle.

After oscillation		ν_e	ν_μ	ν_τ
Before oscillation	ν_e	○ [9]		
	ν_μ	○ [38]	○ [39]	○ [40]
	ν_τ			
After oscillation		$\overline{\nu}_e$	$\overline{\nu}_\mu$	$\overline{\nu}_\tau$
Before oscillation	$\overline{\nu}_e$	○ [41]		
	$\overline{\nu}_\mu$		○ [27]	
	$\overline{\nu}_\tau$			

2.5 Accelerator neutrino experiments

To solve the outstanding issues, the long baseline accelerator neutrino experiments takes an important role. The accelerator experiments measure the $\nu_\mu \to \nu_e$, $\nu_\mu \to \nu_\mu$, $\overline{\nu}_\mu \to \overline{\nu}_e$ and $\overline{\nu}_\mu \to \overline{\nu}_\mu$ oscillations[2]. At present, topics explained in Sec. 2.4 are physics goals of the accelerator neutrino experiments: observation of the CP violation in the lepton sector, measurement of the oscillation parameters of θ_{23}, Δm^2_{32}, θ_{13}, δ_{CP} as well as mass hierarchy and observation of the $\overline{\nu}_\mu \to \overline{\nu}_e$ oscillation.

Figure 2.10 shows a schematic view of the accelerator neutrino experiment. In the accelerator neutrino experiments, ratio of the flight distance and neutrino energy (L/E in Eq. 2.13) is optimized to about 500 km/GeV to maximize the oscillation probabilities. As shown in Table 2.3, the flight distance is set to a few hundreds kilometers because the neutrino energy should be more than a few hundreds MeV by considering size of neutrino-nucleus cross sections for neutrino detection, as described in Chapter 3. In order to detect neutrinos with long flight distance, high intensity neutrino beam and huge target detectors are used as shown in Table 2.3.

Table 2.3: Summary of the long baseline accelerator neutrino experiments

Data taking period	Experiment	Beam power	ν beam energy	Flight distance	Detector mass	Note
1999-2004	K2K [42]	5 kW	∼1 GeV	250 km	22.5 kton	
2005-2012	MINOS [27]	350 kW	∼3 GeV	735 km	5 kton	
2013-2016	MINOS+ [43]	700 kW	∼7 GeV	735 km	5 kton	
2009-	T2K [28]	500kW	∼0.6 GeV	295 km	22.5 kton	at present
2014-	NOνA [29]	700kW	∼2 GeV	810 km	14 kton	at present
Middle of 2020s -	Hyper-K [44]	1.3MW	∼0.6 GeV	295 km	190 kton	future
Middle of 2020s -	DUNE [45]	1.2MW	∼3 GeV	1300 km	68 kton	future

In the accelerator neutrino experiment, the muon neutrino beam is produced with decay of the pions emitted by hadronic interactions of the primary proton beam and fixed target. In

---

[1] In addition, sum of the $\nu_e \to \nu_e$, $\nu_e \to \nu_\mu$ and $\nu_e \to \nu_\tau$ is observed by solar neutrino experiment (SNO) [20]. Sum of the $\nu_e \to \nu_\mu$, $\overline{\nu}_e \to \overline{\nu}_\mu$, $\nu_\mu \to \nu_\mu$ and $\overline{\nu}_\mu \to \overline{\nu}_\mu$ and sum of the $\nu_e \to \nu_\tau$, $\overline{\nu}_e \to \overline{\nu}_\tau$, $\nu_\mu \to \nu_\tau$ and $\overline{\nu}_\mu \to \overline{\nu}_\tau$ are observed by atmospheric neutrino experiment (SK) [1].

[2] except for OPERA experiment measuring $\nu_\mu \to \nu_\tau$

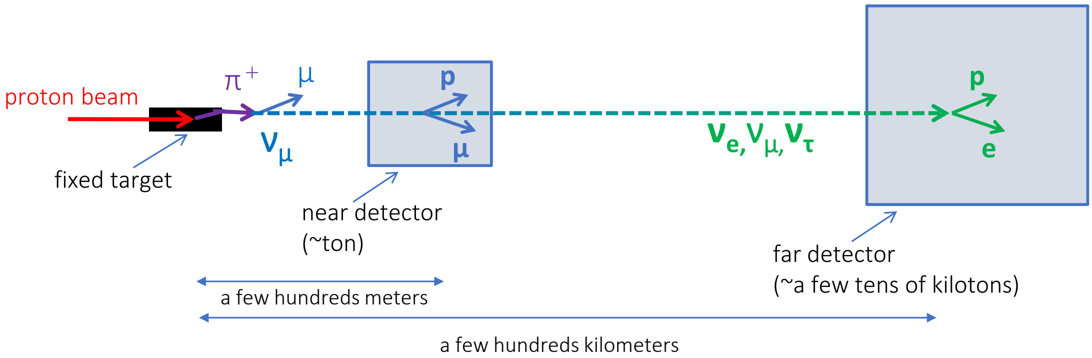

Figure 2.10: Schematic view of the general long baseline accelerator neutrino experiment.

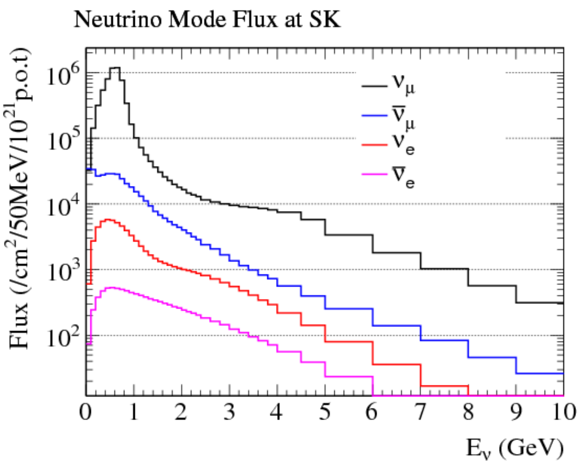

Figure 2.11: Expected muon neutrino flux at T2K far detector [46]. The stacked histgrams represent the particle content.

on-going experiments, the energy of the proton beam is 30 GeV(T2K) or 120 GeV (NOνA). Figure 2.11 shows the expected neutrino flux for the T2K and NOνA. The neutrino energy is not monochromatic due to the way of the beam production.

The produced neutrino beam is measured by two detectors in general. The first detector called "near detector" is a few tons target mass detector located at a few hundred meters downstream of the target for the neutrino beam production. Purpose of the near detector is to constrain uncertainties of the neutrino flux and neutrino-nucleus interaction, which are sources of systematic uncertainties of the oscillation measurement. Without the constraint of the near detector, their uncertainties are more than 10%. In order to constrain the neutrino flux and interaction, the near detector measures the number of neutrinos before the oscillations by detecting secondary particles emitted from the neutrino interactions with the target nucleus. The number of observed neutrino events at the near detector, $N^{\mathrm{obs}}_{\mathrm{near}}$, is written as follows:

$$N^{\mathrm{obs}}_{\mathrm{near}} = \Phi_{\mathrm{near}} \times \sigma \times \varepsilon_{\mathrm{near}} \times T_{\mathrm{near}} \tag{2.24}$$

where Φ_{near} is the time integrated neutrino flux at the near detector, σ is the cross section of neutrino-nucleus interactions, $\varepsilon_{\mathrm{near}}$ is detection efficiency of the near detector and T_{near} is the number of target nuclei of the near detector. Typical values $N^{\mathrm{obs}}_{\mathrm{near}}$ is a few of tens thousand in the on-going experiments. Through the measurement of $N^{\mathrm{obs}}_{\mathrm{near}}$, $\Phi_{\mathrm{near}} \times \sigma$ is constrained with a few percents accuracy.

The second detector called "far detector" is a few of tens kilotons target mass detector located at a few hundred kilometers away from the source of the neutrino beam. The far detector measures the number of neutrinos after the oscillations. The number of observed electron neutrino and muon neutrino events at the far detector, $N^{\text{obs}}_{\text{far electron}}$ and $N^{\text{obs}}_{\text{far muon}}$, are written as follows:

$$N^{\text{obs}}_{\text{far electron}} = \Phi_{\text{far}} \times \sigma \times \varepsilon_{\text{far electron}} \times T_{\text{far}} \times P_{\text{osc } \nu_\mu \to \nu_e}(\theta, \delta_{CP}, \Delta m^2, E_\nu) \tag{2.25}$$

$$N^{\text{obs}}_{\text{far muon}} = \Phi_{\text{far}} \times \sigma \times \varepsilon_{\text{far muon}} \times T_{\text{far}} \times P_{\text{osc } \nu_\mu \to \nu_\mu}(\theta, \delta_{CP}, \Delta m^2, E_\nu) \tag{2.26}$$

where Φ_{far} is the integrated muon neutrino flux at the far detector assuming no oscillation, ε_{far} is detection efficiency of the far detector and T_{far} is the number of target nuclei of the far detector. P_{osc} is the probability of the neutrino oscillation which depends on the oscillation parameters and neutrino energy. Through the measurement of $N^{\text{obs}}_{\text{far}}$ with the neutrino energy, we can measure the oscillation probabilities. The uncertainties of $\Phi_{\text{far}} \times \sigma$ is constrained by the measurement of the near detector with a strong correlation of Φ_{near} and Φ_{far}. Typical values $N^{\text{obs}}_{\text{far electron}}$ is a few tens and $N^{\text{obs}}_{\text{far muon}}$ is one – two hundreds in the on-going experiments.

When the oscillation probability is measured, information of the neutrino energy must be needed because the oscillation probability depends on the neutrino energy. In the accelerator neutrino experiments, the neutrino energy is reconstructed at the far detector based on information of the secondary particles because the neutrino beam is not monochromatic. In a few hundred MeV region of the neutrino energy (T2K), the neutrino energy is reconstructed based on kinematics of the secondary lepton. The main neutrino interaction with the target nucleus is charged current quasi elastic interaction ($\nu_l + n \to l + p$) at that energy. Because this interaction is a 2-body scattering, the neutrino energy is reconstructed as follows:

$$E_\nu = \frac{m_n E_l - m_l^2/2 + (m_p^2 - m_n^2)/2}{m_n - E_l + p_l \cos\theta_l} \tag{2.27}$$

where E_ν is energy of neutrino, m_n is a mass of a neutron, m_p is a mass of a proton, E_l, p_l and θ_l are energy, momentum and angle to the beam direction of the lepton (electron or muon), respectively.

This equation is correct if the target nucleon is free and stopped. However, if the target nucleon is in a nucleus, the equations are not correct anymore as shown in Fig. 2.12 because the nucleon is not stopped in bound states and it is correlated with other nucleons in a nucleus. This effect of neutrino-nucleus cross section on the neutrino oscillation analysis is a few percent in gengeral and it is one of the largest systematic uncertainties of the accelerator neutrino experiments. Table 2.4 shows an example of the systematic uncertainties of the T2K oscillation analysis. In order to achieve more precise neutrino oscillation measurement, more understanding of the neutrino-nucleus interaction is needed.

Table 2.4: Summary of the systematic errors of the predicted event rate at the T2K far detector in 2016 [46].

Error source	ν_μ	$\overline{\nu}_\mu$	ν_e	$\overline{\nu}_e$
Neutrino flux and cross section constrained by near detector	2.8%	3.3%	2.9%	3.2%
Neutrino cross section not constrained by near detector	0.7%	0.8%	3.0%	3.3%
Far detector response	3.9%	3.3%	2.4%	3.1%
Interaction of secondary particle	1.5%	2.1%	2.5%	2.5%
Total systematic uncertainty	5.0%	5.2%	5.4%	6.2%

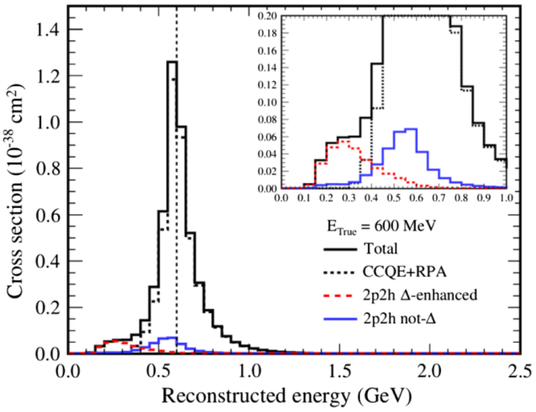

Figure 2.12: Reconstructed energy based on Eq. 2.27 minus true neutrino energy in the T2K experiment [47] with MC simulation. The true neutrino energy is fixed with 600 MeV. Black dotted, red dotted and blue lines show the charged current quasi elastic like interactions with various effect of the nucleus described in Chapter 3. Black solid line is a sum of them.

Chapter 3

Neutrino interaction with a nucleus

In this chapter, basic of neutrino-nucleus interactions is described briefly in order to introduce motivations of the first and second analyses described in Chapters 6 and 7 and the systematic uncertainties of the oscillation analysis described in Chapter 8.

The neutrino interacts with a nucleus through weak interaction, which is one of the fundamental interactions in the SM. The interaction exchanging a W boson is called charged current interaction (CC) and that with a Z boson is called neutral current interaction (NC). A charged lepton is produced corresponding to the flavor of the neutrino in the CC but not in the NC. As shown in Figs. 3.1 and 3.2, the CC is separated into several interaction modes based on the final state of secondary particles.

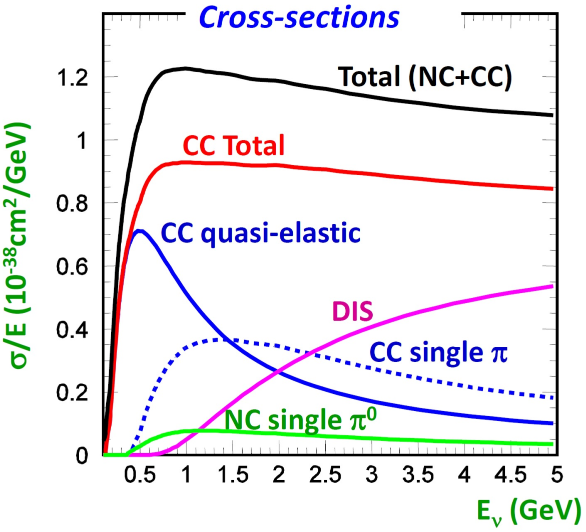

Figure 3.1: Cross sections of the neutrino-nucleus interactions with several interaction modes calculated with MC simulation. [48, 49]

3.1 Charged current quasi-elastic interaction with a nucleon

Charged current quasi elastic interaction (CCQE, $\nu_l(k) + n \rightarrow l(k') + p$, l is e or μ) is the main signal of the T2K far detector because it is two body scattering and the neutrino energy is reconstructed by kinematics of lepton and neutrino direction as shown in Eq. 2.27. Differential

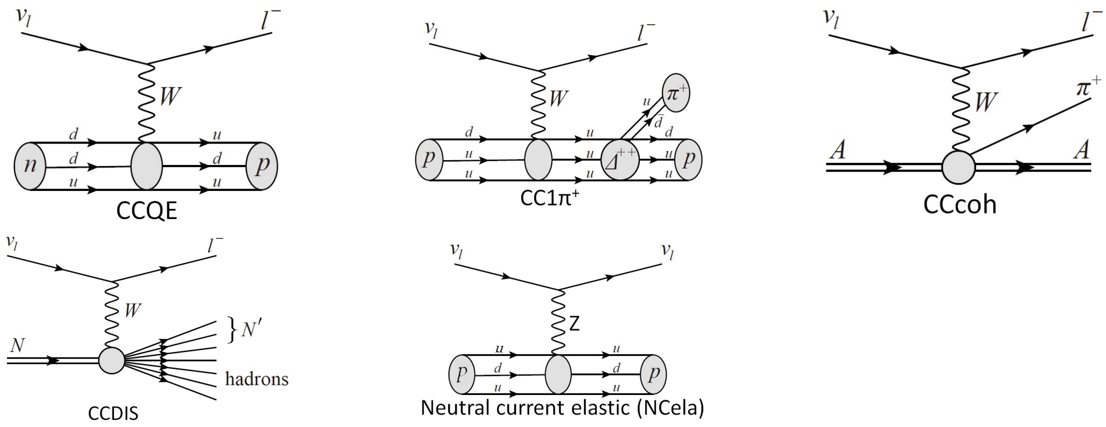

Figure 3.2: Neutrino interaction mode with a nucleus

cross section of the CCQE interaction is written as follows [50]:

$$\frac{d\sigma}{dq^2} \quad = \quad \frac{1}{32\pi}\frac{1}{M^2E_\nu^2}G^2c_{CC}^2L_{\alpha\beta}H^{\alpha\beta} \tag{3.1}$$

where q is 4 momentum transfer ($q^2 = (k'^0 - k^0)^2 - (\boldsymbol{k'} - \boldsymbol{k})^2$), $E_\nu = k^0$ is the neutrino energy in the laboratory frame, M is the nucleon mass, G is the Fermi constant and $c_{cc} = \cos(\theta_C)$ in terms of the Cabibbo angle. $L_{\alpha\beta}$ is leptonic tensor and $H^{\alpha\beta}$ is hadronic tensor as described in appendix A in detail. The hadronic part is approximated by dipole form factor and the CCQE cross section is parameterized by an axial vector mass (M_A^{QE}) [51]. [1] The M_A^{QE} is measured to be 1.016 ± 0.026 GeV by neutrino-hydrogen scattering experiment in the early 1980s. [54] As shown in Fig. 3.1, the CCQE is dominant with neutrino energy of a few hundred MeV.

3.2 Charged current quasi-elastic interaction with a nucleus

It is experimentally known that the neutrino interaction with nucleus is not the same as the neutrino interaction with a nucleon. For example, the first double differential cross section measurement of CCQE with carbon as a function of angle and momentum of out going muon by MiniBooNE [55] indicates that a cross section per nucleon is about 20% higher than the measurement of the neutrino-hydrogen scattering. The measured value of M_A^{QE} by MiniBooNE, 1.35 ± 0.17 GeV, is inconsistent with that by the measurement of the neutrino-hydrogen scattering. The similar values of the M_A^{QE} around 1.2 GeV are reported by the several experiments with carbon and oxygen target [50]. At present, the origin of the discrepancy is not understood accurately but considered to be effect of the nucleus as many body system. Models of the neutrino interaction with nucleus have been developed based on many body framework (MBF) of electroweak interactions with nucleus, which successfully describe the measurement of inclusive electron-nucleus scattering [56].

Figure 3.3 shows an example of possible diagrams of the neutrino-nucleus interaction. Because it is difficult to calculate all diagrams precisely, effect of a few models which are considered to have large effect have been estimated. The diagrams with a pair of particle and hole, corresponds to (a) of Fig. 3.3, are called 1p1h or CCQE interactions in custom. The diagrams with two pairs of particle and hole, corresponds to (b) of Fig. 3.3, are called 2p2h interactions. The CC interaction with no pions emitted from a nucleus is called CC0π interaction, includes

---

[1] There have been a few models to improve the dipole approximation [52] [53]

1p1h and 2p2h interactions. Some of the main models of the CC0π interactions are described as follows.

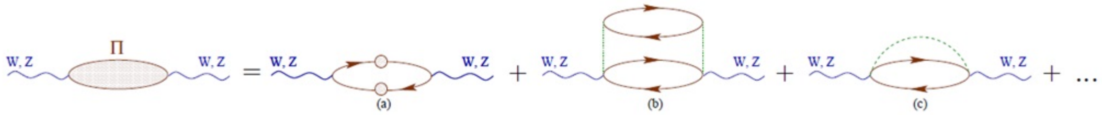

Figure 3.3: Diagram of many-body contributions to the polarization propagator.[50] Solid (dashed) lines correspond to free nucleon (pion) propagators, dotted lines stand for effective nucleon-nucleon interactions. The solid lines with a blob represent full (dressed) nucleon propagators. For nucleons, the lines pointing to the right (left) denote particle (hole) states.

3.2.1 Momentum of nucleon and Pauli blocking

Inside the nucleus, nucleons are in the bound state and moving. Global Fermi gas (RFG) model is the simplest model to describe the behavior of the nucleons in the nucleus [57]. This model assumes that the nucleons are distributed uniformly inside a nucleus. They have binding energy [57][58] and uniform momentum less than Fermi momentum, which is calculated by the number of nucleons in a nucleus. The typical values of the binding energy (E_b) is 25 MeV for ^{12}C and 27 MeV for ^{16}O and that of the Fermi surface momentum (p_F) is 217 MeV for ^{12}C and 225 MeV for ^{16}O. When the secondary protons and neutrons are produced by the neutrino interaction with a nucleon, if their momentum is less than the Fermi momentum, the interactions are not allocated due to Pauli blocking. Figure 3.4 shows the neutrino cross section with carbon target, with and without the RFG. It is suppressed at low energy transfer region due to the Pauli blocking. In addition, momentum of the out going lepton is shifted by the binding energy. By assuming this effect, Eq. 2.27 is modified as follows:

$$E_\nu = \frac{(m_n - E_b)E_l - m_l^2/2 + m_n E_b - E_b^2/2 + (m_p^2 - m_n^2)/2}{m_n - E_b - E_l + p_l \cos\theta_l} \tag{3.2}$$

Not only RFG but other models are being developed. Local Fermi gas (LFG) model [59][60] is the extended model of the RFG motivated by pion-nucleus scattering measurement. It assumes that the density of nucleon is not uniform but depends on the distance between the nucleon and center of the nucleus. There is another approach to determine the momentum distribution of nucleons by fitting the result of the electron scattering measurement (Spectral function, SF) [61] [62] as shown in Fig. 3.5. At present, it is not obvious which is the best model to explain the experimental result of the neutrino-nucleus scattering. These alternative models affects the CC0π interactions on carbon with a few percents roughly.

3.2.2 Random phase space approximation

Following the MBF, the 1p1h contribution is estimated by random phase space approximation (RPA) [63] [64]. In this approximation, many body interaction is assumed as an interaction of a particle in an averaged potential. Effect of RPA correction on the CCQE cross section is about 10%, as shown in Fig. 3.6. It suppressed the cross section with low energy transfer and enlarge that with around 1 GeV.

In addition, more experimentally motivated models than the RPA approximation are being developed, although none of them is available in the MC of the neutrino-nucleus interactions

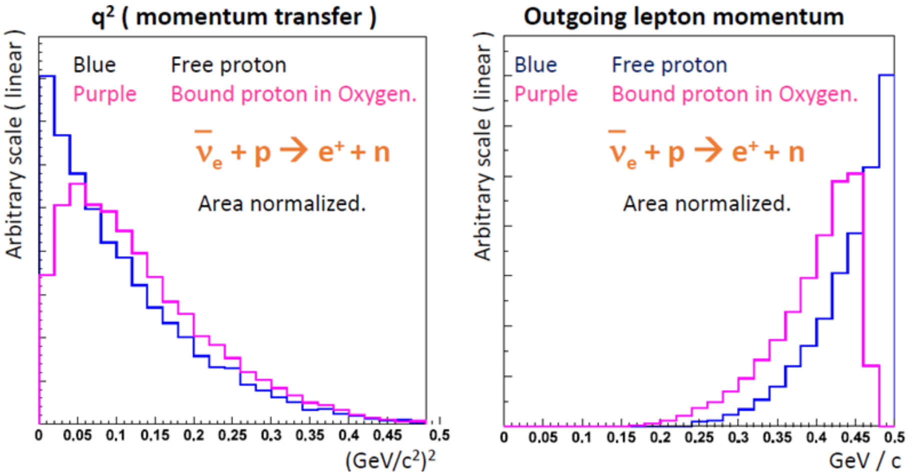

Figure 3.4: CCQE cross section on free proton and bound proton on carbon by assuming the RFG. [49]

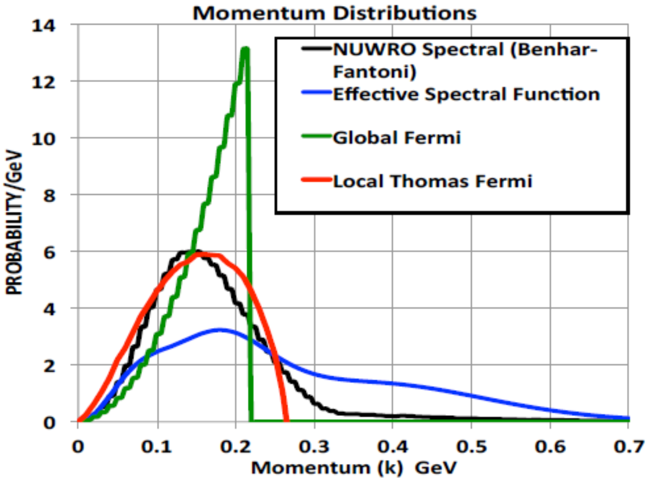

Figure 3.5: Nucleon momentum distributions with several models. [62]

yet. One candidate is continuous RPA correction(CRPA) [65] [66], which is an expansion of the RPA by adding the effect of giant resonance based on result of electron and photon scattering experiment. Figure 3.7 shows the calculated CCQE cross section with the CRPA with several target nucleus. In the CRPA model, dependence of the number of nucleons in a nucleus (A-dependence) is larger than the RPA. The expected difference of the CCQE cross section between CH and H_2O is 10% at maximum by the CRPA, although it is less than 3% in the case of the RPA.

3.2.3 2p2h interaction

Following the MBF, the polarization effects in 2p2h contribution corresponding to (b) of Fig. 3.3 is estimated as short range correlations between the nucleons. Part of the diagrams with propagators of nucleons, pions and Δ particles have been approximately taken into account based on pion and electron scattering measurements [67] [68]. Figure 3.8 shows the calculated cross section of the 2p2h contributions. The expected fraction of the 2p2h interaction is about 10% of the 1p1h interaction. The 2p2h interaction emits two nucleons but it can be miss-recognized as

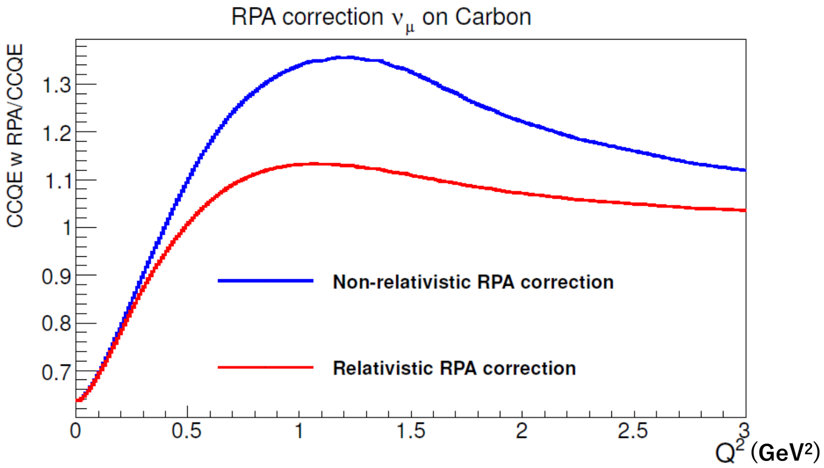

Figure 3.6: Ratio of RPA corrected [64] differential CCQE cross-section to nominal CCQE cross-section for ν_μ on carbon. Non-relativistic (relativistic) nucleon is assumed in blue(red) line.

1p1h interaction because most of the protons can not be detected by the neutrino detectors due to the limited resolution. By adding the 1p1h and 2p2h contributions into the CCQE interaction, the prediction of the MC agree with the data from MiniBooNE as shown in Fig. 3.9, although the 2p2h interaction has not been observed directly by neutrino scattering measurements so far.

3.3 Charged current single pion production

In charged current single π interaction (CC1π, $\nu_l + N \to l + N^{'} + \pi$), a pion is produced due to baryon resonance, mainly Δ baryon. It can be main background events when we select CCQE if the pion is not reconstructed. In addition, this is one of the signals of the T2K because the neutrino energy can be reconstructed by assuming a two body scattering with Δ recoil. It is written as follows:

$$E_{\nu_e}^{\Delta} = \frac{m_N E_e + m_{\Delta^{++}}^2 - m_N^2/2 - m_l^2/2}{m_N - E_e + p_e \cos\theta_e} \tag{3.3}$$

where m_N is a mass of a nucleon. Differential cross section of the CC1π interaction is calculated by assuming the process is composed of excitation of the Δ resonance ($\nu + N \to l + \Delta$) and decay of Δ ($\Delta \to N^{'}\pi$) [70], as described in appendix A. Hadronic tensor is approximated by a form factor parametrized by $C_5^A(0)$ and M_A^{RES}, which determine the cross section of the CC1π interaction. In many neutrino interaction generators, Reign-Sehgal model [71] is used to calculate the cross section with not only Δ but also other resonances. The parameters of the form factor are tuned to be $C_5^A(0) = 0.96 \pm 0.15$ and $M_A^{RES} = 1.07 \pm 0.15$ by neutrino-deuterium scattering measurements [72] [73] [74]. As shown in Fig. 3.1, the CC1π interaction is dominant with neutrino energy of 1-2 GeV. It is known that the Rein-Sehgal model does not explain the electron scattering data and the distributions of the pion produced by neutrino interaction is not consistent with this model with about 20% accuracy [50]. A few models are being developed [75] [76] [77] to be consistent with the electron scattering data.

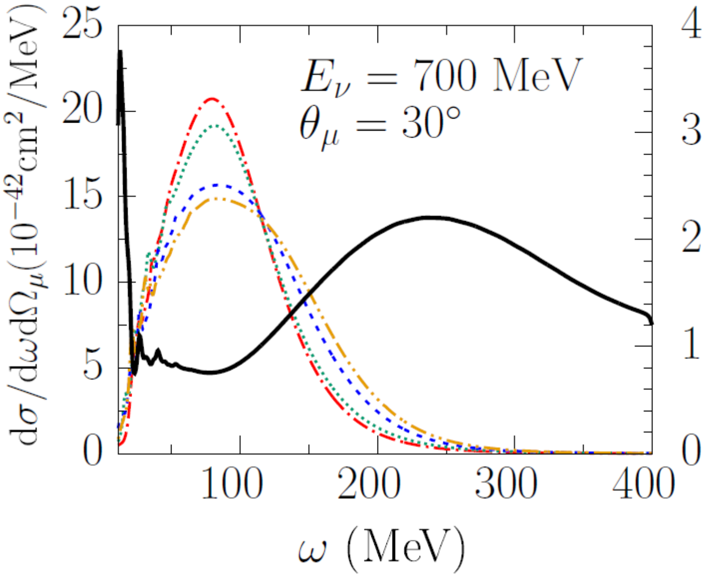

Figure 3.7: Double differential cross sections per neutron (left vertical axis) for monochromatic neutrino energy and muon scattering angle, as a function of w (energy transfer). Line key: ^{12}C dash-dotted, ^{16}O dotted, ^{40}Ar dash dotted and ^{56}Fe dash-double dotted. The cross section ratio $\sigma_{\mathrm{Ar}}/\sigma_{\mathrm{C}}$ is shown in solid black (right vertical axis). [66]

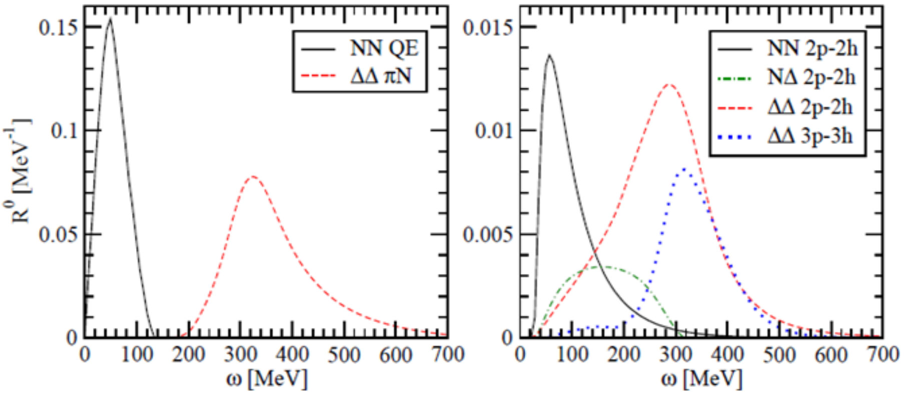

Figure 3.8: Cross sections on ^{12}C at q=300 MeV as a function of the energy transfer with 1p1h(left) and 2p2h(right) [67].

3.4 Charged current deep inelastic scattering

The charged current deep inelastic scattering (CCDIS, $\nu_l + N \rightarrow l + N' +$hadrons), mainly occurs at high neutrino energy region of around or more than a few GeV as shown in Fig. 3.1. The nucleon is broken and many hadrons are produced. It can be approximated as an interaction with a quark and the cross section is written as described in appendix A. The parton distribution functions are well measured, and summarized as library like PYTHIA [78] in high energy transfer region, more than 10 GeV. DIS interaction in this energy region is well understood compared with the other interactions. On the other hand, the parton distribution functions are not well measured in low energy transfer region less than a few GeV. It is extrapolated with parametrized function [79] and measurements with higher energy transfer. DIS is not understood in this energy region experimentally because only a few neutrino scattering experiments (mainly Minerva [80] and MINOS [81]) are available, which agree with the model around 10% accuracy.

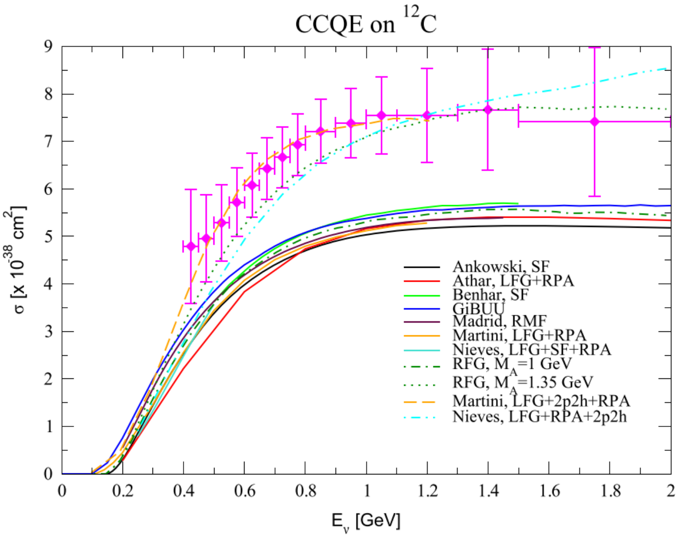

Figure 3.9: Summary of CCQE integrated cross sections as a function of the neutrino energy with several models (line) and data from MiniBooNE [50][69].

3.5 Charged current coherent interaction

In charged current coherent pion production (CC coherent, $\nu_l + N \to \nu_l + N' + \pi$), a neutrino interacts with entire nucleus and produce a pion without changing state of the nucleus. The interaction occurs with low energy transfer. In the T2K, size of the CC coherent cross section is a few percent of the CCQE interactions and not dominant. The cross section of CC coherent is measured by Minerva [82] and it is consistent with interaction model [83] with 30% uncertainty.

3.6 Interaction of secondary pions in nucleus

Pions are produced with the neutrino interactions and interact with nucleus before emitted from the nucleus. The secondary interaction (Final state interaction, FSI) affects the neutrino oscillation measurement because if a pion produced with the CC1π interaction is absorbed, it mimics the CCQE interaction and the relation between the lepton kinematics and true neutrino energy is affected for example. For a few hundreds MeV pions, there are three types of secondary interactions mainly [84]: Scattering, absorption and charge exchange as shown in Fig. 3.10. Because these interactions are hadronic interactions, it is difficult to calculate their cross sections precisely. They are measured by pion scattering measurements with nucleus target and they are understood with a few tens of percents accuracy in general as shown in Fig. 3.11.

3.7 Event generator of neutrino interaction

There are a few event generators to simulate the neutrino-nucleus interactions and NEUT [86] is one of them used in the T2K experiment. NEUT simulates the neutrino interaction with a target nucleus, including final state interactions of the secondary particles inside the nucleus. In NEUT, several types of models of the neutrino-nucleus interactions are selected. The T2K chooses nominal models used for the oscillation analysis based on the results of the external experiments as listed in Table 3.1. Common models of the interactions are used between the ν_μ and ν_e. Common models of the interactions are used between the CC and NC interactions. In addition, secondary interactions of pions in nucleus are simulated based on cascade model [87].

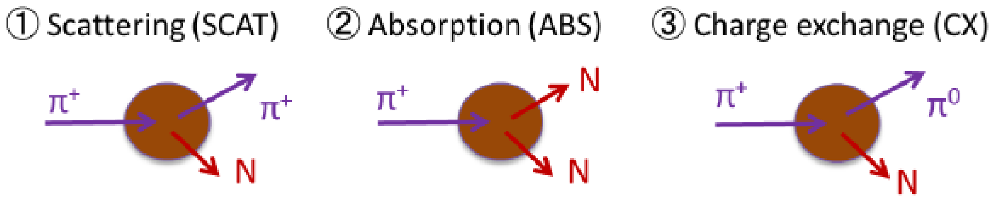

Figure 3.10: Pion interactions on nuclei [84]

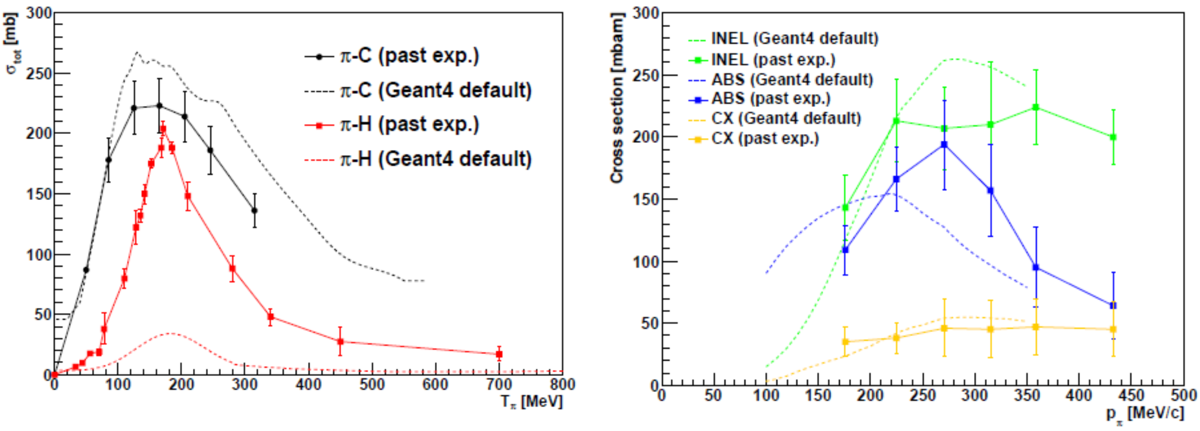

Figure 3.11: Comparison of elastic (left) and inelastic (right) inclusive cross sections as a function of pion momentum in the past experiments and Geant4 default. [84] [85]

The uncertainties of the neutrino interactions are also estimated based on the current understanding. The uncertainties used for the T2K oscillation analysis are briefly described here. The uncertainty of M_A^{QE} and Fermi momentum (p_F) are assigned based on the ND280 measurement. The uncertainty of CC1π parameters are based on deuterium experiments and MiniBooNE experiment. For taking into account the uncertainty of the interaction models, there are effective parameters to tune the interactions. Some of the interactions, 2p2h on ^{12}C, 2p2h on ^{16}O, CC coherent, NC and ν_e interactions have a normalization parameter to scale the total number of interactions with default value of 100%. 100% uncertainty of the 2p2h normalization is assumed for the ν_μ and $\overline{\nu}_\mu$ independently because the 2p2h interaction is not observed by any neutrino scattering measurement so far. In addition, 20% normalization uncertainty is assumed between the 2p2h on ^{12}C and ^{16}O based on theoretical prediction [68]. 30% and 100% normalization are taken as 1σ uncertainties of the coherent and NCγ interactions respectively based on measurement [82]. Based on theoretical prediction, 3% normalization of the ν_e interaction is taken as 1σ uncertainty [88]. The random phase space approximation is effectively parametrized by five parameters, A, B, C, D and U, to cover the difference of the correction between the RFG and

LFG assumption as shown in Fig. 3.12:

$$
\begin{aligned}
f(x) &= \begin{cases} A(1-x')^3 + 3B(1-x')^2x' + 3p_1(1-x')x'^2 + Cx'^3 & (x < U) \\ 1 + p2\exp(-D(x-U)) & (x > U) \end{cases} && (3.4) \\
p_1 &= C + \frac{UD(C-1)}{3} && (3.5) \\
p_2 &= C - 1 && (3.6)
\end{aligned}
$$

The 2p2h interaction has a shape parameter to change fraction of the interactions propagating Δ particle by normalization while keeping the total number of interactions. Because we are not sure which diagrams are dominant based on the experimental result, ±100% is assumed as 1σ uncertainty. The CCDIS interactions has energy dependent normalization parameter x, which scales the event rate by $1+x/E_\nu$ (GeV) with default value of $x = 0$. Because the CCDIS interaction is measured with 10% accuracy at 4 GeV and the accuracy is higher at the higher neutrino energy, $x = 0.4$ is assumed as 1σ uncertainty. In addition, uncertainties of the secondary interactions of pions are estimated based on pion scattering measurements as normalization uncertainties. In addition to these uncertainties, effects of the alternative cross section models are taken into account for the oscillation analysis, as discussed in Sec. 8.

Table 3.1: Used models of the neutrino-nucleus interactions in the T2K experiment and this thesis.

Interaction	Nominal model	Parameter
CC0π	Dipole type axial form factor	$M_A^{QE} = 1.20 \pm 0.03$ GeV
	Relativistic Fermi Gas model(RFG) [57]	E_b=27 MeV± 18 MeV for ^{16}O
		p_F=225± 13 MeV for ^{16}O
	Relativistic random phase space approximation(RPA) [64]	A=0.59±0.12
		B=1.05±0.21
		C=1.13±0.17
		D=0.88±0.35
		U=1.20
	Nieves 2p2h interaction [68]	Normalization=100±100%
		^{16}O/^{12}C Normalization=100±20%
		Shape=100±100%
CC1π	Rein-Sehgal model [71]	$C_5^A(0) = 0.96 \pm 0.15$
		$M_A^{RES} = 1.07 \pm 0.15$ GeV
		Isospin$\frac{1}{2}$bg $= 0.96 \pm 0.40$
CCDIS	PYTHIA [78]	$x = 0 \pm 0.4$
	Parton distribution function GRV98	
	with Bodek and Yang correction [79]	
CC coherent	Barbar-Sehgal model [83]	Normalization=100±30%
ν_e/ν_μ		Normalization=100±3%

3.7.1 Remained questions of neutrino-nucleus interaction measurement

As discussed in the earlier sections, the effect of nucleus on the neutrino-nucleus interaction is not understood accurately and it is a main source of the systematic uncertainties for the neutrino oscillation measurement, as shown in Table 2.4. More precise measurements are needed with a various point of views for choosing the best model to explain the all of the experimental results. The important neutrino-nucleus measurements related to this thesis are picked up as follows.

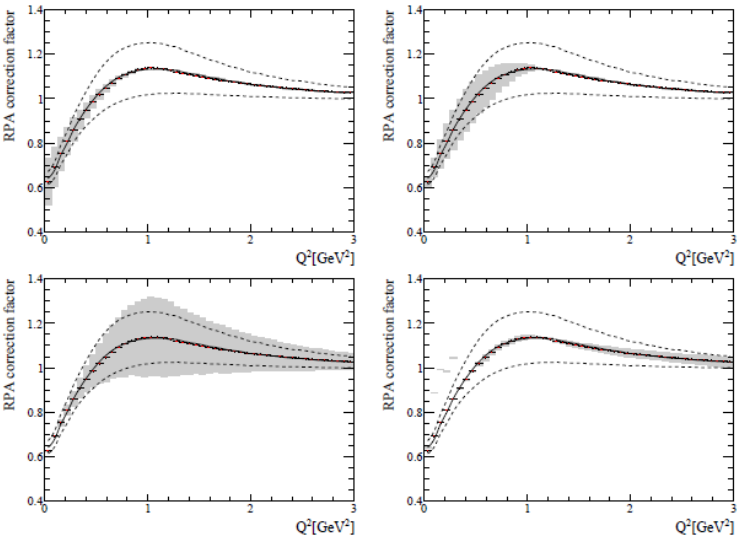

Figure 3.12: RPA correction (solid line) as a function of Q^2 and assumed uncertainty (Gray band) with the parameters of A, B, C and D. The parameter of U is fixed.

3.7.2 Cross section measurement with different target nucleus

The predicted target dependence of the neutrino-nucleus cross section is different between the models due to the resonance structure. To improve and choose the best model, it is important to measure the neutrino-nucleus scattering with several kinds of target nucleus. At present, the cross sections results with several targets are available by different experiments. However, it is difficult to understand the target dependency because treatment of the systematic uncertainties are different between the different experiments. There are only a few successful measurements to measure the target dependency by T2K [89] and MINERνA [90] by measuring ratios of the cross sections with the different targets. The T2K measures the CC inclusive cross section ratio of plastic(CH) and iron(Fe) target with neutrino energy of 1.5 GeV and the result is consistent with the standard modeling of CCQE interaction. On the other hand, the MINERνA measures the cross section ratios of carbon(C), plastic(CH), iron (Fe) and lead (Pb) with neutrino energy from 2 to 20 GeV and part of the results are not consistent with any model at large values of Bjoken x. In order to understand these differences, more measurements with the different target, different neutrino energy and different detector acceptance are needed.

3.7.3 Measurement of leptons with large angular acceptance

It is known that neutrino-nucleus interaction with forward scattered leptons are easily affected by the modeling of the nucleus because the low energy transfer events are dominant, which is sensitive to the momentum distribution of nucleons and the coherent scattering. If the CCQE interaction is measured only with the forward scattered events, the results can be largely biased by the nuclear effects, compared with the case of the full phase space measurement. However, most of recent neutrino cross section measurements are sensitive to only the forward scattered leptons. For example, sensitive area of the T2K near detector is less than 45 degrees of muon angle and that of MINERνA is less than 20 degrees. Only a measurement by MiniBooNE [55]

[91] is available as a cross section measurement with 4π angular acceptance so far but it is difficult to translate the result of MiniBooNE with a framework of the other analyses because systematic uncertainty provided by MiniBooNE does not include covariance between bins and treatment of the background events is dedicated. A new cross section measurements with large angular acceptance is needed to choose the best model of the CCQE.

3.7.4 Measurement of proton

We could not determine the best model of the neutrino interactions based on the information of the leptons only, because the momentum and angle distributions of the leptons are affected by many models and parameters of the neutrino interactions. What we observe is a sum of the all effects and it is difficult to extract the best model in general. Then, not only measurement of leptons but also protons are needed which has significant information of the neutrino-nucleus interactions. For example, it is predicted that the number and momentum of emitted protons are different between the 1p1h and 2p2h interactions. However, at present, most of the neutrino cross section measurements in a few hundreds MeV are mainly sensitive to the leptons and pions and not sensitive to the protons due to the limited detector resolution. It is important to measure the protons produced with the neutrino-nucleus interactions and compare the result with the neutrino interaction model.

Chapter 4

T2K experiment

T2K (Tokai to Kamioka) experiment is one of the long baseline neutrino oscillation experiments, started from 2009 [92]. The ν_μ beam produced by J-PARC in Tokai is detected by near detector (ND280) and far detector (Super-Kamiokande) to measure the oscillation probability of $\nu_\mu \to \nu_e$, $\nu_\mu \to \nu_\mu$ and their anti neutrino mode.

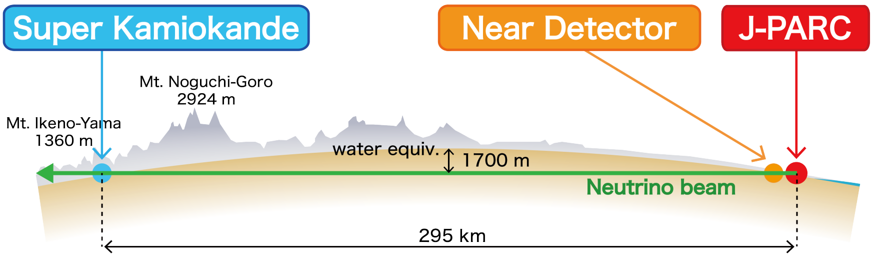

Figure 4.1: Schematic view of the T2K experiment [93]

4.1 J-PARC neutrino beam

J-PARC proton accelerator consists of three accelerators: a 400 MeV linear accelerator (LINAC), a 3 GeV rapid cycling synchrotron (RCS) and a 30 GeV main ring synchrotron (MR). Table 4.1 shows the beam parameters of the MR in May 2018. Figure 4.2 shows a schematic view of the T2K neutrino beam line. To produce the neutrino beam, 30 GeV protons are extracted from the synchrotron ring to strike a graphite target. Emitted pions are focused by three electromagnetic horns. The pions decay in a 96 m decay volume and produce a neutrino beam. By switching the polarity of the horn current, either of the neutrino or anti neutrino beam is selected. With the positive horn current mode (FHC), the neutrino beam is produced. With the negative horn current mode (RHC), the anti neutrino beam is produced. The beam is aimed 2.5° away from the target to the far detector axis to optimize the neutrino energy spectrum. This configuration produces a narrow band beam by the kinematics of pion decays. By the energy conservation law, the relation between the neutrino energy and pion momentum is written as follows:

$$E_\nu = \frac{m_\pi^2 - m_\mu^2}{2(E_\pi - P_\pi \cos\theta)} \tag{4.1}$$

where E_ν is neutrino energy, E_π, P_π are the energy and momentum of pion respectively and θ is the off-axis angle. Dependency of the neutrino energy on the pion momentum is small with the off-axis of a few degrees as shown in Fig. 4.3. The angle of 2.5° is set so that the spectrum has a peak at the first oscillation maximum, around 600 MeV, as shown in Fig. 4.4. At the on-axis, on the other hand, the neutrino energy broadly spread around 1.5 GeV.

Table 4.1: Parameters of the J-PARC MR.

Beam energy	30 GeV
Beam power	500 kW
Spill cycle	2.48 s
Number of bunches	8
Width of a bunch	58 nsec
Bunche cycle	581 nsec

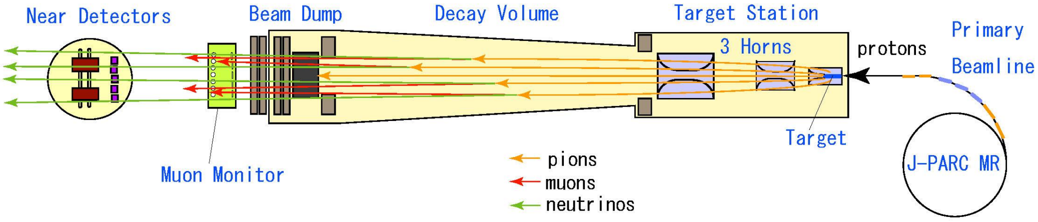

Figure 4.2: View of the T2K neutrino beam line.

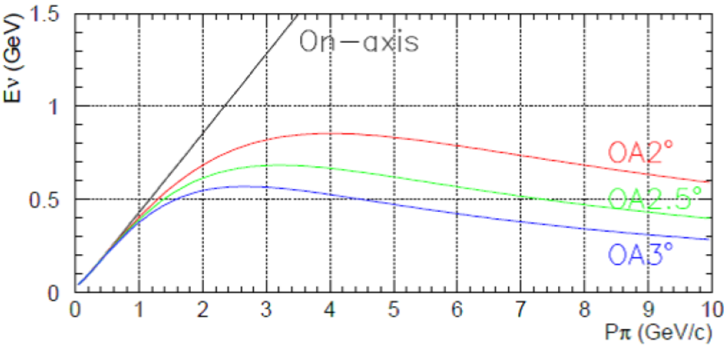

Figure 4.3: Neutrino energy as a function of the moment of pion with different off-axis angles [84].

4.2 Near detector

T2K has two near detectors located 280m downstream from the target. One is located at on-axis and the other is located at off-axis, as shown in Fig. 4.5. One of the on-axis near detectors, INGRID [94], measures the neutrino event rate and the direction of the neutrino beam. As shown in Fig. 4.7, it is composed of 14 modules and each module is a sandwich structure comprised of 9 iron plates and 11 tracking planes which are surrounded by veto planes. The tracking

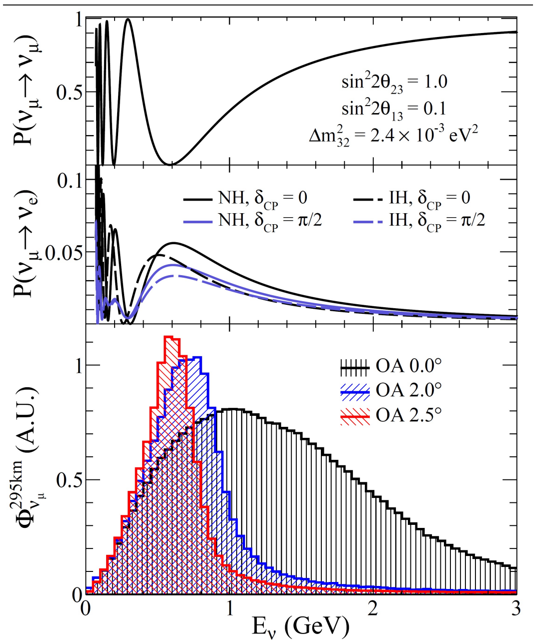

Figure 4.4: The probability of the neutrino oscillation (top) and the muon neutrino flux (bottom).

planes are formed from two layers of plastic scintillators, each of which is composed of 24 bars, that are oriented perpendicularly to one another. The thickness of the iron plate is 6.5 cm, and the thickness of the scintillator is 1.0 cm. In addition, there are plastic target neutrino detector (Proton Module, PM) and water target neutrino detector (water module, WM) for measurements of the neutrino-nucleus interaction. The Proton Module is composed of plastic scintillator planes which serve as an active target. It consists of 34 tracking planes surrounded by six veto planes, where each tracking plane is an array of two types of 32 bars. The tracking planes also serve as the neutrino interaction target. The water module is a main detector in this thesis and composed of water target and plastic scintillators, as described in Section 5 in detail. For all of the three detectors, scintillation light from the scintillator is collected by a wavelength shifting fiber and measured by multi-pixel photon counter (MPPC). In July 2016, the Proton Module was replaced with the water module as shown in Fig. 4.7. The INGRID modules are located at the downstream of the water module and Proton Module. The INGRID modules are used for tagging muons produced by neutrino interaction in the water module and Proton Module.

The off-axis near detector, ND280 [95], measures the neutrino flux and neutrino-nucleus cross section and constrains their uncertainties. It consists of several detectors inside the magnet, as shown in Fig. 4.8. The main detectors are FGD1 (Fine Grained Detector), FGD2 and TPC (Time Projection Chamber). The FGD1 consists of plastic scintillator bar that works as an active target and detects the secondary particles produced by the neutrino interaction. On the other hand, FGD2 has a sandwich structure of water target and plastic scintillator planes. FGD1, FGD2 and three TPCs are arranged alternately along with the beam axis. Secondary particles, produced by neutrino-nucleus interaction occurred in FGD and FGD2, enter the TPC. The TPC identifies kind of the secondary charged particles (muon, electron, proton and charged pion) and measures their momentum with about 10% accuracy based on energy deposit and curvature of reconstructed tracks with the magnet. The ND280 is mainly sensitive to the forward scattered muons because the TPCs are located only up and downstream of the FGDs. Besides the FGDs

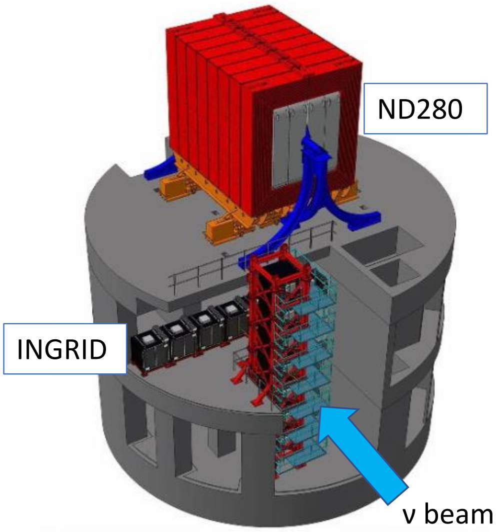

Figure 4.5: View of the T2K near detectors. [95]

and TPCs, the ND280 has a target detector to measure π^0 produced by the neutrino interactions (P0D) and electromagnetic calorimeters (ECAL) at downstream and side of the target detectors.

4.3 Far detector

The far detector, Super-Kamiokande (SK) [96], measures four types of the neutrinos after the neutrino oscillation:ν_μ, ν_e, $\overline{\nu}_\mu$ and $\overline{\nu}_e$. The SK consists of water target and 11,200 20-inch photo multiplier tubes (PMT) for the inner detector and 1185 8-inch PMTs for veto. The total target mass is 50 kton and fiducial mass is 22.5 kton. The 20-inch PMTs cover inside the inner tank with 40% coverage of the surface and angular acceptance of 4π. The neutrino interacts with the water target and a charged lepton with the same flavor of the neutrino is produced. The charged lepton emits Cherenkov light in the water. The light is detected by the PMTs and neutrino is

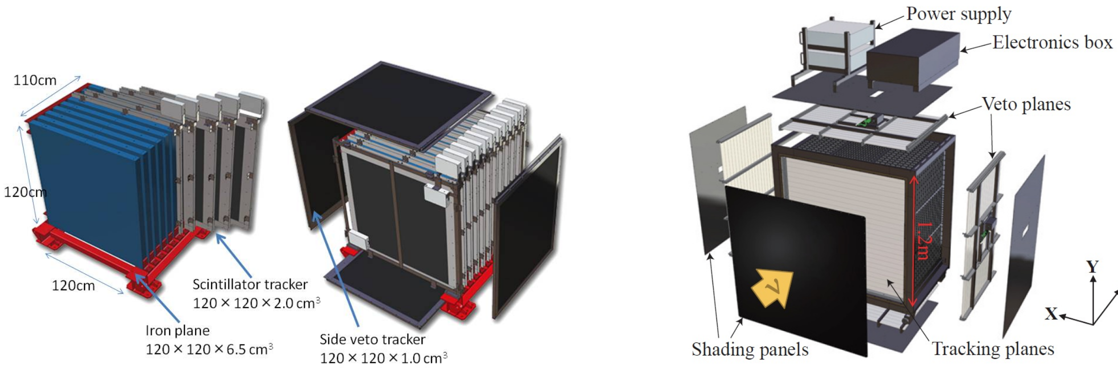

Figure 4.6: Schematic view of one of the INGRID modules (left and middle) and Proton Module (right) [94]

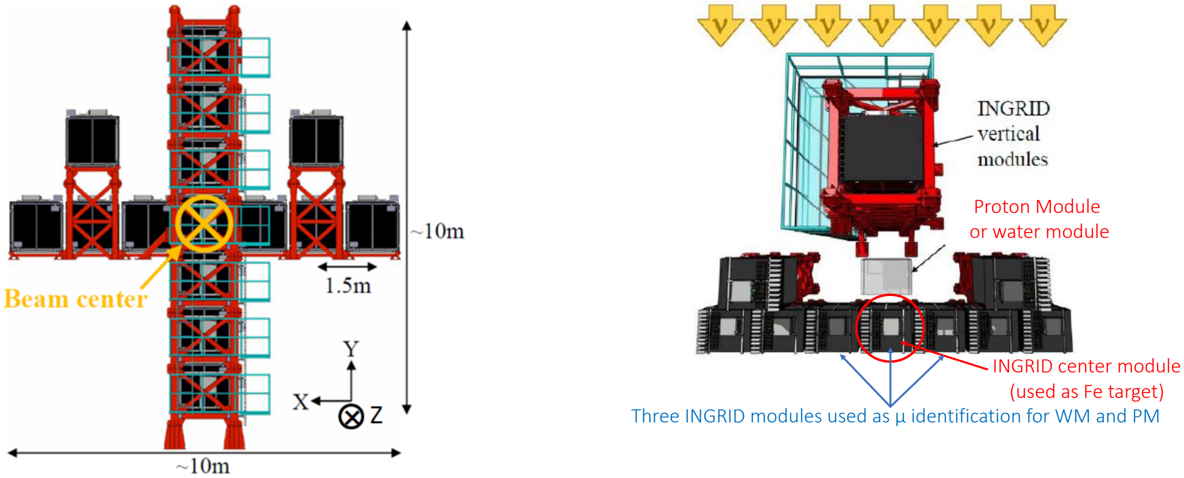

Figure 4.7: View of the INGRID detectors(top) and position of the Proton Module and water module viewed from above (bottom). The coordinate system used in this note is shown in the top figure.

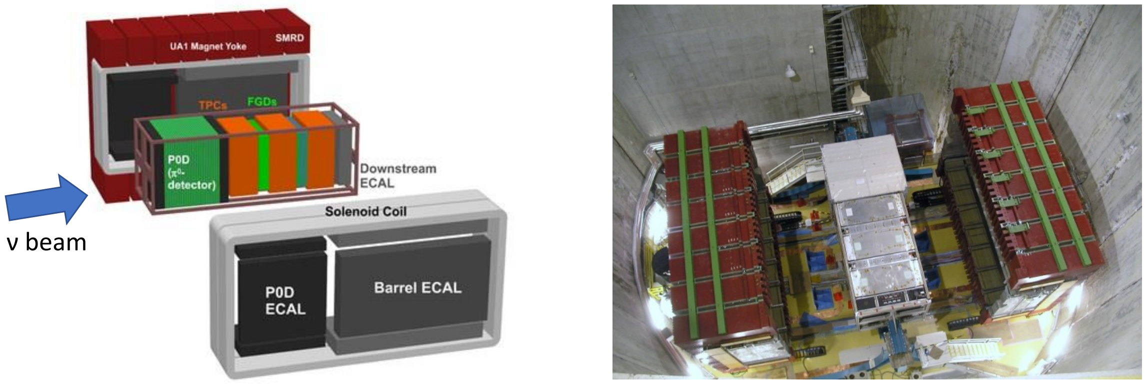

Figure 4.8: Schematic view of the ND280 (left) and a photo from above the detector (right). The magnets are opnened in these figures. They are closed to cover the FGDs and TPCs as shown in Fig. 4.5 when the ND280 is operated.

identified. Type of the charged particle is identified based on the shape of the Cherenkov ring. For example, an electron makes a electromagnetic shower and muon does not. In the ν_μ (ν_e) like sample for the T2K, the purity of muon (electron) is more than 99%. Because no magnetic field is applied at the SK, muon and anti-muon (electron and anti-electron) are not identified by the SK. Momentum of muon and electron is measured by amount of the emitted light. The resolution of momentum is about 2% at the main energy region of the T2K.

4.4 Overview of oscillation analysis

T2K measures the probabilities of the neutrino oscillations of $\nu_\mu \to \nu_\mu$, $\nu_\mu \to \nu_e$, $\overline{\nu}_\mu \to \overline{\nu}_\mu$ and $\overline{\nu}_\mu \to \overline{\nu}_e$. The analysis procedure is basically the same as described in Sec. 2.5. Figure 4.10 shows a flow of the analysis. First, the ND280 measures the muon produced by the neutrino-nucleus interactions as a function of muon angle and momentum. It constrains the uncertainties of the neutrino flux and interactions based on Eq. 2.24. The neutrino flux used for the analysis is modeled by external hadron scattering experiments, NA61 experiment [97] for example. The neutrino-nucleus interaction is modeled by external electron, pion and neutrino scattering measurements with nucleus, as described in Sec. 3. The ND280 detector efficiency is modeled

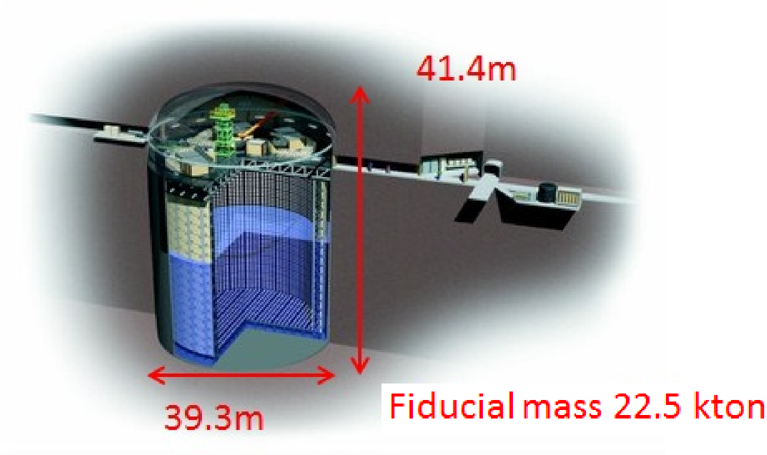

Figure 4.9: A schematic view of the Super-Kamiokande

by dedicated detector simulation which is modeled based on cosmic rays and sand muons data, which are muons produced by neutrino interaction with walls of building. The SK measures the four types of the neutrinos(ν_μ, ν_e, $\overline{\nu}_\mu$ and $\overline{\nu}_e$) and the oscillation probabilities are measured based on Eq. 2.25. They are sensitive to the oscillation parameters as shown in Figs. 4.11 and 4.12. The four samples are jointly fitted to extract the oscillation parameters of θ_{23}, θ_{13}, Δm^2_{32}, δ_{CP} and mass hierarchy. The neutrino energy is reconstructed based on the momentum and angle of the leptons based on Eq. 3.2 and 3.3. The flux and interactions are constrained from the ND280. The SK detector efficiency is modeled by dedicated detector simulation which is modeled based on cosmic rays and atmospheric neutrino data.

4.5 Current status and future prospects

The T2K experiment observed the ν_e appearance more than 7.3 σ significance in 2013 [38]. The T2K has measured the oscillation parameters of the PMNS matrix. Table 4.2 shows the measured parameters with 1σ uncertainties in the last analysis performed in 2016. A part of the parameter space of the CP phase δ_{CP} is excluded by combining the result of the T2K and the reactor experiments. The Δm^2_{32} and θ_{23} are measured with the best accuracy in the world. On the other hand, $\overline{\nu}_\mu \to \overline{\nu}_e$ appearance is not observed so far and $\delta_{CP} = 0$ is not excluded. Determination of mass hierarchy is not done significantly.

The nearest goal of the T2K is to observe $\overline{\nu}_\mu \to \overline{\nu}_e$ appearance predicted by the flavor mixing. In addition, the T2K will aim to the more precise measurement of the neutrino oscillations for the first observation of non-zero δ_{CP} with a significance of 3σ and more precise validation of the three flavor mixing model by comparison between the T2K and other neutrino oscillation measurements. To achieve that, we need to reduce statistical uncertainty less than 5% by increasing statistics more than 20×10^{21} protons on target, which is about 10 times larger than the current statistics. In addition, we need to reduce systematic uncertainty from 5% to 3%. Table 2.4 shows a summary of the systematic errors in the T2K oscillation measurement. The largest uncertainty comes from the neutrino-nucleus interactions, which affects the relation between neutrino energy and lepton momentum used in Eq. 2.27. More understanding of the neutrino-nucleus interaction is crucial for the future oscillation measurement.

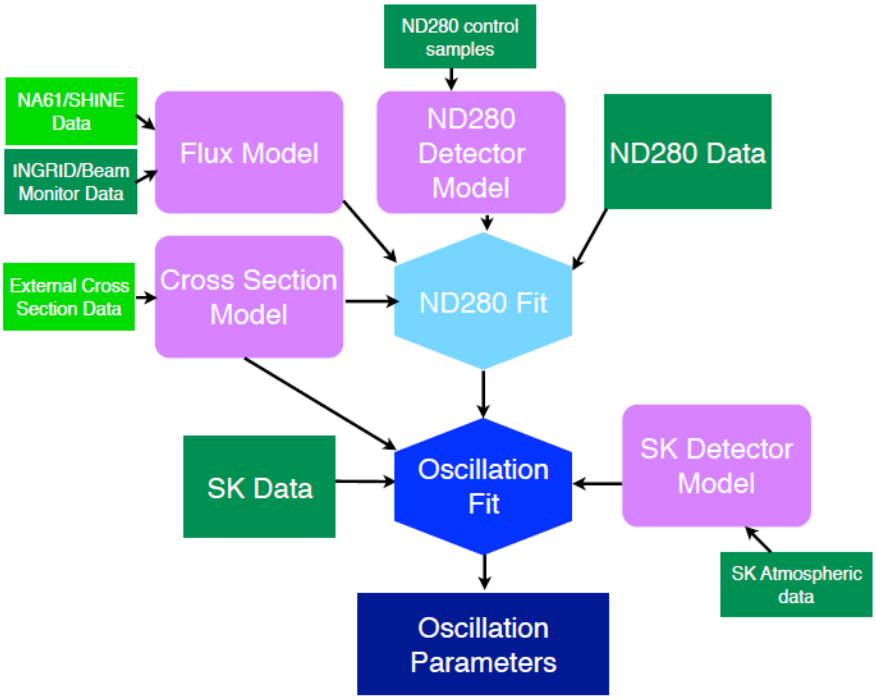

Figure 4.10: A flow of oscillation analyses at the T2K [98]. Green boxes show data (light green for external data) which inform models (magenta boxes).

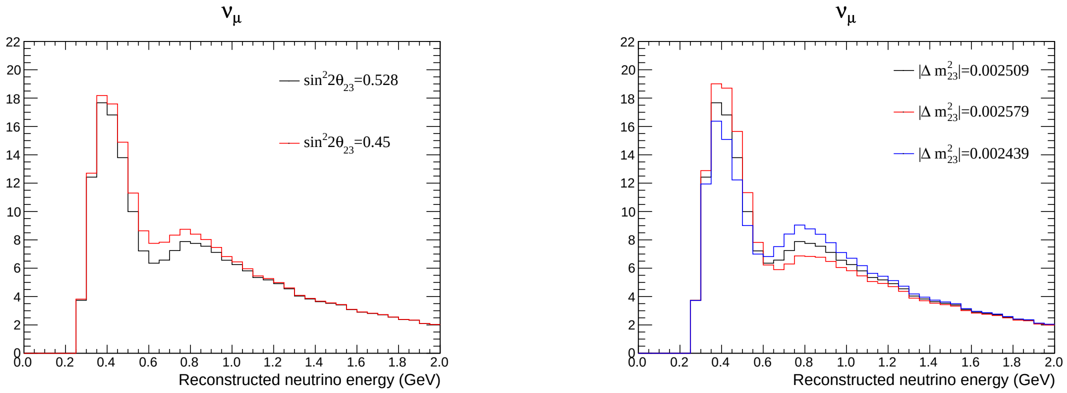

Figure 4.11: Expected reconstructed neutrino energy distribution of muon neutrino like events at the T2K far detector with the various oscillation parameters. The θ_{23} (left) and Δm^2_{32} (right) is varied with 1σ uncertainty. The other oscillation parameters are fixed at the best fit values.

4.6 Goals of this thesis

In order to achieve the precise measurement of the neutrino oscillation in the T2K experiment, three analyses are performed in this thesis as follows.

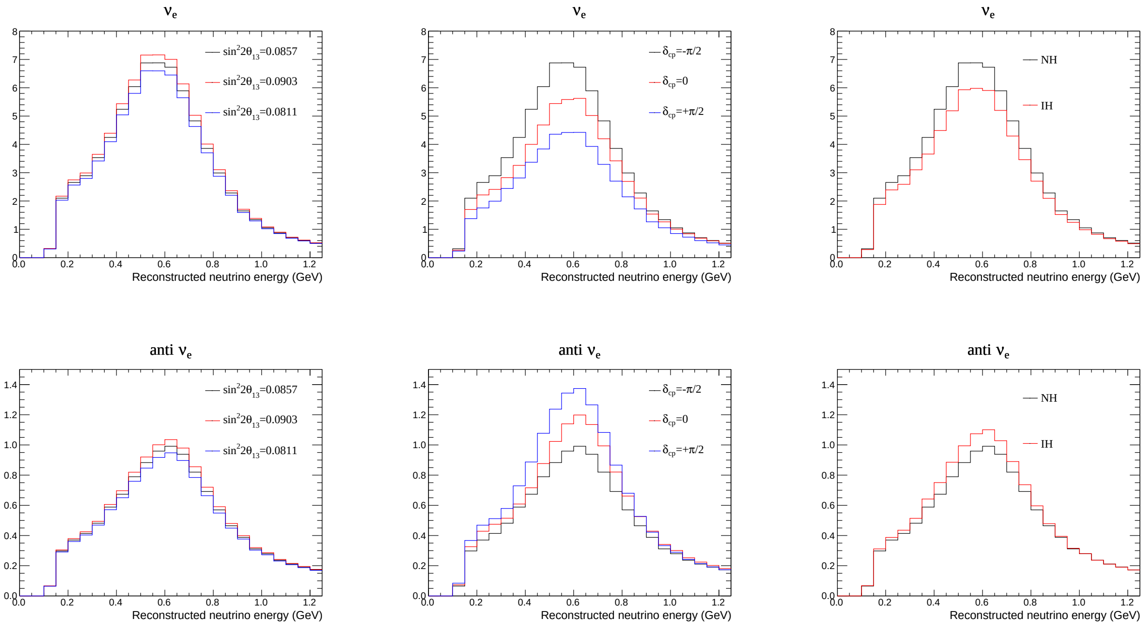

Figure 4.12: Expected reconstructed neutrino energy distribution of electron neutrino like events (top) and anti electron neutrino like events (bottom) at the T2K far detector with the various oscillation parameters. The θ_{13} (left) and δ_{CP} (middle) are varied with 1σ uncertainty. The other oscillation parameters are fixed at the best fit values.

Table 4.2: 1σ (68.3%) credible intervals of the 1D contour of the oscillation parameters measured by T2K in 2016 [46] with 7.48×10^{20} POT with FHC and 7.47×10^{20} POT with RHC.

Parameters	1σ interval	
	Normal hierarchy	Inverted hierarchy
With reactor constraint		
$\sin^2\theta_{13}$	0.0220 ± 0.0013	0.0221 ± 0.0013
δ_{CP}	$-1.84^{+0.94}_{-0.85}$	$-1.38^{+0.73}_{-0.78}$
Δm^2_{32}	$(2.549 \pm 0.082) \times 10^{-3}$	$(2.516^{+0.082}_{-0.081}) \times 10^{-3}$
$\sin^2\theta_{23}$	$0.530^{+0.039}_{-0.055}$	$0.532^{+0.037}_{-0.055}$
Without reactor constraint		
$\sin^2\theta_{13}$	$0.0338^{+0.0100}_{-0.0080}$	$0.0375^{+0.0105}_{-0.0090}$
δ_{CP}	$-1.91^{+1.20}_{-1.11}$	$-1.31^{+0.93}_{-0.99}$
Δm^2_{32}	$(2.550 \pm 0.083) \times 10^{-3}$	$(2.517^{+0.083}_{-0.062}) \times 10^{-3}$
$\sin^2\theta_{23}$	$0.502^{+0.055}_{-0.041}$	$0.496^{+0.057}_{-0.038}$

4.6.1 Cross section measurement with water and plastic targets

It is important to understand the nucleus target dependency of the neutrino-nucleus interaction. Especially, it is important to understand the difference of the cross section between the water and plastic for the T2K experiment because the main neutrino interactions targets of T2K near detector consists of plastic scintillators while the far detector, Super-Kamiokande, uses water. At present, there is almost no data of the neutrino interactions with water target. It has been tried to measure by several experiments: K2K 1kton water Cherencov detector[99], Scifi [100], Mizuche [101], P0D [102], FGD [103] and Minerva [104] but only two papers of charged current cross section measurement are published [105] [106] so far and their uncertainties are large(around 30% and 20%). Difficulty of these measurements with water target is background events from neutrino interactions with non-water materials.

For a good understanding of the water target, we have constructed a new water target neutrino detector, water module, which has less contamination of the non-water material inside the detector. In the first analysis, by using the water module, we measure the CC inclusive cross section on water, plastic and iron and their ratios with the neutrino energy of 1.5 GeV with the best accuracy of in the world. The uncertainty of the ratio measurement is expected to be small because some of the systematic uncertainties are canceled. The ratio measurement is sensitive to the difference of the neutrino interactions between the plastic and water.

4.6.2 Validation of the constraint of neutrino flux and interaction from the ND280

Validation of the constraint from the ND280 measurement

The method to constrain the neutrino flux and interaction by the near detector, $\Phi \times \sigma$ in Eq. 2.24 and 2.25, is generally used in the long baseline accelerator experiments. However, it is impossible to check if the constraint of the flux and interactions is correct or not at the far detector directly because not only the flux and interactions but also the neutrino oscillations affect the neutrino events at the far detector.

In the second analysis, to cross check the constraint from the ND280, observed neutrino event rates at the water module and Proton Module are compared with Monte Carlo predictions with the constraint from the ND280. Because there is no effect of the neutrino oscillations at the water module and Proton Module located 280 m downstream from the beam target, the constraint of the flux and interactions are validated. Because typical long baseline oscillation experiment has only one near detector, this analysis is the first direct validation of the constraint of the flux and interaction from the near detector by using real data of the independent detectors.

Measurement of muons with large angle

It is important to measure the neutrino interaction with large angular acceptance for the T2K because the ND280 is mainly sensitive to the forward scattered muons of less than 45 degrees while the SK has 4π acceptance. The MC prediction of the large angle muons may be biased at the SK because it is extrapolated based on the model of the neutrino interactions and data with the forward scattered events. In order evaluate the biases and their effects on the oscillation analysis, the measurement of muons with the large angular acceptance is needed.

For that measurement, the water module is designed to have a large angular acceptance. In the second analysis, CC0π interaction with the muons of large scattered angle (30–80 degrees) with a proton is measured by the water module and compared with the MC expectation with the constraint from the near detector.

Measurement of protons

It is important to measure the protons produced with the neutrino-nucleus interactions for the T2K because information of only muons and pions are used by the ND280 for the oscillation analysis. The information of the protons include significant information of the neutrino-nucleus interactions which can not be accessed through the muons and pions. The measurement of the protons is needed to improve the modeling of the neutrino-nucleus interactions.

For the measurement of protons, the water module has scintillators with an interval of 5 cm, which is sensitive to a proton with momentum of more than 500 MeV. In addition, the water module is located at the on-axis and detection of protons is relatively easier than that at the off-axis because the neutrino energy (1.5 GeV) is higher than that at off-axis (0.6 MeV) and momentum of the proton is also higher. In the second analysis, CC0π interaction is measured with the information of the protons by the water module and Proton Module and compared with the MC prediction with the constraint from the ND280.

4.6.3 Measurement of neutrino oscillations

The third analysis is a measurement of the neutrino oscillations. The analysis is performed with twice larger statistics than the last analysis performed by T2K in 2016, with 1.5 times accumulated neutrino beam statistics and enlarged fiducial volume of the SK by improvement of Cherenkov ring reconstruction algorithm. The main purposes of the third analysis are as follows.

Observation of CP violation in lepton sector

CP violation can be a key to explain the matter-antimatter asymmetry in the universe but there is no measurement of the CP violation in the lepton sector so far. T2K has an unique sensitivity of the CP violation because δ_{CP} can be measured only through the accelerator neutrino experiments by comparing the $\nu_\mu \rightarrow \nu_e$ and $\overline{\nu}_\mu \rightarrow \overline{\nu}_e$ oscillations. This thesis aims to exclude $\delta_{CP} = 0$ with the best significance of more than 2σ in the world. The comparison is important because it is sensitive to any CP violations including effect of a new physics behind the standard three flavor mixing model.

Measurement of mixing parameters

It is important to measure the mixing parameters for the validation of the three flavor mixing model. By fitting the four oscillations at the far detector, this thesis aims to measure the θ_{23} and Δm^2_{32} with the best accuracy in the world with around 10% smaller contours than the last T2K analysis in 2016. In addition, θ_{13} is measured and compared with the result of the reactor experiments with the best accuracy among the accelerator neutrino experiments. At the same time, mass hierarchy is measured through the matter effect.

Observation of $\overline{\nu}_\mu \rightarrow \overline{\nu}_e$ appearance

$\overline{\nu}_\mu \rightarrow \overline{\nu}_e$ oscillation is predicted by the standard oscillation framework but it is not observed so far. This thesis aims to observe the $\overline{\nu}_\mu \rightarrow \overline{\nu}_e$ oscillation for the first time in the world with a significance of 3σ. Observation of $\overline{\nu}_\mu \rightarrow \overline{\nu}_e$ is one of milestones for the validation of the standard oscillation framework and an exciting challenge to search for a new physics beyond the SM.

Chapter 5

Water module detector

A new water target neutrino detector, water module [107] [108], has been developed to measure the charged current cross sections on water, plastic targets and their ratio with 1.5 GeV energy of muon neutrino. Feature of the water module is that the fraction of water in target region is more than 80% for reducing the background events from neutrino interactions with non-water materials. This is a main background event in the previous researches [95][100] because their fraction of the water is around 50%. In addition, the water module has an advantage of large angular acceptance to measure the phase space inaccessible with other near detectors. These innovative features give the precise understanding of the neutrino interactions with water target.

5.1 Overview of the water module detector

The water module detector is designed to satisfy various requirements:

- It must have around 0.5 ton target mass to achieve better than two percent statistical uncertainty with two months run, corresponding to 2×10^{20} POT.
- Fraction of water in the water target region must be more than 80% to reduce background events from neutrino interactions with non-water materials.
- It must be capable of detecting muon and pion, of which momentum is more than 200 MeV, produced at the interaction vertex with large angular acceptance.
- It must be capable of detecting proton of which momentum is more than 500 MeV, produced at the interaction vertex with large angular acceptance.
- It must identify protons from muons and pions by using dE/dx measurements with 80%.
- Difference in the injected neutrino flux and detection efficiency of neutrino interaction must be less than a few percents between the water module and Proton Module for the ratio measurement.

As shown in Fig. 5.1, the water module consists of a stainless steel tank filled with 0.5 ton water and 16 scintillator tracking planes immersed in the water, where each plane is an array of 80 scintillator bars. The 40 bars, called parallel scintillators, are placed perpendicularly to the beam as shown in Fig. 5.2. The other 40 bars, called grid scintillators, are placed in parallel to the beam with grid structure as shown in Fig. 5.2. The tracking planes are placed alternately in the x-direction and y-directions so that 3D tracks can be reconstructed. Spaces between the scintillators are filled with water which serves as the neutrino interaction target. Scintillation light from the scintillator is collected by a wavelength shifting fiber and read by multi-pixel photon counter (MPPC). The electric signal is processed by front-end electronics and the integrated charge and hit timing are digitized and recorded with 1.5 photon-electron(p.e.) threshold.

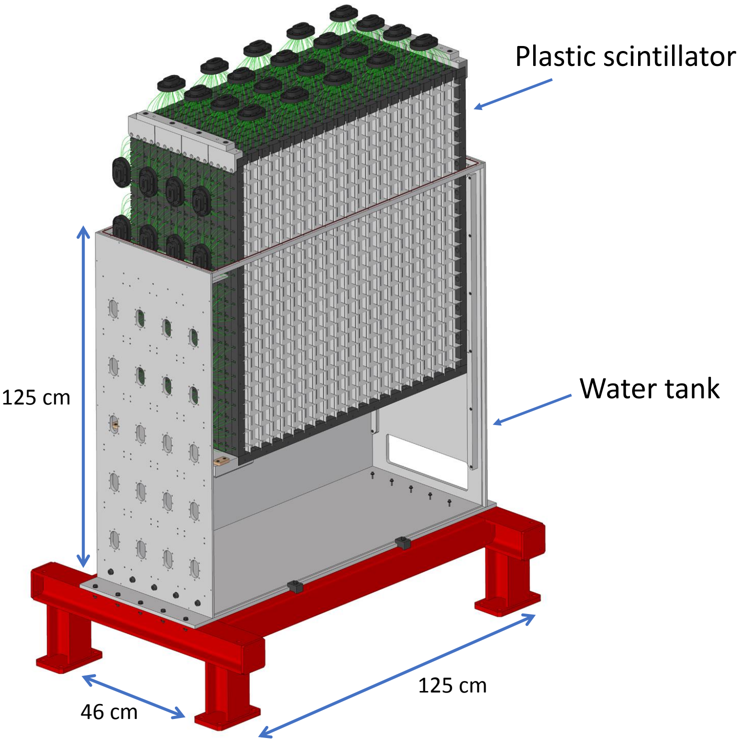

Figure 5.1: Schematic view of the water module

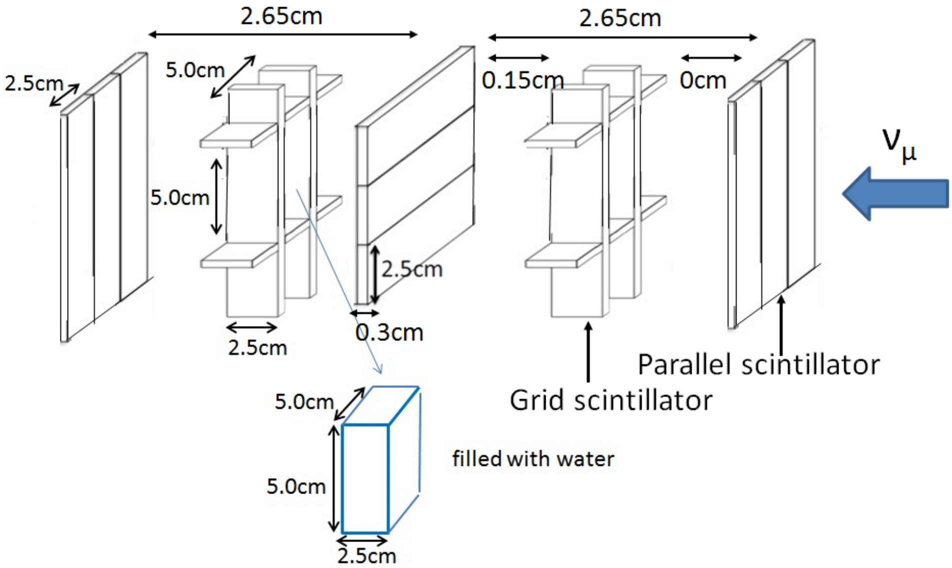

Figure 5.2: Schematic view of the scintillators of the water module. The written size is the design values.

5.2 Detector components

5.2.1 Scintillator

For detecting charged particles produced by neutrino-nucleus interaction, water module uses plastic scintillators, which have been used for the T2K near detector successfully. It is easy to process and cheap enough to cover all of the target region of the detector. In addition, the scintillator is chemically robust and works in the water stably. Figure 5.3 shows the size of each scintillator bar. It is produced in Fermi National Accelerator Laboratory and machined by G-tech company. The thickness of 3 mm is optimized as thin as possible while keeping enough amount of light yield for reducing fraction of non-water material inside the target region. The scintillator has a straight groove to put a wavelength shifting (WLS) fiber[109]. In addition, grid scintillator has machined slits to make the 3D grid structure. The scintillator is made of polystyrene (C_8H_8), infused with the fluors PPO ($C_{15}H_{11}NO$) and POPOP ($C_{24}H_{16}N_2O_2$). Wavelength of the emitted light is 420 nm. Surface of the scintillator is covered with co-extruded reflective coating and black silicon painting to reduce optical crosstalk. The WLS fiber is put inside the groove of the scintillator and glued by optical cement. Optical and mechanical performance of the scintillator had been evaluated by cosmic ray and positron beam as summarized in Table 5.1.

The scintillators are put in water directly to reduce the fraction of non-water material inside the target region. They are fixed with frames made by ABS resin to keep 3D grid like structure in water with 2 mm accuracy, as shown Fig. 5.4. Edge of the fibers from the scintillators are extracted from a water tank and bundled by a plastic jig named fiber bundle, as shown in Fig. 5.5. Edge of the fiber is polished by a diamond cutter to keep uniformity and increase amount of the light yield.

Table 5.1: Performance of the scintillator

Parameters	Value
Mean light yield for MIP	24 p.e.(parallel), 18 p.e.(grid)
Hit efficiency for MIP	99.9%
Stability of light yield	Decrease less than 3% per year
Optical crosstalk between scintillators	<1%
Attenuation length of fiber	240 mm
Position dependency of scintillator	$\exp(-y/\lambda)$, λ =30 mm (parallel), 25 mm (grid) (y=distance between hit point and fiber)

5.2.2 MPPC

The water module requires a silicon photodetector which have high photo detection efficiency and low noise due to low light yield of the 3 mm thickness plastic scintillators. It also should be compact and cheap because of the large number of the readout channels. In order to satisfy these requirement, the water module uses a low noise MPPC (S13660(ES2)) developed by Hamamatsu photonics. The MPPC is a photon-counting device made up of multiple APD pixels operated in the Geiger mode. The total output charge of the MPPC is proportional to the number of pixels which photons hit. The performance of the MPPC is evaluated as shown in Table 5.2.

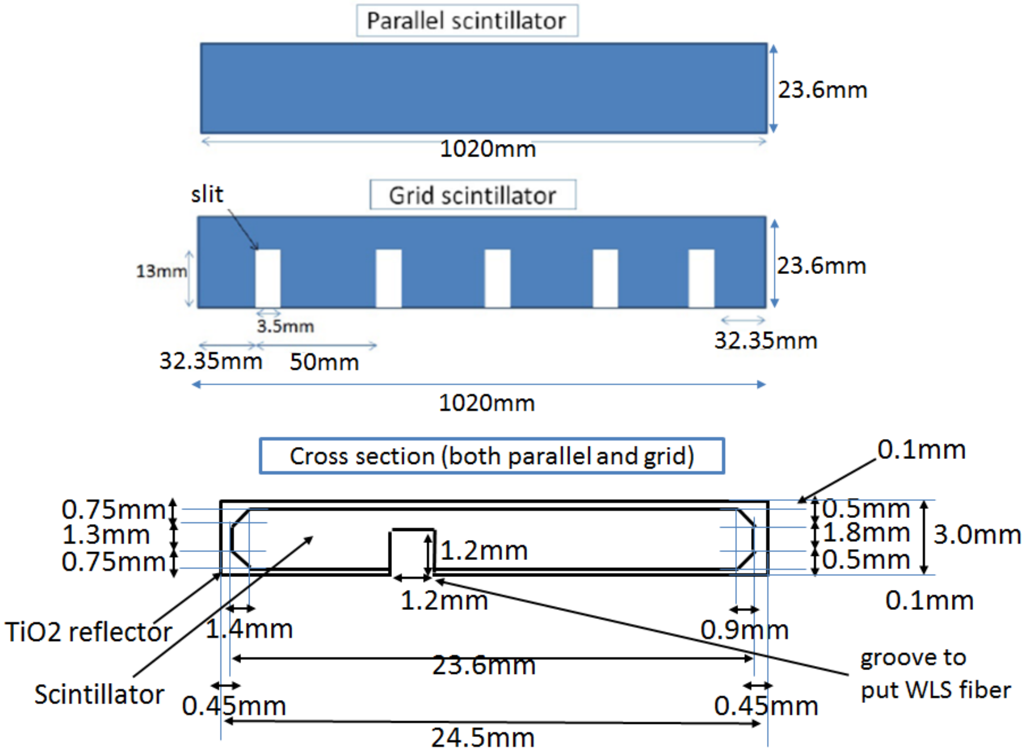

Figure 5.3: Geometry of the scintillators of the water module

Table 5.2: Performance of MPPC

Parameter	Value
Size of a pixel	$50 \times 50\ \mu\text{m}^2$
Number of pixel	716
Size of a device	ϕ 1.5 mm^2
Break down voltage(V_{bd})	54.0 V
Operation voltage	V_{bd} + 3.5 V
Gain	2.6×10^6
Dark noise rate	36 kHz
Crosstalk and afterpulse rate	0.052
Photo detection efficiency	40% (500 nm)

5.2.3 Electronics

The electric signal from the MPPC is digitized to integrated charge and hit timing information by Trip-t front-end board [110] (TFB), which has been used for the T2K near detectors. Figure 5.6 shows an overview of the Trip-t based readout system. Each TFB instruments up to 64 MPPC channels and the water module has 20 front-end boards to cover all 1280 channels. The readout and control data from up to 48 TFBs, for not only water module but also INGRID and Proton

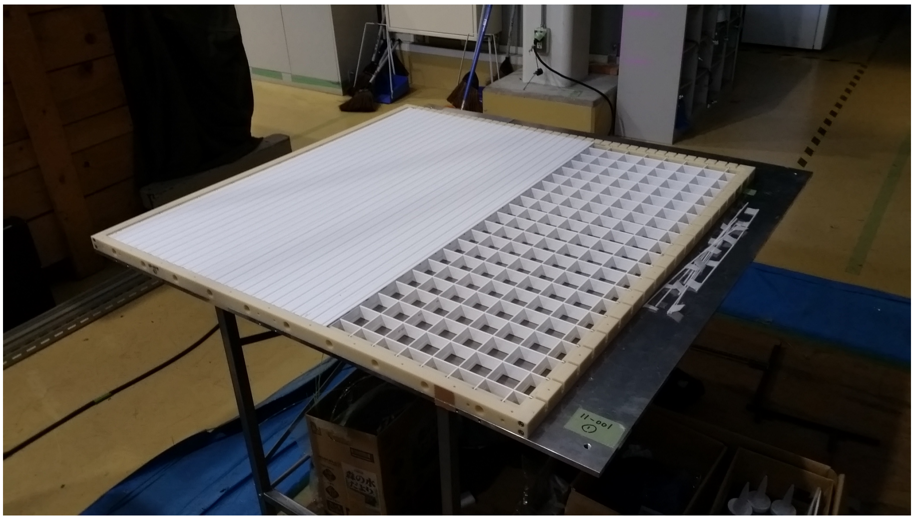

Figure 5.4: Picture of the frame. The yellow part is frame and white part is scintillator.

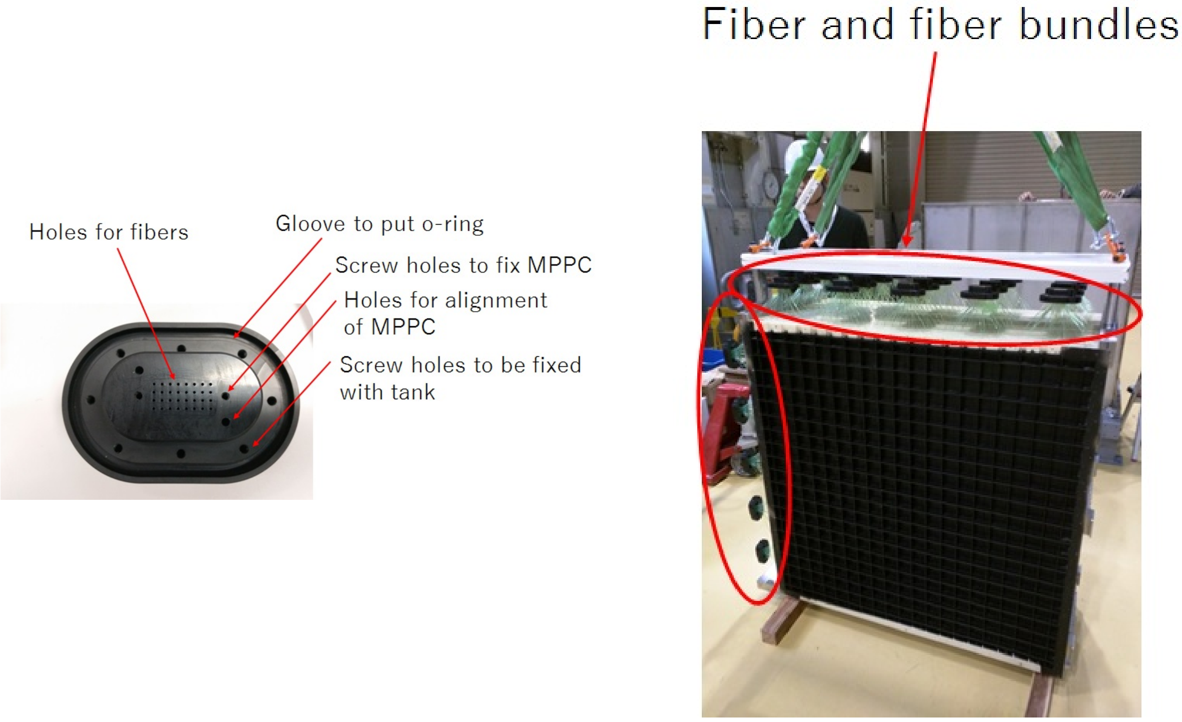

Figure 5.5: View of the fiber bundle (left) and glued fiber and fiber bundle by optical cement (right).

Module, are processed through a Readout Merger Module (RMM) and communicate with data acquisition system. Data is taken with beam, cosmic ray and periodic triggers. Charge of all channels are recorded. Hit timing of all channels which have more than 1.5p.e. charge are recorded. Beam trigger provided from the accelerator (kicker timing) is received by a timing module and data is taken bunch by bunch with timing structure as shown in Fig. 5.7. Cosmic ray trigger is provided by cosmic trigger module when specific TFBs have time coincidence hits. Periodic trigger is taken through the data acquisition system during the beam off period for calibration.

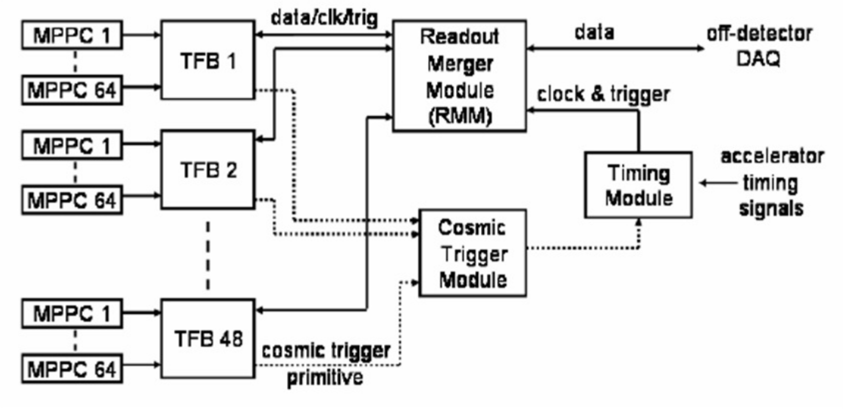

Figure 5.6: The Trip-t based front end electronics readout system. [110]

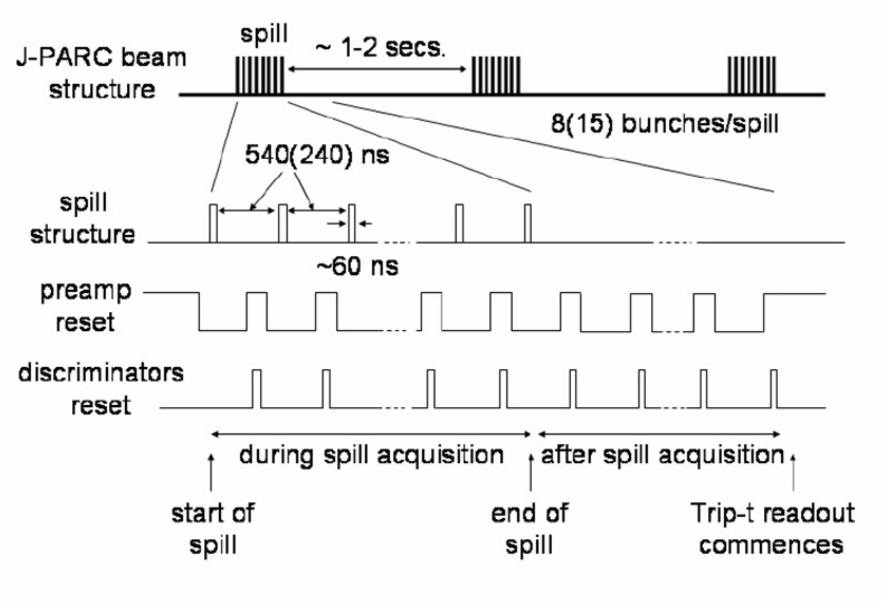

Figure 5.7: T2K beam structure and corresponding Trip-t sequencing. [110]

Table 5.3: Performance of front end electronics

Parameters	Value	Requirement
Dynamic range	0 to 250 p.e.	0 to 200 p.e.
Noise	< 0.2 p.e.	0.2 p.e.
Timing resolution	2.5nsec	10nsec
Bias voltage trimming resolution	20mV	20mV

5.2.4 Water tank

Figure 5.8 shows a view of the water tank. It is made of stainless steel not to be rusted. Size of the tank is $125 \times 125 \times 50cm^3$. It is designed to have sufficient mechanical strength to keep 0.6 ton of water. It has holes for extracting fiber bundles and panels to put water level sensors and a hose line to drain/put water. In order to prevent water leak, stainless steel parts are welded and o-rings are used for contact of the holes and panels. At the side and top of the tank, there are electronics hut for the MPPC, TFBs, humidity and temperature sensors. Water level and water leak are monitored by the sensors online.

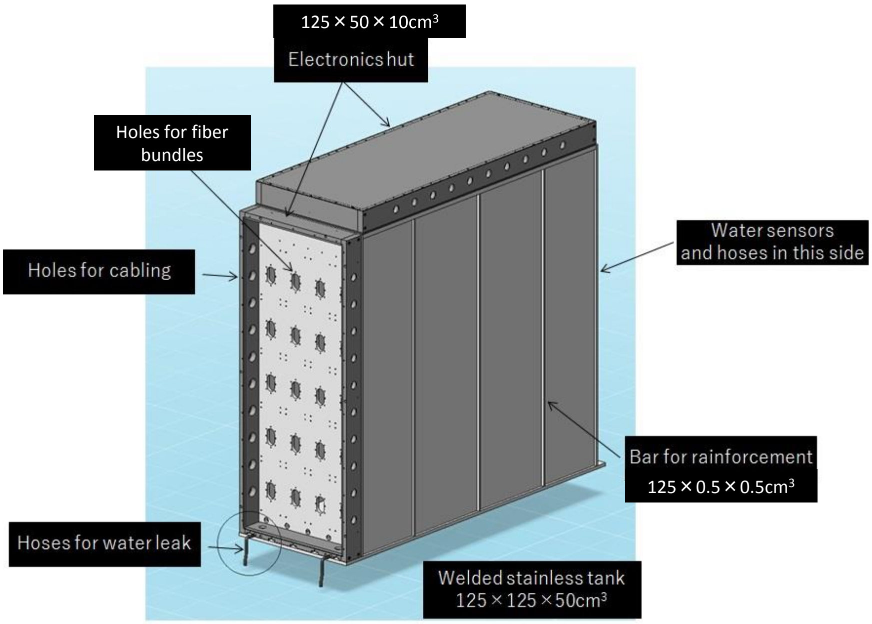

Figure 5.8: View of the water tank.

5.3 Detector simulation

Monte Carlo simulation (MC) is used for the estimation of background contamination and detection efficiency which are used in the physics analysis. Three pieces of software are used for the simulation: JNUBEAM [111] for the neutrino flux expectation, NEUT [86] for the neutrino interaction with a nucleus and Geant4-based dedicated detector simulation. JNUBEAM simulates interaction of incident 30 GeV proton and carbon target, behavior of the secondary particles and decay of the pion and kaon in decay volume which predicts the neutrino flux at the detector. NEUT simulates neutrino interaction with a nucleus of detector target, including final state interaction inside the nucleus. GEANT4 simulates behavior of the secondary particles in the detector and calculate energy deposit in the plastic scintillators.

In the detector simulation, the water module geometry is modeled by three components:

- A stainless steel tank
- Water in the tank
- Scintillators in the water

The size of the water tank, 1280 mm × 1288 mm × 508 mm outer volume and 1256 mm × 1256 mm × 500 mm inner volume, is modeled based on a drawing. The tank is filled with water based on the monitored water level during the detector operation. The shape of the scintillators is modeled based on the measurement during the detector construction. Responses of scintillator and MPPC are modeled based on measurements, as listed in Table 5.4. Energy deposition estimated by GEANT4 is converted to the observed number of photons by multiplying a constant determined by measurements with MIP particles during the detector operation. The quenching effect of the scintillator, position-dependent light collection efficiency of fibers, photon attenuation and the propagation time of the photons in the fiber, crosstalk between grid scintillators, MPPC noise, MPPC crosstalk and after pulse, MPPC saturation, electronic noise and photon statistics are included based on the measurements. The detector is placed in front of the INGRID with a position accuracy of 1 mm based on the survey after the detector installation.

Table 5.4: Summary of response of scintillator and MPPC used in the detector simulation

Parameter	Value	Collection of light yield (p.e.) (α is each parameter)
Conversion factor from energy deposit (dE) to p.e.	~31.5 p.e./MeV	p.e. = $\alpha \times$ dE
Birk's constant	0.0208 cm/MeV	$1./(1+\alpha \times dE/dx)$
Scintillator position dependency	3.5 cm	$\exp(-x/\lambda)$ (x=distance from fiber)
Light attenuation in fiber	241.7 cm	$\exp(-x/\lambda)$ (x=length of fiber propagation)
Crosstalk between scintillators	0.0065	crosstalk=($\alpha \times$ p.e.$_{\text{next}}$) (p.e.$_{\text{next}}$=hit of the next scintillator)
Number of MPPC pixels	716	$\alpha \times (1-\exp(-\text{p.e.}/\alpha))$
Crosstalk and after pulse rate of MPPC	0.09	$(1+\alpha)$
Width of pedestal	13%	Gaus(p.e., p.e. $\times\ \alpha$)

In the detector simulation, ν_μ, $\overline{\nu}_\mu$, ν_e and $\overline{\nu}_e$ interactions on H_2O(water), CH (scintillator) of the water module, CH of the Proton Module, Fe and CH of the INGRID modules are generated. In addition, as background sources, ν_μ interactions on the stainless steel tank of the water module and a wall of the building are also generated.[1] Used MC statistics are 1×10^{21} protons on target (POT) for neutrino interactions on the wall and 1×10^{23} POT for others. The former is 100 times smaller than the latter because the simulated area of the wall is geometrically large. Cosmic ray is simulated by a single muon which angle is zenith angle distribution. The cosmic ray is simulated only for the commissioning of the detector and not used for the physics analysis because it is negligible as a background source as described later.

5.4 Commissioning and data taking

Commissioning of the water module is done with cosmic ray and sand muons, which are muons produced by neutrino interaction with the wall of the building. Totally 5×10^5 cosmic ray tracks and 7.25×10^{21}POT are used for the commissioning. In this section, result of the commissioning is described.

5.4.1 Calibration of electronics

Figure 5.9 shows an ADC distribution of a typical channel taken with the periodic trigger. This is fitted by a double Gaussian function and the pedestal peak and the 1 photo-electron peak is

---

[1] Effect of mechanical structure of the detectors is studied and it is negligible (less than 0.2%).

calculated. By using them, the ADC count is converted to photo-electrons as follows:

$$\text{p.e.} = (\text{adc} - \text{pedestal})/(1\text{p.e.} - \text{pedestal}) \tag{5.1}$$

where p.e. is observed photo-electrons, adc is the ADC count, pedestal is the position of the pedestal peak and 1p.e. is the position of the 1 photo-electron peak. The denominator is defined as gain and tuned with 9.1 ADC count, which corresponds to breakdown voltage plus 3.5 V, by adjusting operation voltages channel by channel. In addition, responses of ADC and TDC, linearity of ADC, offset of TDC and effect of time walk are calibrated and corrections are applied in Eq. 5.1. One of the front-end boards has 10 electric dead channels because it was damaged by water drop from cooling fan. These channels are masked for the analysis.

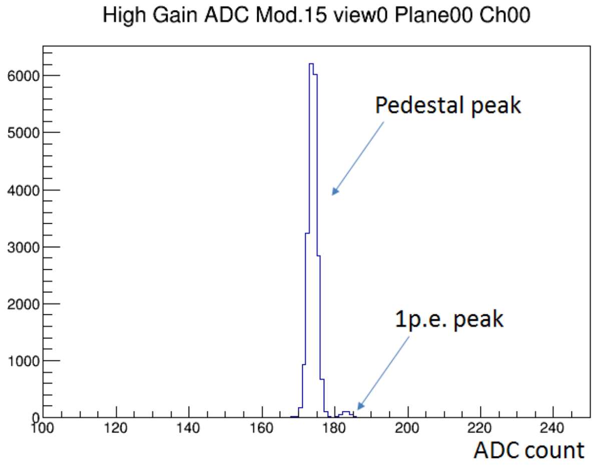

Figure 5.9: ADC distribution of the typical channel taken with periodic trigger.

5.4.2 Performance of MPPC

Figure 5.10 shows the tuned MPPC gain of each channel during the detector operation. For ensuring data quality, the number of MPPCs whose deviation of gain from their reference is larger than 10% is required to be less than 10 channels. The gain is stable and all run period passes this criterion. Figure 5.11 shows the measured MPPC dark noise rate of each channel measured with no beam data. Because the noise rate is different between the channels, the charge and timing of the noise are measured and implemented to the MC simulation channel by channel. Figure 5.12 shows time dependency of the mean noise rate. They are stable with the mean value of the 2.3 hits/cycle/module. Although data is taken with 1.5 photo-electrons hit threshold, 2.5 photo-electrons threshold is used for this analysis and the dark noise rate decrease one order of magnitude compared with this plot.

5.4.3 Performance of scintillator

Light yield of scintillator

Light yield of the scintillators is checked by the sand muon and cosmic ray. The sand muon is selected by requiring upstream of reconstructed track is the most upstream layer of the scintillators. Track is reconstructed in x-z view and y-z view independently and they are merged as 3D track, based on the pattern of the scintillator hits as described in App. C. Figure 5.13 shows

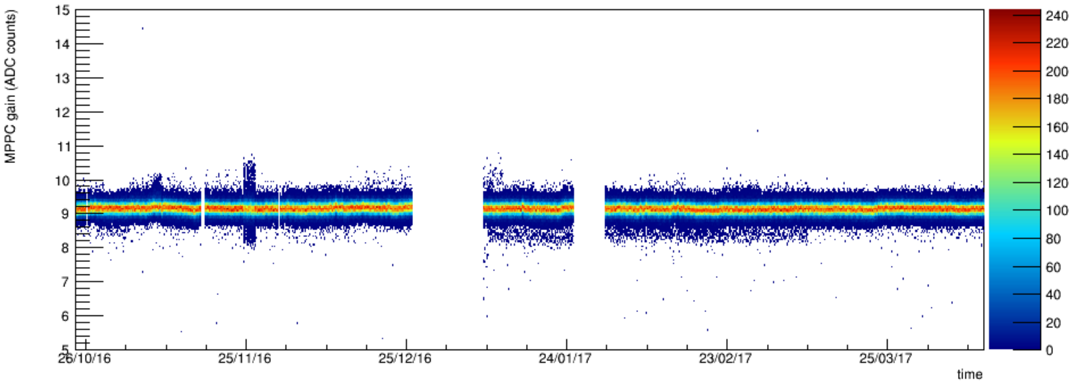

Figure 5.10: Tuned MPPC gain during the detector operation. A small fluctuation of the gain between 24th and 27th of November is due to miss-operation of the gain tuning.

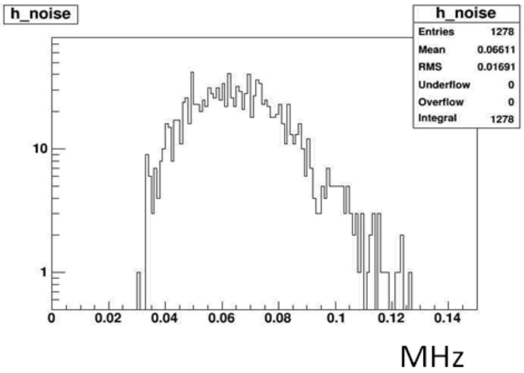

Figure 5.11: MPPC noise rate of each channel(left) and typical charge vs timing distribution of the noise (right).

the mean light yield of each scintillators normalized by a path length based on the reconstructed track angle. There are individual differences mainly due to non-uniformity of the optical cement that glues the wavelength shifting fiber to the scintillator. In the MC, a factor to convert an energy deposit to light yield is tuned channel by channel, based on this mean light yield measurement. The water module has 1280 scintillators and 23 of them have low light yield due to damaged wavelength shifting fiber during the installation work of the scintillator layers into the water tank and they are masked for the analysis. As shown in Fig. 5.14, the water module has totally 35 dead channels which correspond to 2.7% of the total number of channels.

The light yield more than threshold of 4.5p.e. is used for particle identification. The light yield distribution is compared between data and simulation. Figure 5.15 shows light yield distribution of typical channel, observed by sand muon. There is a discrepancy of less than 5% between data and simulation. Figure 5.16 shows the mean light yield vs reconstructed track angle and data and simulation agree with 10% level.

Hit efficiency of scintillator layer

Hit efficiency of the scintillator layers are measured by sand muon and cosmic ray. For calculation of the hit efficiency, the scintillators are divided as planes along with z-axis and xy-axis to check both forward and large scattering angle muons. The former is checked by sand muon sample and the latter is checked by cosmic muon sample. Figure 5.17 shows the calculated hit efficiency

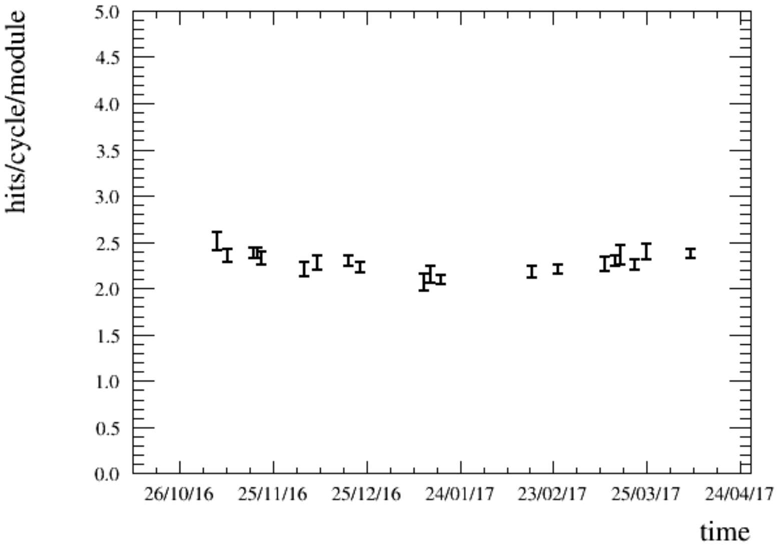

Figure 5.12: MPPC dark noise rate history with 1.5 photo-electrons hit threshold

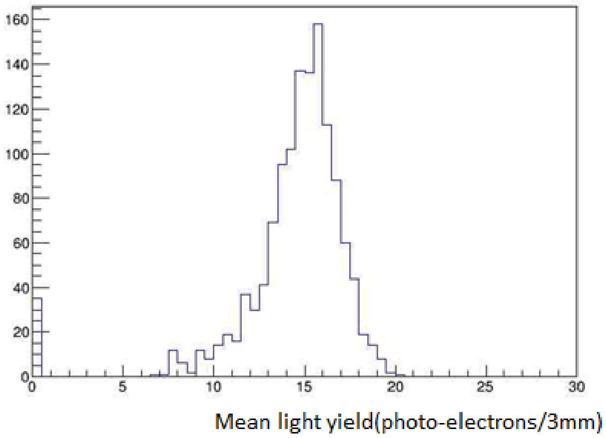

Figure 5.13: The mean light yield of sand muon hit of each scintillator. The small peak at 0 photo-electron contains 35 masked channels due to electronics problems, low sensitivity of the MPPC, or a low scintillator light yield.

as a function of the reconstructed 3D track angle respect to the neutrino beam. The data and MC expectation agree within 1%. The main reason for the inefficiency is gaps between the scintillators.

2D tracking efficiency

2D tracking efficiency of the water module is checked by using reconstructed tracks of the INGRID. As shown in Fig. 5.18, when the INGRID has a reconstructed 3D track, the track is extended to the water module and the distance between the track and hits of the water module

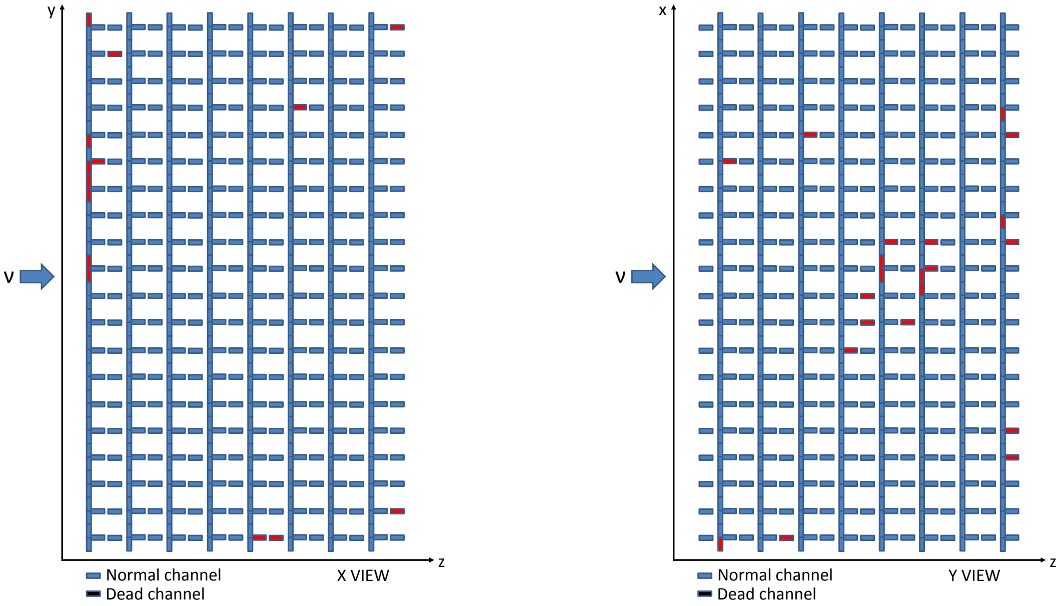

Figure 5.14: Position of the dead channels masked in y-z view (left) and x-z view (right) for this analysis. Scintillators orthogonal to the page are shown in each view. The scintillators perpendicular to the beam are parallel scintillators and that parallel to the beam is grid scintillators.

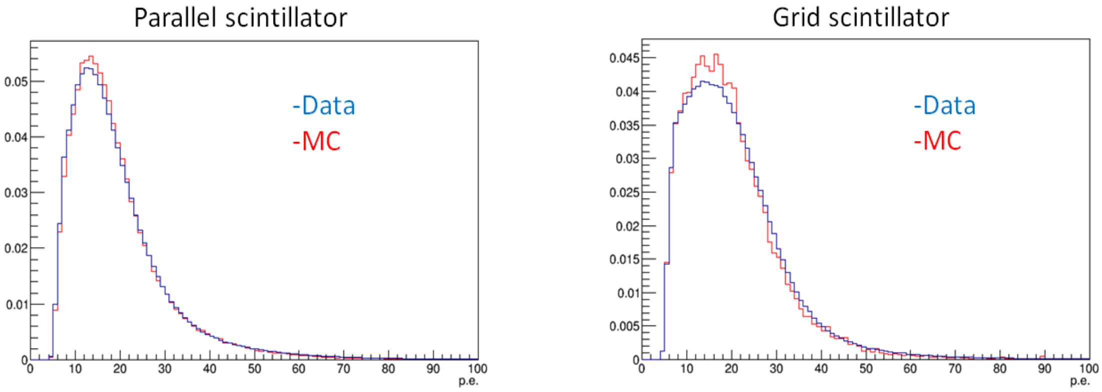

Figure 5.15: Light yield distribution of sand muon of the parallel scintillator(left) from data(black) and Monte Carlo simulation(red) and that of grid scintillator(right). The simulation is normalized by area.

is calculated. When there are more than 2 hits within 20 cm distance, it is checked whether the 2D track is reconstructed or not in the water module. The efficiency of the track reconstruction is estimated with several sub-samples categorized by the number of hits and reconstructed track angle of the INGRID. Figure 5.19 shows the results for the data and MC and they agree with 1% level.

The 2D tracking efficiency of large angle track is also checked without the INGRID because the INGRID is located at downstream of the water module. It is checked as a function of the number of the planes which have at least one hit of the sand muon or cosmic muon. If the number of hit planes along with z axis is larger than that along with xy-axis, sand muon sample is used for the checking. If not, cosmic muon sample is used. Figure 5.20 shows the calculated 2D tracking efficiency by MC and its difference between data and MC. The difference is less

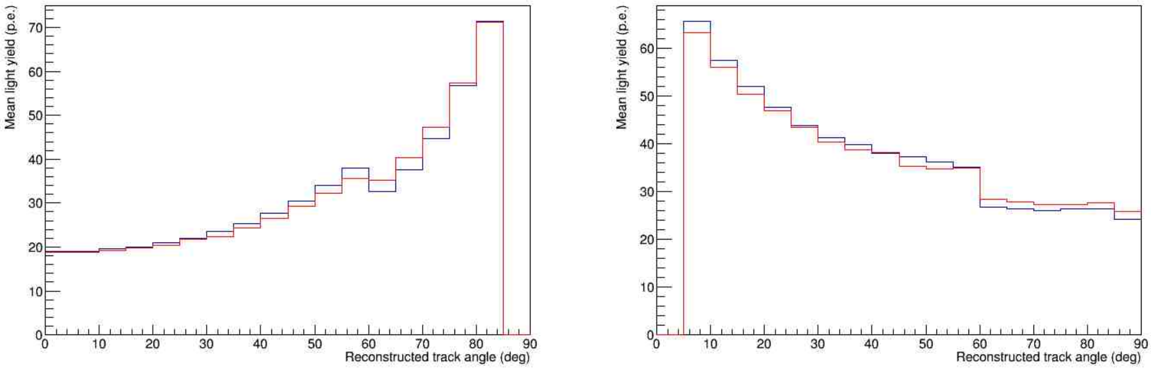

Figure 5.16: Mean light yield of parallel (left) and grid (right) scintillators in each reconstructed angle bin. Data is black and Monte Carlo simulation is red.

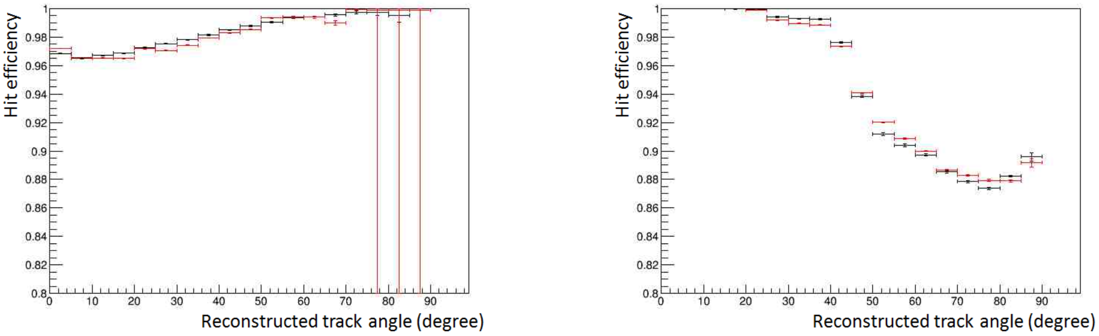

Figure 5.17: Calculated hit efficiency for forward scattering angle muon (left) by sand muon and for large scattering angle muon (right) by cosmic muon. Black is data and red is MC.

than 2% for most of bins but a few bins of small number of hit plane have a discrepancy of a few percents.

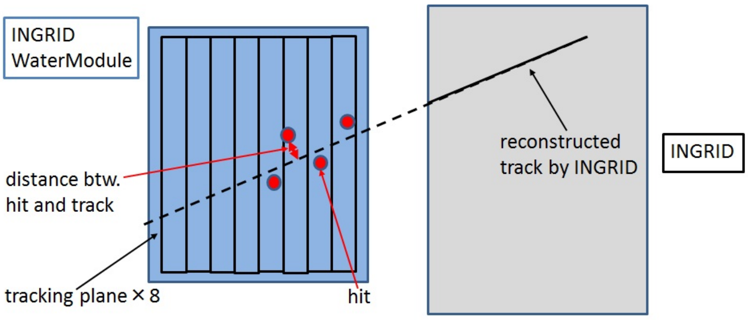

Figure 5.18: View of the checking method of the 2D track reconstruction efficiency

Crosstalk between scintillators

Optical crosstalk of the scintillators occurs between the grid scintillators along with x and y axis through the cross point of the slits. Its uncertainty should be estimated because the crosstalk sometimes results in mis-vertexing and track mis-reconstruction. Figure 5.21 shows the relation

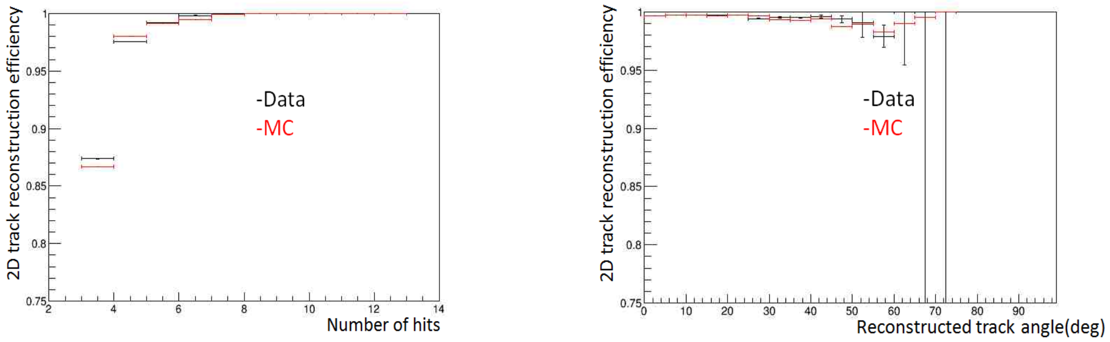

Figure 5.19: 2D track reconstruction efficiency as a function of the number of hits (left) and reconstructed angle of the INGRID (right)

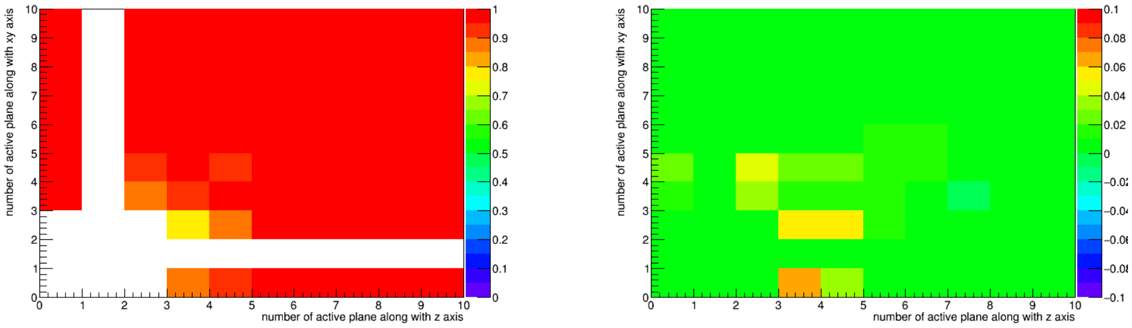

Figure 5.20: Calculated 2D tracking efficiency by data (left) and its difference between the data and MC (right).

of the sand muon light yield of the grid scintillator along with x and y axis. There are positive linear relations and its slope is 0.67%. In the MC, when a grid scintillator has a hit, crosstalk hits are generated on the grid scintillator in the opposite view. The size of the light yield of the crosstalk hit is determined based on the Poisson distribution of which mean value is calculated as follows:

$$\text{p.e.}_{\text{cross}} = \text{p.e.}_{\text{hit}} \times 0.67\% \tag{5.2}$$

Conservatively, the effect of the crosstalk for the physics analysis will be estimated by comparing with and without the crosstalk in the MC.

5.4.4 Summary of detector performance

Table 5.5 shows a summary of the performance of the water module evaluated by the commissioning. These results will be used for estimating uncertainty of the detector responses for physics analysis in Section 6 and 7.

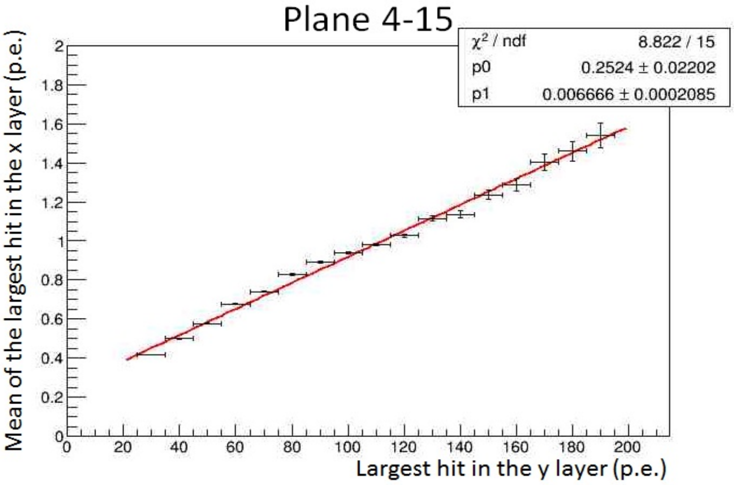

Figure 5.21: Relation between light yield of the grid scintillators along with the x and y axis. Horizontal axis is the maximum light yield of the vertical grid layer and vertical axis is mean light yield of the horizontal grid layer of the same planes.

Table 5.5: Evaluated performance of the water module detector

Parameter	Performance
Width of pedestal (electric noise)	13% of gain (Fig. 5.9)
MPPC gain	Tuned to breakdown voltage+3.5 V with a stability better than 10% (Fig. 5.10)
MPPC noise	2.3 ± 0.5 hits/cycle/module (Fig. 5.12)
Scintillator mean light yield	16 p.e. /3 mm/MIP (Fig. 5.13)
Scintillator mean light yield angle by angle	10 % discrepancy between data and MC (Fig. 5.16)
Scintillator light yield distribution	5 % discrepancy between data and MC (Fig. 5.15)
Scintillator hit efficiency	1 % discrepancy between data and MC (Fig. 5.17)
2D track reconstruction efficiency	5 % discrepancy between data and MC (Fig. 5.19,5.20)
Scintillator crosstalk	0.67% (Fig. 5.21)

Chapter 6

Measurement of charged current inclusive cross sections

6.1 Analysis overview

For a precise study of the neutrino oscillation, a good understanding of neutrino interactions on nucleus is indispensable. Especially, it is important to understand the difference of the cross section between the water and plastic for the T2K experiment because the main neutrino interactions targets of the T2K near detector consists of plastic scintillators while the far detector, Super-Kamiokande, uses water. However, there is almost no data of the neutrino interactions with water target and the difference of the plastic and water is not understood experimentally and the uncertainty of the difference is estimated based on only theoretical assumption for the oscillation analysis.

Purpose of this analysis is to validate if the assumed uncertainty of the difference between the plastic and water is consistent with experimental data. In this analysis, the flux averaged inclusive ν_μ charged current cross sections on H_2O, CH, Fe and their ratios at the T2K beam center are measured by using water module, Proton Module and INGRID detectors. Measurement of absolute cross section suffers from more than 10% uncertainty of neutrino flux but it is expected to be canceled for the cross section ratios. This method was established in the last analysis [89] for measurement of the cross section ratio between plastic and iron by using the Proton Module and INGRID. In this analysis, water target data is newly added by using the water module. In addition, this analysis provides more model independent measurement than the last analysis because a method of the cross section extraction is improved by using information of reconstructed track angle. This enables all of external neutrino interaction researchers to interpret the result easily without dedicated detector simulation.

Figure 6.1 shows the expected neutrino energy spectrum and interactions at on-axis simulated by MC. As shown in a left figure in Fig. 6.1, the on-axis neutrino beam has the mean energy of 1.5 GeV and $+0.85-0.75$ GeV for 1 sigma spread. As shown in a left figure in Fig. 6.1, the main charged current neutrino interaction modes are CCQE, CC1π and CCDIS and their ratio is about 2: 2: 1. The fraction of NC interaction is 30% of all interactions. Figure 6.2 shows expected momentum and angle distribution of muons produced by the CC interactions. In this chapter, we define the signal as CC-inclusive interactions with muon angle of less than 45 degrees and momentum of more than 0.4 GeV due to limited INGRID detector acceptance, which is used for muon identification. Background events in this analysis are from neutrino interactions with the wall of the building, CC-inclusive interactions outside the signal regions, interactions with non water target materials (mainly plastic scintillators), $\overline{\nu}_\mu, \nu_e, \overline{\nu}_e$ interactions and NC interactions.

The CC-inclusive cross sections on Fe, CH and H_2O are calculated from the number of selected events in the horizontal center module of INGRID, Proton Module and water module, respectively. In addition, the Proton Module is used for the statistical subtraction of neutrino interactions on the scintillators of the water module. The three horizontal INGRID modules near the beam center are used for muon identification for the water module and Proton Module. The horizontal center INGRID module is located directly behind the Proton Module and water module and the term "INGRID" hereafter refers to this specific module, unless otherwise stated. The total cross section is calculated as a sum of the differential cross sections as a function of muon angle to reduce model dependency, although the last analysis [89] did not. For each measurement, Monte Carlo simulation is used for subtraction of background events, calculation of detection efficiency and an estimation of relations between the reconstructed track angle and true muon angle. The CC-inclusive cross section per nucleon is predicted to be different between H_2O, CH and Fe as shown in Table. 6.1. The difference is mainly coming from the fraction of neutrons in a nucleus as summarized in Table 6.2 and CC coherent interaction which depends on $\sim (A)^2$.

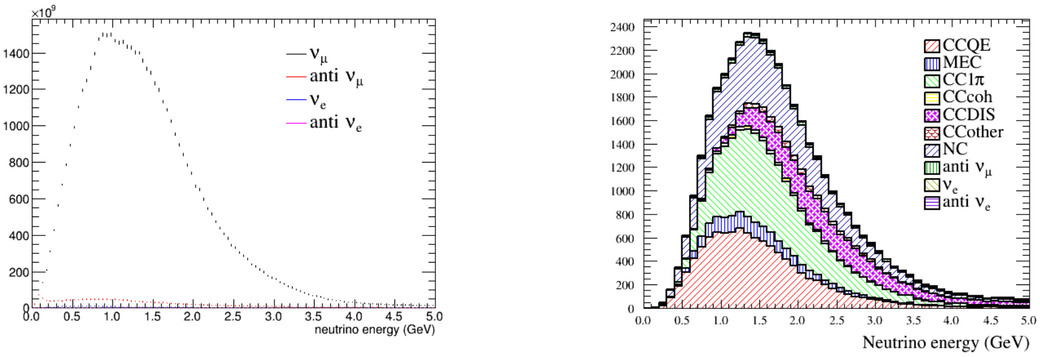

Figure 6.1: Expected neutrino flux predicted by JNUBEAM(left) and the energy of neutrinos that interacted with H_2O predicted by NEUT (right) at on-axis.

Table 6.1: Expected flux averaged inclusive ν_μ charged current cross section on Fe, CH and H_2O by NEUT. Neutrino interaction parameters used for calculation are described in Sec. 6.6.2.

Used CC0πmodel	Cross section	NEUT expectation
RPA+RFG+2p2h	$\sigma_{\mathrm{H_2O}}$	0.819×10^{-38} cm^2
	σ_{CH}	0.832×10^{-38} cm^2
	σ_{Fe}	not available
	$\sigma_{\mathrm{H_2O}}/\sigma_{\mathrm{CH}}$	0.984
	$\sigma_{\mathrm{Fe}}/\sigma_{\mathrm{H_2O}}$	not available
	$\sigma_{\mathrm{Fe}}/\sigma_{\mathrm{CH}}$	not available
RFG+2p2h	$\sigma_{\mathrm{H_2O}}$	0.860×10^{-38} cm^2
	σ_{CH}	0.875×10^{-38} cm^2
	σ_{Fe}	0.904×10^{-38} cm^2
	$\sigma_{\mathrm{H_2O}}/\sigma_{\mathrm{CH}}$	0.983
	$\sigma_{\mathrm{Fe}}/\sigma_{\mathrm{H_2O}}$	1.051
	$\sigma_{\mathrm{Fe}}/\sigma_{\mathrm{CH}}$	1.033

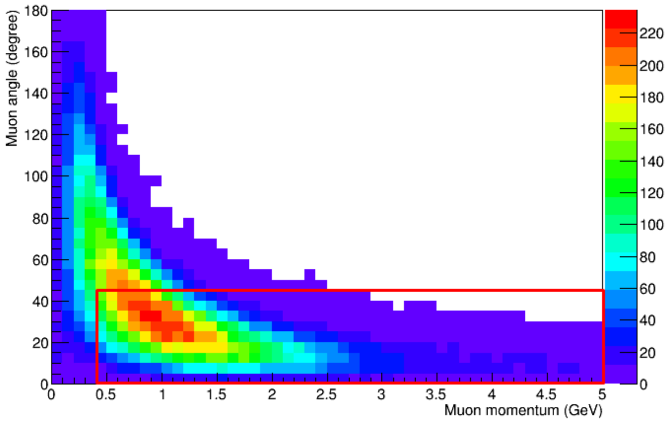

Figure 6.2: Expected angle and momentum of muons produced by CC-inclusive interactions on H_2O predicted by NEUT. Red square part, the muon angle is less than 45 degree and momentum is larger than 400 MeV, is defined as signal in this measurement. As discussed in Sec. 6.3.5, the angle is limited because the INGRID, which is used for muon identification, is located at only the downstream side of the water module and Proton Module. The momentum is limited because we required to penetrate two iron plates (13 cm) of the INGRID.

Table 6.2: Number of protons and neutrons per nucleus and their fraction.

	Protons per nucleus	Neutrons per nucleus	Proton fraction	Neutron fraction
Fe	26	29.91	46.5%	53.5%
H_2O	10	8.004	55.5%	44.5%
CH	7	6.01	53.8%	46.2%

6.2 Data set

For the INGRID and Proton Module, the beam data from Nov. 2010 to Mar. 2011, from Apr. to Jun. 2012 and Oct. 2012 to May 2013 are analyzed. The total number of POT is 5.89×10^{20} with FHC. Because the water module was installed and the Proton Module was removed in July 2016, different run period is used for the water module. For the water module, the beam data from Oct. 2016 to Apr. 2017 are analyzed. The total number of POT is 7.25×10^{20} with FHC.

6.3 Event selection

6.3.1 Event selection for water module

In order to select signal among the background events, event selections are applied based on information of track reconstructed by the hit pattern of the scintillators. Characteristic of the signal (CC-inclusive interactions) is that a muon is produced inside the target. On the other hand, background events from NC interactions and the wall do not produce muon or its vertex is outside the target. The event selections are as follows:

1. Time clustering
2. Two-dimensional track reconstruction
3. Track matching with INGRID

4. Three-dimensional track matching
5. Vertexing
6. Beam timing cut
7. Front-veto cut
8. Fiducial volume cut
9. Track angle cut

The details of these selections are explained in this section. Figure 6.3 shows an event display of typical signal event passing the event selection criteria.

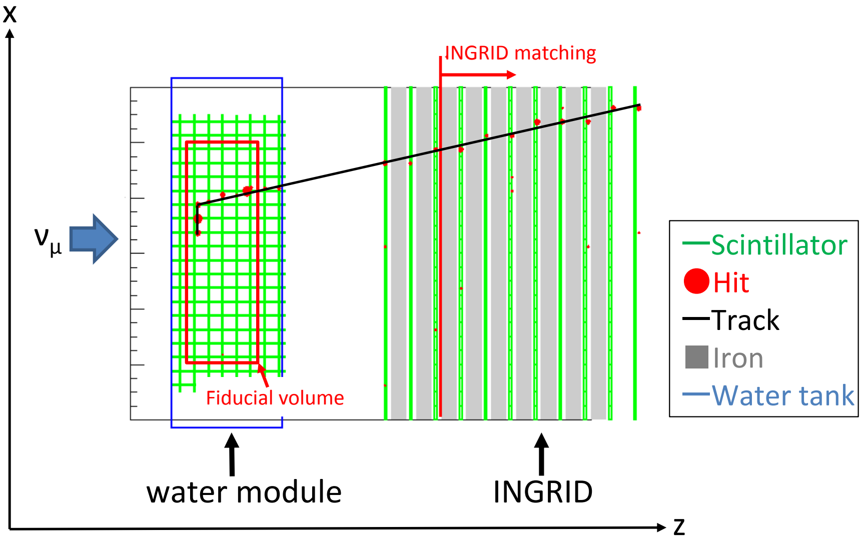

Figure 6.3: An event display of the typical signal events passing the event selection criteria with the water module.

Time clustering

Scintillator channels having an ADC signal larger than 2.5 p.e. are defined as "hit". Hits are clustered with the following criteria: If there are more than three hits within 100 nsec in the water module, all the hits within 50 nsec from the average time are classified into a cluster, as shown in Fig. 6.4. By this clustering, random MPPC noise hits are reduced.

Two-dimensional track reconstruction

The next step is the reconstruction of 2D tracks. The tracks in x-z and y-z view are reconstructed independently based on hits of the scintillators. The tracks are reconstructed in the water module and INGRID independently. An algorithm used for the track reconstruction is described in Appendix C in detail.

Track matching with INGRID

Because the INGRID is located downstream of the water module, a muon produced in the water module can hit both of the water module and INGRID. In order to identify muon by using the

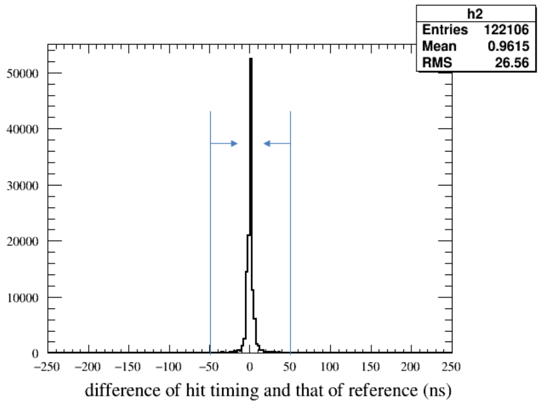

Figure 6.4: Difference of the hit timing from average time in the same bunch.

INGRID, when two-dimensional tracks are reconstructed in the same beam bunch for both the INGRID and water module, it is judged if a pair of the track in the water module and INGRID is merged as a track or not. The tracks are merged if they meet the following requirements:

- The most upstream z point of the INGRID track is in either of the first two layers of the INGRID
- Difference between the reconstructed angle of the INGRID and water module tracks with respect to z-axis is less than 35 degrees.:

$$|\Delta\theta| = |\theta_{\mathrm{INGRID}} - \theta_{\mathrm{WM}}| < 35 \text{ deg.} \tag{6.1}$$

- At the halfway z point between the INGRID and water module, the distance between the INGRID and water module tracks along with x or y axis is less than 150 mm:

$$|\Delta x| = |x_{\mathrm{INGRID}} - x_{\mathrm{WM}}| < 150 \text{ mm.} \tag{6.2}$$

If there are multiple candidates to satisfy the criteria, a track with the smallest quadratic sum of $\Delta\theta/35$ (deg) and $\Delta x/150$ (mm) is selected. Figure 6.5 shows distributions of the $\Delta\theta$ and Δx. When a pair of the tracks is merged, all hits which compose the pair of the tracks are re-fitted to get a merged track. 2D tracks not matched with INGRID are not used for this analysis.

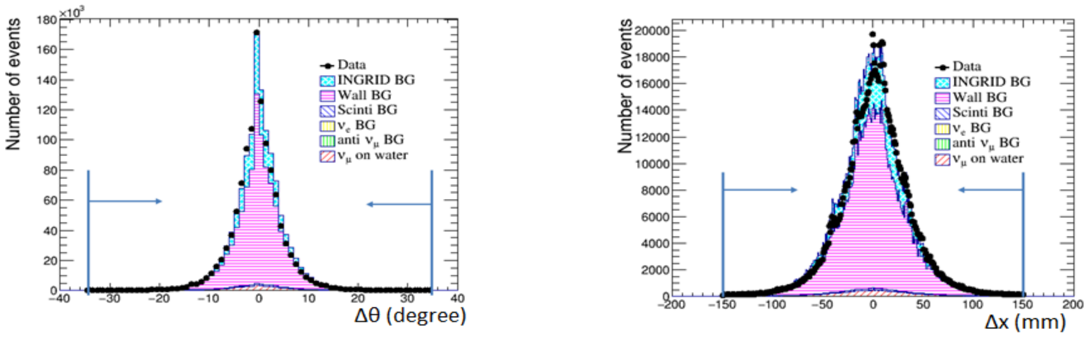

Figure 6.5: Distributions of $\Delta\theta$ (left) and Δx (right) defined in Eq. 6.1 and 6.2.

Three-dimensional track matching

Three-dimensional tracks are formed among the pairs of two-dimensional INGRID matched tracks in x-z view and that in y-z view. They are formed based on the difference of the upstream point z of them. The difference should be less than two planes of the parallel scintillators. If there are multiple candidates, a pair with the smallest difference of the downstream point z is selected.

Vertexing

After the three-dimensional track reconstruction, the upstream point z of each INGRID matched three-dimensional track is identified as a reconstructed vertex. If a pair of INGRID-matched three-dimensional tracks meet the following conditions they are identified as tracks coming from a common vertex:

- The sum of the z position difference between the upstream z of the two tracks in the x-z view and y-z views is less than three planes of the parallel scintillators:

  $$|\Delta z_x| + |\Delta z_y| <= 2 \text{ planes } (10 \text{ cm}) \tag{6.3}$$

  where Δz_x and Δz_y are the z position differences between the upstream z point of the two tracks in the x-z and y-z views.

- The distance between the upstream edges of the two tracks in the x-z and y-z view is less than 150 mm:

  $$\sqrt{\Delta x^2 + \Delta y^2} < 150 \text{ mm} \tag{6.4}$$

  where Δx and Δy are the distances between the x and y positions of the upstream z point of the two tracks.

These cuts are applied to every vertex since each one is expected to correspond to a single neutrino interaction. The vertex position is re-defined as that of the longest track among the common vertex. Information about the number of track from a vertex is not used for this analysis.

Beam timing cut

In order to reduce non-beam background events, such as cosmic-rays, only events within 100 nsec of the expected beam bunch timing are selected as shown in Fig. 6.6. The individual event timing is defined as the time recorded by the channel with the largest number of photo-electrons.

Front-veto cut and fiducial cut

Two cuts are applied to reduce background events from neutrino interactions in material upstream of the water module (mainly from the wall of the building and the INGRID vertical modules). The first is front-veto cut. If the upstream point of a track is more upstream than the second plane of the parallel scintillators, that event is rejected. Second, fiducial volume cut is applied. The fiducial volume is a cubic volume which is defined as the central 70 cm×70 cm transverse area of the water module from tracking plane 5 through to 14 (Fig. 6.7). Figures 6.8 and 6.9 show the vertex distribution before applying these cut.

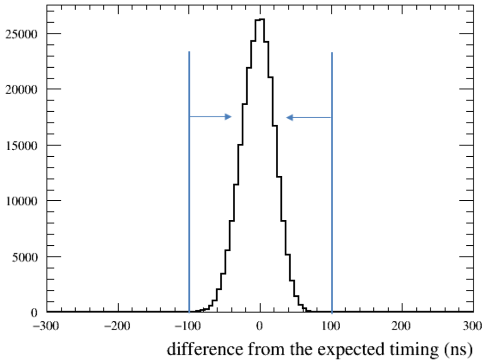

Figure 6.6: Difference between the observed and expected event timing with data.

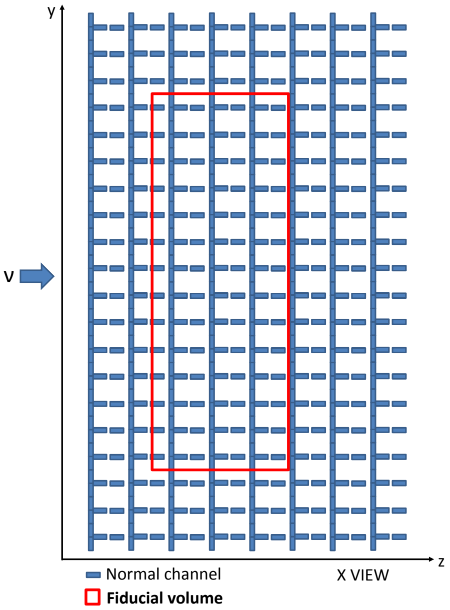

Figure 6.7: View of the fiducial volume in y-z view (left) and x-z view(right). Scintillators orthogonal to the page are shown in each view. The scintillators perpendicular to the beam are parallel scintillators and that parallel to the beam is grid scintillators.

Reconstructed angle cut

The 3D angle of the longest reconstructed track from a vertex is required to be less than 45 degrees because the definition of the signal is CC-inclusive interaction whose muon angle is less than 45 degrees. Figure 6.10 shows the reconstructed angle distribution.

Event selection summary

The number of selected events and fraction of the background events in the water module at each selection step are summarized in Table 6.3 and Figs. 6.11– 6.14. 1.73×10^4 events are expected by Monte Carlo simulation after the event selection. The purity of the ν_μ CC interaction on H_2O is 69.0% and main background source is neutrino interaction on scintillator(19.8%). Remaining background sources are neutral current(NC) interaction(2.9%), other flavor neutrino

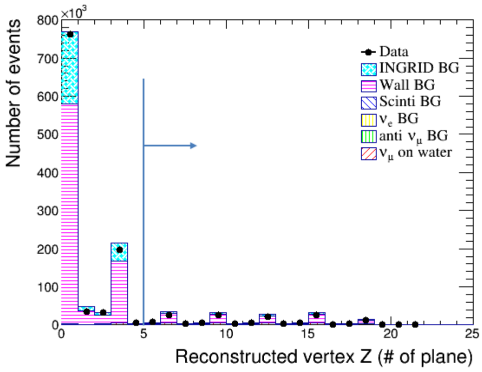

Figure 6.8: Reconstructed vertex z distribution before the front-veto cut for the water module. In x-axis, 0 correspond the most upstream plane.

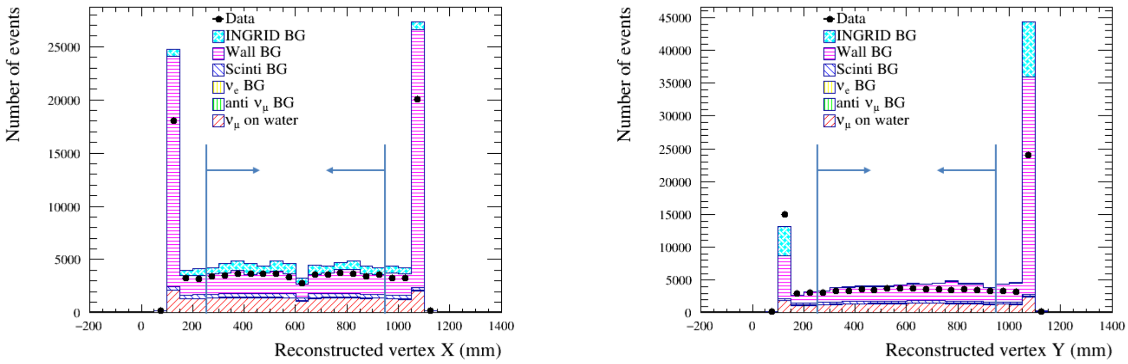

Figure 6.9: Reconstructed vertex x (left) and y (right) distribution after the front-veto cut for the water module. Center of the detector is set to 600mm.

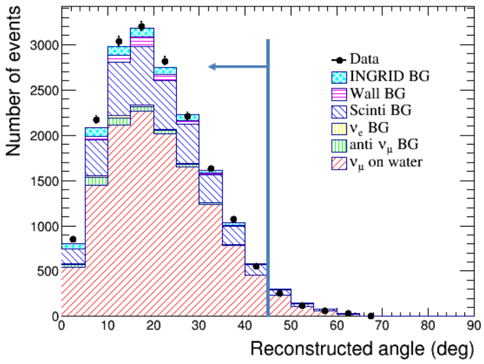

Figure 6.10: Reconstructed angle distribution of the longest track from a vertex after the front-veto and fiducial volume cut for the water module

interactions(2.0%), gamma from π^0 produced by neutrino interaction on wall(2.4%) and back scattered muons produced by neutrino interactions with the INGRID(3.1%). Although the former tree does not produce muon, they are remained after the event selection due to miss-identification of muon. Figure 6.15 shows the neutrino energy before and after the event selection.

Main selected interaction modes are CCQE, CC1π and CCDIS and their fraction is about 3 : 2 : 1. Figure 6.16 shows true momentum and angle of muons produced on H_2O target after the event selection.

Table 6.3: Summary of the event selection for the water module

Selection	Data	MC						
		CC	NC	$\overline{\nu}_\mu$, ν_e, $\overline{\nu}_e$	CH B.G.	Wall B.G.	INGRID B.G.	All
Vertexing	1175980	4.39×10^4	1.66×10^2	1.12×10^3	1.08×10^4	9.10×10^5	2.77×10^5	1.24×10^6
Front-veto	100790	2.77×10^4	1.04×10^3	9.38×10^2	6.66×10^3	8.09×10^4	1.46×10^4	1.32×10^5
Fiducial	17992	1.25×10^4	4.68×10^2	4.42×10^2	3.51×10^3	3.49×10^2	5.84×10^2	1.78×10^4
Track angle	17528	1.20×10^4	4.53×10^2	4.39×10^2	3.39×10^3	3.47×10^2	5.64×10^2	1.73×10^4

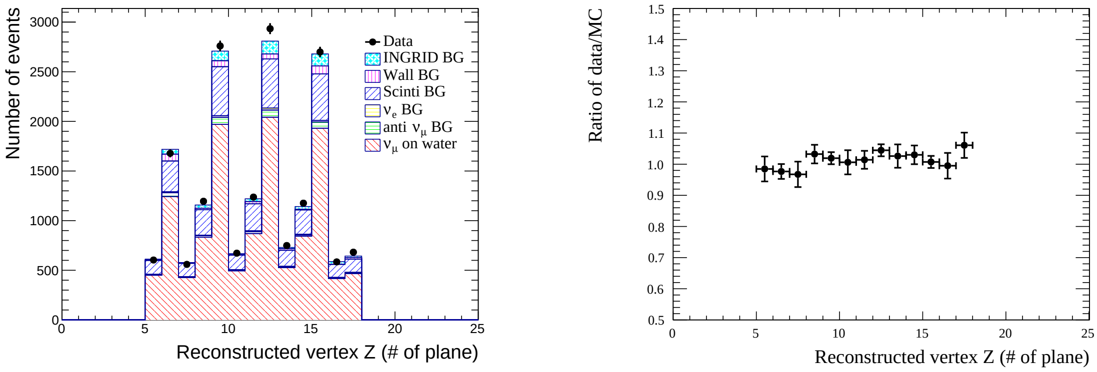

Figure 6.11: Reconstructed vertex z in y-z view (left) and their ratio between data and Monte Carlo simulation (right) of the selected events for the water module. Peaks are seen in the parallel scintillator layers (number of plane = 3, 6, 9, 12). The other are grid scintillator layers.

6.3.2 Event selection for Proton Module

The event selection for the Proton Module is almost same as that for water module, although a few parameters to determine the criteria are tuned for the Proton Module as described in Appendix C because the arrangement of scintillators are different between detectors.

Event selection summary

The number of selected events and fraction of the background events in the Proton Module at each selection step are summarized in Table 6.4 and Fig. 6.17. 2.23×10^4 events are expected by MC after the event selection. The purity of the signal is 85.4%. Background sources are NC interaction(4.2%), the other flavor neutrino interaction (2.4%), gamma from π^0 produced by neutrino interaction on the wall(2.1%) and backward going events from neutrino interactions in the INGRID(5.2%).

6.3.3 Event selection for INGRID

The event selection for the INGRID is almost the same as that for water module, although a few parameters to determine the criteria are tuned for the INGRID as described in Appendix C because the arrangement of scintillators are different between detectors. In addition, additional selection named “acceptance cut” is applied for getting similar angular acceptance with the

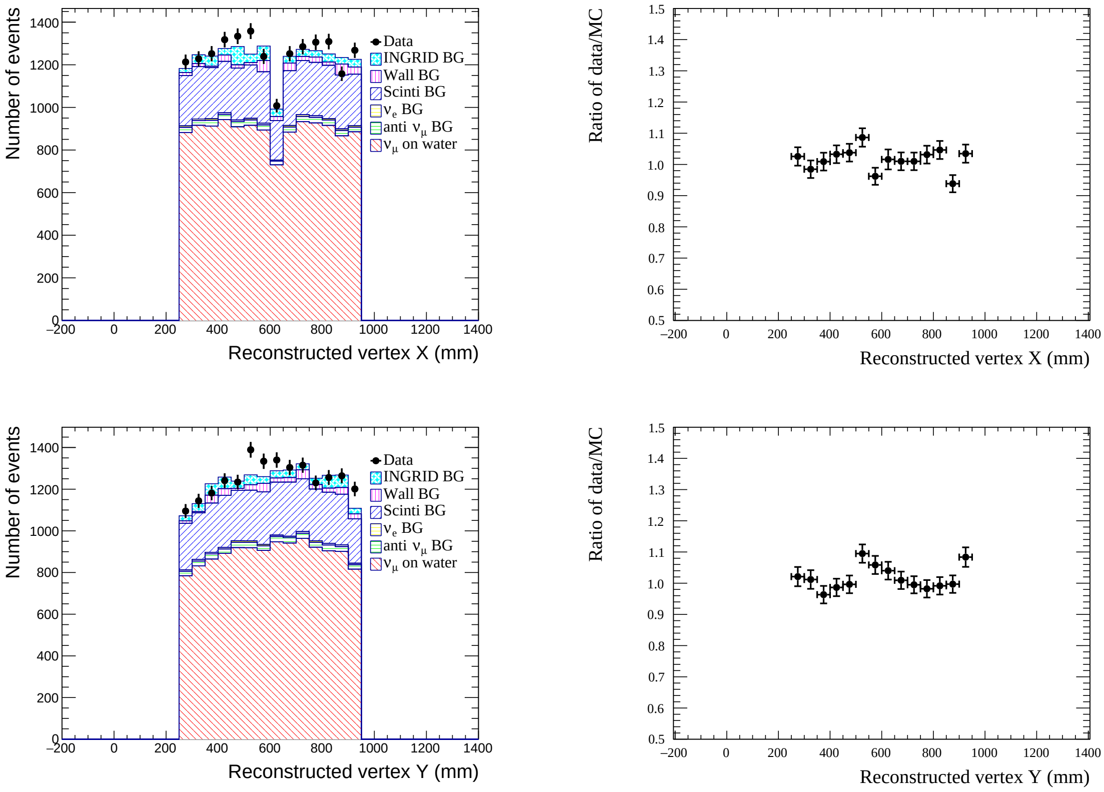

Figure 6.12: Reconstructed vertex x (upper left) and y (lower left) and their ratio between data and Monte Carlo simulation (right) of selected event for the water module. A valley in vertex x is due to dead channels, concentrated in one TFB damaged by water drop.

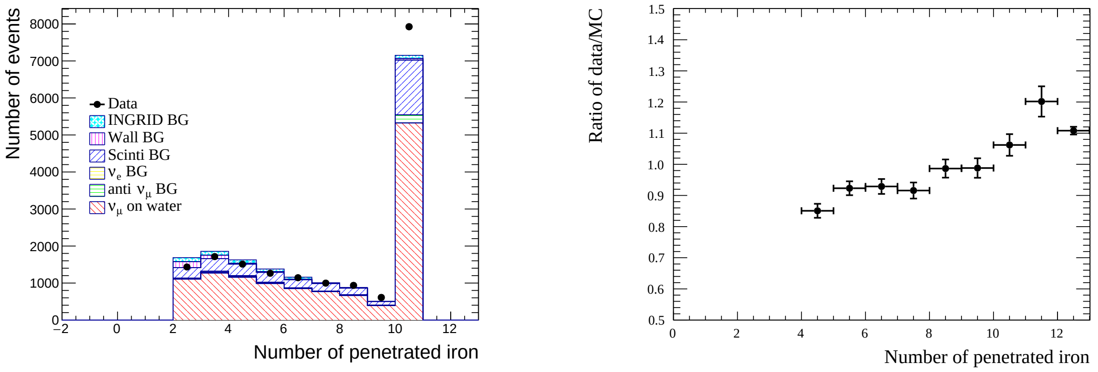

Figure 6.13: The number of INGRID iron layers penetrated by the longest track from a vertex (left) and their ratio between data and Monte Carlo simulation (right) of the selected event for the water module

water module as follows. An imaginary module is defined directly behind the INGRID module as shown in Fig. 6.18. The distance between the INGRID module and the imaginary module is the same as that between the water module and the INGRID module. The reconstructed tracks are then extended further downstream, even if the track has stopped in INGRID. If at least one reconstructed track from the vertex reaches the imaginary module, that event is selected. If no

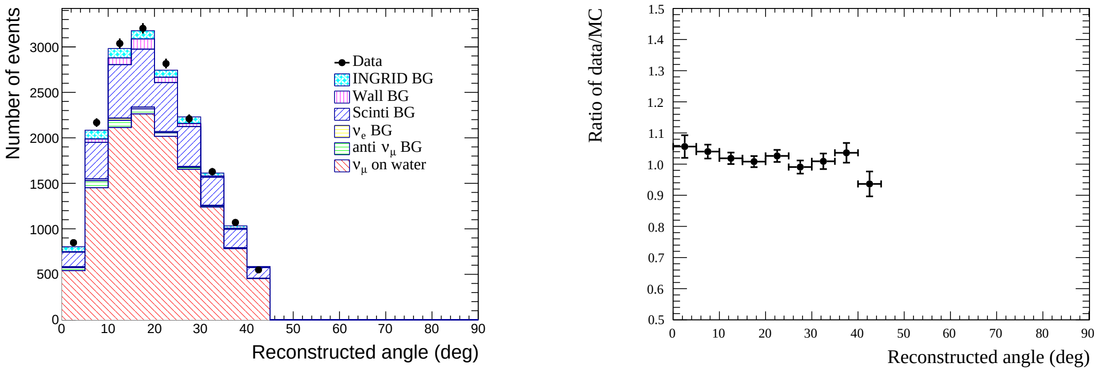

water module

Figure 6.14: Reconstructed angle (left) and their ratio between data and Monte Carlo simulation (right) for the longest track of the selected event for the water module

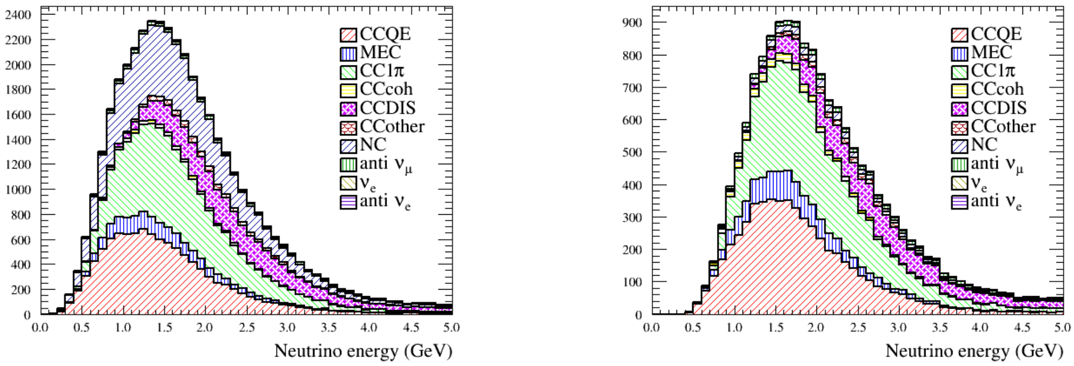

Figure 6.15: True energy of neutrino that interacted with H_2O before event selection (left) and after event selection (right) for the water module

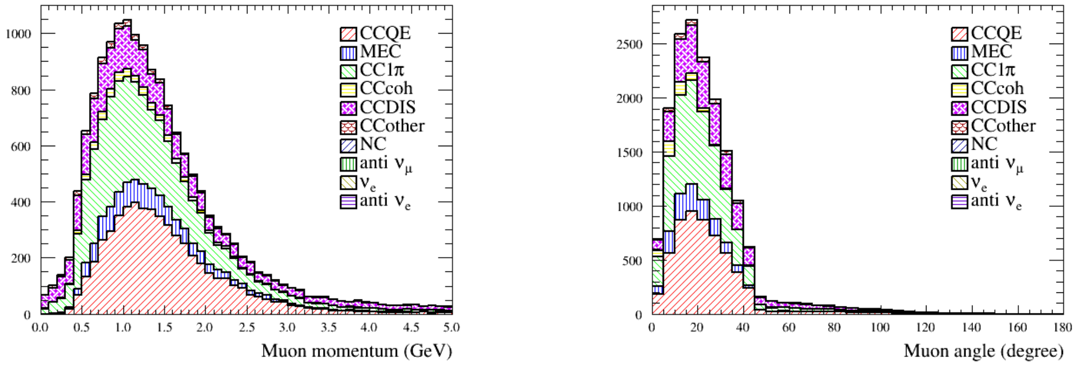

Figure 6.16: True angle (left) and momentum (right) of muon produced by neutrino interaction on H_2O after event selection for the water module

tracks reach the imaginary module the event is rejected. By using this cut, the difference of the

Table 6.4: Summary of the event selection for the Proton Module

Selection	Data	MC					
		CC	NC	$\overline{\nu}_\mu$, ν_e, $\overline{\nu}_e$	Wall B.G.	INGRID B.G.	All
Vertexing	1321290	5.56×10^4	$2.66{\times}10^3$	2.00×10^3	1.03×10^6	2.77×10^5	1.36×10^6
Front-veto	264550	4.69×10^4	$2.25{\times}10^3$	1.72×10^3	2.17×10^5	3.63×10^4	3.04×10^5
Fiducial	22930	1.98×10^4	$9.52{\times}10^2$	7.31×10^2	5.54×10^2	9.97×10^2	2.32×10^4
Track angle	22165	1.92×10^4	$9.14{\times}10^2$	7.26×10^2	5.51×10^2	9.50×10^2	2.23×10^4

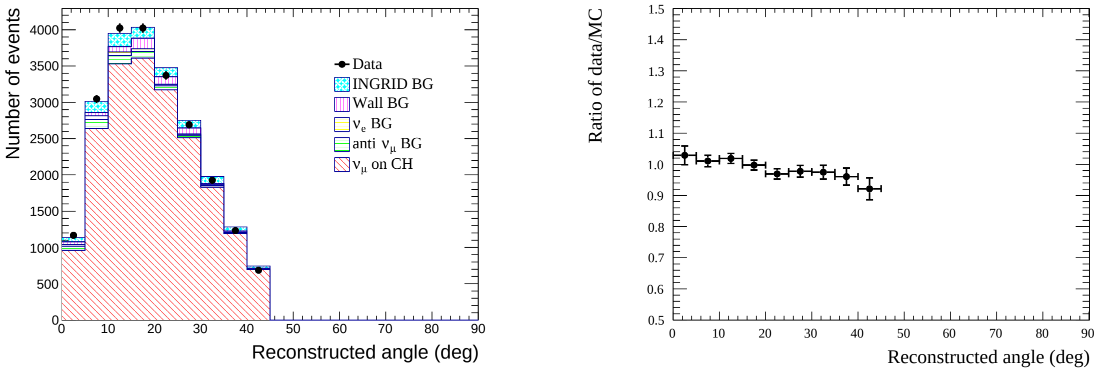

Proton module

Figure 6.17: Reconstructed angle (left) and their ratio between data and Monte Carlo simulation (right) of the longest track of the selected event for the Proton Module.

efficiency between the INGRID and the other two detectors changed from 50% to less than 10%.

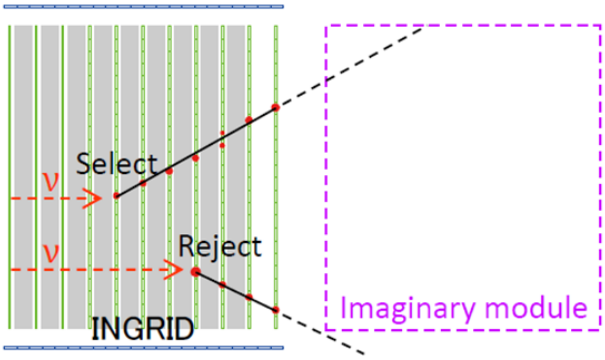

Figure 6.18: Example of a selected and rejected event by acceptance cut for the INGRID [112].

Event selection summary

The number of selected events and fraction of the background events in the INGRID at each selection step are summarized in Table 6.5 and Fig. 6.19. 3.12×10^5 events are expected by MC after the event selection. The purity of the signal is 88.1%. Background sources are NC interaction(5.2%), the other flavor neutrino interaction (2.9%), neutrino interaction on scintillator(3.3%), gamma from π^0 produced by neutrino interaction on wall and INGRID(0.3% and 0.2%)

Table 6.5: Summary of the event selection for the INGRID

Selection	Data	MC						
		CC	NC	$\overline{\nu}_\mu$, ν_e, $\overline{\nu}_e$	CH B.G.	Wall B.G.	INGRID B.G.	All
Vertexing	3019430	1.11×10^6	6.98×10^4	3.20×10^4	4.49×10^4	9.45×10^5	3.36×10^5	2.54×10^6
Front-veto	1468490	1.07×10^6	6.74×10^4	3.07×10^4	3.97×10^4	1.98×10^5	4.33×10^4	1.45×10^6
Fiducial	431211	4.10×10^5	2.58×10^4	1.14×10^4	1.49×10^4	1.52×10^3	1.06×10^2	4.65×10^5
Acceptance	308971	2.88×10^5	1.81×10^4	9.56×10^3	1.07×10^4	9.26×10^2	6.73×10^2	3.28×10^5
Track angle	293418	2.74×10^5	1.72×10^4	9.31×10^3	1.02×10^4	8.70×10^2	6.38×10^2	3.12×10^5

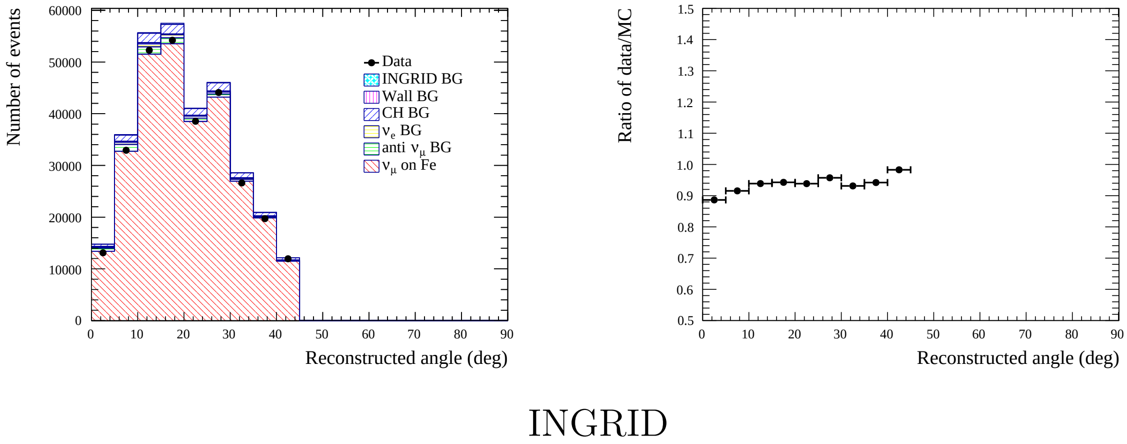

Figure 6.19: Reconstructed angle (left) and their ratio between data and MC (right) of the longest track of the selected event for the INGRID

6.3.4 Event pileup correction

If more than one neutrino or sand muon events are detected by the detectors at the same time, sometimes we fail to count the number of events. Then a correction must be applied to account for this event pileup effect. For the INGRID, this effect is estimated by using event loss constant (C_{loss}) defined as follows.

$$N_{\text{corr}} = \frac{N_{\text{sel}}}{1 - C_{\text{loss}} n_{\text{ppb}}} \tag{6.5}$$

Where N_{sel} is the number of the selected events, N_{corr} is the number of the selected events after the pileup correction and n_{ppb} is the number of protons in a bunch. The event loss constant is calculated by data as follows. Hits of two bunches are piled up to make single bunch. In this data, the number of POT per bunch and noise are virtually doubled:

$$N_{\text{corr}} = \frac{N_{\text{sel2}}}{1 - C_{\text{loss}} 2 n_{\text{ppb}}} \tag{6.6}$$

where N_{sel2} is the number of selected events in the double bunched data. In addition, hits of a bunch with beam and that without beam are piled up to make another single bunch. In this data, the number of noise per bunch is virtually doubled:

$$N_{\text{corr}} = \frac{N_{\text{sel1}}}{1 - C_{\text{loss}} n_{\text{ppb}}} \tag{6.7}$$

By using Eq. 6.6 and 6.7, the event loss constant is calculated as follows:

$$C_{\text{loss}} = \frac{N_{\text{sel2}} - N_{\text{sel1}}}{n_{\text{ppb}}(2N_{\text{sel2}} - N_{\text{sel1}})} \tag{6.8}$$

Figure 6.20 and Table 6.6 show the calculated event loss constant and N_{corr} for the INGRID. For the water module and Proton Module, effect of the pileup is small because their mass is relatively small. Then, no pileup corrections are applied for the water module and Proton Module.

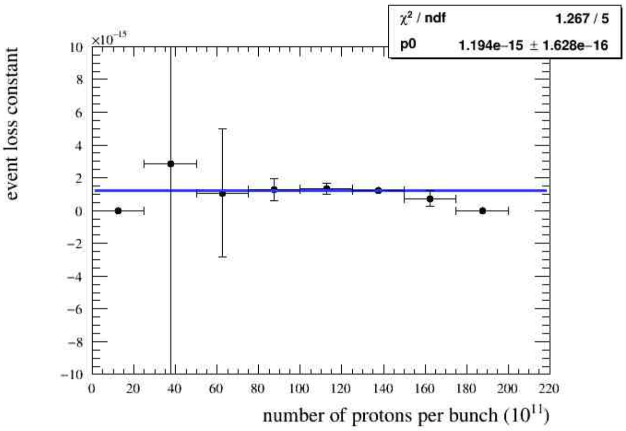

Figure 6.20: Calculated event loss constant

6.3.5 CC-inclusive selection efficiency

Figure 6.21 shows CC-inclusive selection efficiency for the water module, proton module and INGRID detectors as a function of muon angle and momentum, estimated by MC simulation. Because the efficiency is small, less than 10%, at large angle region due to the limited INGRID

Table 6.6: Calculated event loss constant for the INGRID

reconstructed angle bin	C_{loss} (10^{-15})	N_{sel}	N_{corr}
0-5 deg	2.80	13106	13582.0
5-10 deg	1.98	32928	33765.3
10-15 deg	2.08	52272	53671.3
15-20 deg	1.86	54205	55500.6
20-25 deg	1.19	38540	39119.4
25-30 deg	1.61	44097	45002.4
30-35 deg	1.09	26615	26984.1
35-40 deg	1.30	19709	20036.4
40-45 deg	0.98	11946	12094.0
Total		293418	299755.5

detector acceptance, only the CC interactions whose muon angle is less than 45 degrees is defined as the signal in this analysis. In addition, because the efficiency is small, less than 10%, at low momentum region due to the requirement of the INGRID track matching cut, only the CC interactions whose muon momentum is more than 0.4 GeV is defined as signal in this analysis. Figure 6.22 shows the CC-inclusive selection efficiency as a function of muon angle with the limited phase space. Even in the limited phase space, the efficiency is not flat as a function of muon angle. In order to reduce effect on the cross section estimation due to the non-flat efficiency, cross section is calculated by a sum of the differential cross section as a function of the muon angle, as described in Sec. 6.4. On the other hand, efficiency is almost flat as a function of the muon momentum if the muon angle is fixed, as shown in Fig. 6.21. Then sum of cross section is taken only by the muon angle but not muon momentum. Figure 6.23 shows the efficiency of the signal as a function of true neutrino energy. They are similar to each other among the detectors.

Table 6.7: Calculated detection efficiency of the signal with the limited phase space. The values are same as that of the left figure in Fig. 6.22.

True muon angle bin	WM	PM	INGRID
0-5 deg	0.849	0.833	0.907
5-10 deg	0.863	0.857	0.921
10-15 deg	0.878	0.865	0.913
15-20 deg	0.854	0.837	0.861
20-25 deg	0.796	0.782	0.788
25-30 deg	0.735	0.722	0.697
30-35 deg	0.646	0.633	0.584
35-40 deg	0.527	0.534	0.441
40-45 deg	0.372	0.409	0.310

6.4 Cross section extraction

In this section, a method to calculate central values of the cross sections and their ratios is described. A method to calculate their uncertainties is estimated in Sections 6.5 and 6.6. The

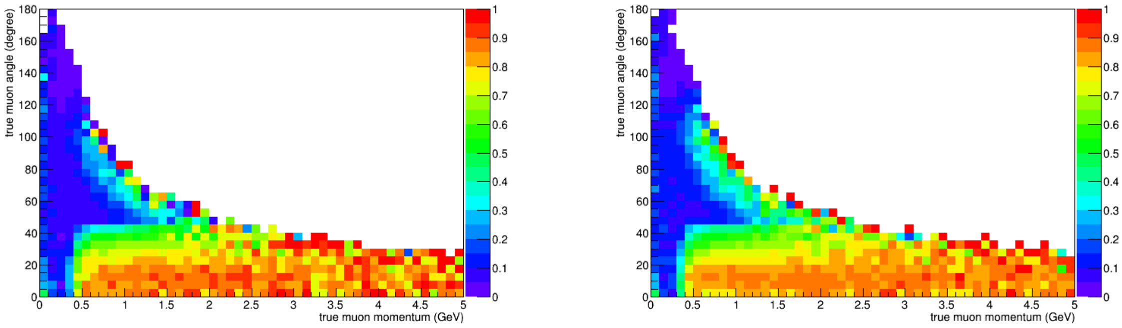

water module

Proton Module

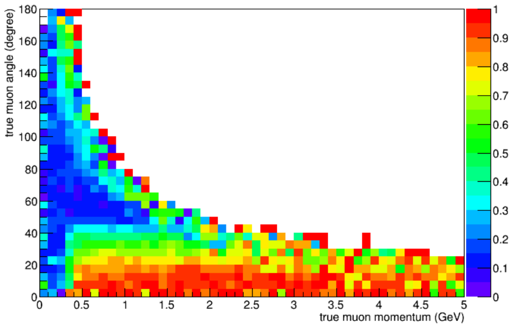

INGRID

Figure 6.21: Neutrino selection efficiency for all CC-inclusive interactions as a function of true muon angle and momentum for the water module(upper left), Proton Module(upper right) and INGRID(lower left).

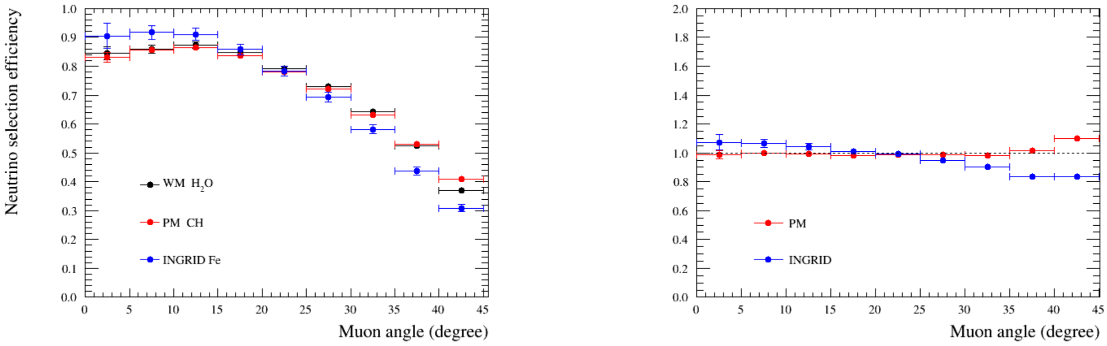

Figure 6.22: Neutrino selection efficiency for CC-inclusive interactions with limited phase space as a function of muon angle for the three detectors (left) and their ratios (right).

flux averaged ν_μ CC-inclusive cross section is calculated based on unfolding method [113] as follows:

$$\sigma_{\mathrm{H_2O}} = \sum_{ij} \frac{U_{\mathrm{ij\ WM}}(N^{\mathrm{sel}}_{\mathrm{j\ WM}} - N^{\mathrm{BG}}_{\mathrm{j\ WM}})}{\Phi^{\mathrm{H_2O}}_{\mathrm{WM}} T^{\mathrm{H_2O}}_{\mathrm{WM}} \varepsilon^{\mathrm{H_2O}}_{\mathrm{i\ WM}}} \tag{6.9}$$

$$\sigma_{\mathrm{CH}} = \sum_{ij} \frac{U_{\mathrm{ij\ PM}}(N^{\mathrm{sel}}_{\mathrm{j\ PM}} - N^{\mathrm{BG}}_{\mathrm{j\ PM}})}{\Phi^{\mathrm{CH}}_{\mathrm{PM}} T^{\mathrm{CH}}_{\mathrm{PM}} \varepsilon^{\mathrm{CH}}_{\mathrm{i\ PM}}} \tag{6.10}$$

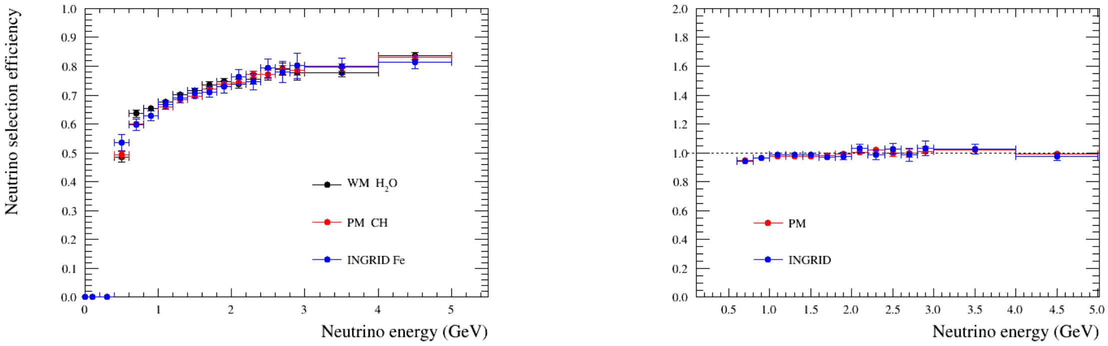

Figure 6.23: Neutrino selection efficiency for CC-inclusive interactions with limited phase space as a function of neutrino energy (left) and their ratios (right).

$$\sigma_{\rm Fe} = \sum_{ij} \frac{U_{\rm ij\ INGRID}(N^{\rm sel}_{\rm j\ INGRID} - N^{\rm BG}_{\rm j\ INGRID})}{\Phi^{\rm Fe}_{\rm INGRID} T^{\rm Fe}_{\rm INGRID} \varepsilon^{\rm Fe}_{\rm i\ INGRID}} \tag{6.11}$$

where $N^{\rm sel}$ is the number of selected events, $N^{\rm BG}$ is the number of expected background events, Φ is the integrated ν_μ flux, T is the number of target nucleons and ε is the detection efficiency for all CC events. The subscript i is true muon angle bin and subscript j is a bin of the reconstructed angle of the longest track from a vertex. Their binning are defined as shown in Table 6.8 determined by detector resolution. U_{ij} is a probability that events in true muon angle bin i is observed in reconstructed angle bin j. The subscript WM, PM and INGRID are the water module, Proton Module and INGRID detectors, respectively. Superscript of H_2O, CH and Fe is kind of the target materials. Because the water module has not only H_2O but also CH, the subscripts and superscripts are separated.

The background events for this analysis are from CC interactions with muon angle of more than 45 degrees or muon momentum of less than 0.4 GeV, NC interactions, $\bar{\nu}_\mu$, ν_e, $\bar{\nu}_e$ interactions, interactions on elements other than the measuring elements in the detector and interactions outside the target. All of the backgrounds are estimated by MC except for CC-inclusive interactions on plastic scintillator of the water module, which is a main background for $\sigma_{\rm H_2O}$. It is estimated by using the Proton Module as follows:

$$\begin{aligned}
N^{\rm BG}_{\rm WM} &= N^{\rm ScintillatorCCBG}_{\rm WM} + N^{\rm OtherBG}_{\rm WM} && (6.12)\\
N^{\rm ScintillatorCCBG}_{\rm WM} &= \sum_i \sigma_{i\ \rm CH} \Phi^{\rm CH}_{\rm WM} T^{\rm CH}_{\rm WM} \varepsilon^{\rm CH}_{i\ \rm WM} && (6.13)\\
&= \sum_{ij} U_{\rm ij\ PM}(N^{\rm sel}_{\rm j\ PM} - N^{\rm BG}_{\rm j\ PM}) \frac{\Phi^{\rm CH}_{\rm WM} t^{\rm CH}_{\rm WM} \varepsilon^{\rm CH}_{i\ \rm WM}}{\Phi^{\rm CH}_{\rm PM} T^{\rm CH}_{\rm PM} \varepsilon^{\rm CH}_{i\ \rm PM}} && (6.14)
\end{aligned}$$

where ${}^{\rm CH}_{\rm WM}$ is the scintillator of the water module and $\sigma_{i\ \rm CH}$ is the differential cross section on the CH target with i th muon angle bin.

The U_{ij}, probability that events in reconstruct angle bin j are in the true muon angle bin i, is calculated as follows based on Bayes's theorem:

$$\begin{aligned}
U_{ij} &= P(\theta^{true}_i | \theta^{recon}_j) && (6.15)\\
&= P(\theta^{recon}_j | \theta^{true}_i) \times P(\theta^{true}_i) / P(\theta^{recon}_j) && (6.16)\\
&= P(\theta^{recon}_j | \theta^{true}_i) \times P(\theta^{true}_i) / \sum_k P(\theta^{recon}_j | \theta^{true}_k) P(\theta^{true}_k) && (6.17)
\end{aligned}$$

where $P(\theta_j^{recon}|\theta_i^{true})$ is calculated by MC. On the other hand, $P(\theta_i^{true})$ is calculated by the iterative procedure based on data as follows:

1. $P(\theta_i^{true})$ is set to flat prior
2. calculate U_{ij}
3. $P(\theta_i^{true})$ is set to $\sum_j U_{ij}(N_j^{sel} - N_j^{BG}) / \sum_{ij} U_{ij}(N_j^{sel} - N_j^{BG})$
4. repeat 2-3

This procedure makes the prior independent of the MC. The number of required iteration is set to 10 as described in Sec. 6.4.7.

The CC-inclusive cross section ratios are calculated as follows by using Eq. 6.9–6.11:

$$\frac{\sigma_{\mathrm{H_2O}}}{\sigma_{\mathrm{CH}}} = \sum_{ij} \frac{U_{ij}(N^{\mathrm{sel}}_{\mathrm{j\ WM}} - N^{\mathrm{BG}}_{\mathrm{j\ WM}})}{\Phi^{\mathrm{H_2O}}_{\mathrm{WM}} T^{\mathrm{H_2O}}_{\mathrm{WM}} \varepsilon^{\mathrm{H_2O}}_{\mathrm{i\ WM}}} / \sum_{ij} \frac{U_{ij}(N^{\mathrm{sel}}_{\mathrm{j\ PM}} - N^{\mathrm{BG}}_{\mathrm{j\ PM}})}{\Phi^{\mathrm{CH}}_{\mathrm{PM}} T^{\mathrm{CH}}_{\mathrm{PM}} \varepsilon^{\mathrm{CH}}_{\mathrm{i\ PM}}} \tag{6.18}$$

$$\frac{\sigma_{\mathrm{Fe}}}{\sigma_{\mathrm{H_2O}}} = \sum_{ij} \frac{U_{ij}(N^{\mathrm{sel}}_{\mathrm{j\ INGRID}} - N^{\mathrm{BG}}_{\mathrm{j\ INGRID}})}{\Phi^{\mathrm{Fe}}_{\mathrm{INGRID}} T^{\mathrm{Fe}}_{\mathrm{INGRID}} \varepsilon^{\mathrm{Fe}}_{\mathrm{i\ INGRID}}} / \sum_{ij} \frac{U_{ij}(N^{\mathrm{sel}}_{\mathrm{j\ WM}} - N^{\mathrm{BG}}_{\mathrm{j\ WM}})}{\Phi^{\mathrm{H_2O}}_{\mathrm{WM}} T^{\mathrm{H_2O}}_{\mathrm{WM}} \varepsilon^{\mathrm{H_2O}}_{\mathrm{i\ WM}}} \tag{6.19}$$

$$\frac{\sigma_{\mathrm{Fe}}}{\sigma_{\mathrm{CH}}} = \sum_{ij} \frac{U_{ij}(N^{\mathrm{sel}}_{\mathrm{j\ INGRID}} - N^{\mathrm{BG}}_{\mathrm{j\ INGRID}})}{\Phi^{\mathrm{Fe}}_{\mathrm{INGRID}} T^{\mathrm{Fe}}_{\mathrm{INGRID}} \varepsilon^{\mathrm{Fe}}_{\mathrm{i\ INGRID}}} / \sum_{ij} \frac{U_{ij}(N^{\mathrm{sel}}_{\mathrm{j\ PM}} - N^{\mathrm{BG}}_{\mathrm{j\ PM}})}{\Phi^{\mathrm{CH}}_{\mathrm{PM}} T^{\mathrm{CH}}_{\mathrm{PM}} \varepsilon^{\mathrm{CH}}_{\mathrm{i\ PM}}} \tag{6.20}$$

Table 6.8: Definition of the angle binning for both reconstructed track angle and true muon angle

Bin number	angle
0	0-5 deg
1	5-10 deg
2	10-15 deg
3	15-20 deg
4	20-25 deg
5	25-30 deg
6	30-35 deg
7	35-40 deg
8	40-45 deg

6.4.1 Number of selected events

Table 6.9 shows the number of selected events. These values are based on Figs. 6.14, 6.17 and 6.19. For the INGRID, pileup correction is applied as described in Sec. 6.3.4.

Table 6.9: Summary of the number of selected events

Detector	Reconstructed track angle	N^{sel}(Data)	N^{sel}(MC)
water module	0-5 deg	848	802.8
	5-10 deg	2168	2084.1
	10-15 deg	3037	2981.4
	15-20 deg	3203	3177.5
	20-25 deg	2816	2743.7
	25-30 deg	2209	2229.9
	30-35 deg	1628	1613.4
	35-40 deg	1070	1032.5
	40-45 deg	549	586.3
	Total	17528	17251.6
PM	0-5 deg	1167	1134.3
	5-10 deg	3046	3014.2
	10-15 deg	4024	3950.3
	15-20 deg	4023	4033.4
	20-25 deg	3370	3477.3
	25-30 deg	2691	2753.0
	30-35 deg	1926	1976.2
	35-40 deg	1232	1282.7
	40-45 deg	686	744.6
	Total	22165	22366.0
INGRID	0-5 deg	13582.0	14724.7
	5-10 deg	33765.3	35878.5
	10-15 deg	53671.3	55589.5
	15-20 deg	55500.6	57425.1
	20-25 deg	39119.4	40995.0
	25-30 deg	45002.4	45985.9
	30-35 deg	26984.1	28543.3
	35-40 deg	20036.4	20899.1
	40-45 deg	12094.0	12128.6
	Total	299755.5	312170.0

6.4.2 Integrated ν_μ flux

The neutrino flux is predicted by the MC simulation that begins with the primary proton beam and ends with the decay of hadrons or muons that produce neutrinos. The simulation is driven by measurements of primary proton beam profile, horn current, horn magnetic field and hadron production data. The first interaction of incident proton with the target is called primary interaction. The interaction of the secondary particles, which are produced by the primary interaction, with the target and out-of-target materials is called secondary interaction. The primary and secondary interactions are tuned based on hadron production data. The multiplicity of the secondary mesons (charged pion, charged kaon and neutral kaon) produced by the primary interaction is tuned based on the NA61/SHINE measurement [97][114]. That produced by the secondary interaction is also tuned by the NA61/SHINE measurement with the target scaling and energy scaling method to scale the NA61/SHINE measurement from 30 GeV/c $p + C$ scattering to appropriate energy and target material(C, Al, Ti and Fe) based on [115][116][117]. The phase space not covered by NA61/SHINE measurement is extrapolated by parametrized fitting [118] result of the NA61 data. The multiplicity of secondary baryons (proton, neutron, Λ_s and Σ_s) produced by the primary interactions is tuned by NA61/SHINE and Allaby [116] measurement. The most significant difference in the procedure for tuning baryons than that for mesons is the baryon number conservation constraint, which is used to constrain the integrated baryon multiplicity. Finally, the interaction rates of primary and secondary interactions are tuned by using a few external data [119][120][121][122][123].

A left figure in Fig. 6.1 shows the expected neutrino flux at on-axis with the several tuning. Table 6.10 shows the number of the integrated ν_μ flux in the fiducial volume region of the water module, Proton Module and INGRID. The flux is lower for the INGRID because it is 1.2 m further downstream of the water module and Proton module.

Table 6.10: Integrated ν_μ flux in the fiducial volume region of each detector

Module	WM	PM	INGRID
Integrated ν_μ flux (cm^2) per 10^{21} POT	5.13×10^{13}	5.13×10^{13}	5.08×10^{13}
Amount of the used POT	7.25×10^{20}	5.96×10^{20}	5.96×10^{20}
Integrated ν_μ flux (cm^2) per the used POT	3.72×10^{13}	3.02×10^{13}	2.99×10^{13}

6.4.3 Number of target nucleons

The mass of the target and its composition is calculated based on measurement during detector construction. The calculated masses are summarized in Table 6.11.

Table 6.11: Summary of the number of target nucleons

Target	The number of target nucleon
$T_{\mathrm{WM}}^{\mathrm{H_2O}}$	4.939×10^{28}
$T_{\mathrm{WM}}^{\mathrm{CH}}$	1.090×10^{28}
$T_{\mathrm{PM}}^{\mathrm{CH}}$	9.230×10^{28}
$T_{\mathrm{ING}}^{\mathrm{Fe}}$	1.206×10^{30}

6.4.4 Detection efficiency of CC events

The detection efficiency of the signal, CC-inclusive interactions which muon angle is less than 45 degrees and muon momentum is more than 0.4 GeV, is estimated from MC as shown in Fig. 6.22 and Table 6.7. The detection efficiency is defined as the number of the selected signal divided by the total number of the signal in the detector fiducial volume.

6.4.5 Expected number of background events

Expected number of the background events are shown in Table 6.12. In this table, CC interactions on scintillators in the water module are not included because they are constrained by the Proton Module. In order to estimate the fraction of background events caused by the neutrino interactions in the wall of the ND280 pit in the real data, the number of generated wall backgrounds in MC is normalized so that the number of events rejected by the upstream veto cut in the MC, which consist mainly of the backgrounds from the wall, is equal to the number rejected in data.

Table 6.12: Summary of the background events fraction after the event selection. Target element means neutrino interactions not on CH and H_2O for the water module, on O, N and Ti for the Proton Module and on scintillators for the INGRID.

Detector	angle bin	CC out of phase space	Target element	NC	$\overline{\nu}_\mu$, ν_e, $\overline{\nu}_e$	Wall	INGRID	All BG
WM	0-5 deg	44.5	26.1	28.6	43.5	4.90	55.2	216
	5-10 deg	98.2	55.1	67.4	99.2	36.7	96.6	477
	10-15 deg	145	72.0	83.7	103	73.8	10.3	615
	15-20 deg	171	76.3	86.4	75.6	113	90.0	654
	20-25 deg	165	58.2	76.7	51.7	58.9	77.2	527
	25-30 deg	113	43.6	54.8	30.9	32.7	72.9	377
	30-35 deg	84.4	27.6	32.4	19.6	13.2	33.4	229
	35-40 deg	35.0	15.6	16.3	10.9	12.4	25.8	126
	40-45 deg	40.2	7.70	6.99	4.72	1.24	9.74	82.4
	Total	896	382	453	439	3.47	564	3300
PM	0-5 deg	99.0	12.9	60.3	79.7	38.2	57.2	346
	5-10 deg	255	35.7	145	172	47.4	154	905
	10-15 deg	338	48.0	174	162	75.2	183	975
	15-20 deg	352	49.1	177	129	145	150	997
	20-25 deg	313	43.3	144	78.8	104	124	803
	25-30 deg	243	34.5	101	50.6	83.7	107	616
	30-35 deg	148	25.3	63.4	30.1	23.9	90.4	379
	35-40 deg	67.6	16.6	32.4	15.2	20.5	56.1	207
	40-45 deg	83.5	9.69	17.3	8.96	12.4	28.3	159
	Total	1870	275	914	726	551	950	5290
INGRID	0-5 deg	1370	507	769	766	95.7	7.96	3540
	5-10 deg	2910	1310	1690	1740	145	101	7900
	10-15 deg	4990	1990	2680	2020	147	122	11900
	15-20 deg	5630	2020	3280	1720	114	216	13000
	20-25 deg	3990	1440	2100	1010	109	49.0	8690
	25-30 deg	5520	1680	3070	993	126	88.8	11500
	30-35 deg	3320	997	1660	588	58.0	19.7	6650
	35-40 deg	3650	702	1170	338	34.9	19.2	5920
	40-45 deg	3080	456	801	144	40.2	13.2	4530
	Total	34500	11100	17200	9310	870	638	73600

6.4.6 P matrix

$P(\theta_j^{recon}|\theta_i^{true})$ is calculated by MC as shown in Fig. 6.24. Normalization is taken as $\Sigma_j P(\theta_j^{recon}|\theta_i^{true}) = 1$.

6.4.7 Closure test

From the number of selected events and the quantities described earlier in this chapter, the flux averaged CC-inclusive cross section on H_2O, CH and Fe and the cross section ratios between H_2O, CH and Fe are calculated based on Eq. 6.9–6.19. In this section, closure test is done by replacing the number of selected events of data with that of the MC expectation. Figure 6.25 shows the relation between the number of iterations and calculated cross sections. They have good convergence. Based on that, the number of iteration is set to 10. Table 6.13 shows the calculated cross sections and they are consistent with the MC expectation.

In order to validate the calculation method with many iterations and flat prior, the cross sections are calculated with an iteration and prior calculated by nominal MC. Table 6.14 shows the results with the method with an iteration and they are consistent with the nominal method.

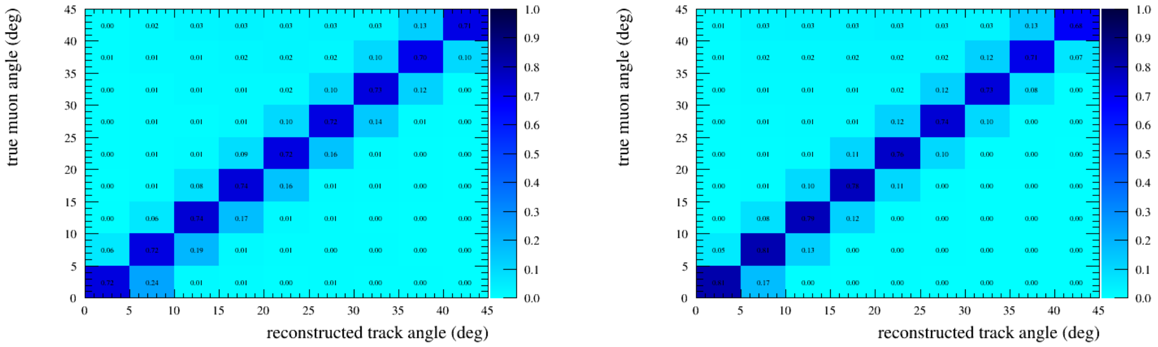

water module

Proton Module

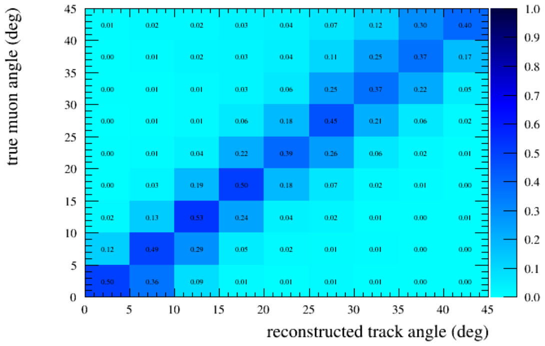

INGRID

Figure 6.24: Calculated P matrix for the water module (upper left), Proton Module (upper right) and INGRID (lower left).

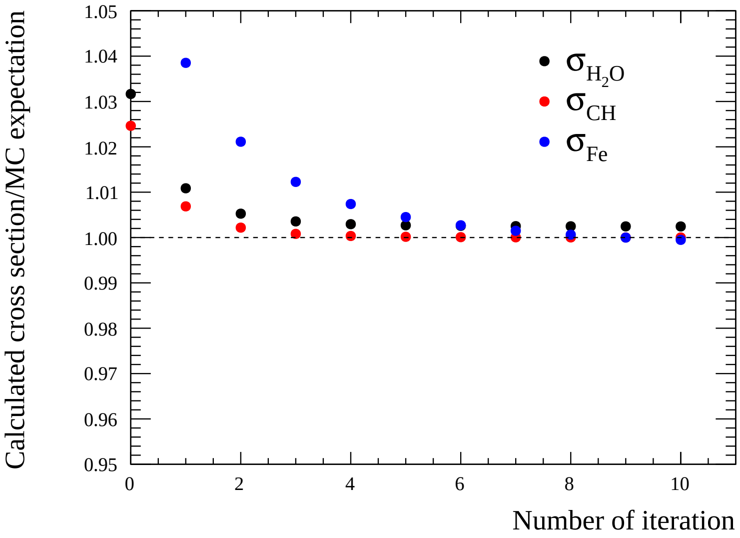

Figure 6.25: Relation between the number of iterations and calculated cross section with MC simulation. Black is $\sigma_{\mathrm{H_2O}}$, red is σ_{CH} and blue is σ_{Fe}.

6.4.8 Cross section calculation

By using obtained data, the cross sections are calculated as shown in Table 6.15.

Table 6.13: Calculated cross sections with MC and their true values.

Target	Calculated cross sections	expected cross sections
Selected number of events is replaced with nominal MC		
H_2O	0.821×10^{-38} cm^2	0.819×10^{-38} cm^2
CH	0.832×10^{-38} cm^2	0.832×10^{-38} cm^2
Fe	0.904×10^{-38} cm^2	0.904×10^{-38} cm^2
Selected number of events is replaced with MC that $\mathrm{M_A^{QE}}$ is varied $+1\sigma$		
H_2O	0.774×10^{-38} cm^2	0.781×10^{-38} cm^2
CH	0.783×10^{-38} cm^2	0.792×10^{-38} cm^2
Fe	0.846×10^{-38} cm^2	0.857×10^{-38} cm^2

Table 6.14: Calculated cross sections with MC with other method of an iteration and MC based prior

Target	Calculated cross sections	expected cross sections
Selected number of events is replaced with nominal MC		
H_2O	0.821×10^{-38} cm^2	0.819×10^{-38} cm^2
CH	0.831×10^{-38} cm^2	0.832×10^{-38} cm^2
Fe	0.910×10^{-38} cm^2	0.904×10^{-38} cm^2
Selected number of events is replaced with MC that $\mathrm{M_A^{QE}}$ is varied $+1\sigma$		
H_2O	0.774×10^{-38} cm^2	0.781×10^{-38} cm^2
CH	0.783×10^{-38} cm^2	0.792×10^{-38} cm^2
Fe	0.854×10^{-38} cm^2	0.857×10^{-38} cm^2

Table 6.15: Calculated cross sections results with data.

	Calculated cross sections
$\sigma_{\mathrm{H_2O}}$	0.840×10^{-38} cm^2
σ_{CH}	0.817×10^{-38} cm^2
σ_{Fe}	0.859×10^{-38} cm^2
$\sigma_{\mathrm{H_2O}}/\sigma_{CH}$	1.028
$\sigma_{Fe}/\sigma_{\mathrm{H_2O}}$	1.023
$\sigma_{Fe}/\sigma_{\mathrm{CH}}$	1.049

6.5 Statistical errors

The number of selected events have statistical uncertainty. To evaluate that, they are fluctuated in each reconstructed angle bin and each detector by assuming the Poisson distributions and the variations of the cross section results are calculated. This is repeated for 10k toy data sets and the 68% range of the distribution of the cross section variation is taken as the size of the systematic error. The calculated uncertainties are shown in Table 6.16.

Table 6.16: Calculated statistical uncertainty

Cross section	statistical uncertainty
$\sigma_{\mathrm{H_2O}}$	± 1.17%
σ_{CH}	± 0.87%
σ_{Fe}	± 0.28%
$\sigma_{\mathrm{H_2O}}/\sigma_{\mathrm{CH}}$	± 1.60%
$\sigma_{\mathrm{Fe}}/\sigma_{\mathrm{H_2O}}$	± 1.19%
$\sigma_{\mathrm{Fe}}/\sigma_{\mathrm{CH}}$	± 0.93%

6.6 Systematic errors

6.6.1 Systematic errors from neutrino flux

The uncertainty of the flux is estimated in each neutrino energy bin defined as Table 6.17 including correlations between the bins. Figure 6.26 shows estimated muon neutrino flux uncertainty at on-axis with positive horn current mode. Uncertainty of the neutrino flux prediction at on-axis is estimated for each tuning of hadron interaction and beam line monitor, as described in Sec. 6.4.2. The uncertainties of hadron production are estimated based on the uncertainty of hadron scattering measurements used for the tuning, as shown in the first line named “NA61 mult. and A-scaling” in Fig. 6.26. In addition, uncertainty of the tuning method is estimated by comparing two or more independent tuning methods, as shown in the second to 8th line in Fig. 6.26. In addition, following non-hadronic uncertainties related to beam line components are estimated based on measurement: proton beam and neutrino beam profile, horn current and horn field, alignment of horn and target and effect of scattering with materials in beam line (for example, cooling water for horn). Sum of their effect is shown in the last red line named “Not hadron multiplicity” in Fig. 6.26. Total uncertainty including both of hadronic and non-hadronic uncertainties is shown in black line in Fig. 6.26.

Table 6.17: Energy binning for flux uncertainty evaluation

Energy range	Number of bins	Energy width per bin
0.0-3.0 GeV	15	0.2
3.0-4.0 GeV	1	1.0
4.0-10.0 GeV	3	2.0
10.0-30.0 GeV	1	20.0

The uncertainty of the neutrino flux causes the systematic uncertainties on the number of expected background events (N^{BG}), integrated flux (Φ), detection efficiency (ε) and U matrix. To evaluate the systematic error on the cross section measurement, the number of produced and selected neutrino events in each bin is fluctuated by using the flux covariance matrix and

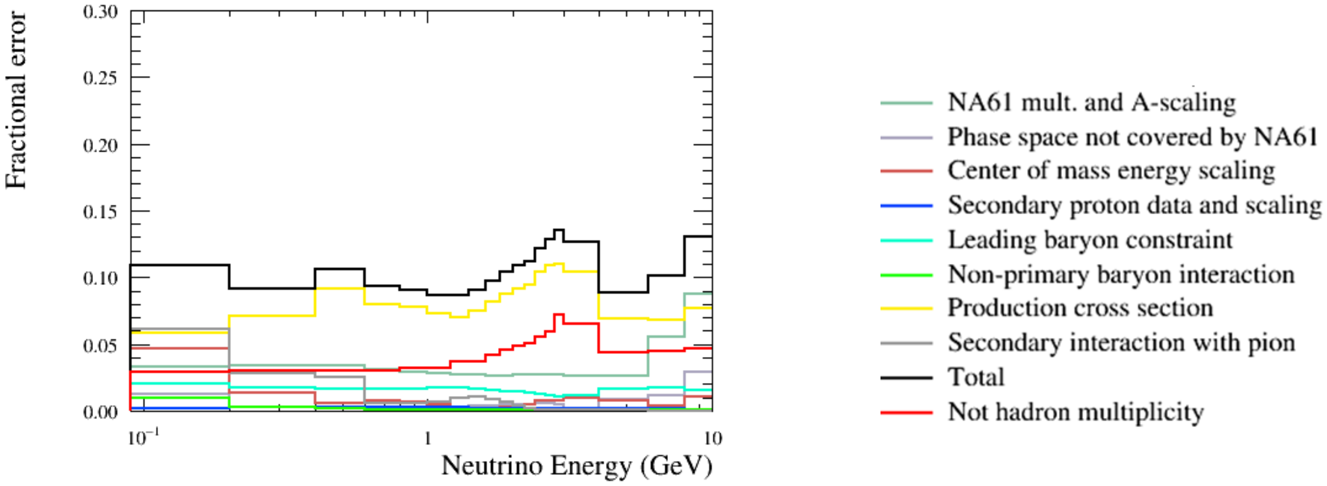

Figure 6.26: Diagonal term of the covariance matrix of the flux uncertainty at an on-axis.

the variations of N^{BG}, Φ, ε and U are calculated. By using them, the variation of the cross section result is calculated. This is repeated for 10k toy data sets and the 68% range of the distribution of the cross section variation is taken as the size of the systematic error. The first row in Table 6.18 shows the calculated result.

In addition, uncertainty due to difference of the position of the detector and difference of the run period between water module and Proton Module is taken as another systematic separately. The former is estimated to be 0.31% based on measurement of detector location. The latter is estimated to be 1.03% based on beam stability measurement by the INGRID between the different run periods.

Table 6.18: Variation of the cross sections due to flux uncertainty

Cross sections	Variation due to flux prediction(%)	Variation due to relative difference of detector position and run period (%)
$\sigma_{\mathrm{H_2O}}$	$+10.8, -8.9$	±0.3
σ_{CH}	$+11.5, -9.6$	0
σ_{Fe}	$+12.9, -10.6$	0
$\sigma_{\mathrm{H_2O}}/\sigma_{\mathrm{CH}}$	±0.6	±1.3
$\sigma_{\mathrm{Fe}}/\sigma_{\mathrm{H_2O}}$	±1.8	±1.1
$\sigma_{\mathrm{Fe}}/\sigma_{\mathrm{CH}}$	±1.2	±0.3

6.6.2 Systematic errors from neutrino interaction model

The NEUT neutrino interaction models have a number of uncertainties that can affect the detection efficiency (ε), background contamination (N^{BG}) and U matrix. In order to evaluate the systematic error on the cross section measurement from the uncertainty on the neutrino interaction, variations of ε, N^{BG} and U matrix are calculated when each interaction parameter is varied within its uncertainty (1σ). Then the variation of the cross section result from the variation is taken as the systematic error. Table 6.19 shows the nominal values and the uncertainties of the interaction parameters. The size of uncertainties are determined to cover the current understanding of the neutrino interactions, as described in Sec. 3. For modeling of the CCQE, RFG with RPA correction is used for σ_{H_2O} and σ_{CH}. On the other hand, RFG without RPA correction is used for σ_{Fe} because RPA for Fe is not available in the current generator.

When the uncertainty is calculated, no correlation is assumed between different target nucleus for the Fermi momentum, binding energy, 2p2h and CC coherent parameters. Full correlation between the different target is assumed for the other parameters. Table 6.20 and Fig. 6.27 show the calculated uncertainties. Dominant terms are axial vector mass of the CCQE ($\mathrm{M_A^{QE}}$), CC1π ($\mathrm{M_A^{RES}}$) and energy dependent normalization of the CCDIS. In this estimation, $\overline{\nu}_\mu$, ν_e and $\overline{\nu}_e$ interactions on target and ν interactions outside of the target are not reweighted, although they affect the N^{BG}. They are taken as one of the detector systematic error in more conservative way, as described in Sec. 6.6.3.

In addition to the systematic uncertainties estimated by NEUT, uncertainty of backward protons and pions are estimated independently. Some of the events generated inside the fiducial volume have reconstructed vertex outside the fiducial volume due to back scattered secondary proton or pions. Fraction of the events is 3.0% for the water module, 1.6% for the Proton Module and 2.0% for the INGRID respectively, compared to the total number of selected events. The amount and uncertainty of such back scattered secondary particles may not be simulated well by NEUT. To cover this uncertainty conservatively, 50% ($3.0\% \times 50\% = 1.5\%$ totally for the water module) is taken as 1σ uncertainty for all reconstructed angle bins commonly. In addition, no correlation between the target materials are assumed for this uncertainty.

6.6.3 Systematic errors from detector response

Uncertainties of detector responses are estimated based on the results of detector commissioning with sand muon and cosmic muon, as described in Section 5.4. Sources of the uncertainties are listed in Table 6.21. For translating these uncertainties to the cross section measurement, Monte Carlo simulation is produced with a varied detector parameter of 1σ. Difference of the number of selected events in each reconstructed track angle bin between nominal simulation and 1σ varied simulation is taken as uncertainty of 1σ. Their effect to the measured cross sections are calculated by Eq. 6.9–6.11 and 6.18–6.20 finally. In addition, uncertainties for the event selection criteria are evaluated with varied criteria as listed in Table 6.22. Difference of the number of selected events between nominal criteria and varied criteria are calculated for both data and simulation. Their difference between data and simulation is taken as 1σ uncertainty and it is translated to uncertainties of the cross sections by Eq. 6.9–6.11 and 6.18–6.20. Table 6.23 and 6.24 show a summary of the calculated uncertainties. The uncertainties for Proton Module and INGRID are estimated in a common way as the water module. No correlation is assumed between the three detectors except for beam related BG of which background source, neutrino interaction with the wall of the building, is common for three detectors.

.

6.6.4 Summary of systematic errors

Table 6.25 shows the summary of the systematic uncertainties for the cross section measurements. A quadratic sum of the neutrino flux, neutrino interaction and detector response is taken as a total systematic uncertainty.

Table 6.19: List of used interaction model and parameters of neutrino interaction.

Parameter	Nominal value	Uncertainties(1σ)
CC0π modeled by RFG [57], RPA [64] and 2p2h [68]		
M_A^{QE}	1.15 GeV	0.18 GeV
p_F ^{12}C	217 MeV	31 MeV
p_F ^{16}O	225 MeV	31 MeV
p_F ^{56}Fe	250 MeV	35 MeV
E_b ^{12}C	25 MeV	9 MeV
E_b ^{16}O	27 MeV	9 MeV
E_b ^{56}Fe	33 MeV	11 MeV
2p2h normalization^{12}C	1.00	1.00
2p2h normalization^{16}O	1.00	1.00
2p2h normalization^{56}Fe	1.00	1.00
CC1π modeled by Rein Sehgal [71] with tuning of form factor by deuterium experiments		
C_{A5}	1.01	0.12
M_A^{Res}	0.95 GeV	0.15 GeV
Isospin$\frac{1}{2}$bg	1.30	0.20
CCDIS Normalization uncertainty is applied depends on neutrino energy by $0.4/E_\nu$ (GeV)		
CC coherent modeled by Barbar Sehgal [83]		
CCcoh normalization ^{12}C	1.00	0.30
CCcoh normalization ^{16}O	1.00	0.30
NC interactions		
NCcoh normalization	1.00	0.30
NCother normalization	1.00	0.30
Secondary interaction of pions		
Pion Absorption normalization	100%	50 %
Pion ChargeExchange (low E) normalization	100%	50 %
Pion ChargeExchange (high E) normalization	100%	30 %
Pion QuasiElastic (low E) normalization	100%	50 %
Pion QuasiElastic (high E) normalization	100%	30 %
Pion Inelastic normalization	100%	50 %

Table 6.20: Summary of the variation of measured cross section due to neutrino interaction uncertainty (%)

Measured cross sections	σ_{H_2O}	σ_{CH}	σ_{Fe}	$\sigma_{H_2O}/\sigma_{CH}$	$\sigma_{Fe}/\sigma_{H_2O}$	σ_{Fe}/σ_{CH}
Total uncertainty	±2.64	±3.10	±5.22	±2.29	±3.99	±2.68

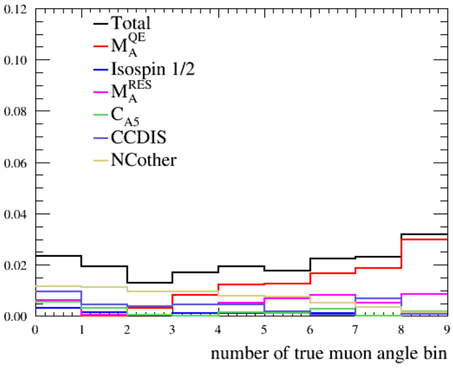

$\sigma_{\mathrm{H_2O}}$

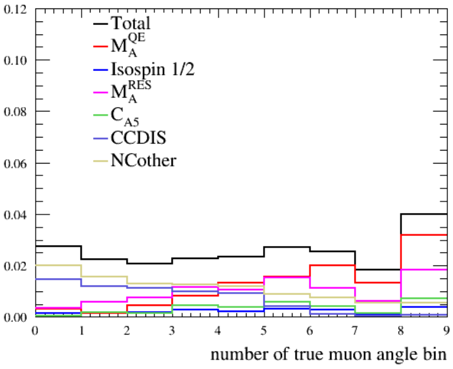

σ_{CH}

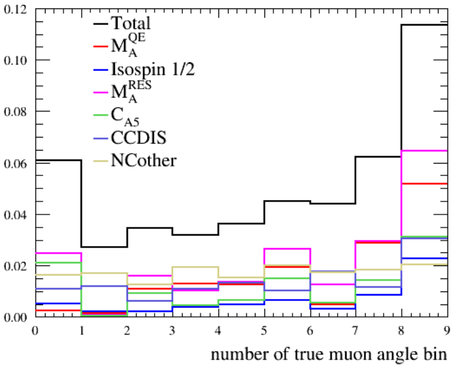

σ_{Fe}

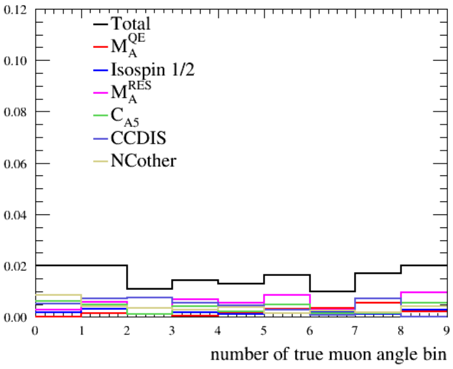

$\sigma_{\mathrm{H_2O}}/\sigma_{\mathrm{CH}}$

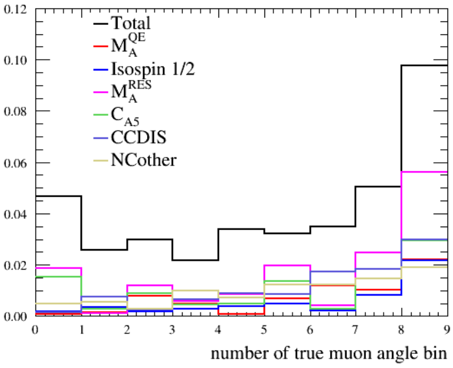

$\sigma_{\mathrm{Fe}}/\sigma_{\mathrm{H_2O}}$

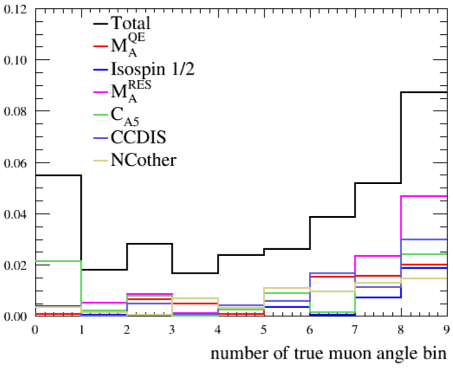

$\sigma_{\mathrm{Fe}}/\sigma_{\mathrm{CH}}$

Figure 6.27: Fractional uncertainties in each true muon angle bins due to neutrino interaction systematic uncertainties for $\sigma_{\mathrm{H_2O}}$ (upper left), σ_{CH} (upper right), σ_{Fe} (middle left), $\sigma_{\mathrm{H_2O}}/\sigma_{\mathrm{CH}}$ (middle right), $\sigma_{\mathrm{Fe}}/\sigma_{\mathrm{H_2O}}$ (lower left) and $\sigma_{\mathrm{Fe}}/\sigma_{\mathrm{CH}}$ (lower right). Uncertainty of backward proton and pions are not included.

Table 6.21: Sources of detector response uncertainty for the water module evaluated by commissioning.

Source	How to take 1σ uncertainty
Target mass	Mass measurement during detector construction (0.68%)
Event pileup	Statistical uncertainty of event loss constant (∼0.5%)
Beam related background	Difference of sand muon between data and simulation (∼20%+15%)
Non beam background	Estimated with data of non-beam cycle (less than 1 events per 3000 spills)
Beam timing cut	Number of rejected events (∼ 0.06% of selected events)
Scintillator crosstalk	Difference of with and without crosstalk (Table 5.5)
MPPC noise	Stability of noise rate during operation (Table 5.5)
Hit efficiency	Difference between data and simulation (Table 5.5)
2D track reconstruction	Difference between data and simulation (Table 5.5)

Table 6.22: Sources of detector response uncertainty of event selection criteria for the water module.

Source	Nominal criteria	Varied criteria
INGRID track matching cut	$\|\Delta\theta\| < 35$ deg.	30 deg, 40 deg
	$\|\Delta x\| < 150$ mm.	140 mm, 160 mm
3D track matching cut	$\|\Delta z\| <2$ plane	1 plane, 3 plane
Vertexing cut	$\|\Delta z_x\| + \|\Delta z_y\| < 3$ plane	2 plane, 3 plane
	$\sqrt{\Delta x^2 + \Delta y^2} < 150$ mm	100 mm, 200 mm
Veto and fiducial volume cut	vertex z is more than second plane	Third plane
	vertex xy is in 70×70 cm^2	50×50 cm^2

Table 6.23: Summary of the detector systematics for absolute cross section measurement.

cross section	$\sigma_{\mathrm{H_2O}}$		σ_{CH}	σ_{Fe}
Detector	WM	PM	PM	INGRID
Target mass	0.68%	0.05%	0.27%	0.14%
MPPC noise	0.01%	0.09%	0.39%	0.09%
Scintillator crosstalk	0.30%	–	–	–
Hit efficiency	0.27%	0.02%	0.50%	0.94%
Event pileup	0.72%	0.15%	0.64%	0.09%
Beam-related BG.	1.09%	0.31%	1.31%	0.38%
Non-beam-related BG	0.04%	0.02%	0.02%	0.01%
2D Track reconstruction	0.60%	0.28%	1.18%	0.43%
Track matching with INGRID	1.42%	0.20%	0.84%	–
3D track matching	0.89%	0.13%	0.56%	0.35%
Vertexing	0.44%	0.05%	0.20%	0.28%
Beam timing cut	0.06%	0.01%	0.01%	0.01%
VETO and FV cut	1.19%	0.18%	0.72%	0.52%
Acceptance cut	–	–	–	0.61%
Total	2.88%		2.52%	1.54%

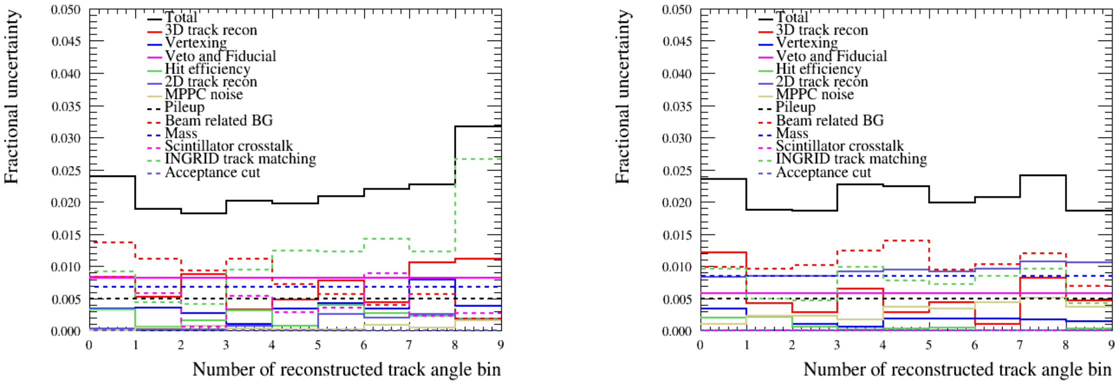

water module

Proton Module

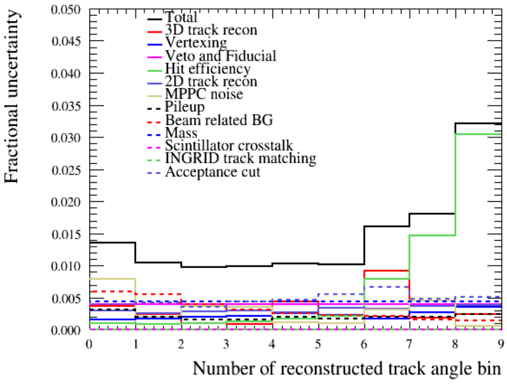

INGRID

Figure 6.28: Fractional uncertainties of the detector systematics in each reconstructed track angle bin and error sources for the water module(upper left), Proton Module(upper right) and INGRID(lower left).

Table 6.24: Summary of the detector systematics for cross section ratio measurement.

cross section	$\sigma_{H_2O}/\sigma_{CH}$		$\sigma_{Fe}/\sigma_{H_2O}$			σ_{Fe}/σ_{CH}	
Detector	WM	PM	WM	PM	INGRID	PM	INGRID
Target mass	0.68%	0.32%	0.68%	0.05%	0.14%	0.27%	0.14%
MPPC noise	0.01%	0.48%	0.01%	0.13%	0.09%	0.39%	0.09%
Scintillator crosstalk	0.30%	–	0.30%	–	–	–	–
Hit efficiency	0.27%	0.08%	0.27%	0.06%	0.94%	0.50%	0.94%
Event pileup	0.72%	0.78%	0.72%	0.15%	0.09%	0.64%	0.09%
Beam-related BG.	1.09%	1.64%	1.09%	0.36%	0.38%	1.31%	0.38%
Non-beam-related BG	0.04%	0.02%	0.04%	0.02%	0.01%	0.02%	0.01%
2D Track reconstruction	0.60%	1.45%	0.60%	0.32%	0.43%	1.18%	0.43%
Track matching with INGRID	1.42%	1.03%	1.42%	0.25%	–	0.84%	–
3D track matching	0.89%	0.68%	0.89%	0.17%	0.35%	0.56%	0.35%
Vertexing	0.44%	0.25%	0.44%	0.09%	0.28%	0.20%	0.28%
Beam timing cut	0.06%	0.01%	0.06%	0.01%	0.01%	0.01%	0.01%
VETO and FV cut	1.19%	0.89%	1.19%	0.75%	0.52%	0.72%	0.52%
Acceptance cut	–	–	–	–	0.61%	–	0.61%
Total	4.49%		3.35%			2.78%	

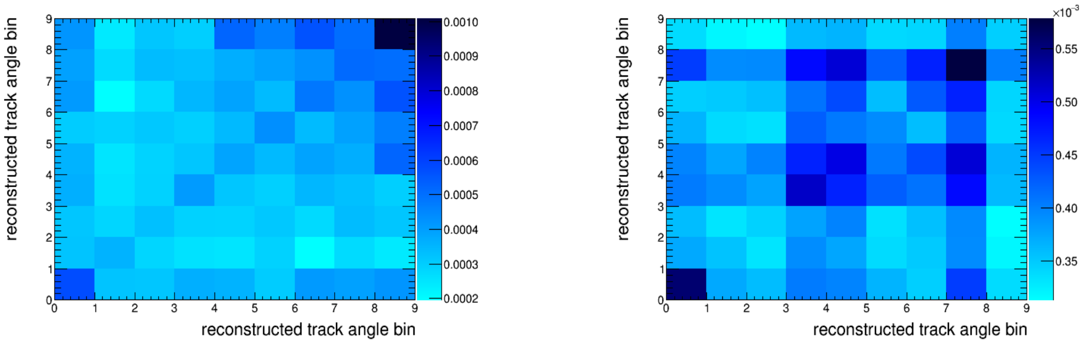

water module

Proton Module

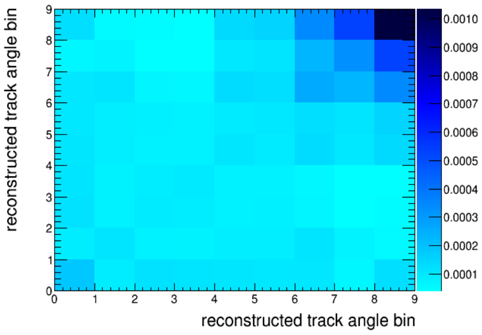

INGRID

Figure 6.29: Fractional covariance matrix of the detector systematic uncertainties for the water module(upper left), Proton Module(upper right) and INGRID(lower left).

Table 6.25: Summary of the systematic uncertainties of the measured cross section (%)

Systematics	$\sigma_{\mathrm{H_2O}}$	σ_{CH}	σ_{Fe}	$\sigma_{\mathrm{H_2O}}/\sigma_{\mathrm{CH}}$	$\sigma_{\mathrm{Fe}}/\sigma_{\mathrm{H_2O}}$	$\sigma_{\mathrm{Fe}}/\sigma_{\mathrm{CH}}$
Neutrino flux	$+11, -8.9$	$+12, -9.6$	$+13, -11$	±1.4	$+2.2, -2.0$	$+1.2, -1.3$
Neutrino interaction	±2.6	±3.1	±5.2	±2.3	±4.0	±2.7
Detector response	±2.9	±2.5	±1.5	±4.5	±3.4	±2.8
Total	$+12, -9.7$	$+13, -10$	$+14, -12$	±5.2	±5.7	±4.1

6.7 Results

The measured flux averaged inclusive ν_μ charged current cross section on H_2O, CH and Fe per nucleon are

$$\sigma_{\mathrm{CC}}^{\mathrm{H_2O}} = (0.840 \pm 0.010(\mathrm{stat.})^{+0.10}_{-0.081}(\mathrm{syst.})) \times 10^{-38}\ \mathrm{cm^2/nucleon} \tag{6.21}$$

$$\sigma_{\mathrm{CC}}^{\mathrm{CH}} = (0.817 \pm 0.007(\mathrm{stat.})^{+0.11}_{-0.082}(\mathrm{syst.})) \times 10^{-38}\ \mathrm{cm^2/nucleon} \tag{6.22}$$

$$\sigma_{\mathrm{CC}}^{\mathrm{Fe}} = (0.859 \pm +0.003(\mathrm{stat.})^{+0.12}_{-0.10}(\mathrm{syst.})) \times 10^{-38}\ \mathrm{cm^2/nucleon} \tag{6.23}$$

the cross section ratios are

$$\frac{\sigma_{\mathrm{CC}}^{\mathrm{H_2O}}}{\sigma_{\mathrm{CC}}^{\mathrm{CH}}} = 1.028 \pm 0.016(\mathrm{stat.}) \pm 0.053(\mathrm{syst.}) \tag{6.24}$$

$$\frac{\sigma_{\mathrm{CC}}^{\mathrm{Fe}}}{\sigma_{\mathrm{CC}}^{\mathrm{H_2O}}} = 1.023 \pm 0.012(\mathrm{stat.}) \pm 0.058(\mathrm{syst.}) \tag{6.25}$$

$$\frac{\sigma_{\mathrm{CC}}^{\mathrm{Fe}}}{\sigma_{\mathrm{CC}}^{\mathrm{CH}}} = 1.049 \pm 0.010(\mathrm{stat.}) \pm 0.043(\mathrm{syst.}) \tag{6.26}$$

6.8 Discussion

These results are the best measurement of the neutrino interaction with water target and the first measurement of the cross section ratio of water and plastic. The results are compared with predictions of models of the neutrino-nucleus interactions. Figures 6.30, 6.31 and Table 6.26 show the cross section values predicted by NEUT with various parameters listed in Table 6.19 with data. All of the predictions agree with data within about 1σ. Because there has been almost no data of the water target, the uncertainty of the difference of the neutrino interaction with water and plastic have been assigned based on only prediction with the modeling of the neutrino interaction without data for the T2K oscillation analysis. This measurement ensures correctness of the uncertainty with experimental data for the first time in the world and improves reliability of the oscillation analysis of the T2K.

The measured $\sigma_{\mathrm{Fe}}/\sigma_{\mathrm{CH}}$ in previous result by using the INGRID and Proton Module in 2015 [89], 1.047±0.007(stat.)±0.035(syst.), is consistent with the result in this analysis although the definition of signal is different between these two measurements. In the previous analysis, all CC-inclusive interactions are defined as signal without any phase space limitations. This analysis provides more model independent measurement since the last analysis and it is easy to interpret the result without dedicated detector simulation for external neutrino interaction researchers.

This analysis measures the total cross section of the CC-inclusive interactions. For more understanding of the water target, differential cross section measurement is needed as a function of the momentum and angle of the muon because the CRPA models predict the large A-dependence especially at the low energy transfer region. In addition, separations of the interaction modes are needed. In order to achieve that, we are measuring the differential cross sections of the CCQE and CC1π interactions on water, plastic and their ratios as a function of the muon angle and momentum by using the water module with the same data set of the CC-inclusive analysis and their results is planned to be released within two years. In addition, we plan to perform the differential cross section measurement with large angular acceptance with a new muon range detector which is consist of iron and plastic scintillators. Data taking with the muon range detector will start in 2019.

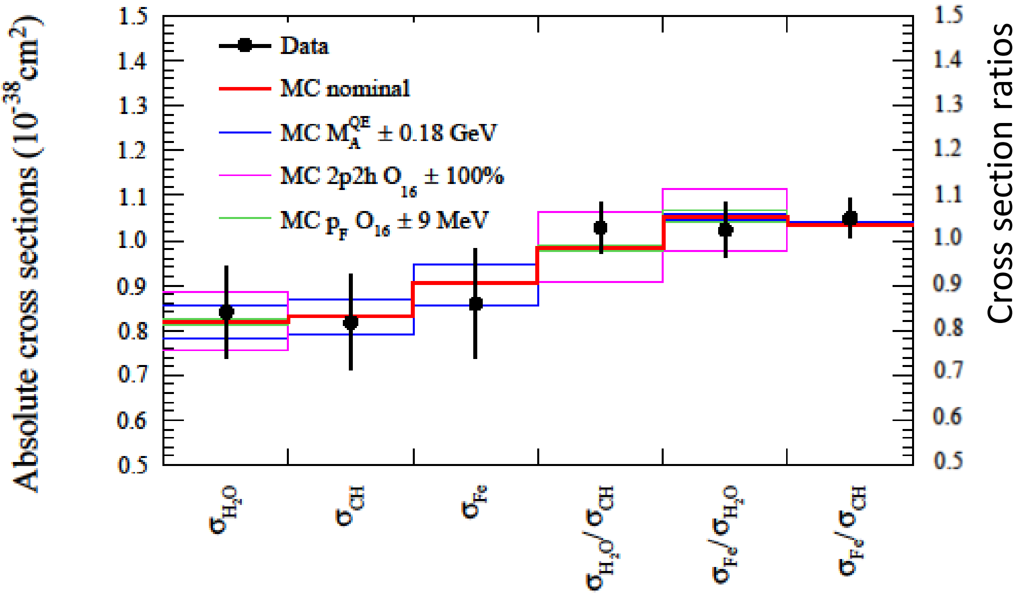

Figure 6.30: Results of the cross section measurements (black point) with total uncertainties (black line) and theoretical predictions by NEUT(solid lines).

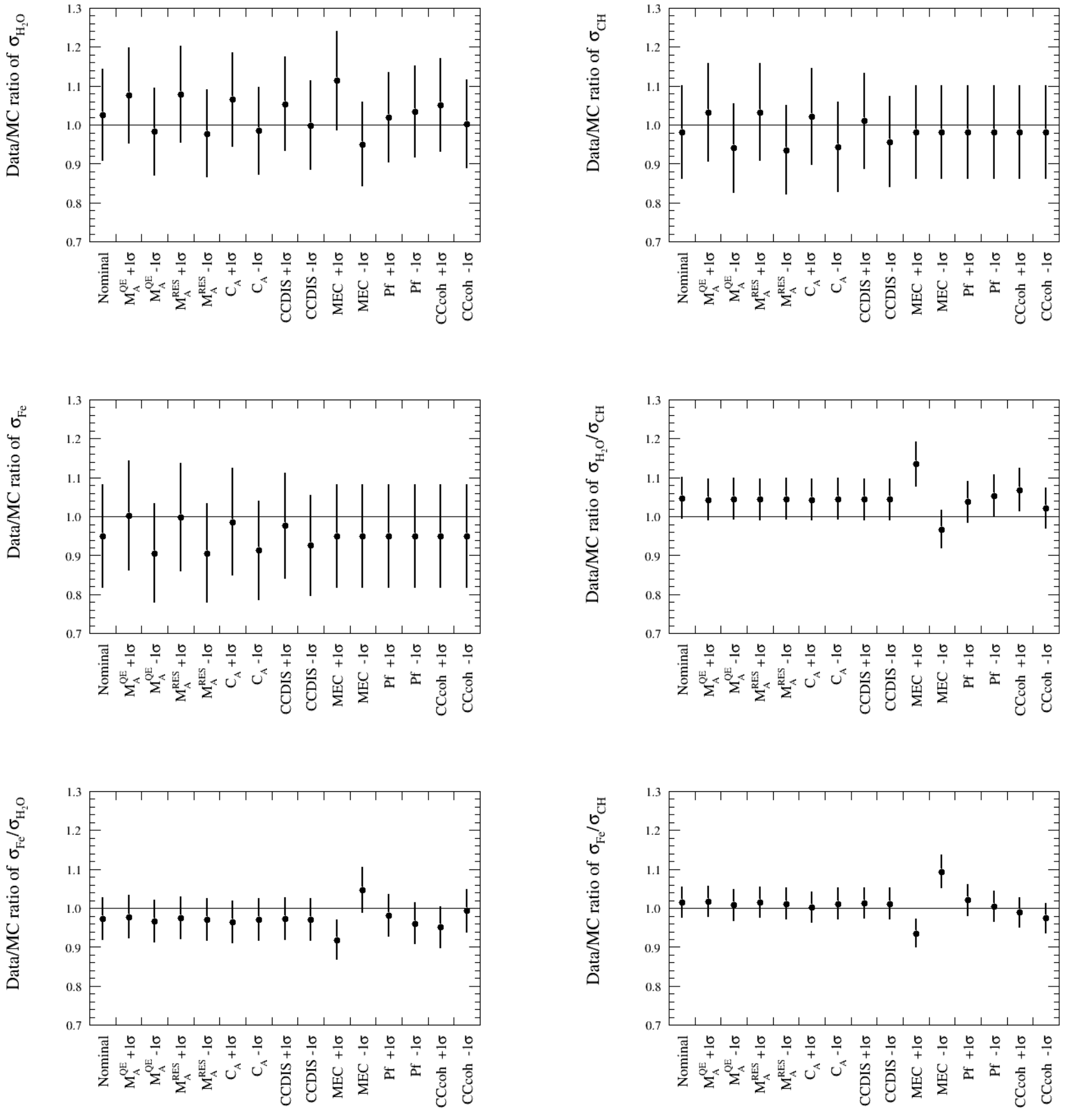

Figure 6.31: Ratio of the cross sections between data and NEUT predictions with the various cross section parameters listed in Table 6.19. Error bars show sum of the statistical and systematic uncertainties of the measurement.

Table 6.26: Summary of the cross sections predicted by NEUT with the various parameters listed in Table 6.19 ($\times 10^{-38}\mathrm{cm}^2$/nucleon for the absolute cross sections).

Parameter	$\sigma_{\mathrm{H_2O}}$	σ_{CH}	σ_{Fe}	$\sigma_{\mathrm{H_2O}}/\sigma_{\mathrm{CH}}$	$\sigma_{\mathrm{Fe}}/\sigma_{\mathrm{H_2O}}$	$\sigma_{\mathrm{Fe}}/\sigma_{\mathrm{CH}}$
Nominal for $\mathrm{H_2O, CH, H_2O/CH}$ (RPA+RFG+2p2h)	0.819	0.832	–	0.985	–	–
Nominal for $\mathrm{Fe, H_2O/Fe, Fe/CH}$ (RFG+2p2h)	0.860	0.875	0.904	0.982	1.052	1.034
$\mathrm{M_A^{QE}} - 1\sigma$	0.781	0.792	0.857	0.986	1.046	1.031
$\mathrm{M_A^{QE}} + 1\sigma$	0.855	0.869	0.948	0.984	1.058	1.041
$\mathrm{M_A^{Res}} - 1\sigma$	0.779	0.791	0.861	0.985	1.050	1.034
$\mathrm{M_A^{Res}} + 1\sigma$	0.859	0.873	0.948	0.984	1.054	1.037
$\mathrm{C_{A5}} - 1\sigma$	0.789	0.800	0.871	0.986	1.061	1.046
$\mathrm{C_{A5}} + 1\sigma$	0.853	0.866	0.941	0.984	1.054	1.037
$\mathrm{Isospin}\frac{1}{2}\mathrm{bg} - 1\sigma$	0.806	0.818	0.889	0.985	1.051	1.035
$\mathrm{Isospin}\frac{1}{2}\mathrm{bg} + 1\sigma$	0.835	0.848	0.923	0.985	1.053	1.037
CCother shape $- 1\sigma$	0.797	0.809	0.880	0.985	1.052	1.036
CCother shape $+ 1\sigma$	0.841	0.854	0.928	0.985	1.053	1.037
$\mathrm{p_F}$ C $- 1\sigma$	0.819	0.835	0.904	0.981	1.052	1.028
$\mathrm{p_F}$ C $+ 1\sigma$	0.819	0.825	0.904	0.993	1.052	1.045
$\mathrm{p_F}$ O $- 1\sigma$	0.824	0.832	0.904	0.991	1.043	1.034
$\mathrm{p_F}$ O $+ 1\sigma$	0.812	0.832	0.904	0.976	1.065	1.034
$\mathrm{E_b}$ C $- 1\sigma$	0.819	0.831	0.904	0.986	1.052	1.035
$\mathrm{E_b}$ C $+ 1\sigma$	0.819	0.833	0.904	0.984	1.052	1.032
$\mathrm{E_b}$ O $- 1\sigma$	0.818	0.832	0.904	0.984	1.054	1.034
$\mathrm{E_b}$ O $+ 1\sigma$	0.820	0.832	0.904	0.986	1.051	1.034
2p2h norm C $- 1\sigma$	0.819	0.764	0.904	1.072	1.052	1.121
2p2h norm C $+ 1\sigma$	0.819	0.900	0.904	0.910	1.052	0.959
2p2h norm O $- 1\sigma$	0.754	0.832	0.904	0.906	1.139	1.034
2p2h norm O $+ 1\sigma$	0.884	0.832	0.904	1.063	0.978	1.034
CCcoh norm C $- 1\sigma$	0.819	0.809	0.904	1.013	1.052	1.061
CCcoh norm C $+ 1\sigma$	0.819	0.855	0.904	0.958	1.052	1.007
CCcoh norm O $- 1\sigma$	0.800	0.832	0.904	0.962	1.076	1.034
CCcoh norm O $+ 1\sigma$	0.838	0.832	0.904	1.007	1.030	1.034
CCcoh norm Fe $- 1\sigma$	0.819	0.832	0.896	0.958	1.043	1.023
CCcoh norm Fe $+ 1\sigma$	0.819	0.832	0.913	0.958	1.062	1.044

Chapter 7

Neutrino event rate comparison between on-axis detectors and ND280

7.1 Analysis overview

In the long baseline accelerator neutrino experiments, the method to constrain the neutrino flux and interaction by using the near detector is generally used. However, it is impossible to check if the constraint is correct or not at the far detector directly because not only the flux and interactions but also the neutrino oscillations affect the neutrino events at the far detector. In this section, for validation of the constraint of the neutrino flux and interactions by the ND280 measurement, observed neutrino event rate at the T2K on-axis near detectors, water module and Proton Module, are compared with the MC predictions with the constraint from the ND280. Because there is no effect of the neutrino oscillations at the on-axis detectors located at the 280 m from the target, the constraint of the flux and interactions are validated.

The analysis is performed in following steps. First, the constraint from the ND280 is propagated to on-axis by considering the correlation of the neutrino flux between the ND280 and on-axis. Second, event selections of the on-axis detectors are tuned to select the CC interactions separated by the number of tracks, including the events with a proton and large angle muons which are not measured by the ND280. Finally, the observed number of events of each event sample is compared with the predictions using constraint from the ND280.

7.2 ND280 measurement

7.2.1 Analysis method

The ND280 constrains the uncertainties of the neutrino flux and interactions by measuring muon neutrinos before the neutrino oscillations at 280 m downstream from the target for the neutrino beam production. At the ND280, the charged current muon neutrino interactions are selected by detecting muons. The selected events are categorized into a few samples based on the number of detected pions to identify each type of charged current interaction. The neutrino flux at the ND280 and cross section parameters are extracted and constrained by fitting the muon angle and momentum in each event sample. The flux parameters at the on-axis detectors are also constrained because the neutrino fluxes at the ND280 and on-axis are correlated each other.

The analysis method of the ND280 is the same as that for the T2K oscillation analysis [47] basically. The ND280 measures ν_μ interaction with plastic and water target as a function of muon angle and momentum. ND280 defines a sample of neutrino interactions which originates in the FGD1 or FGD2 detector and contains one muon track crossing the TPCs, which are located at downstream of the FGD. To select the sample, event selections are applied based on information of tracks reconstructed by hit pattern of the FGD and TPC detectors. Simplified event selection criteria are as follows:

1. Timing of reconstructed event is in the expected beam timing
2. At least one track is reconstructed in the TPC
3. Reconstructed vertex is inside the central region of the FGD1 or FGD2, named fiducial volume, to reject background events of neutrino interactions coming from outside the target
4. The upstream TPC is used as veto to reject the miss-reconstruction of the vertex
5. At least one muon candidate is required based on particle identification by using dE/dx information of the TPC.

In addition, events are categorized by the number of detected pions as shown in Figure 7.1. Three samples are used with FHC: CC-0-pion sample has no pion track, CC-1-pion sample has one positive pion track and CC-Other sample has more than one charged pion. The CC-0-pion, CC-1-pion and CC-Other samples constrain the CC0π, CC1π and CCDIS interactions respectively. There are two samples with RHC for both ν_μ and $\overline{\nu_\mu}$: CC-0-pion sample has no pion track and CC-N-pion samples has at least one pion track. Table 7.1 shows the observed number of selected events and MC expectation. Used statistics is 5.80×10^{20} POT with FHC and 3.86×10^{20} POT with RHC.

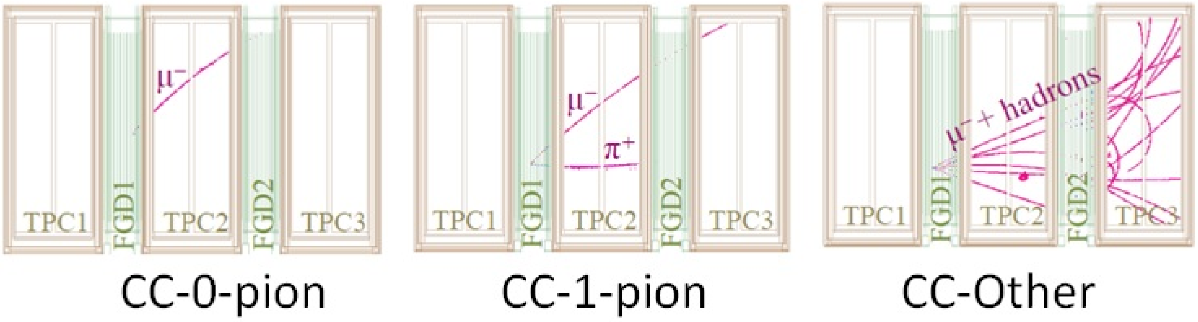

Figure 7.1: Examples of event displays for the event samples of the ND280 with FHC.

Momentum and angle (p-cosθ) of the muons are binned for each event sample and binned likelihood is formed with parameters of the neutrino flux, neutrino interactions and ND280

Table 7.1: The number of selected events for each event sample of the ND280. MC is normalized by POT.

Horn polarity	Sample	Data	MC after fitting	MC before fitting
Positive	FGD1 CC-0-pion	17136	17122.22	16723.69
Positive	FGD1 CC-1-pion	3954	4061.65	4381.48
Positive	FGD1 CC-Other	4149	4095.58	3943.95
Negative	$\overline{\nu_\mu}$ FGD1 CC-0-pion	3527	3503.79	3587.65
Negative	$\overline{\nu_\mu}$ FGD1 CC-multi-pion	1054	1052.69	1066.91
Negative	ν_μ FGD1 CC-0-pion	1363	1353.44	1272.17
Negative	ν_μ FGD1 CC-multi-pion	1370	1354.02	1357.45
Positive	FGD2 CC-0-pion	17443	17494.56	16959.19
Positive	FGD2 CC-1-pion	3366	3416.28	3564.23
Positive	FGD2 CC-Other	4075	3915.36	3570.95
Negative	$\overline{\nu_\mu}$ FGD2 CC-0-pion	3732	3685.46	3618.27
Negative	$\overline{\nu_\mu}$ FGD2 CC-multi-pion	1026	1097.38	1077.24
Negative	ν_μ FGD2 CC-0-pion	1320	1330.49	1262.63
Negative	ν_μ FGD2 CC-multi-pion	1253	1263.12	1246.71
Total		64768	64746.02	63632.53

detector systematics. We define $\Delta\chi^2_{ND280}$ as -2 times the log of the likelihood:

$$\begin{aligned}\Delta\chi^2_{ND280} &= 2\sum_i^{Nbins} N_i^p(\vec{b},\vec{x},\vec{d}) - N_i^d + N_i^d ln(N_i^d/N_i^p(\vec{b},\vec{x},\vec{d})) + \\ &\sum_i^{Flux}\sum_j^{Flux}\Delta b_i(V_b^{-1})_{ij}\Delta b_j + \sum_i^{Interaction}\sum_j^{Interaction}\Delta x_i(V_x^{-1})_{ij}\Delta x_j + \\ &\sum_i^{Detector}\sum_j^{Detector}\Delta d_i(V_d^{-1})_{ij}\Delta d_j \end{aligned} \tag{7.1}$$

Here, N_i^d is the observed number of events in i-th bin of the muon p-cosθ defined in Table 7.2. N_i^p is the MC predicted number of events in the i-th bin and it depends on the flux ($\vec{b}$), cross section ($\vec{x}$) and detector ($\vec{d}$) systematic parameters. The systematic parameters have prior probability distributions that are modeled as multivariate Gaussian with covariances of V_b,V_x, and V_d for flux, cross section and detector parameters respectively. Δ_b,Δ_x and Δ_d are the deviation of the systematic parameters away from their prior mean values. The prior of systematic parameters are listed in Figs. 7.2, 7.3 and Table 7.5. The neutrino flux is modeled by external hadron scattering measurements as described in Sec. 6.6.1, including correlation of the flux between the ND280 and on-axis. The uncertainty of the integrated flux ratio between the ND280 and on-axis is 2.7%, as summarized in Table 7.4. The neutrino interactions are modeled based on the current knowledge of the neutrino interactions as described in Sec. 3. ND280 detector systematics is evaluated based on the detector responses to the sand muons, calibration during the detector operation and informations during the detector construction. ND280 detector systematics includes uncertainties of the secondary particles interactions with detector materials. The parameters are fitted to minimize the binned likelihood.

7.2.2 Constraint of neutrino flux and interaction

Figure 7.4 shows an example of the muon p-cosθ distributions of the FGD1 CC-0-pion sample after the fitting. The $\Delta\chi^2$ at the minimum of the data fit is 1895.37 and corresponds p-value is

47.3%, which is calculated by toy experiments generated with set of the systematic parameters thrown based on the prior. Figures 7.5 and 7.6 show the parameters of the neutrino flux and cross sections before and after the fitting. The uncertainties of the flux × cross section of CC-inclusive interactions at the on-axis are decreased from $> 10\%$ to around 4% as shown in Table 7.6.

Table 7.2: Momentum and angle binning of ND280. Common binning are used for FGD1 and FGD2.

Sample	Polarity	Binning
CC-0-pion	positive	Momentum (GeV/c) :0, 0.3, 0.4, 0.5, 0.6, 0.7, 0.8, 0.9, 1, 1.25, 1.5, 2.0, 3.0, 5.0, 30
		Angle (cosθ):-1, 0.6, 0.7, 0.8, 0.85, 0.90, 0.92, 0.94, 0.96, 0.98, 0.99, 1
CC-1-pion	positive	Momentum (GeV/c) :0, 0.3, 0.4, 0.5, 0.6, 0.7, 0.8, 0.9, 1, 1.25, 1.5, 2.0, 5.0, 30
		Angle (cosθ):-1, 0.6, 0.7, 0.8, 0.85, 0.90, 0.92, 0.94, 0.96, 0.98, 0.99, 1
CC-other	positive	Momentum (GeV/c) :0, 0.3, 0.4, 0.5, 0.6, 0.7, 0.8, 0.9, 1, 1.25, 1.5, 2.0, 3.0, 5.0, 30
		Angle (cosθ):-1, 0.6, 0.7, 0.8, 0.85, 0.90, 0.92, 0.94, 0.96, 0.98, 0.99, 1
$\overline{\nu}_\mu$CC-1-track	negative	Momentum (GeV/c) :0, 0.4, 0.5, 0.6, 0.7, 0.8, 0.9, 1.1, 1.4, 2.0, 10
		Angle (cosθ):-1, 0.6, 0.7, 0.8, 0.85, 0.88, 0.91, 0.93, 0.95, 0.96, 0.97, 0.98, 0.99, 1
$\overline{\nu}_\mu$CC-N-track	negative	Momentum (GeV/c) :0, 0.7, 0.95, 1.2, 1.5, 2.0, 3.0, 10
		Angle (cosθ):-1, 0.75, 0.85, 0.88, 0.91, 0.93, 0.95, 0.96, 0.97, 0.98, 0.99, 1
ν_μCC-1-track	negative	Momentum (GeV/c) :0, 0.4, 0.6, 0.8, 1.1, 2.0, 10
		Angle (cosθ):-1, 0.7, 0.8, 0.85, 0.90, 0.93, 0.95, 0.96, 0.97, 0.98, 0.99, 1
ν_μCC-N-track	negative	Momentum (GeV/c) :0, 0.5, 0.7, 1.0, 1.5, 2.0, 3.0, 10
		Angle (cosθ):-1, 0.7, 0.8, 0.85, 0.90, 0.93, 0.95, 0.96, 0.97, 0.98, 0.99, 1

Table 7.3: Format of the flux covariance matrix. ν_e and $\overline{\nu}_e$ are not included because their contamination is small at the near detectors.

Bin	Detector	Horn polarity	Flavor	energy binning
0-10	ND280	FHC	ν_μ	0.0,0.4,0.5,0.6,0.7,1.0,1.5,2.5,3.5,5.0,7.0,30.0
11-15	ND280	FHC	$\overline{\nu_\mu}$	0.0,0.7,1.0,1.5,2.5,30.0
16-20	ND280	RHC	ν_μ	0.0,0.7,1.0,1.5,2.5,30.0
21-31	ND280	RHC	$\overline{\nu_\mu}$	0.0,0.4,0.5,0.6,0.7,1.0,1.5,2.5,3.5,5.0,7.0,30.0
32-42	WM and PM	FHC	ν_μ	0.0,0.4,0.8,1.2,1.4,1.6,2.0,2.4,3.0,4.0,8.0,30.0
43-47	WM and PM	FHC	$\overline{\nu_\mu}$	0.0,0.7,1.0,1.5,2.5,30.0
48-52	WM and PM	RHC	ν_μ	0.0,0.7,1.0,1.5,2.5,30.0
53-63	WM and PM	RHC	$\overline{\nu_\mu}$	0.0,0.4,0.8,1.2,1.4,1.6,2.0,2.4,3.0,4.0,8.0,30.0

Table 7.4: Uncertainty of the integrated ν_μ flux at the water module, ND280 and their ratio with FHC.

Error sources	WM	ND280	Ratio of WM/ND280
Horn current	1.8%	0.9%	0.9%
Beam line alignment	0.3%	0.3%	0.3%
Interaction with beam line material	1.4%	0.9%	0.5%
Proton beam profile	0.2%	1.3%	1.3%
Neutrino beam profile	0.1%	0.8%	0.8%
Hadronic interaction	8.0%	7.6%	1.9%
Total	8.8%	8.0%	2.7%

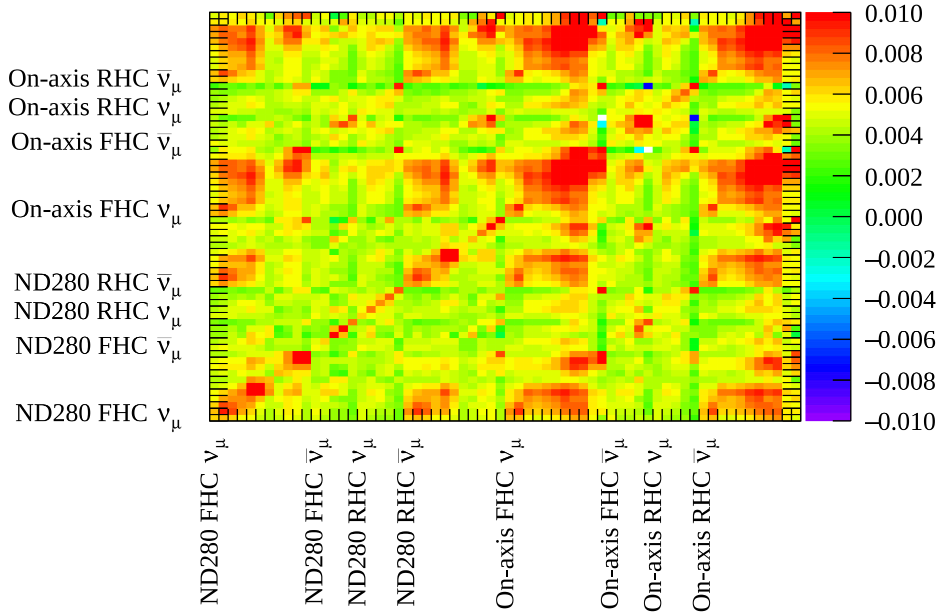

Figure 7.2: Covariance matrix of flux uncertainty in each neutrino energy bin. Table 7.3 shows a definition of the bin number.

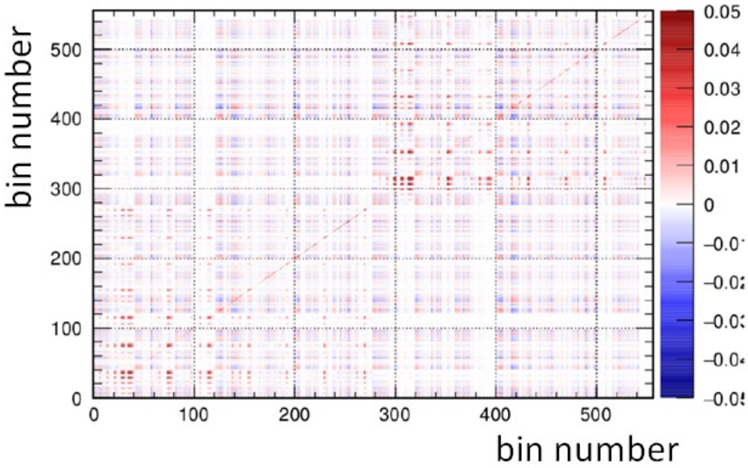

Figure 7.3: Covariance matrix of ND280 detector systematic uncertainty in muon momentum and angle bin.

Table 7.5: List of used interaction model and parameters of neutrino interaction. The first five parameters are used with flat prior. (Others are with Gaussian prior.) Some of the parameters are correlated based on fitting results with external data.

Parameter	Nominal value	Uncertainties(1σ)
CC0π modeled by RFG [57], RPA [64] and 2p2h [68] 2p2h shape change fraction of 2p2h interactions with and without Δ resonance RPA is effectively parametrized with 5 parameters (A,B,C,D,E)		
$\mathrm{M_A^{QE}}$	1.20 GeV	0.03 GeV
$\mathrm{p_F}$ ^{12}C	217 MeV	13 MeV
$\mathrm{p_F}$ ^{16}O	225 MeV	13 MeV
2p2h normalization ν	1.00	1.00
2p2h normalization $\overline{\nu}$	1.00	1.00
2p2h normalization ratio ^{12}C to ^{16}O	1.00	0.20
2p2h shape ^{12}C	100%	±100%
2p2h shape ^{16}O	100%	±100%
parameter of RPA A	0.59	0.12
parameter of RPA B	1.05	0.21
parameter of RPA C	1.13	0.17
parameter of RPA D	0.88	0.35
parameter of RPA U	1.20	fixed
CC1π modeled by Rein Sehgal [71] with tuning of form factor by deuterium experiments		
$\mathrm{C_{A5}}$	0.96	0.15
$\mathrm{M_A^{Res}}$	1.07 GeV	0.15 GeV
Isospin$\frac{1}{2}$bg	0.96	0.40
CCDIS Normalization uncertainty is applied depends on neutrino energy by $0.4/E_\nu$ (GeV)		
CC coherent modeled by Barbar Sehgal [83]		
CCcoh normalization ^{12}C	1.00	0.30
CCcoh normalization ^{16}O	1.00	0.30
NC interactions		
NCcoh normalization	1.00	0.30
NC1γ normalization	1.00	1.00
NCother normalization	1.00	0.30
Difference of ν_e and ν_μ interactions		
ν_e/ν_μnormalization	1.00	0.03
$\overline{\nu}_\mathrm{e}/\overline{\nu}_\mu$normalization	1.00	0.03
Secondary interaction of pions		
Pion Absorption normalization	100%	41 %
Pion ChargeExchange (low E) normalization	100%	57 %
Pion ChargeExchange (high E) normalization	100%	28 %
Pion QuasiElastic (low E) normalization	100%	41 %
Pion QuasiElastic (high E) normalization	100%	50 %
Pion Inelastic normalization	100%	34 %

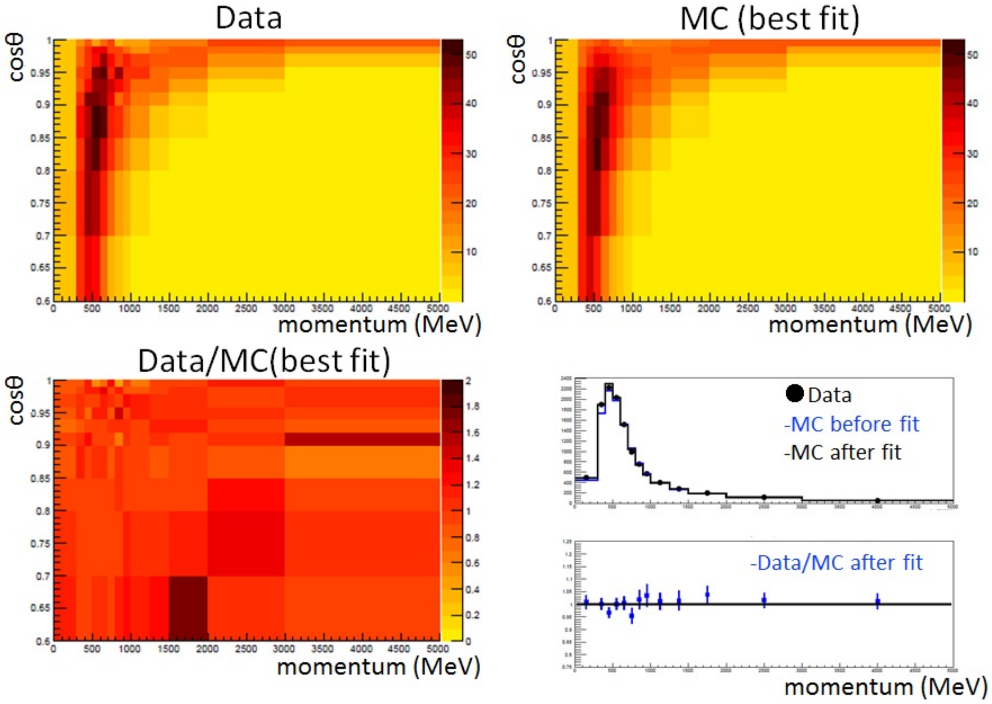

Figure 7.4: Momentum and angle of muons selected by FGD1 CC-0-pion sample. Upper left is data, upper right is best fit of the MC, lower left is ratio of data and MC and lower right is 1D momentum distribution.

Table 7.6: Fraction and uncertainties of event rate of muon neutrino interactions with H_2O target at the on-axis detector simulated by MC with the constraint from the ND280.

Interaction mode	Fraction	Uncertainty		
		flux × cross section	flux	cross section
CC+NC	100%	4.3%	4.9%	3.8%
CC	72.9%	4.2%	5.0%	4.1%
CCQE	23.7%	4.1%	4.7%	4.2%
2p2h	7.7%	21.4%	4.8%	22.4%
CC1pi	22.2%	6.3%	5.0%	4.8%
CCcoh	1.1%	24.9%	5.0%	25.8%
CCDIS	16.4%	7.6%	5.7%	7.1%
CCother	1.8%	9.1%	5.6%	9.2%
NC	27.1%	9.7%	4.9%	9.0%

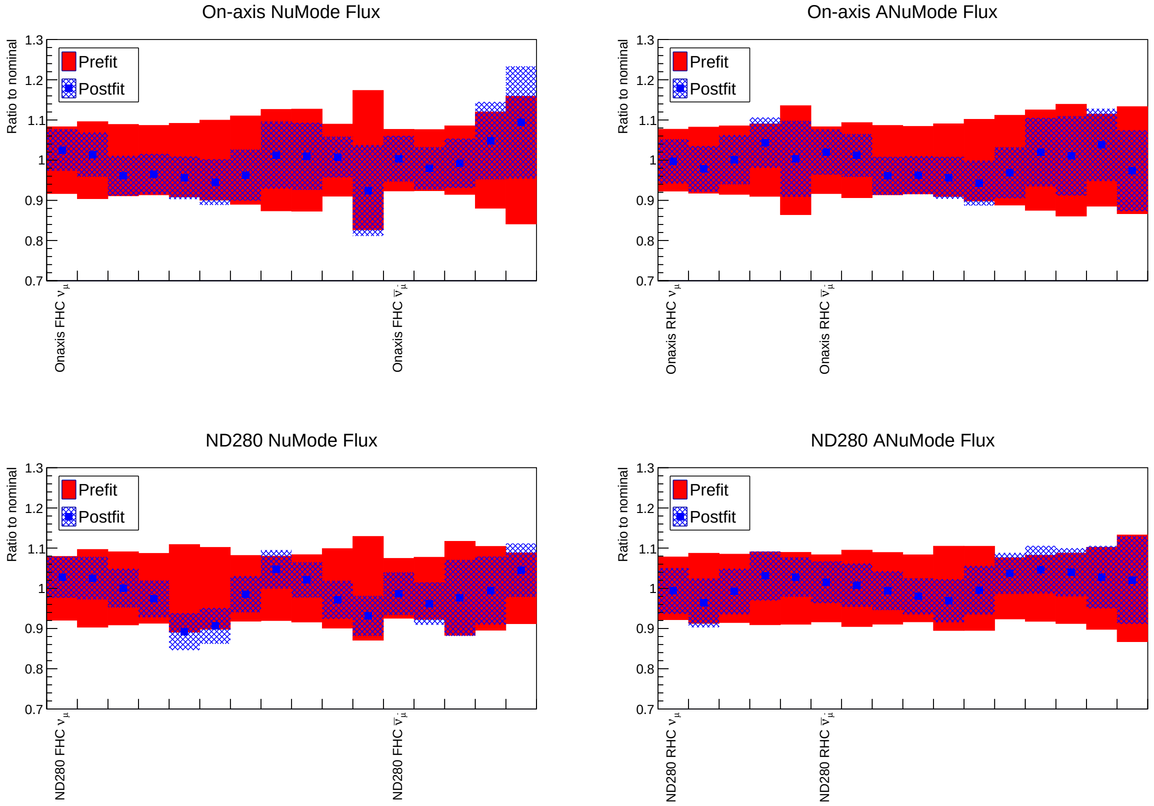

Figure 7.5: Flux parameters before (red) and after the fitting (blue). X axis is bin of the neutrino energy.

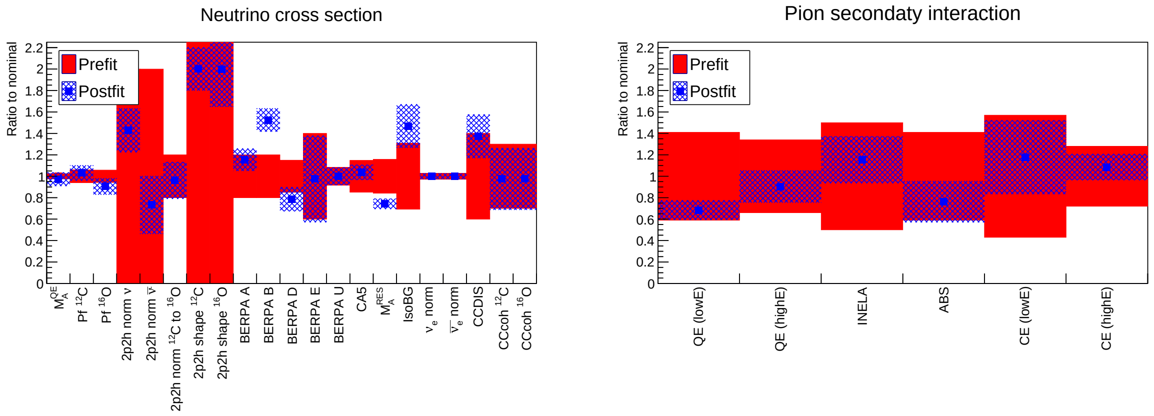

Figure 7.6: Cross section parameters before (red) and after the fitting (blue).

7.3 On-axis detector measurements

The on-axis detectors measure neutrino interactions before the neutrino oscillations and compare them with the MC predictions with the constraint from the ND280. The on-axis detectors select the charged current muon neutrino interactions by detecting muons. The selected events are categorized into a few samples based on the number of reconstructed tracks to identify each type of charged current interaction, similar to the ND280: 1μ like track (1 track sample), 1μ like + 1 proton like track (2 track sample) and more than two tracks (multi track sample). In the 1 track and 2 track samples, the CCQE like interactions are enhanced, which are the main signal of the T2K and main interest in this analysis. In the multi track sample, CC1π and CCDIS interactions are enhanced. The samples are binned with the track topology to identify the momentum of the muon and proton. The number of events in each bins is compared with the MC predictions with the constraint from the ND280.

In this analysis, the water module detector and Proton Module detectors are used as the water and plastic target detectors. The INGRID detector is used for the muon identification. The used data set is the same as that for the CC-inclusive cross section measurement, as described in Sec. 6.2. The event selection criteria is basically the same as that for the CC-inclusive cross section measurement, as described in Sec. 6.3.1. In addition, the events are categorized by the number of reconstructed track:one track, two tracks and more than two tracks (multi track) as shown in Fig. 7.9. When the number of tracks is counted, not only INGRID matched tracks but also INGRID un-matched tracks are used. In addition, large-angle 2 track sample, which requires two INGRID un-matched tracks, is used only for the water module which has large angular acceptance. Due to gamma background from outside the detector, large-angle 1 track sample is not used in this analysis. For each event sample, particle identification is applied for each reconstructed track based on the dE/dx information of the scintillators. We define muon confidence level (MuCL) as follows:

$$\mathrm{MuCL} = P \times \sum_{i=0}^{n-1} \frac{(-lnP)^i}{i!}, P = \prod_{i=0}^{n-1} CL_i \tag{7.2}$$

$$CL_i = \int_{pe=pe_i}^{+\infty} \rho(pe)dpe \tag{7.3}$$

where n is the number of hits included in the reconstructed track, pe_i is the light yield of the i-th hit and $\rho(pe)$ is probability density function of light yield obtained by sand muon data as shown in Fig. 7.7. Figure 7.8 shows an example of the confidence level distributions of the 2 tracks sample with MC. In this analysis, $CL > 0.6$ is selected as muon like track and $CL < 0.3$ is selected as proton like track. For the 1 track sample, the track should be muon like. For the 2 tracks sample, one track should be muon like and the other track should be proton like to select CCQE like event. For the multi track sample, no particle identification is applied. Table 7.7 shows the summary of the event selection criteria. Each sample is binned based on the topology of the tracks: if muon like track is stopping in the INGRID, escaping from the side of the INGRID or penetrating all of the iron plates of the INGRID and if proton like track is stopped in the target detectors or not stopped.

7.3.1 Event selection summary for the water module

Table 7.8 shows a summary of the event selection for the water module. Figures 7.10–7.14 show true neutrino energy, muon p-θ and proton p-θ distributions for each sample and their feature is summarized in Table 7.9. Reconstructed track angle distributions are in Appendix D.

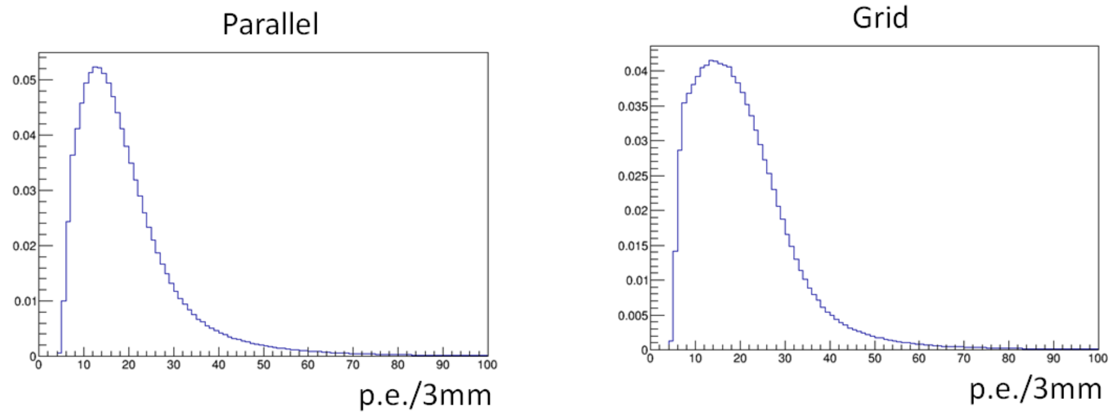

Figure 7.7: Probability density function of light yield of the parallel (left) and grid (right) scintillators of the water module obtained by sand muon data.

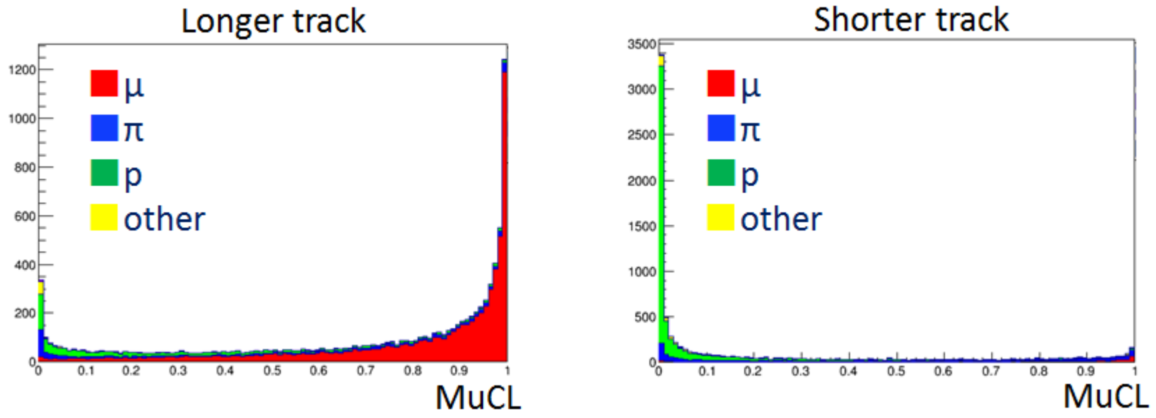

Figure 7.8: Muon confidence level of the longer (left) and shorter (right) track of the 2 tracks sample of the MC.

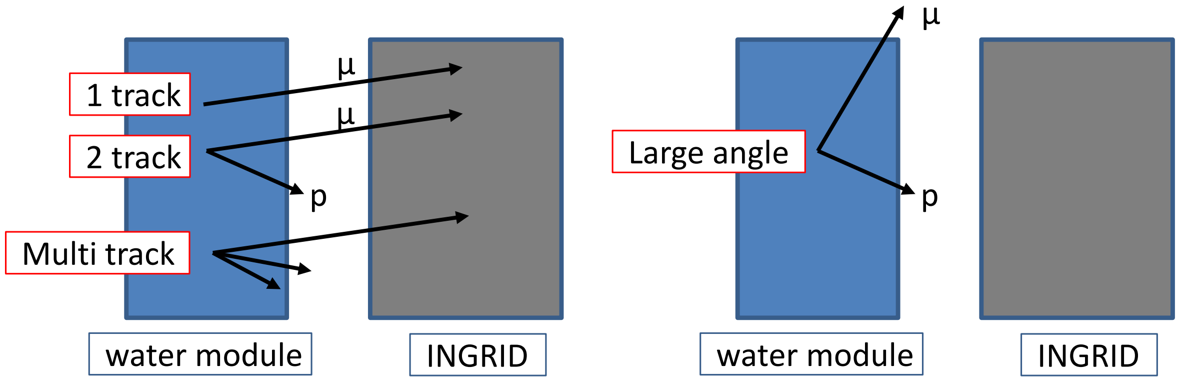

Figure 7.9: View of the event topology for each event sample.

Table 7.7: Summary of the event selection criteria

Cut	1 track	2 track	Multi track	Large angle
Time clustering	○	○	○	○
Two-dimensional track reconstruction	○	○	○	○
Track matching with INGRID	○	○	○	
No track matching with INGRID				○
Three-dimensional track matching	○	○	○	○
Vertexing	○	○	○	○
Beam timing cut	○	○	○	○
Front-veto cut	○	○	○	○
Fiducial volume cut	○	○	○	○
The number of tracks is 1	○			
The number of tracks is 2		○		○
The number of tracks is more than 2			○	
The number of muon like tracks is 1	○	○		○
The number of proton like tracks is 1		○		○

Table 7.8: Summary of the number of selected events for the water module and MC expectation with the parameters of the neutrino flux and interaction tuned with the best fit of the ND280 measurement. The values in parentheses are without the tuning.

Sample		Data	MC				
			CC on H_2O	$\overline{\nu_\mu}$, ν_e, $\overline{\nu_e}$	CC on CH	Outside B.G.	All
1 track	inclusive	3654	$2.66(2.43)\times10^3$	1.46×10^2	$7.21(6.72)\times10^2$	8.21×10^1	$3.60(3.33)\times10^3$
			73.9%	4.1%	20.0%	2.2%	100%
	μ stop	369	$2.95(2.71)\times10^2$	1.05×10^1	$8.17(7.61)\times10^1$	2.72×10^1	$4.15(3.86)\times10^2$
	μ escape	653	$4.76(4.48)\times10^2$	1.91×10^1	$1.25(1.16)\times10^2$	9.92×10^0	$6.30(5.93)\times10^2$
	μ penetrate	2390	$1.72(1.56)\times10^3$	1.09×10^2	$4.70(4.39)\times10^2$	4.20×10^1	$2.34(2.15)\times10^3$
2 track	inclusive	3099	$2.69(2.59)\times10^3$	3.77×10^1	$7.37(6.96)\times10^3$	1.54×10^1	$3.48(3.34)\times10^3$
			77.3%	1.1%	21.2%	0.4%	100%
	μ stop, p stop	147	$1.26(1.19)\times10^2$	1.26×10^0	$3.39(3.10)\times10^1$	2.22×10^0	$1.63(1.54)\times10^2$
	μ stop, p escape	117	$1.30(1.27)\times10^2$	1.17×10^0	$3.74(3.65)\times10^1$	3.57×10^0	$1.73(1.69)\times10^2$
	μ escape, p stop	351	$3.13(3.02)\times10^2$	2.05×10^0	$8.60(8.21)\times10^1$	1.71×10^{-1}	$4.01(3.87)\times10^2$
	μ escape, p escape	397	$3.64(3.72)\times10^2$	3.32×10^0	$9.87(9.79)\times10^1$	1.55×10^0	$4.67(4.74)\times10^2$
	μ penetrate, p stop	951	$7.72(7.16)\times10^2$	1.56×10^1	$2.13(1.97)\times10^2$	4.01×10^{-1}	$1.00(0.93)\times10^3$
	μ penetrate, p escape	801	$6.88(6.67)\times10^2$	1.02×10^1	$1.93(1.82)\times10^2$	1.63×10^0	$8.93(8.61)\times10^3$
Multi track	inclusive	4526	$3.23(3.22)\times10^3$	9.18×10^1	$8.10(8.10)\times10^2$	9.57×10^1	$4.23(4.23)\times10^3$
			76.4%	2.2%	19.1%	2.3%	100%
Large angle	inclusive	1225	$1.53(1.59)\times10^3$	1.22×10^1	$3.82(3.84)\times10^2$	7.77×10^1	$2.00(2.08)\times10^3$
			76.5%	0.6%	19.1%	3.9%	100%

True neutrino energy

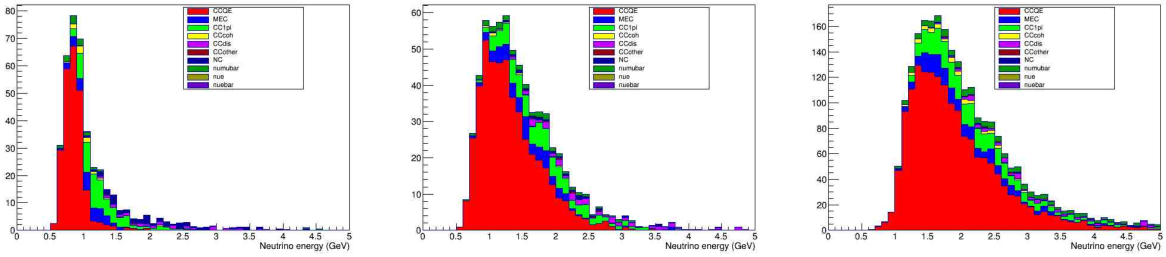

1 track,
μ stop

1 track,
μ escape

1 track,
μ penetrate

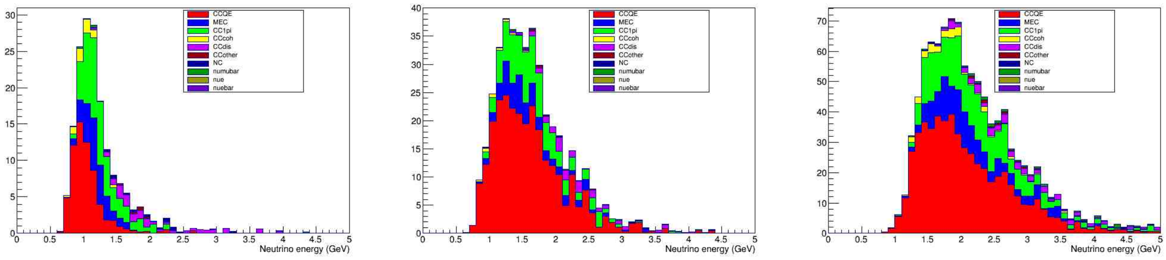

2 track,
μ stop, p stop

2 track,
μ escape, p stop

2 track,
μ penetrate, p stop

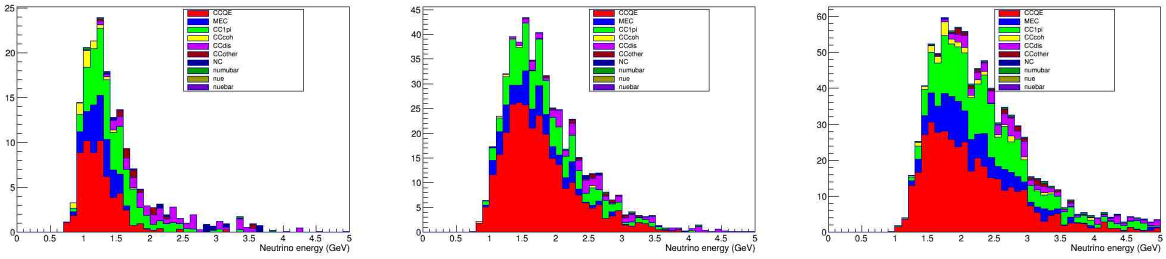

2 track,
μ stop, p escape

2 track,
μ escape, p escape

2 track,
μ penetrate, p escape

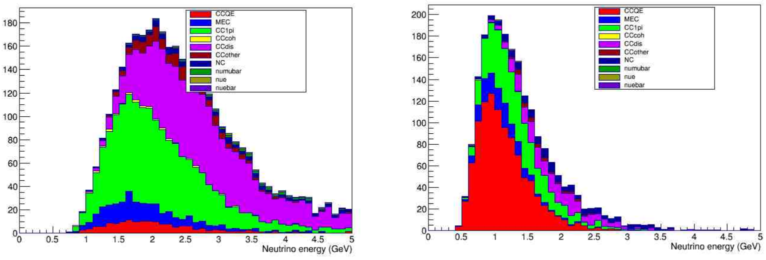

multi track

large angle

Figure 7.10: True neutrino energy for each sample for the water module predicted by MC with the parameters of the neutrino flux and interaction tuned with the best fit of the ND280 measurement.

True muon momentum

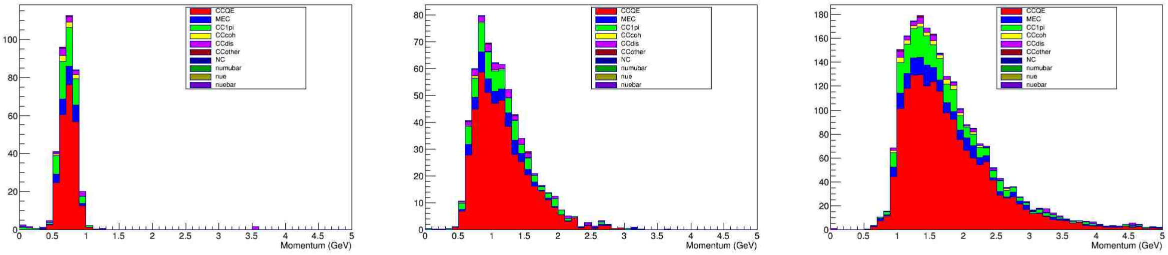

1 track,
μ stop

1 track,
μ escape

1 track,
μ penetrate

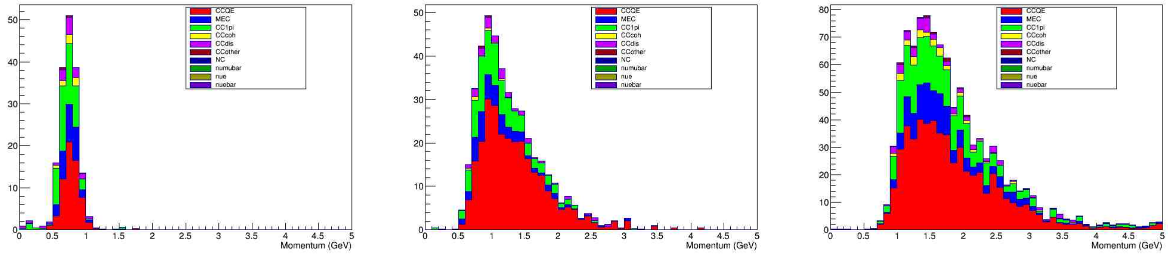

2 track,
μ stop, p stop

2 track,
μ escape, p stop

2 track,
μ penetrate, p stop

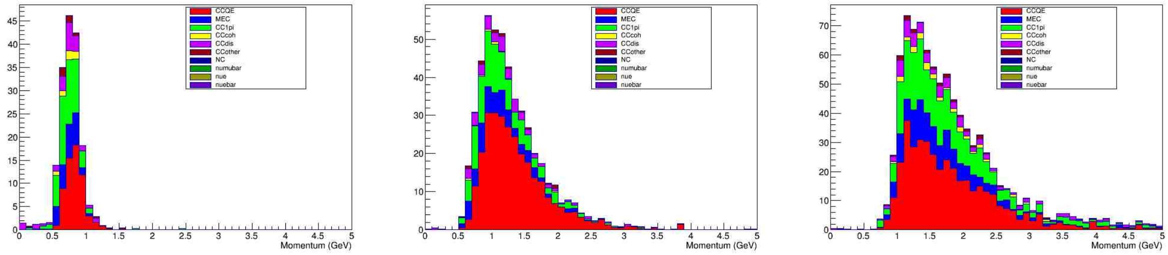

2 track,
μ stop, p escape

2 track,
μ escape, p escape

2 track,
μ penetrate, p escape

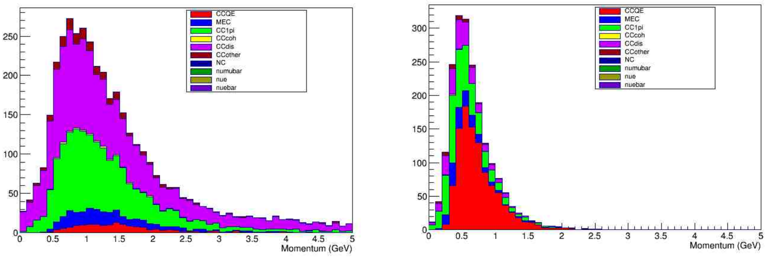

multi track

large angle

Figure 7.11: True muon momentum for each sample for the water module predicted by MC with the parameters of the neutrino flux and interaction tuned with the best fit of the ND280 measurement.

True muon angle

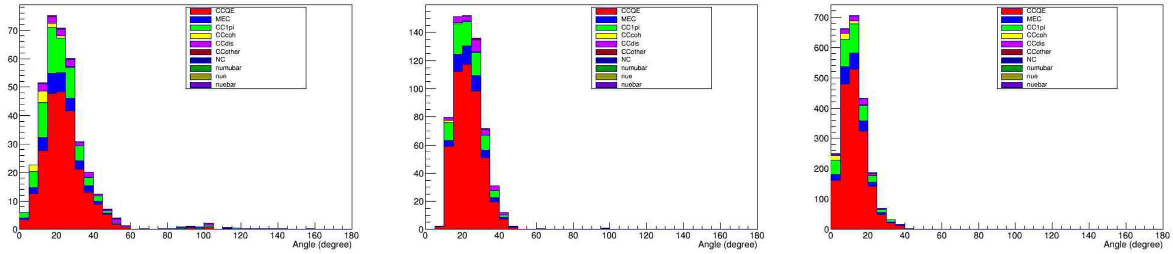

1 track,
μ stop

1 track,
μ escape

1 track,
μ penetrate

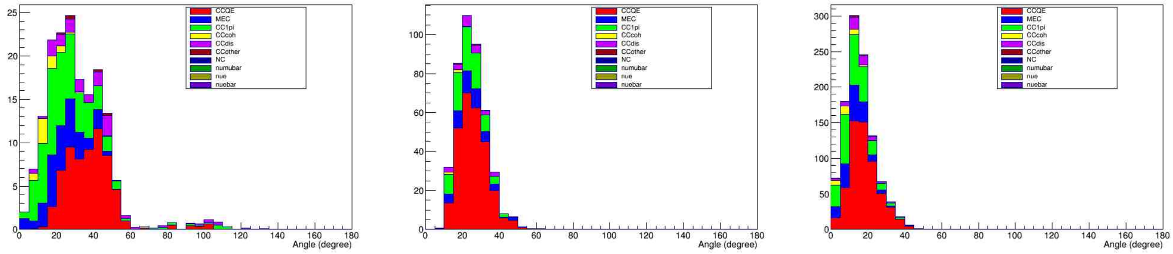

2 track,
μ stop, p stop

2 track,
μ escape, p stop

2 track,
μ penetrate, p stop

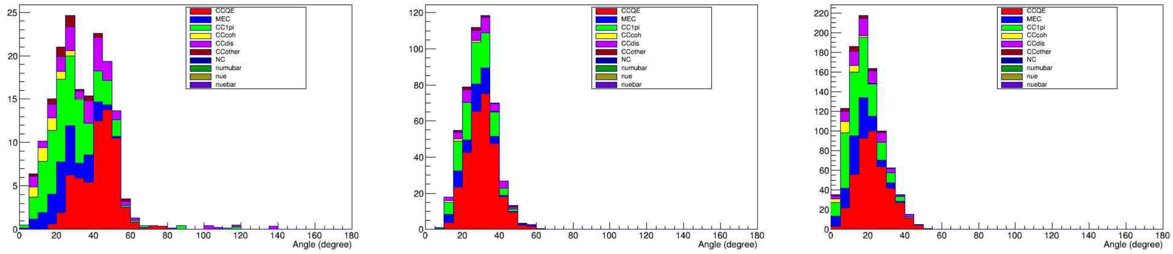

2 track,
μ stop, p escape

2 track,
μ escape, p escape

2 track,
μ penetrate, p escape

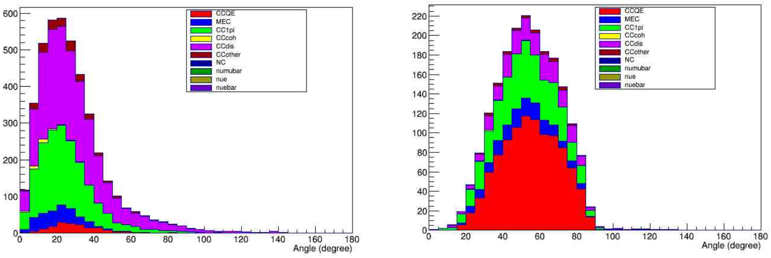

multi track

large angle

Figure 7.12: True muon angle for each sample for the water module predicted by MC with the parameters of the neutrino flux and interaction tuned with the best fit of the ND280 measurement.

True proton momentum

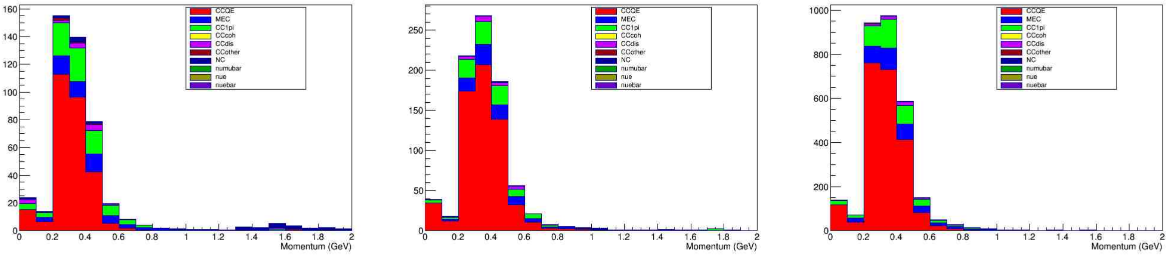

1 track,
μ stop

1 track,
μ escape

1 track,
μ penetrate

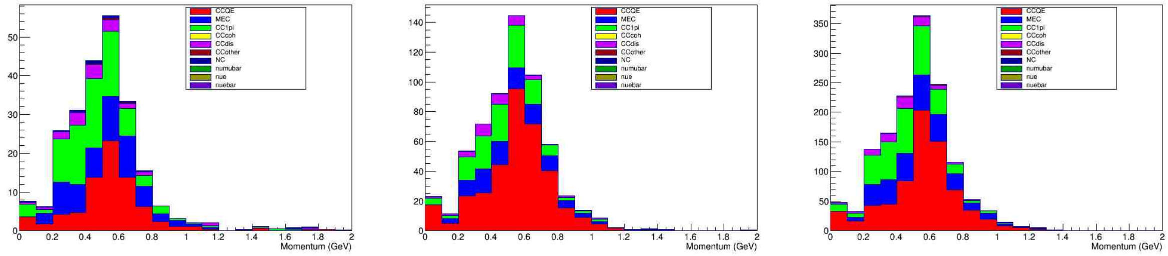

2 track,
μ stop, p stop

2 track,
μ escape, p stop

2 track,
μ penetrate, p stop

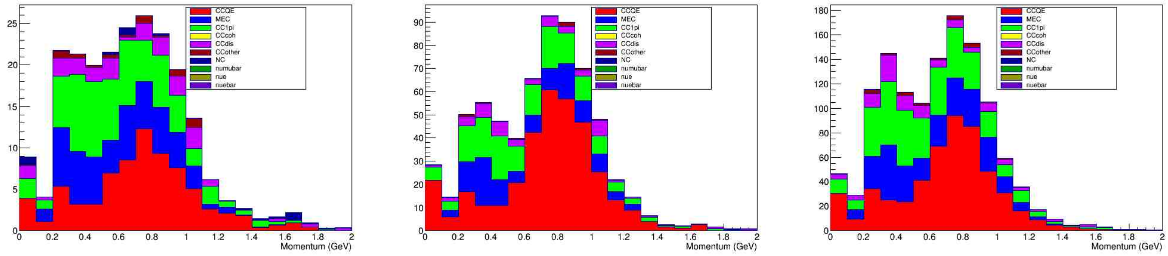

2 track,
μ stop, p escape

2 track,
μ escape, p escape

2 track,
μ penetrate, p escape

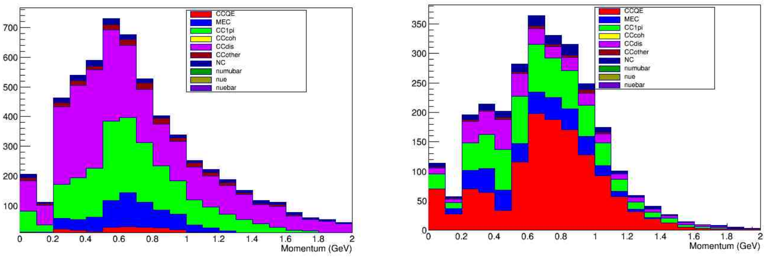

multi track

large angle

Figure 7.13: True proton momentum for each sample for the water module predicted by MC with the parameters of the neutrino flux and interaction tuned with the best fit of the ND280 measurement.

True proton angle

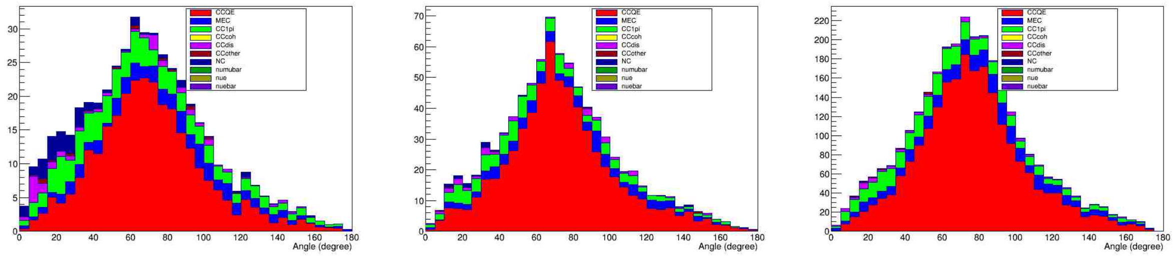

1 track,
μ stop

1 track,
μ escape

1 track,
μ penetrate

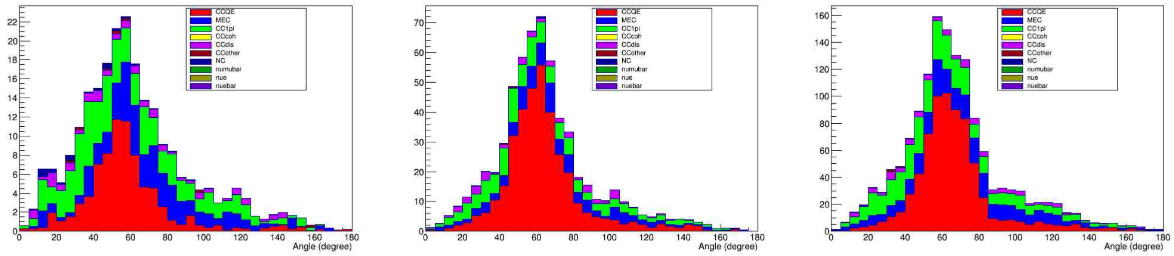

2 track,
μ stop, p stop

2 track,
μ escape, p stop

2 track,
μ penetrate, p stop

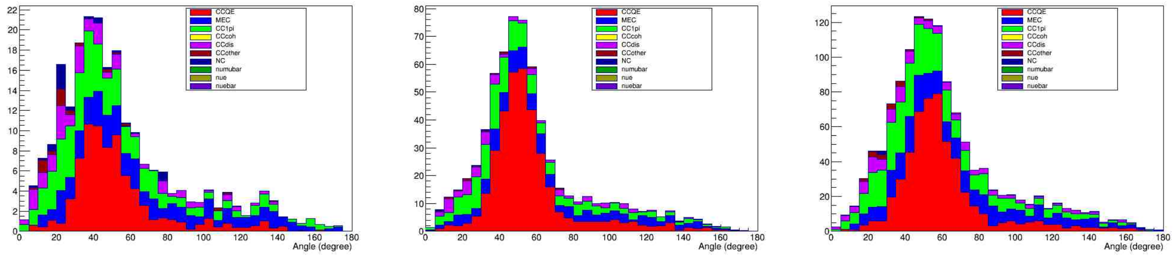

2 track,
μ stop, p escape

2 track,
μ escape, p escape

2 track,
μ penetrate, p escape

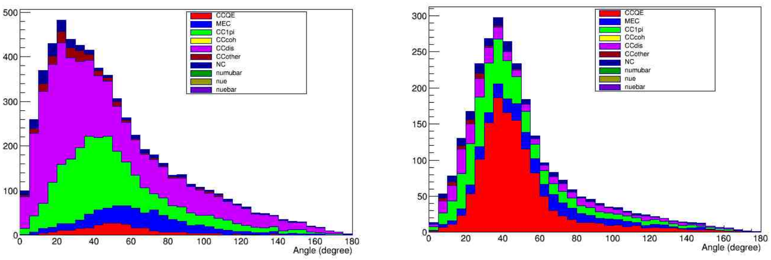

multi track

large angle

Figure 7.14: True proton angle for each sample for the water module predicted by MC with the parameters of the neutrino flux and interaction tuned with the best fit of the ND280 measurement.

Table 7.9: Summary of the mean values of true neutrino energy, muon and proton pθ for each event sample of the water module. Background events from outside is not included in this table.

Sample	E_ν	Muon p (GeV)	Muon θ (GeV)	Proton p (GeV)	Proton θ (deg)
1 track μ stop	1.0	0.74	25.0	–	–
μ escape	1.5	1.18	23.7	–	–
μ penetrate	2.0	1.80	12.7	–	–
2 track μ stop, p stop	1.2	0.74	31.3	0.51	62.9
2 track μ stop, p escape	1.5	0.77	34.1	0.66	55.9
2 track μ escape, p stop	1.7	1.29	25.3	0.53	65.0
2 track μ escape, p escape	1.8	1.31	29.4	0.69	57.9
2 track μ penetrate, p stop	2.2	1.84	15.7	0.52	67.0
2 track μ penetrate, p escape	2.3	1.83	19.0	0.64	61.0
Multi track	2.4	1.43	28.6	–	–
Large angle	1.3	0.66	54.2	–	–

7.3.2 Event selection summary for the Proton Module

Table 7.10 shows a summary of the event selection for the Proton Module. True neutrino energy, muon p-θ and proton p-θ distributions for each sample are similar to that for the water module as shown in Table 7.11 and Appendix D. Reconstructed track angle distributions are in Appendix D.

Table 7.10: Summary of the number of selected events for the Proton Module and MC expectation with the parameters of the neutrino flux and interaction tuned with the best fit of the ND280 measurement. The values in parentheses are without the tuning.

Sample		Data	MC			
			ν_μ on CH	$\overline{\nu_\mu}$, ν_e, $\overline{\nu_e}$	Outside B.G.	All
1 track sample	inclusive	6585	$5.81(5.45)\times10^3$	3.17×10^2	1.56×10^2	$6.28(5.92)\times10^3$
			92.5%	5.0%	2.5%	100%
	μ stop	671	$6.58(6.24)\times10^2$	2.48×10^1	5.28×10^1	$7.36(7.01)\times10^2$
	μ escape	1240	$1.07(1.03)\times10^3$	4.07×10^1	3.17×10^1	$1.15(1.10)\times10^3$
	μ penetrate	4236	$3.70(3.44)\times10^3$	2.37×10^2	5.81×10^1	$3.99(3.74)\times10^3$
2 track sample	inclusive	3135	$3.57(3.43)\times10^3$	3.38×10^1	4.54×10^0	$3.60(3.47)\times10^3$
			99.1%	0.9%	0.1%	100%
	μ stop, p stop	92	$1.05(0.98)\times10^2$	1.23×10^0	1.89×10^0	$1.08(1.01)\times10^2$
	μ stop, p escape	210	$2.51(2.40)\times10^2$	2.78×10^0	2.06×10^0	$2.56(2.45)\times10^2$
	μ escape, p stop	294	$2.84(2.74)\times10^2$	1.68×10^0	3.05×10^{-1}	$2.86(2.76)\times10^2$
	μ escape, p escape	619	$7.18(7.18)\times10^2$	2.82×10^0	4.51×10^{-2}	$7.21(7.20)\times10^2$
	μ penetrate, p stop	505	$5.60(5.28)\times10^2$	9.71×10^0	2.70×10^{-1}	$5.70(5.38)\times10^2$
	μ penetrate, p escape	1204	$1.40(1.33)\times10^3$	1.44×10^1	2.47×10^{-1}	$1.42(1.34)\times10^3$
Multi track sample	inclusive	2668	$2.42(2.39)\times10^3$	6.33×10^1	2.53×10^1	$2.51(2.48)\times10^3$
			96.4%	2.5%	1.0%	100%

Table 7.11: Summary of the mean values of true neutrino energy, muon and proton pθ for each event sample of the Proton Module. Background events from outside is not included in this table.

Sample	E_ν	Muon p (GeV)	Muon θ (GeV)	Proton p (GeV)	Proton θ (deg)
1 track μ stop	1.2	0.71	29.7	–	–
μ escape	1.6	1.18	25.4	–	–
μ penetrate	2.1	1.81	13.6	–	–
2 track μ stop, p stop	1.2	0.72	30.8	0.56	56.7
2 track μ stop, p escape	1.4	0.75	33.7	0.69	52.3
2 track μ escape, p stop	1.7	1.27	25.2	0.57	59.0
2 track μ escape, p escape	1.8	1.28	29.0	0.73	53.9
2 track μ penetrate, p stop	2.2	1.80	16.0	0.56	60.7
2 track μ penetrate, p escape	2.3	1.83	18.3	0.70	58.0
Multi track	2.5	1.38	30.6	–	–

7.4 Uncertainties

7.4.1 Statistical uncertainty of on-axis measurement

Statistical uncertainty is evaluated for each event sample of the on-axis detectors by assuming Poisson distribution. Figure 7.15 shows a summary of the statistical uncertainty in each event sample.

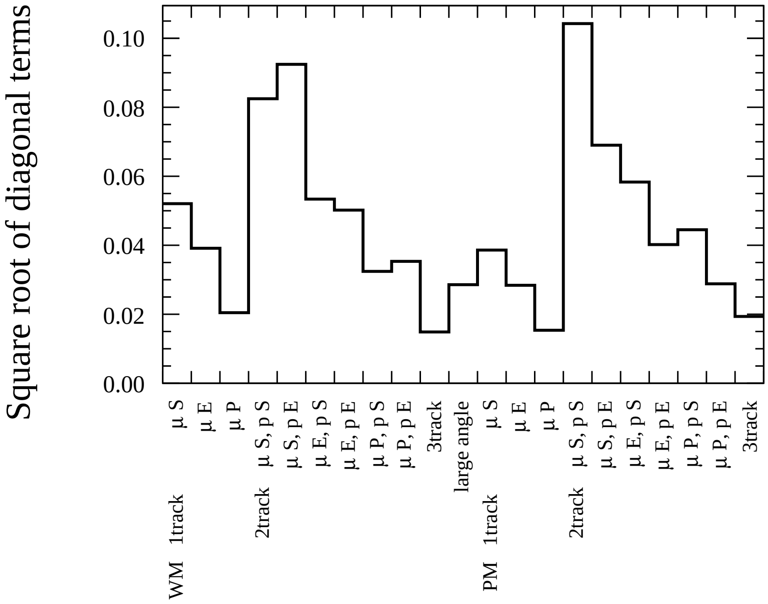

Figure 7.15: Statistical uncertainty in each event sample. S, E and P in label of the figure mean stop, escape and penetrate respectively.

7.4.2 Systematic uncertainty of on-axis detectors

Detector systematic uncertainties of the water module and Proton Module are calculated in the same manner as that performed for the CC-inclusive analysis. Because proton tracks are used with the particle identification in this analysis, uncertainty of the light yield distribution and secondary interactions are newly estimated. Following error sources are newly considered:

- Difference of the light yield distributions of the sand muon between data and MC (Figs. 5.15 and 5.16)
- Uncertainty of Birk's constant of the scintillator (0.0208 ± 0.0023 cm/MeV)
- Uncertainty of the position dependency of the scintillator (attenuation length=3.0±0.5 cm)
- Uncertainty of the secondary interactions simulated in GEANT4 (comparison of physics lists: QGSP, QGSP BERT,QGSP BIC, FTP BIC and FTFP BERT)
- Uncertainty of the secondary interactions of proton simulated in NEUT (interaction length= 100 ± 30%)

In addition, uncertainties of tracking efficiency of the non-INGRID matched tracks are newly estimated by using the cosmic muons and sand muons (Fig. 5.20). Table 7.12 and Fig. 7.16 show the summaries of the detector systematics.

Table 7.12: Summary of the total systematic uncertainties of on-axis measurement.

Uncertainties	Total		Secondary interaction		Light yield		Others	
Detector	WM	PM	WM	PM	WM	PM	WM	PM
1 track μ stop	9.6%	8.5%	1.3%	3.4%	7.7%	6.1%	5.6%	4.8%
1 track μ escape	8.5%	6.5%	5.8%	2.1%	5.3%	5.4%	3.1%	2.9%
1 track μ penetrate	6.6%	4.0%	3.1%	1.5%	4.9%	2.4%	3.2%	2.8%
2 track μ stop, p stop	9.9%	12.6%	5.9%	5.6%	7.2%	3.8%	3.4%	10.6%
2 track μ stop, p escape	12.0%	4.8%	7.7%	2.9%	6.2%	1.4%	6.8%	3.5%
2 track μ escape, p stop	7.6%	5.6%	5.1%	3.2%	4.8%	3.1%	3.0%	3.3%
2 track μ escape, p escape	9.9%	4.1%	7.6%	2.9%	5.3%	1.4%	3.5%	2.6%
2 track μ penetrate, p stop	7.2%	7.8%	4.2%	6.4%	4.7%	1.7%	3.4%	4.3%
2 track μ penetrate, p escape	8.5%	4.3%	5.3%	2.8%	5.8%	2.5%	3.3%	2.2%
Multi track	5.9%	4.5%	3.7%	3.3%	0.8%	1.1%	4.5%	2.8%
Large angle	9.0%	–	3.6%	–	3.4%	–	7.5%	–

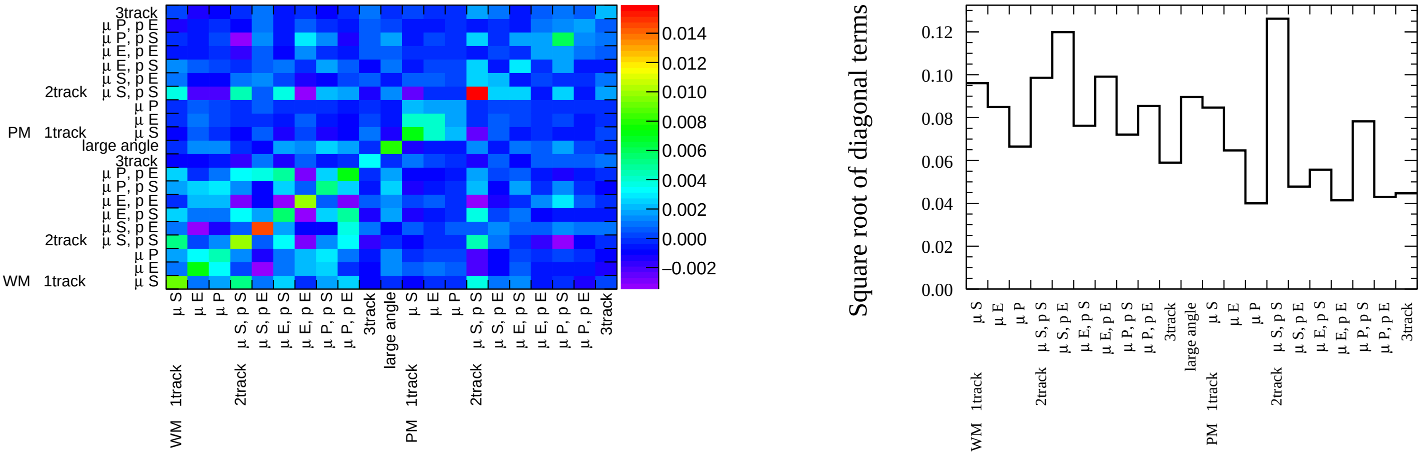

Figure 7.16: Covariance of the total detector systematics in each event sample (left) and square root of the diagonal term (right). S, E and P in label of the figure mean stop, escape and penetrate respectively.

7.4.3 Systematic uncertainty of neutrino flux and interaction

For an estimation of the uncertainties of the neutrino flux and interactions of each sample, the flux and cross section parameters are thrown following the constraint from the ND280 measurement. For each throw, the number of selected events in each sample is calculated and 68% range of the distribution of the event rate fluctuation is taken as the size of the 1σ uncertainty. In addition, covariance between each event sample is calculated. Table 7.13 and Fig. 7.17 show a summary of the uncertainties of neutrino flux and interaction.

Table 7.13: Summary of the uncertainties of neutrino flux and interactions with the constraint of the ND280. Values in parentheses are without the constraint of the ND280.

Uncertainties	Flux×Cross section		Flux		Cross section	
Detector	WM	PM	WM	PM	WM	PM
1 track μ stop	3.5% (16.3%)	3.4% (15.1%)	4.5% (8.6%)	4.6% (8.8%)	4.8% (13.8%)	4.6% (12.3%)
1 track μ escape	4.0% (18.4%)	3.6% (15.8%)	5.0% (9.1%)	5.1% (9.2%)	4.9% (15.9%)	4.5% (12.8%)
1 track μ penetrate	4.4% (19.0%)	4.1% (17.2%)	5.5% (9.7%)	5.6% (9.8%)	4.9% (16.2%)	4.5% (14.2%)
2 track μ stop, p stop	4.0% (15.5%)	3.8% (14.8%)	4.9% (8.9%)	4.8% (8.9%)	4.4% (12.7%)	4.3% (11.8%)
2 track μ stop, p escape	4.4% (14.7%)	4.4% (16.2%)	5.0% (9.0%)	5.0% (9.0%)	4.8% (11.5%)	4.6% (13.5%)
2 track μ escape, p stop	3.8% (14.9%)	3.7% (14.0%)	5.2% (9.4%)	5.2% (9.4%)	4.2% (11.6%)	4.0% (10.4%)
2 track μ escape, p escape	4.3% (14.1%)	4.3% (14.1%)	5.4% (9.7%)	5.4% (9.6%)	4.5% (10.3%)	4.4% (10.3%)
2 track μ penetrate, p stop	4.5% (15.6%)	4.5% (15.1%)	5.7% (10.0%)	5.7% (9.9%)	4.3% (12.0%)	4.1% (11.3%)
2 track μ penetrate, p escape	4.9% (15.1%)	4.9% (16.2%)	5.8% (10.1%)	5.8% (10.1%)	4.5% (11.2%)	4.5% (12.6%)
Multi track	5.0% (12.6%)	5.3% (12.9%)	5.7% (10.0%)	5.8% (10.1%)	3.8% (7.7%)	4.0% (8.0%)
Large angle	3.6% (12.4%)	–	4.9% (8.9%)	–	4.3% (8.6%)	–

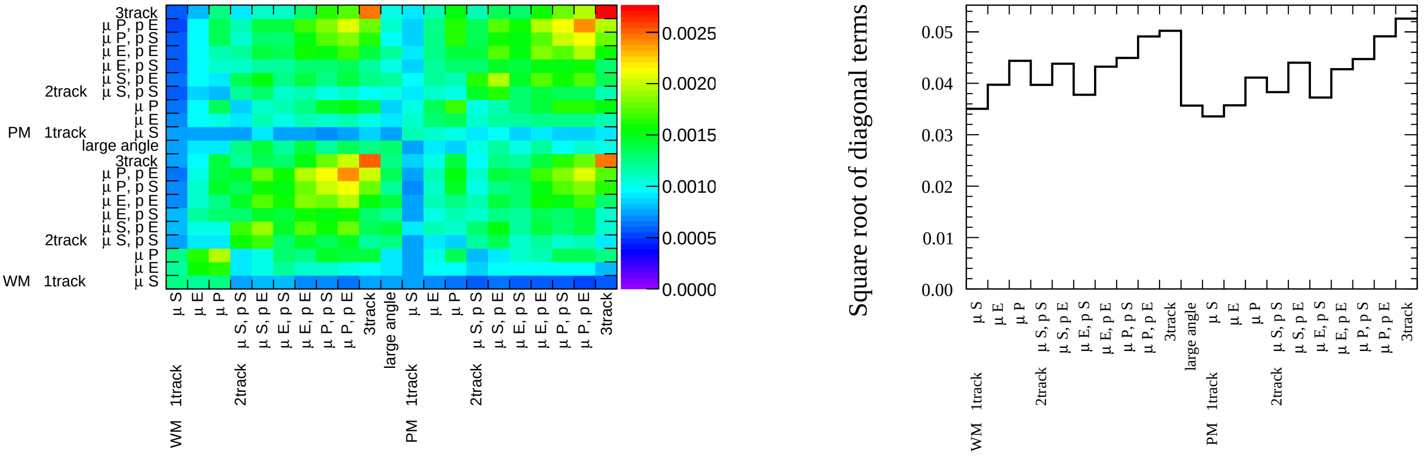

Figure 7.17: Covariance of the total neutrino flux×interactions uncertainty in each event sample (left) and square root of the diagonal terms (right). S, E and P in label of the figure mean stop, escape and penetrate respectively.

7.5 Results

Data and MC with the constraint from the ND280 are compared with two groups of the samples. The first group aims to check the forward scattered muons which are included in the ND280 fitting. It consists of the 1 track, 2 track and multi track samples. The large angle sample is not included. In addition, the 1 track and 2 track samples are merged not to use the information of the protons. Figure 7.18 shows the ratio of the observed number of events on data and MC expectation for each sample with and without the constraint from the ND280. The error bars correspond to the total uncertainty, which is a quadratic sum of the statistical uncertainty, systematic uncertainties of the detector, neutrino flux and interactions. In addition, chi-square test is done including the correlations between the samples to check the consistency of the data and MC. The chi-square is calculated as follows:

$$\chi^2 = \Sigma_{ij}(N_i^{\text{varied}} - N_i^{\text{nominal}})V_{ij}^{-1}(N_j^{\text{varied}} - N_j^{\text{nominal}}) \tag{7.4}$$

where N_i^{nominal} is the expected number of selected events in i-th sample with the nominal systematic parameters (the best fit of the ND280 with the constraint of the ND280), N_i^{varied} is the number of selected events in i-th sample calculated with data or varied set of MC, and V_{ij}^{-1} is an inverse matrix of the total covariance matrix. The chi-square is calculated with data and 10000 sets of MC which is varied based on the covariance matrix of the total uncertainties as well as statistics. Figure 7.19 shows the calculated chi-square distributions with and without the constraint from the ND280. Without the constraint from the ND280, the χ^2 of data is 7.15 and corresponding p-value is 52.6%, which is integral of the right tail of the MC more than data. On the other hand, with the constraint from the ND280, χ^2 of data is 9.5 and corresponding p-value is 30.3%.

The second group consists of all samples with the information of the large angle muons and protons, which are not included in the ND280 fitting. Figures 7.20 and 7.21 show the results of the comparison with the second group. Without the constraint from the ND280, the χ^2 of data is 34.6 and corresponding p-value is 3.1%. On the other hand, with the constraint from the ND280, χ^2 of data is 49.0 and corresponding p-value is 0.04%. The main deviation without the constraint from the ND280 is coming from the large angle sample. Without the large angle sample, the p-value without (with) the constraint from the ND280 is 59.2% (1.3%).

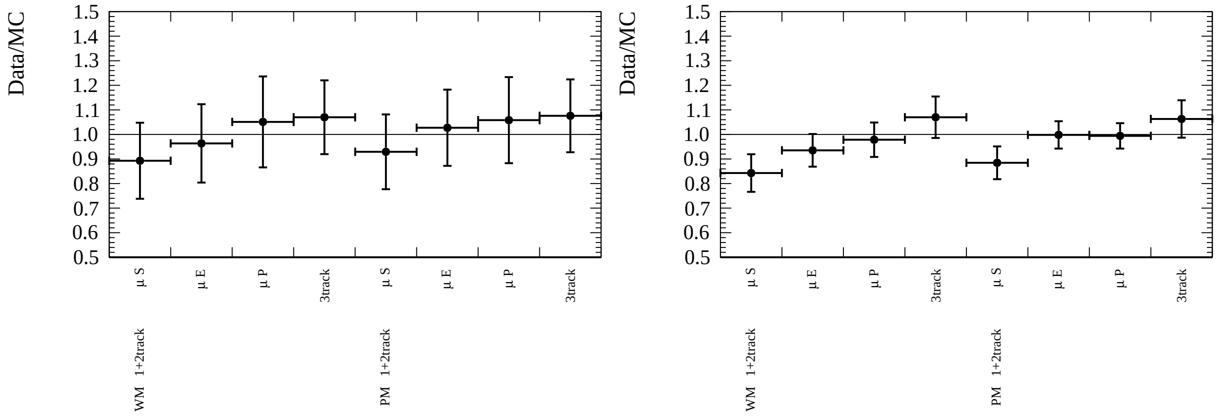

Figure 7.18: Ratio of the total number of selected events for each sample between data and MC prediction without (left) and with(right) the constraint from the ND280. The 1 track and 2 track samples are merged and large angle sample is removed.

7.6 Discussion

First group

In the first group of the samples, the data and MC with the constraint from the ND280 agree with each other with their error sizes and reasonable p-value of 30.3%. This result ensures the correctness of the framework of the ND280 fitting and propagation of the uncertainties. It improves reliability of the oscillation analysis of the T2K.

Second group

On the other hand, In the second group, there are significant deviations between data and MC with and without the constraint from the ND280. It is more or less expected because the proton

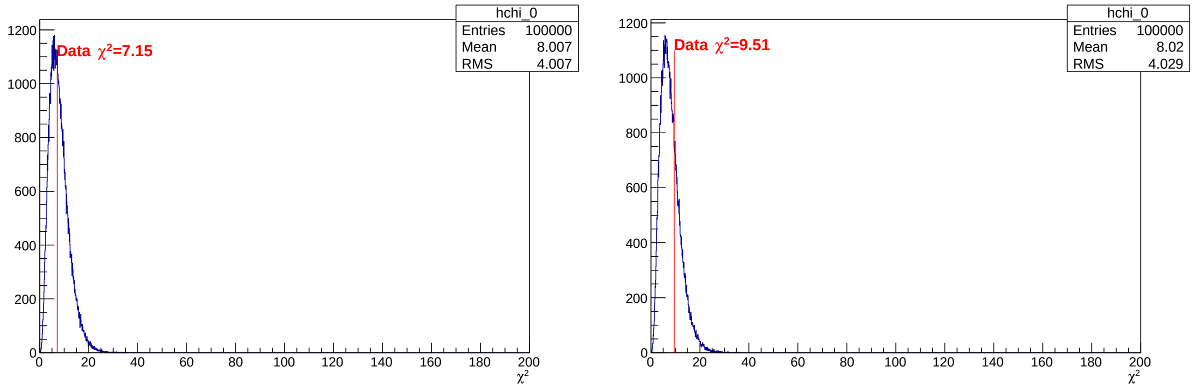

Figure 7.19: Calculated chi-square distributions without(left) and with(right) the constraint from the ND280. The 1 track and 2 track samples are merged and large angle sample is removed.

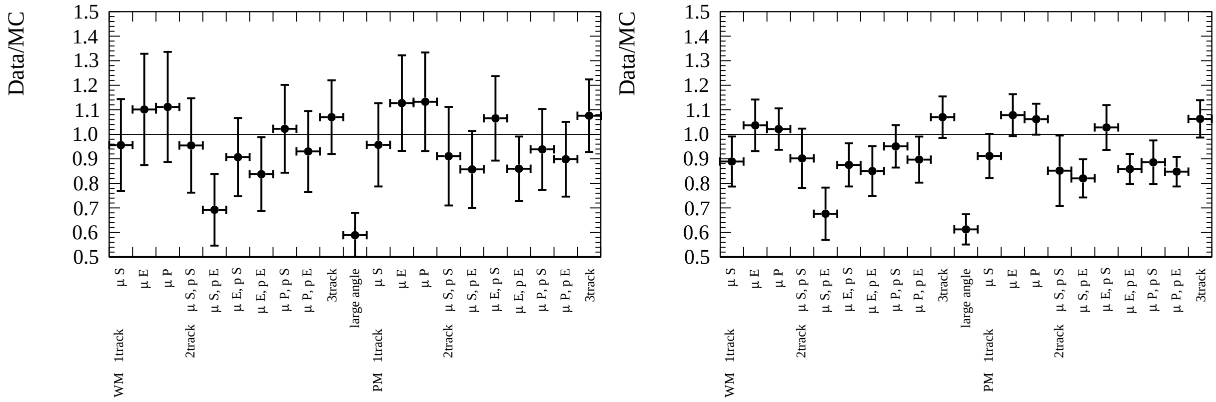

Figure 7.20: Ratio of the total number of selected events for each sample between data and MC prediction without (left) and with(right) the constraint from the ND280.

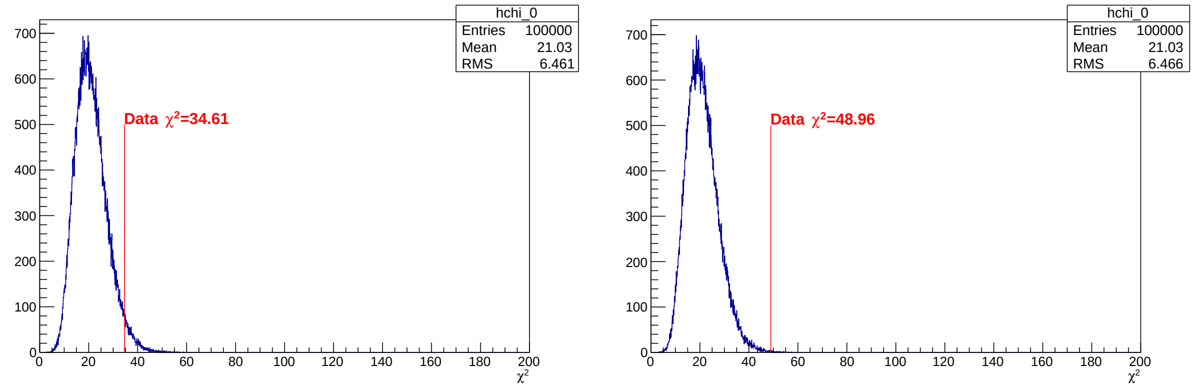

Figure 7.21: Calculated chi-square distributions without(left) and with(right) the constraint from the ND280.

and large angle muon informations are not included for the ND280 fitting.

Without the constraint from the ND280, the large angle sample has more than 3σ difference between data and MC and any uncertainty of the cross section parameters does not cover the difference. We are not sure if origin of the deviation is coming from large angle muon or large momentum proton because we have not measured the large angle 1 track sample and MC overpredicts the number of events in all of the proton escaping samples, similar to the large angle 2 track sample, with the significances of 1–2σ. In order to measure the large-angle 1 track sample, we plan to set additional muon range detector at the side of the water module at the different location as shown in Fig. 7.22. The data taking with the side muon range detector will start in 2019. The origin of the deviation is expected to be clear by this measurement.

With the constraint from the ND280, the MC overpredicts the number of events in the most bins of the 2 track samples more strongly than that without the constraint from the ND280. This tendency is still stronger in the proton escaping samples and it is indicated that the number of high momentum protons emitted from nucleus is overestimated. It could be a hint to improve the modeling of the neutrino-nucleus interactions. Table 7.14 shows the variation of the number of events with varied interaction parameters of 1σ without the ND280 constraint. Most of the parameters increase both of the 1 track and 2 track samples and does not explain the deviation, except for the 2p2h shape parameter. The 2p2h shape parameter decreases the number of 1 track sample and increases the number of 2 track sample by changing the kinematics of proton in non-CCQE interactions. The deviation may indicate the un-modeled kinematics of protons produced in non-CCQE interactions because the 2p2h shape parameters are strangely moved to the physical boundary of 2.0 as shown in Fig. 7.6 with the constraint from the ND280.

In order to understand the deviations more clearly, more precise modeling of the proton kinematics in the neutrino event generator is needed because it is known that the current modeling of the proton kinematics is not perfect. For example, for the 1p1h interaction, the differential cross sections on nucleus are given as a function of muon kinematics (p_μ, θ_μ) but not proton kinematics (p_p, θ_p) and the proton kinematics are approximately estimated. In NEUT, the kinematics of proton is approximately estimated by assuming neutrino interaction on a nucleon. For the 2p2h interaction, the kinematics of two nucleons are more simply simulated: in NEUT, half of energy transfers are given to each nucleons and direction of them are ejected isotropically in their rest frame. In addition, the ways of these approximations are different among the different event generators as well as the final state interactions of the proton. It is important to improve the approximation of the proton kinematics and choose the best model with several measurements in future.

Other neutrino interaction analyses related to the number of emitted protons

The same tendencies as this analysis, over estimation of the number of protons emitted outside the nucleus, are observed by other analyses. Figure 7.23 shows the measured CC0π cross sections on plastic target as a function of the number of protons by the ND280 [124] in 2017 and it also overpredicts the number of emitted protons. Figure 7.24 shows the measured CC inclusive cross sections with argon target as a function of the number of charged particles by MicroBoone [125] in 2018. Although not only protons but also pions are included, the MC overpredicts the number of emitted charged particles.

Effect on oscillation analysis

The observed consistency of data and MC prediction with the constraint from the ND280 with the first group ensure the correctness of the framework of the T2K oscillation analysis. The observed deviations in the second group and other analysis may affect the oscillation analysis

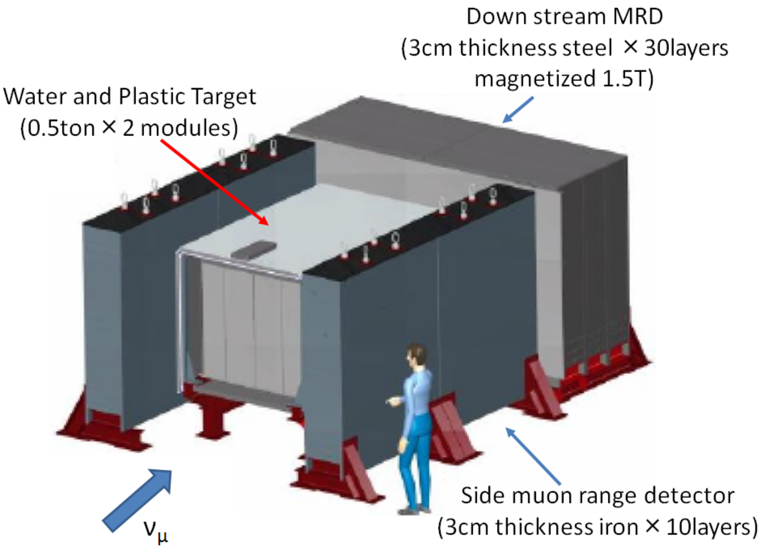

Figure 7.22: View of the WAGASCI experiment with the side muon range detector.

Table 7.14: List of the variation of the number of events with $+1\sigma$ varied parameters of the neutrino interactions. Only the dominant parameters are shown.

Samples	2p2h norm	C_A^5	M_A^{Res}	Iso$\frac{1}{2}$bg	2p2h shape	RPA parameters
WM 1 track μ stop	+8.5%	+4.3%	+2.7%	+3.1%	-3.2%	+6.2%
WM 1 track μ escape	+9.5%	+2.7%	+2.1%	+2.3%	-6.1%	+5.4%
WM 1 track μ penetrate	+9.7%	+2.9%	+1.5%	+1.9%	-5.4%	+7.1%
WM 2 track μ stop, p stop	+8.9%	+6.2%	+3.7%	+2.9%	+1.8%	+2.8%
WM 2 track μ stop, p escape	+7.1%	+5.3%	+4.3%	+3.1%	+2.3%	+3.6%
WM 2 track μ escape, p stop	+6.6%	+3.9%	+2.9%	+1.9%	-0.7%	+5.2%
WM 2 track μ escape, p escape	+5.3%	+3.6%	+3.6%	+1.5%	+1.0%	+5.7%
WM 2 track μ penetrate, p stop	+7.5%	+5.0%	+2.8%	+2.0%	+0.7%	+4.5%
WM 2 track μ penetrate, p escape	+2.0%	+4.8%	+3.7%	+2.3%	+2.2%	+4.2%
WM Multi track	+3.2%	+5.4%	+5.5%	+2.2%	+0.8%	+0.4%
WM large angle	+3.8%	+4.5%	+4.9%	+2.0%	+0.5%	+4.9%
PM 1 track μ stop	+9.9%	+4.8%	+3.2%	+3.8%	-2.0%	+4.7%
PM 1 track μ escape	+9.6%	+3.7%	+3.2%	+3.0%	-4.2%	+4.5%
PM 1 track μ penetrate	+10.9%	+3.9%	+2.1%	+2.5%	-4.2%	+5.7%
PM 2 track μ stop, p stop	+9.9%	+6.6%	+3.3%	+2.7%	+2.1%	+2.7%
PM 2 track μ stop, p escape	+11.6%	+6.2%	+4.7%	+2.7%	+3.9%	+2.4%
PM 2 track μ escape, p stop	+7.6%	+4.5%	+3.5%	+1.6%	-0.4%	+4.8%
PM 2 track μ escape, p escape	+7.3%	+4.2%	+4.2%	+1.5%	+2.1%	+4.8%
PM 2 track μ penetrate, p stop	+9.4%	+6.1%	+3.5%	+2.0%	+0.1%	+3.7%
PM 2 track μ penetrate, p escape	+10.7%	+5.1%	+4.1%	+1.9%	+3.2%	+3.6%
PM Multi track	+2.4%	+4.7%	+5.3%	+1.4%	+0.6%	+0.2%

because they may indicate un-modeled neutrino-nucleus interactions which change the relation between the true neutrino energy and reconstructed neutrino energy. For the conclusion, we should wait the improvement of the modeling in the long term perspective. At present, to reduce the dependency of the neutrino-nucleus interaction modeling for the neutrino oscillation analysis as much as possible, following efforts are performed by the T2K as described in Section 8:

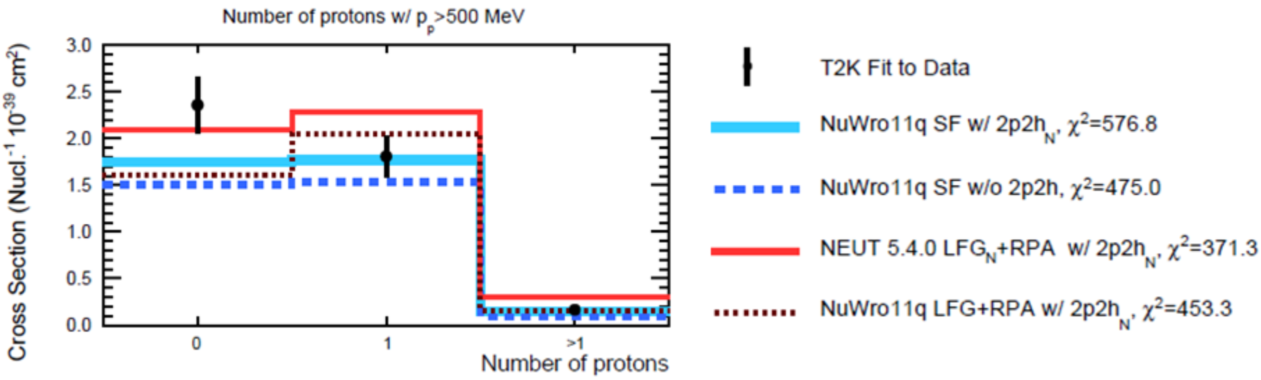

Figure 7.23: Measured CC0π cross section on plastic as a function of the number of protons by the ND280 [124].

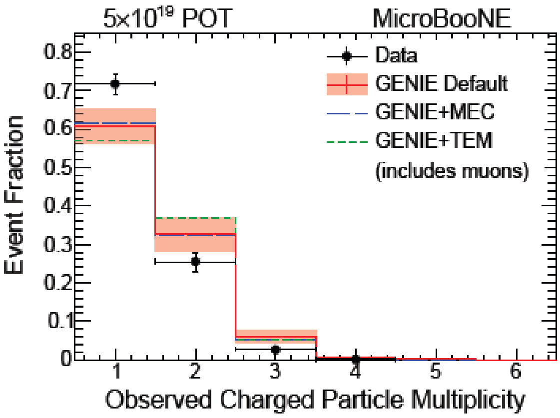

Figure 7.24: Measured CC inclusive interaction rate on argon as a function of the number of charged particles by MicroBooNE [125].

- Information of protons are not used for the oscillation analysis.
- 100% normalization and shape uncertainties are assumed for 2p2h interactions which is the largest error sources to change the relation of true neutrino energy and reconstructed neutrino energy.
- Bias of the analyses are checked for almost all of the existent alternative models of the neutrino interaction as described in Sec. 8.4.2.

By these efforts, uncertainties of the existing neutrino interaction models are covered by T2K oscillation analysis at present.

For further reduction of the systematic uncertainty of the oscillation analysis, fundamental improvement of the modeling of the neutrino-nucleus interaction is needed based on the measurement. This analysis gives important informations for an improvement of the modeling with an innovative way of the validation of the constraint from the ND280 based on real data and new information of the large angle muons and protons.

Chapter 8

Neutrino oscillation analysis

8.1 Analysis overview

In this section, two analyses of the neutrino oscillations are performed. The first analysis is a measurement of the oscillation parameters of the PMNS matrix: θ_{23}, θ_{13}, Δm^2_{32}, δ_{CP} and mass hierarchy. In order to extract the oscillation parameters, the four types of the oscillations, $\nu_\mu \to \nu_\mu$, $\nu_\mu \to \nu_e$, $\overline{\nu}_\mu \to \overline{\nu}_\mu$ and $\overline{\nu}_\mu \to \overline{\nu}_e$, are jointly fitted. For the fitting, information of momentum and angle of leptons are used. These four oscillations are signal of this analysis and they are measured by the Super-Kamiokande in each event sample separately. Background events of this analysis are any other oscillations contaminated in the measured oscillation sample and intrinsic ν_e and $\overline{\nu}_e$, which is initially contaminated in the ν_μ beam due to decays of Kaon.

The second analysis is a search for $\overline{\nu}_\mu \to \overline{\nu}_e$ appearance which is predicted by the standard oscillation framework but not observed so far. Two hypotheses are tested in this analysis. One hypothesis assumes a probability of the $\overline{\nu}_\mu \to \overline{\nu}_e$ is zero (null $\overline{\nu}_\mu \to \overline{\nu}_e$ appearance hypothesis) and the other hypothesis assumes the probability is the same as the prediction from the PMNS matrix parameters. This analysis provides a p-value of each hypothesis with two ways. The first way is to use only the number of $\overline{\nu}_\mu \to \overline{\nu}_e$ like events. The second way is to use not only the number of $\overline{\nu}_\mu \to \overline{\nu}_e$ like events but also p-θ information of the positrons. Signal of this analysis is the $\overline{\nu}_\mu \to \overline{\nu}_e$ appearance. Background events are any other oscillations contaminated in the $\overline{\nu}_e$ like samples and the intrinsic ν_e and $\overline{\nu}_e$. In order to constrain the uncertainty of the oscillation parameters of the PMNS matrix, other oscillations, $\nu_\mu \to \nu_\mu$, $\nu_\mu \to \nu_e$ and $\overline{\nu}_\mu \to \overline{\nu}_\mu$ are jointly fitted.

In these two analyses, to constrain the uncertainty of the neutrino flux and interactions, the constraint from the ND280 is used. The common event samples at the near and far detectors are used for the two analyses. Data taken by the end of December 2017 is used as shown in Table 8.1. It is about 1.5 times larger than the last analysis performed by T2K in 2016. In addition, improvement of ring reconstruction algorithm at SK increases the statistics of RHC ν_e sample, because the size of the fiducial volume is increased about 1.3 times. Totally, the statistics is increased about twice compared with the last analysis. These improvements give us better sensitivity of the oscillation parameters and $\overline{\nu}_e$ appearance search.

8.2 Near detector measurement

T2K near detector, ND280, is used to constrain the uncertainty of neutrino flux and interactions. The analysis method is the same as described in Sec. 7.2. Only the difference from the Sec. 7.2 is that the flux parameters at the far detector is constrained instead of that at the on-axis detectors, as shown in Fig. 8.1 and Table 8.3. The flux parameters before and after the ND280

Table 8.1: Comparison between this analysis and the last analysis performed in 2016. Oscillation parameters defined in Table 8.2 are used to calculate the number of events. BG is defined as any ν_e like events with RHC other than the signal mode.

	This analysis	Analysis in 2016
Run period	2008- Dec.2017	2008-2016
POT with FHC	1.494×10^{21}	0.700×10^{21}
POT with RHC	1.124×10^{21}	0.747×10^{21}
SK ring reconstruction algorithm	fiTQun	APfit
Number of expected RHC ν_e events (BG)	11.76(6.48)	6.01(3.22)

Table 8.2: Set of oscillation parameters used for Monte Carlo simulation. These are similar to the best fit parameters of the T2K analysis in 2016. Values of θ_{12}, Δm^2_{21} and θ_{13} are constrained from the solar and reactor neutrino experiments.

Parameter	Value
$\sin^2\theta_{12}$	0.304
$\sin^2 2\theta_{13}$	0.0857
$\sin^2\theta_{23}$	0.528
Δm^2_{21}	7.53×10^{-5} eV^2
Δm^2_{32}	2.509×10^{-3} eV^2
δ_{CP}	-1.601
Mass hierarchy	Normal

fitting is shown in Fig. 8.2. The neutrino event predictions at the far detector with the constraint from the ND280 are shown in Table 8.4.

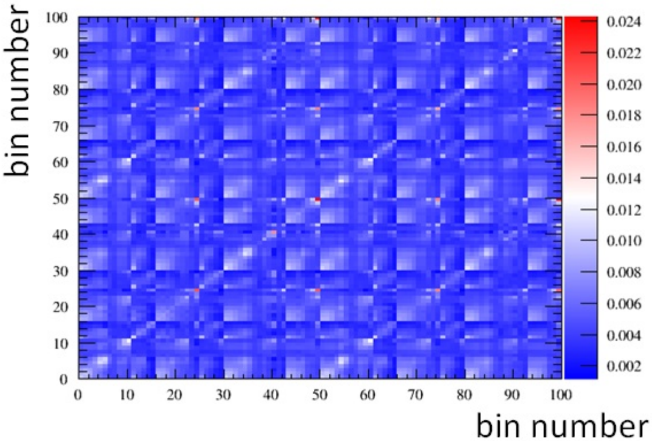

Figure 8.1: Covariance matrix of flux uncertainty in each neutrino energy bin. Table 8.3 shows a definition of the bin number.

Table 8.3: Energy binning for flux uncertainty

Bin number	Detector	Polarity	Flavor	Energy binning (GeV)
0-10	ND280	positive	ν_μ	0.0, 0.4, 0.5, 0.6, 0.7, 1.0, 1.5, 2.5, 3.5, 5.0, 7.0, 30.0
11-15	ND280	positive	$\overline{\nu}_\mu$	0.0, 0.7, 1.0, 1.5, 2.5, 30.0
16-22	ND280	positive	ν_e	0.0, 0.5, 0.7, 0.8, 1.5, 2.5, 4.0, 30.0
23-24	ND280	positive	$\overline{\nu}_e$	0.0, 2.5, 30.0
25-29	ND280	negative	ν_μ	0.0, 0.7, 1.0, 1.5, 2.5, 30.0
30-40	ND280	negative	$\overline{\nu}_\mu$	0.0, 0.4, 0.5, 0.6, 0.7, 1.0, 1.5, 2.5, 3.5, 5.0, 7.0, 30.0
41-42	ND280	negative	ν_e	0.0, 2.5, 30.0
43-49	ND280	negative	$\overline{\nu}_e$	0.0, 0.5, 0.7, 0.8, 1.5, 2.5, 4.0, 30.0
50-60	SK	positive	ν_μ	0.0, 0.4, 0.5, 0.6, 0.7, 1.0, 1.5, 2.5, 3.5, 5.0, 7.0, 30.0
61-65	SK	positive	$\overline{\nu}_\mu$	0.0, 0.7, 1.0, 1.5, 2.5, 30.0
66-72	SK	positive	ν_e	0.0, 0.5, 0.7, 0.8, 1.5, 2.5, 4.0, 30.0
73-74	SK	positive	$\overline{\nu}_e$	0.0, 2.5, 30.0
75-79	SK	negative	ν_μ	0.0, 0.7, 1.0, 1.5, 2.5, 30.0
80-90	SK	negative	$\overline{\nu}_\mu$	0.0, 0.4, 0.5, 0.6, 0.7, 1.0, 1.5, 2.5, 3.5, 5.0, 7.0, 30.0
91-92	SK	negative	ν_e	0.0, 2.5, 30.0
93-99	SK	negative	$\overline{\nu}_e$	0.0, 0.5, 0.7, 0.8, 1.5, 2.5, 4.0, 30.0

Table 8.4: Fraction and uncertainties of event rate of muon neutrino interactions with H_2O target at the far detector with constraint by the ND280. No neutrino oscillation is assumed at the far detector.

Interaction mode	Fraction	Uncertainty		
		flux × cross section	flux	cross section
CC+NC	100%	3.4%	3.8%	3.8%
CC	71.1%	2.4%	3.8%	3.5%
CCQE	33.3%	4.1%	3.9%	4.5%
2p2h	8.2%	20.8%	3.9%	22.1%
CC1pi	15.7%	4.9%	3.8%	4.3%
CCcoh	1.0%	25.6%	3.8%	25.8%
CCDIS	11.1%	4.8%	3.8%	4.9%
CCother	0.8%	6.2%	3.8%	7.0%
NC	29.9%	10.1%	3.8%	9.8%

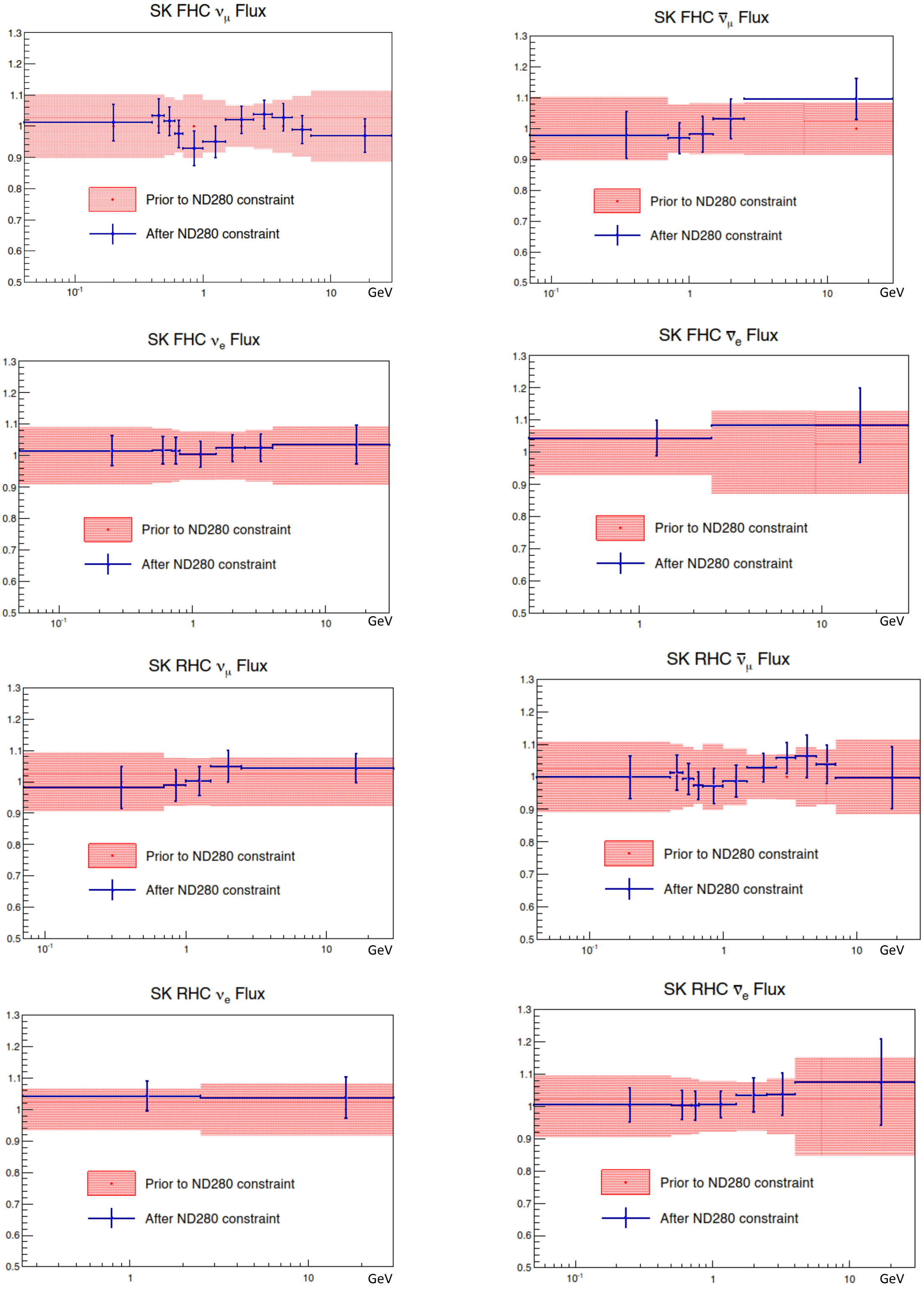

Figure 8.2: Flux parameters with and without the constraint from the ND280.

8.3 Far detector measurement

The T2K far detector measures the neutrinos after the neutrino oscillation. With the FHC, $\nu_\mu \to \nu_\mu$ and $\nu_\mu \to \nu_e$ are measured. With the RHC, $\overline{\nu}_\mu \to \overline{\nu}_\mu$ and $\overline{\nu}_\mu \to \overline{\nu}_e$ are measured. ν_μ and $\overline{\nu}_\mu$ (ν_e and $\overline{\nu}_e$) events are selected with a muon (electron) like Cherenkov ring. For all of the four oscillations, the CCQE like interaction is selected with a single ring of the corresponding lepton to reconstruct neutrino energy by using Eq. 3.2. The four samples are called FHC 1R(1ring)ν_μ, FHC 1Rν_e, RHC 1Rν_μ and RHC 1Rν_e. In addition, only for the $\nu_\mu \to \nu_e$ oscillation, the CC1π like interaction is selected with a single ring of the electron and a decay electron in order to increase statistics. The decay electron is emitted from a muon produced by decay of a pion. The neutrino energy is reconstructed by Eq. 3.3. The sample is called FHC $\nu_e 1\pi$. The CC1π interaction is not used for the $\overline{\nu}_\mu \to \overline{\nu}_e$ due to background events from the $\nu_\mu \to \nu_e$.

In this analysis, the Cherenkov ring reconstruction algorithm is improved since the last analysis and the size of the fiducial volume is enlarged. The new algorithm named fiTQun [126] is briefly described as follows.

8.3.1 Ring reconstruction algorithm, fiTQun

fiTQun is an event reconstruction algorithm for the SK. Each event at SK is a set of charges and timing recorded for every PMT hit. Kinematics of particles is reconstructed based on a likelihood function, which is a product of the probability density function (PDF) of the charge and timing. Since the PDFs vary as a function of the parameters that define the kinematics of the particles in each event, the likelihood is also a function of the particle parameters. The final reconstructed values of the track parameters are those that minimize the value of the likelihood function. The likelihood is written as follows:

$$L(x) = \prod_{j}^{unhit} P_j(unhit|x) \prod_{i}^{hit} \{1 - P_i(unhit|x)\} f_q(q_i|x) f_t(t_i|x) \tag{8.1}$$

where the first index j runs over all PMTs which do not register a hit. For each PMT, $P_j(unhit|x)$ is multiplied which is the probability of the j-th PMT not registering a hit given track parameter x. The second index i runs over all PMTs which register a hit. For the each PMT, the charge likelihood and the time likelihood as well as the hit probability is multiplied, where q_i and t_i represent charge and timing observed by the i-th PMT respectively. The charge likelihood $f_q(q_i|x)$ is a probability density function of observing charge q_i at the i-th PMT given track parameters x. The time likelihood $f_t(t_i|x)$ is a probability density function for a hit being created at time t_i, given x. The following track parameters are optimized: vertex position, time, zenith angle and azimuth angle of direction and momentum. The number of tracks and particle identification are also optimized by comparing the best fit likelihood with several hypotheses.

The last analysis performed in 2016 used APfit algorithm, which is a step-by-step fitter. The track parameters similar to the case of the fiTQun are eventually fitted. Since the fiTQun has better track reconstruction performance than the APfit even near the wall of the inner tank, fiducial volume of SK is about 1.3 times enlarged by the fiTQun. With the APfit, the size of the fiducial volume is determined by "wall">200 cm, where "wall" is the minimum distance between the reconstructed vertex and the inner detector wall as shown in Fig. 8.3. With the fiTQun, "wall">80 cm and "towall">170 cm for ν_e-like samples ("wall">50 cm and "towall">250 cm for ν_μ-like samples) are required, where "towall" is the distance between the vertex and the inner detector wall measured by traveling along the direction of the particle track. They are optimized to maximize sensitivities of θ_{23} and δ_{CP} with the consideration of the backgrounds and detector systematics which is evaluated with data-MC difference of atmospheric neutrino sample and cosmic ray sample.

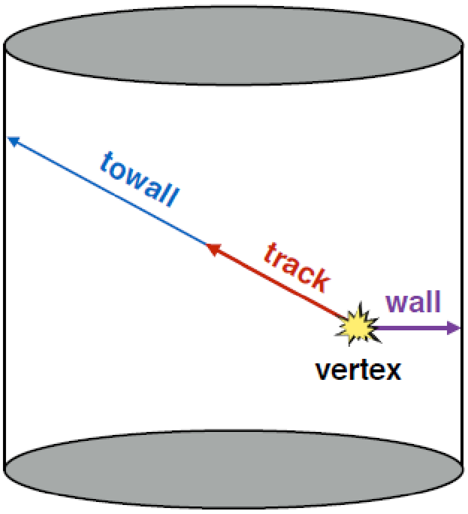

Figure 8.3: Definition of the “wall” and “towall” variables.

8.3.2 Event selection

In order to select electron neutrino and anti electron neutrino like samples at the SK (FHC 1Rν_e, RHC 1Rν_e and FHC $\nu_e 1\pi$), event selections are applied as follows:

1. Event is fully-contained in SK inner detector and vertex is inside the fiducial volume
2. Number of rings is one
3. The ring is identified as electron-like
4. Visible energy is greater than 100 MeV
5. Reconstructed neutrino energy is less than 1250 MeV
6. The number of decay electrons is zero (one) for FHC 1R ν_e and RHC 1Rν_e samples (FHC $\nu_e 1\pi$ sample)
7. π^0 rejection cut

In order to select muon neutrino and anti neutrino like samples (FHC ν_μ and RHC ν_μ), event selections are applied as follows:

1. Event is fully-contained in SK inner detector and vertex is inside the fiducial volume
2. Number of rings is one
3. The ring is identified as muon-like
4. Reconstructed neutrino energy is greater than 200 MeV
5. The number of decay electrons is less than or equal to one

Table 8.5 shows the number of expected event for each sample with oscillation parameters listed in Table 8.2. Figure 8.4 shows spectrum of the selected neutrino events and their prediction by the MC simulation with the oscillation parameters listed in Table 8.2. Figures 8.5 and 8.6 show that with various oscillation parameters used for MC simulation.

Table 8.5: The number of observed events and MC expectation with the oscillation parameters listed in Table 8.2, constraint from the ND280, 1.494×10^{21} POT with FHC and 1.124×10^{21} POT with RHC.

Event Type	Data	MC						
		$\nu_\mu \to \nu_\mu$	$\nu_e \to \nu_e$	$\bar{\nu_\mu} \to \bar{\nu_\mu}$	$\bar{\nu_e} \to \bar{\nu_e}$	$\nu_\mu \to \nu_e$	$\bar{\nu_\mu} \to \bar{\nu_e}$	Total
FHC 1Rν_μ	243	252.140	0.200	16.030	0.021	0.073	0.000	268.465
FHC 1Rν_e	75	3.904	9.135	0.202	0.396	59.815	0.374	73.825
FHC $\nu_e 1\pi$	15	0.472	0.955	0.024	0.011	5.455	0.008	6.925
RHC 1Rν_μ	102	37.803	0.053	57.606	0.035	0.003	0.003	95.503
RHC 1Rν_e	9	0.557	1.178	0.944	1.696	2.100	5.290	11.765

8.3.3 Systematic uncertainties

Systematic uncertainties of the neutrino flux, interaction and SK detector response are evaluated for each sample and p-θ binning for ν_e samples (reconstructed energy binning for ν_μ samples). The uncertainties of the neutrino flux and interactions are estimated based on the constraint from the ND280.[1] The uncertainty of SK detector systematics is evaluated based on the following variables:

- Vertex position
- Number of decay electron
- Particle identification (e/μ,e/π^0,μ/π^0)
- Number of ring counting
- Momentum

In order to evaluate these uncertainties, difference of each variable between data and MC is estimated by cosmic ray and atmospheric neutrino samples. Through the MC simulation, the differences are translated to the 1σ uncertainty of the number of events in the T2K samples in each interaction mode and reconstructed neutrino energy bin defined in Table 8.6. Figure 8.7 shows a covariance matrix of the SK detector systematics. Table 8.7 shows the summary of the uncertainties of the total number of selected events in each sample. Uncertainty of the binding energy (E_b) is evaluated independently from the constraint from the ND280 as described in Sec. 8.4.2.

---

[1] Constraint of the secondary interaction of pions from the ND280 is not propagated to the far detector conservatively due to the difference of the target material between the ND280 and SK.

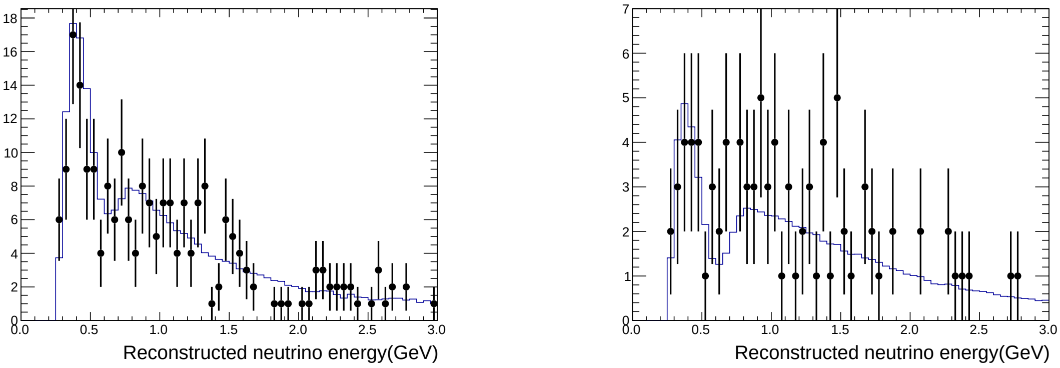

FHC 1Rν_μ RHC 1Rν_μ

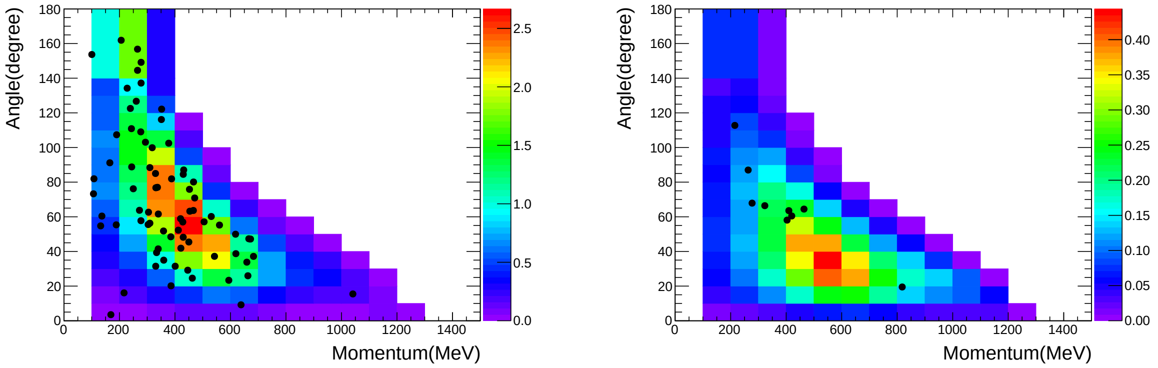

FHC 1Rν_e RHC 1Rν_e

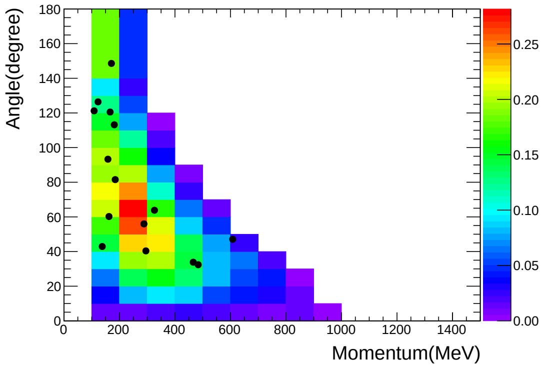

FHC 1R$\nu_e 1\pi$

Figure 8.4: Observed event (black dot) and MC prediction (histogram) of the 1Rν_e (upper left), 1R$\overline{\nu}_e$ (upper right), $\nu_e 1\pi$ (middle left), ν_μ(middle right) and $\overline{\nu}_\mu$ (bottom left) samples. The oscillation parameters used for the MC are listed in Table 8.2.

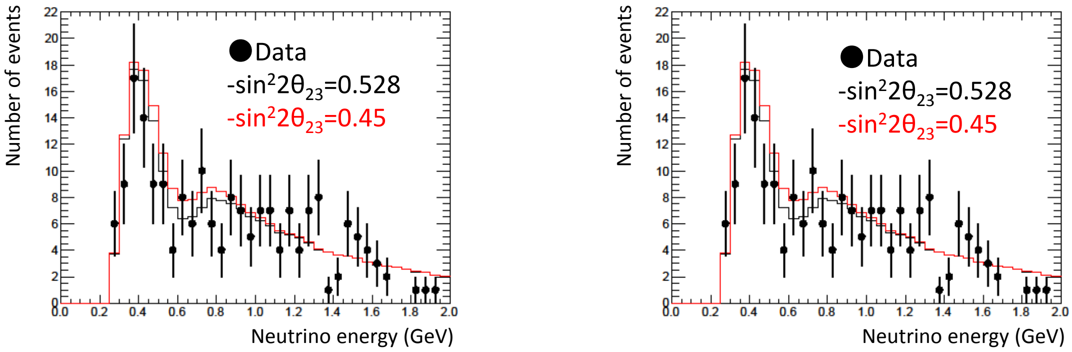

FHC 1Rν_μ, θ_{23} RHC 1Rν_μ, θ_{23}

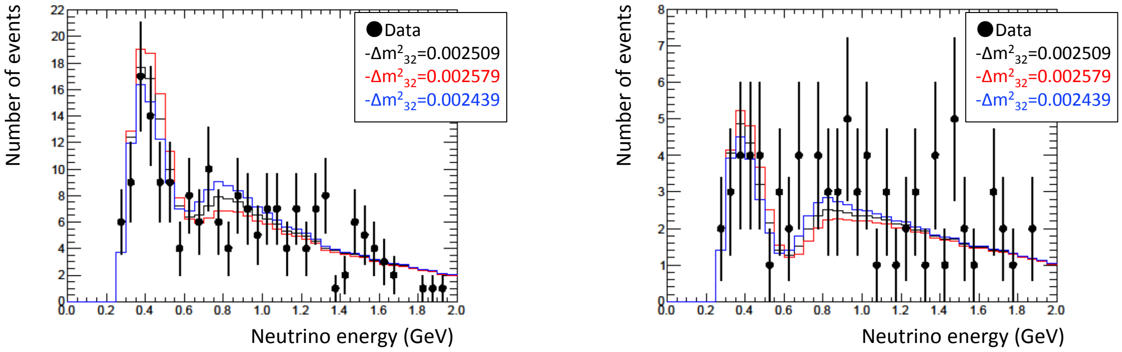

FHC 1Rν_μ, Δm^2_{32} RHC 1Rν_μ, Δm^2_{32}

Figure 8.5: Observed event (black dot) and various MC prediction (histogram) of the FHC 1Rν_μ (left) and RHC 1Rν_μ (right) samples as a function of reconstructed neutrino energy as a function of reconstructed neutrino energy. The oscillation parameters of θ_{23} (top) and Δm^2_{32} (bottom) are varied. Other oscillation parameters are fixed as listed in Table 8.2.

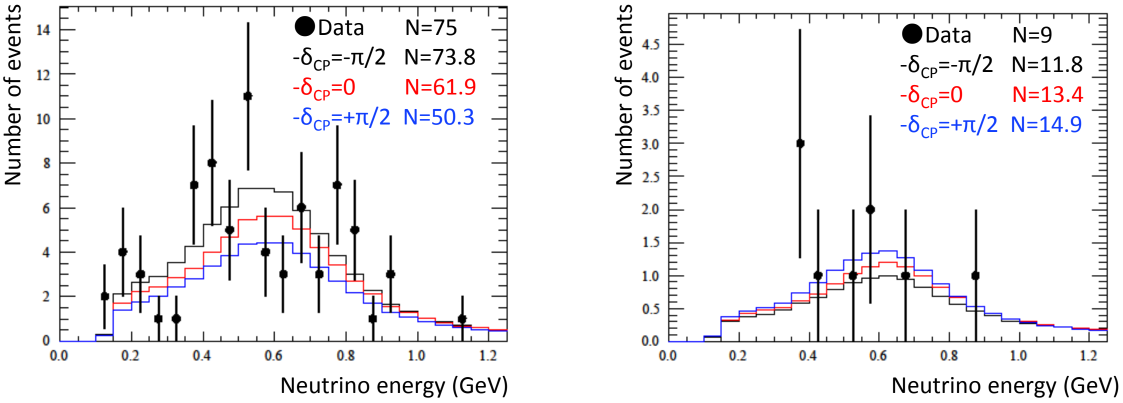

FHC 1Rν_e, δ_{CP} RHC 1Rν_e, δ_{CP}

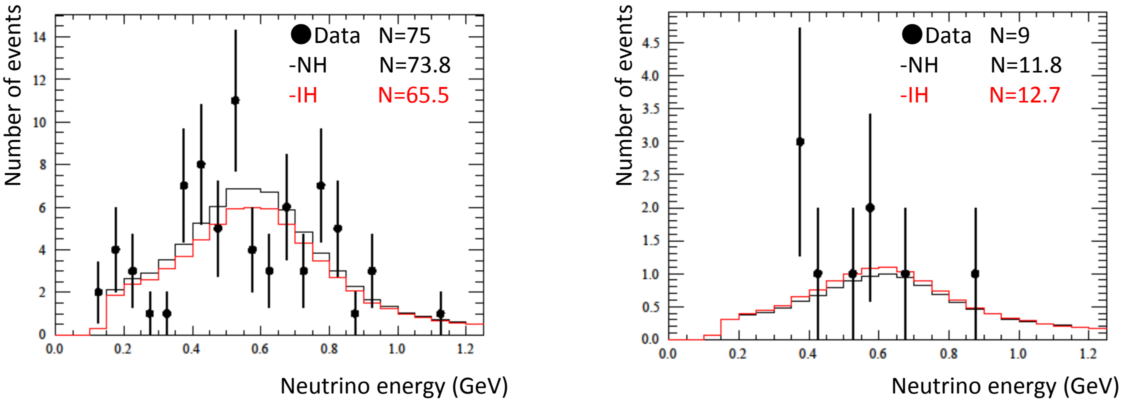

FHC 1Rν_e, MH RHC 1Rν_e, MH

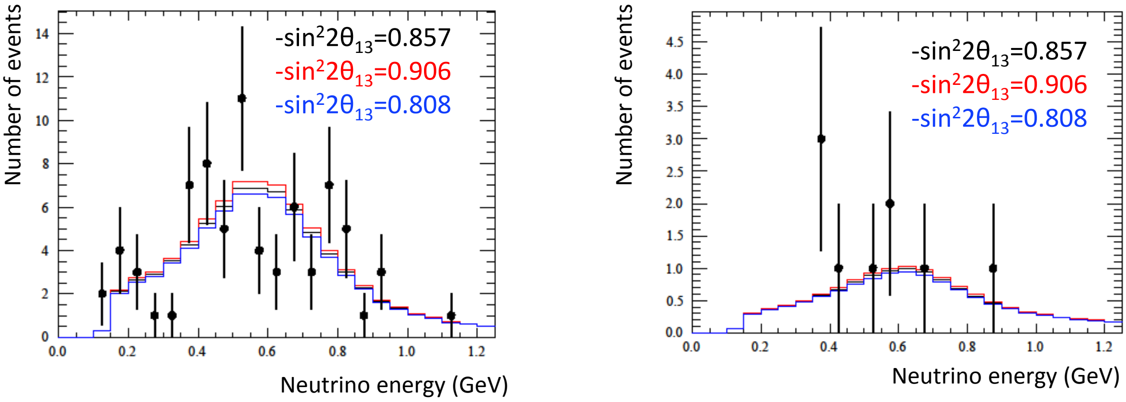

FHC 1Rν_e, θ_{13} RHC 1Rν_e, θ_{13}

Figure 8.6: Observed event (black dot) and various MC prediction (histogram) of the FHC 1Rν_e (left) and RHC 1Rν_e (right) samples as a function of reconstructed neutrino energy as a function of reconstructed neutrino energy. The oscillation parameters of δ_{CP} (top), mass hierarchy (middle) and θ_{13} (bottom) are varied. Other oscillation parameters are fixed as listed in Table 8.2. N is the total number of events.

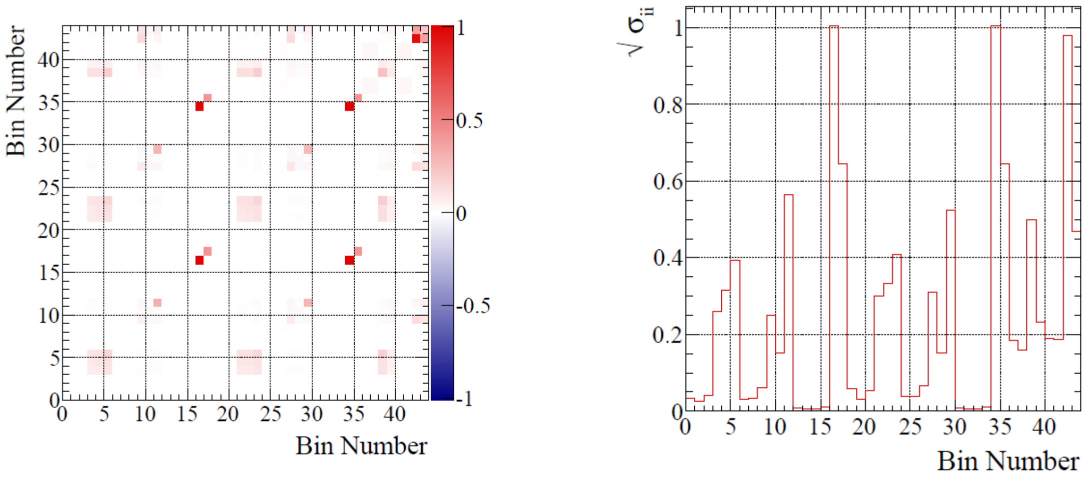

Figure 8.7: Covariance matrix of the SK detector systematics (left) and diagonal term (right). Definition of the binning is shown in Fig. 8.6

Table 8.6: Definition of the binning for SK detector systematics. Non-CCQE interaction is all CC interactions except for the CCQE interactions.

Sample	Component	E_{rec} range	Bin Number
FHC 1R ν_e	Osc.ν_e	0-350	1
		350-800	2
		800-1250	3
	ν_μ	0-350	4
		350-800	5
		800-1250	6
	Beam ν_e	0-350	7
		350-800	8
		800-1250	9
	NC	0-350	10
		350-800	11
		800-1250	12
FHC 1R ν_μ	ν_μ CCQE	0-400	13
		400-1100	14
		1100-30000	15
	ν_μ non-CCQE	0-30000	16
	ν_e	0-30000	17
	NC	0-30000	18
RHC 1R ν_e	Osc.ν_e	0-350	19
		350-800	20
		800-1250	21
	ν_μ	0-350	22
		350-800	23
		800-1250	24
	Beam ν_e	0-350	25
		350-800	26
		800-1250	27
	NC	0-350	28
		350-800	29
		800-1250	30
RHC 1R ν_μ	ν_μ CCQE	0-400	31
		400-1100	32
		1100-30000	33
	ν_μ non-CCQE	0-30000	34
	ν_e	0-30000	35
	NC	0-30000	36
FHC $\nu_e 1\pi$	Osc.ν_e	350-800	37
		800-1250	38
	ν_μ	350-800	39
		800-1250	40
	Beam ν_e	350-800	41
		800-1250	42
	NC	350-800	43
		800-1250	44

Table 8.7: Uncertainty of the number of event in each sample at the far detector.

Error source	FHC 1Rν_μ	RHC 1Rν_μ	FHC 1Rν_e	RHC 1Rν_e	FHC $\nu_e 1\pi$
Flux×interactions (constraint from ND280)	2.9%	2.7%	3.0%	2.9%	3.8%
Binding energy	3.3%	1.3%	7.3%	4.2%	2.9%
Flux×interactions (all)	4.2%	3.1%	7.8%	5.5%	5.4%
SK detector and secondary interactions	3.3%	2.9%	4.1%	4.4%	16.8%
Total	5.3%	4.2%	8.7%	7.1%	17.7%

8.4 Measurement of the oscillation parameters

The parameters of δ_{CP}, Δm^2_{32}, $\sin^2\theta_{23}$, $\sin^2\theta_{13}$ and mass hierarchy are extracted by fitting the all 5 samples at the SK: FHC 1Rν_μ,FHC 1Rν_e,FHC $\nu_e 1\pi$,RHC 1Rν_μ and RHC 1Rν_e. For the fitting, we use information of momentum and angle (p-θ) of leptons for the ν_e and $\overline{\nu}_e$ like samples and reconstructed neutrino energy ($E_{\rm rec}$) for the ν_μ and $\overline{\nu}_\mu$ like samples. Because the expected p-θ distributions are different between the signal and background, p-θ information gives an additional power to distinguish the signal and background events.

8.4.1 Analysis procedure

In order to extract the oscillation parameters, we introduce binned likelihood L_s in each event sample:

$$L_s(N^{\rm obs}, \boldsymbol{x}^{\rm obs}, \boldsymbol{o}, \boldsymbol{f}) \;=\; \exp\left[\sum_j \left\{\left(N^{\rm exp}_{s\,j} - N^{\rm obs}_{s\,j}\right) + N^{\rm obs}_{s\,j} \ln\left(N^{\rm obs}_{s\,j}/N^{\rm exp}_{s\,j}\right)\right\}\right] \tag{8.2}$$

where $N^{\rm obs}$ is the number of observed events in SK. $\boldsymbol{x}^{\rm obs}$ represents measurement variables (momentum p and angle θ for ν_e like samples, and reconstructed energy $E_{\rm rec}$ for ν_μ like samples). $\boldsymbol{f}$ is the systematic (neutrino flux, interaction and SK detector) parameters and $\boldsymbol{o}$ is the oscillation parameters including the mass hierarchy. s is the kind of samples at SK (s=1:FHC 1Rν_μ, s=2:RHC 1Rν_μ, s=3:FHC 1Rν_e, s=4:FHC ν_e 1π and s=5:RHC 1Rν_e). $N^{\rm obs}_{s\,j}$ is the number of events of s-th sample in each of the j-th bins of the measurement variables defined in Table 8.8. $N^{\rm exp}_{s\,j}$ is the predicted number of events of s-th samples in j-th bins, which depends on the $\boldsymbol{o}$ and $\boldsymbol{f}$.

When the best fit point is estimated, a set of the values of the parameters is searched to maximize the likelihood of the 5 samples:

$$(\boldsymbol{o}, \boldsymbol{f})_{\rm Bestfit} = argmax_{\boldsymbol{o},\boldsymbol{f}} \left[\left\{\prod_{s=1}^{5} L_s(N^{\rm obs}, x^{\rm obs}, \boldsymbol{o}, \boldsymbol{f})\right\} L_{\rm syst.}(\boldsymbol{f})\right] \tag{8.3}$$

where

$$L_{\rm syst.}(\boldsymbol{f}) = \exp\left\{-0.5 \sum_{l,m}^{\rm syst.} \Delta f_l \left(V_f^{-1}\right)_{lm} \Delta f_m\right\} \tag{8.4}$$

here, the systematic parameters have prior probability distributions (constraint from the ND280 and SK detector systematics) that are modeled as multivariate Gaussian with covariances of V_f. Δf_l is the deviation of the l-th systematic parameters away from their prior mean values. The best fit parameters are estimated with the normal hierarchy and inverted hierarchy separately.

When a 1D or 2D contour of the specific oscillation parameters(θ_{23}, θ_{13}, Δm^2_{32} and δ_{CP}) are measured, other oscillation parameters and all of the systematic parameters are marginalized as nuisance parameters. The mass hierarchy is fixed with the normal hierarchy or inverted hierarchy separately. For the marginalization, templates of the systematics and oscillation parameters are prepared based on their prior (Table 8.19, constraint from the ND280 and SK detector systematics). By using the M sets of the nuisance parameters, marginalized likelihood, $L_{\rm marg}$, is calculated as follows:

$$L_{\rm marg}(N^{\rm obs}, \boldsymbol{x}^{\rm obs}, \boldsymbol{o}_{\rm measured}) = \frac{1}{M}\sum_{i=1}^{M}\prod_{s=1}^{5} L_s(N^{\rm obs}, \boldsymbol{x}^{\rm obs}, \boldsymbol{o}_i, \boldsymbol{f}_i) \tag{8.5}$$

where $\boldsymbol{o}_i$ and $\boldsymbol{f}_i$ are i-th set of the nuisance parameters. $\boldsymbol{o}_{\text{measured}}$ is the measured oscillation parameter. Confidence level intervals are built by $\Delta\chi^2_{\text{SK jointfit}}$ defined as follows:

$$\Delta\chi^2_{\text{SK jointfit}} = -2 \times ln\left(\frac{L_{\text{marg}}(N^{\text{obs}}, \boldsymbol{x}^{\text{obs}}, \boldsymbol{o}_{\text{measured}})}{L^{\text{max}}_{\text{marg}}}\right) \tag{8.6}$$

where $L^{\text{max}}_{\text{marg}}$ is the maximum of the marginalized likelihood over the range of the $\boldsymbol{o}_{\text{measured}}$. The confidence intervals are defined as where the $\Delta\chi^2_{\text{SK jointfit}}$ is less than the standard threshold. The confidence intervals are estimated with the normal hierarchy and inverted hierarchy separately. Only for the 1D interval of δ_{CP}, Feldman-Cousins method[127] is used by taking account for an effect of physical boundary of $[-\pi, \pi]$.

When the hypothesis of normal hierarchy and inverted hierarchy are tested, their posterior probabilities are estimated with the marginalized likelihood:

$$P(\text{MH}|\text{N}^{\text{obs}}, \boldsymbol{x}^{\text{obs}}) = \frac{\text{L}_{\text{marg}}(\text{N}^{\text{obs}}, \boldsymbol{x}^{\text{obs}}, \text{MH})}{\sum_{\text{MH=NH,IH}} \text{L}_{\text{marg}}(\text{N}^{\text{obs}}, \boldsymbol{x}^{\text{obs}}, \text{MH})} \tag{8.7}$$

here MH is normal or inverted hierarchy and all of the oscillation parameters are marginalized. Bayes factor [128] of $\frac{P(\text{NH}|\text{N}^{\text{obs}}, \boldsymbol{x}^{\text{obs}})}{P(\text{IH}|\text{N}^{\text{obs}}, \boldsymbol{x}^{\text{obs}})}$ is used for the comparison of the mass hierarchies.

Table 8.8: Binning of the SK samples.

Sample	Variable	Binning
ν_e samples	Momentum (GeV/c)	15 bins in (0.0,1.5) with bin width of 100 MeV
	Angle (degree)	14 bins in (0,140) with bin width of 10 degrees 1 bin in 140, 180
ν_μ samples	Neutrino energy (GeV)	60 bins in (0.00, 3.00) with bin width of 50 MeV 13 bins in 3.0, 3.25, 3.5, 3.75, 4.0, 4.5, 5.0, 5.5, 6.0, 7.0, 8.0, 9.0, 10, 30

Table 8.9: Prior of the oscillation parameters for the analysis of the PMNS parameter measurement. Values of θ_{12} and Δm^2_{21} are constrained from the solar neutrino experiments.

Parameter	Prior	Variation range
$\sin^2\theta_{12}$	fixed	0.304
$\sin^2 2\theta_{13}$ with reactor constraint	Gaussian	0.0857 ± 0.0046
$\sin^2 2\theta_{13}$ without reactor constraint	uniform	0,0.4
$\sin^2\theta_{23}$	uniform	$[0.3, 0.7]$
Δm^2_{21}	fixed	7.53×10^{-5} eV^2
Δm^2_{32}	uniform	$[2, 3] \times 10^{-3}$ eV^2
δ_{CP}	uniform	$[-\pi, +\pi]$
Mass hierarchy	fixed	NH or IH

8.4.2 Effects of alternative cross section models

There are a few alternative neutrino interaction models which are not used in the oscillation analysis and not included as the systematic uncertainty of the neutrino interactions. We evaluate their possible effect on the oscillation analysis based on Monte Carlo simulation as described in this section. Because some of the alternative models indicate non-negligible effect on the oscillation analysis, additional systematic uncertainties are added.

In order to evaluate the effect of the alternative cross section models on the measurement of the oscillation parameters, oscillation analysis is performed for MC simulation samples produced with the alternative models. First, the MC simulation of the ND280 and SK are produced with the nominal and alternative cross section models. They are eventually fitted to get the contours of the oscillation parameters. The contours of the alternative models are compared with that of the nominal model to evaluate the effect of the alternative cross section model. In order to achieve the quantitative comparison, for each oscillation parameter and alternative model, we evaluate bias defined as follows:

$$\text{bias} = \frac{\mid (1\sigma \text{ middle})_{\text{alternative}} \; - \; (1\sigma \text{ middle})_{\text{nominal}} \mid}{(1\sigma \text{ interval})_{\text{nominal}}} \tag{8.8}$$

where 1σ middle (1σ interval) is the middle (size) of the 1σ interval of the 1D contour. The 1σ interval is estimated as total (sum of the statistical and systematic) uncertainty and only the systematic uncertainties separately.

In this analysis, more than ten alternative models are tested. Here, we pick up following models which have relatively large effects on the oscillation analysis:

- Nieves-NEUT 1p1h difference [60]
- Martini 2p2h model [67]
- Spectral function [61]
- Minoo pion model [77]
- ND280 data-driven sample
- Binding energy [58]

As an example, a case of the binding energy is described here in detail. The nominal interaction model assumes the binding energy of ^{16}O is 27 MeV (E_b=27 MeV). On the other hand, an alternative model assumes E_b=45 MeV based on the uncertainty of the binding energy suggested in a paper [58]. Figure 8.8 shows the reconstructed neutrino energy distribution of each sample at the far detector with the nominal and alternative models. The prediction with the constraint from the MC simulation of the ND280 with the alternative model is overwritten. There are discrepancies between the alternative model and the MC prediction especially in the ν_μ samples because the uncertainty of E_b is not included in the ND280 fitting due to technical issue.[2] Due to this discrepancy, there are differences of the Δm^2_{32} and $\sin^2\theta_{23}$ contours between the nominal (black solid line) and alternative models (black dashed line) as shown in Fig. 8.9. Table 8.10 shows the calculated bias. Non-negligible bias of the Δm^2_{32} is observed: 82% of the total uncertainty and 216% of the systematic uncertainty. In addition, shape of the contour of $\sin^2\theta_{23}$ is different around $\sin^2\theta_{23} = 0.5$.

In the same way, the biases with other alternative models are estimated as listed in Table 8.11. They are evaluated with two sets of the oscillation parameters listed in Tables 8.2 and 8.12. Similar to the binding energy, large biases of Δm^2_{32} are observed. The largest bias is coming from the binding energy.

---

[2] Reweighting of the MC is difficult because the muon phase space with small momentum is limited in the MC.

Table 8.10: Calculated bias with the alternative model of the binding energy.

	$\sin^2\theta_{23}$	Δm^2_{32}	δ_{CP}
1σ middle$_{\text{alternative}}$	0.525	2.519×10^{-3}	-1.58
1σ interval$_{\text{alternative}}$	0.052	6.0×10^{-5}	1.19
$1\sigma_{\text{stat}}$ interval$_{\text{alternative}}$	0.049	5.6×10^{-5}	1.16
$1\sigma_{\text{sys}}$ interval$_{\text{alternative}}$	0.017	2.1×10^{-5}	0.27
bias with 1σ	13%	82%	2%
bias with $1\sigma_{\text{sys}}$	38%	216%	11%

Table 8.11: Calculated bias with alternative interaction models.

		$\sin^2\theta_{23}$	Δm^2_{32}	δ_{CP}
Oscillation parameters listed in Table 8.2				
Nieves 1p1h	bias with 1σ	9%	36%	7%
	bias with $1\sigma_{\text{sys}}$	26%	98%	30%
Martini 2p2h	bias with 1σ	14%	12%	0.3%
	bias with $1\sigma_{\text{sys}}$	40%	33%	1%
Spectral function	bias with 1σ	3%	24%	0%
	bias with $1\sigma_{\text{sys}}$	10%	65%	0%
Minoo pion	bias with 1σ	6%	38%	1%
	bias with $1\sigma_{\text{sys}}$	18%	102%	4%
ND280 data-driven	bias with 1σ	13%	27%	5%
	bias with $1\sigma_{\text{sys}}$	38%	72%	22%
Binding energy	bias with 1σ	13%	82%	2%
	bias with $1\sigma_{\text{sys}}$	38%	216%	11%
Alternative oscillation parameters listed in Table 8.12				
Nieves 1p1h	bias with 1σ	21%	18%	–
	bias with $1\sigma_{\text{sys}}$	–	35%	–
Martini 2p2h	bias with 1σ	27%	11%	–
	bias with $1\sigma_{\text{sys}}$	–	20%	–
Spectral function	bias with 1σ	7%	21%	–
	bias with $1\sigma_{\text{sys}}$	–	40%	–
Minoo pion	bias with 1σ	13%	27%	–
	bias with $1\sigma_{\text{sys}}$	–	52%	–
ND280 data-driven	bias with 1σ	8%	21%	–
	bias with $1\sigma_{\text{sys}}$	–	39%	–
Binding energy	bias with 1σ	144%	31%	–
	bias with $1\sigma_{\text{sys}}$	–	59%	–

Additional uncertainty from binding energy

In order to reduce the bias, additional uncertainty from the binding energy is added into the far detector fitting based on the discrepancy of the spectrum at the far detector. The difference of the number of events in each bin[3] between the MC with alternative model of the binding energy and the MC prediction with the constraint from the ND280 with the alternative model

---

[3] In detail, the difference is taken in each interaction mode, flavor, true neutrino energy bin and reconstructed neutrino energy (p-θ for ν_e samples) bin.

Table 8.12: Alternative set of the oscillation parameters used for Monte Carlo simulation. These are the case of non-maximal θ_{23} and $\delta_{CP} = 0$. Values of θ_{12}, Δm^2_{21} and θ_{13} are constrained from the solar and reactor neutrino experiments.

Parameter	Value
$\sin^2\theta_{12}$	0.304
$\sin^2 2\theta_{13}$	0.0857
$\sin^2\theta_{23}$	0.45
Δm^2_{21}	7.53×10^{-5} eV^2
Δm^2_{32}	2.509×10^{-3} eV^2
δ_{CP}	0
Mass hierarchy	Normal

of the binding energy is taken as $+1\sigma$ uncertainty from the binding energy. In the same manner, -0.5σ uncertainty is calculated with another alternative model with E_b=18 MeV. By using these two points, the uncertainties between and outside $+1\sigma$ and -0.5σ are extrapolated as shown in Fig. 8.10. Prior of the binding energy uncertainty is assumed to be Gaussian with the width of 1σ with boundary of $(-1.5\sigma, 5\sigma)$ corresponding to (0, 90 MeV) of E_b. By adding this uncertainty, fitting at the far detector is redone for all of the alternative and nominal models as shown in Fig. 8.9 (red lines) and Table 8.13. The bias of Δm^2_{32} is reduced but a few of them are still more than 30% of the total uncertainty and 50% of the systematic uncertainty.

Smearing of Δm^2_{32}

In order to reduce the remained biases of Δm^2_{32}, contour of the Δm^2_{32} is directly smeared. Each bin of Δm^2_{32} is smeared with Gaussian with deviation of the 4.1×10^{-5} eV^2, which is a quadratic sum of all biases with the different alternative cross section models. Figure 8.11 shows the contours with and without the smearing. As shown in Table 8.13, the biases of the Δm^2_{32} are successfully reduced. They are less than 30% of the total uncertainty and 50% of the systematic uncertainty.

Table 8.13: Calculated biases with alternative interaction models with additional uncertainty from the binding energy and smearing of Δm^2_{32}.

		With E_b uncertainty			With E_b uncertainty and smearing		
		$\sin^2\theta_{23}$	Δm^2_{32}	δ_{CP}	$\sin^2\theta_{23}$	Δm^2_{32}	δ_{CP}
Oscillation parameters listed in Table 8.2							
Nieves 1p1h	bias with 1σ	6%	25%	6%	6%	22%	6%
	bias with $1\sigma_{\text{sys}}$	16%	42%	25%	16%	31%	25%
Martini 2p2h	bias with 1σ	11%	14%	0%	11%	12%	0%
	bias with $1\sigma_{\text{sys}}$	28%	24%	0%	28%	18%	0%
Spectral function	bias with 1σ	5%	19%	1%	5%	17%	1%
	bias with $1\sigma_{\text{sys}}$	11%	32%	2%	11%	24%	2%
Minoo pion	bias with 1σ	6%	29%	1%	6%	26%	1%
	bias with $1\sigma_{\text{sys}}$	15%	50%	3%	15%	37%	3%
ND280 data-driven	bias with 1σ	11%	22%	2%	11%	20%	2%
	bias with $1\sigma_{\text{sys}}$	30%	38%	9%	30%	28%	9%
Binding energy	bias with 1σ	9%	28%	2%	9%	23%	2%
	bias with $1\sigma_{\text{sys}}$	23%	47%	6%	21%	42%	6%
Alternative oscillation parameters listed in Table 8.12							
Nieves 1p1h	bias with 1σ	17%	18%	–	17%	17%	–
	bias with $1\sigma_{\text{sys}}$	–	35%	–	–	26%	–
Martini 2p2h	bias with 1σ	30%	11%	–	30%	10%	–
	bias with $1\sigma_{\text{sys}}$	–	20%	–	–	15%	–
Spectral function	bias with 1σ	11%	21%	–	11%	19%	–
	bias with $1\sigma_{\text{sys}}$	–	40%	–	–	30%	–
Minoo pion	bias with 1σ	6%	27%	–	6%	25%	–
	bias with $1\sigma_{\text{sys}}$	–	52%	–	–	39%	–
ND280 data–driven	bias with 1σ	8%	21%	–	8%	19%	–
	bias with $1\sigma_{\text{sys}}$	–	39%	–	–	29%	–
Binding energy	bias with 1σ	31%	31%	–	31%	30%	–
	bias with $1\sigma_{\text{sys}}$	–	59%	–	–	47%	–

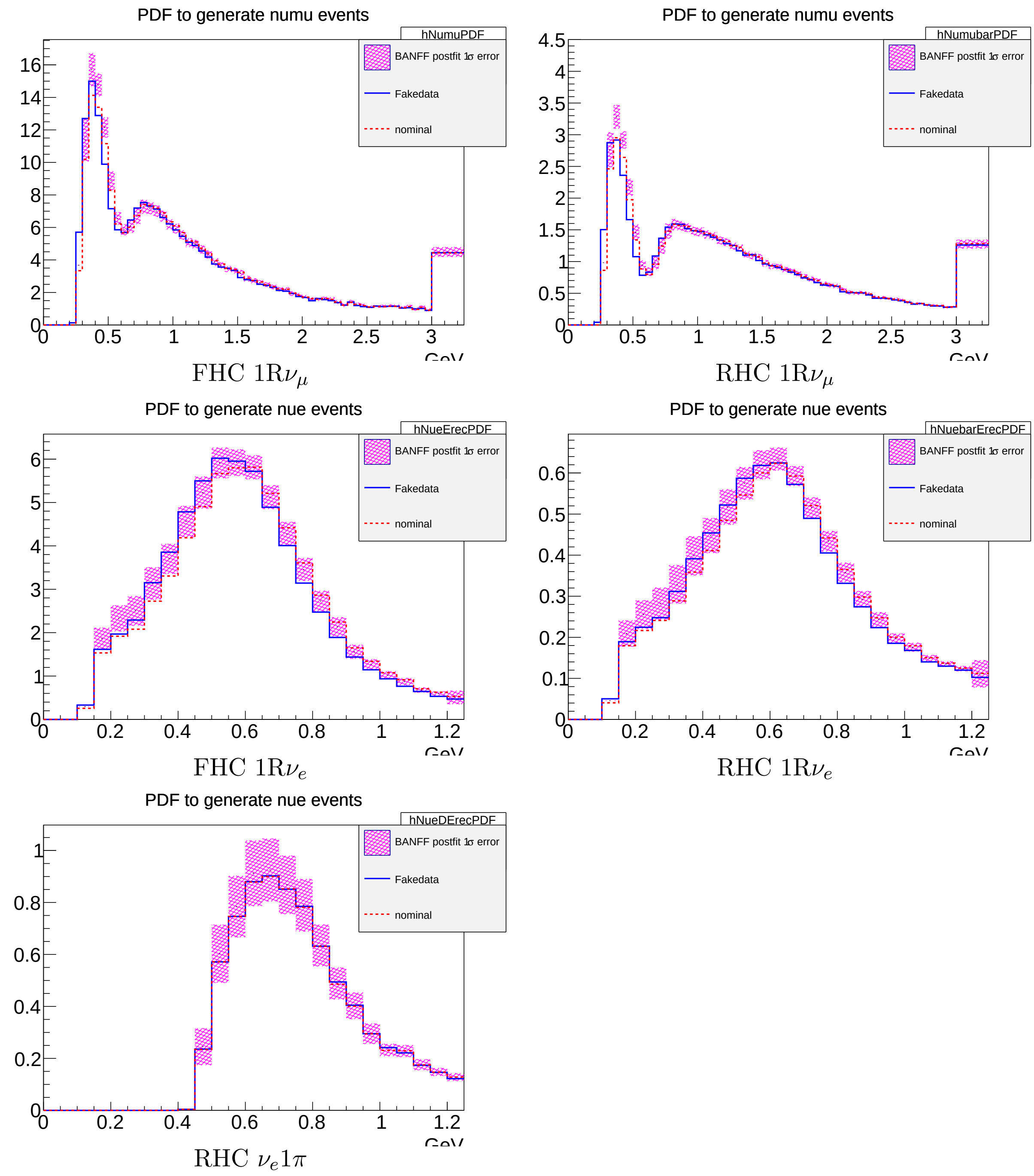

FHC 1Rν_μ RHC 1Rν_μ

FHC 1Rν_e RHC 1Rν_e

RHC $\nu_e 1\pi$

Figure 8.8: Reconstructed neutrino energy of nominal MC sample (red dashed), MC sample with $+1\sigma$ E_b (solid blue) and ND280 constraint with MC sample with $+1\sigma$ E_b (purple). Oscillation parameters listed in Table 8.2 are used.

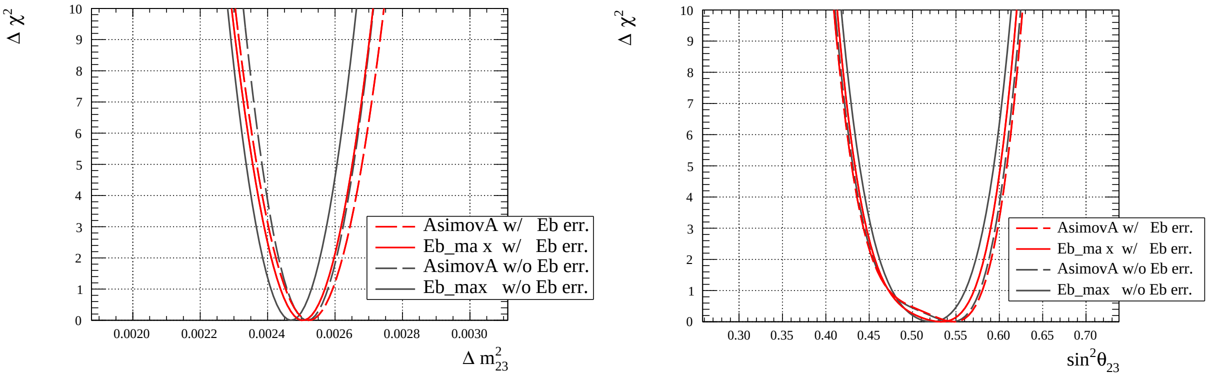

Δm^2_{32} $\sin^2\theta_{23}$

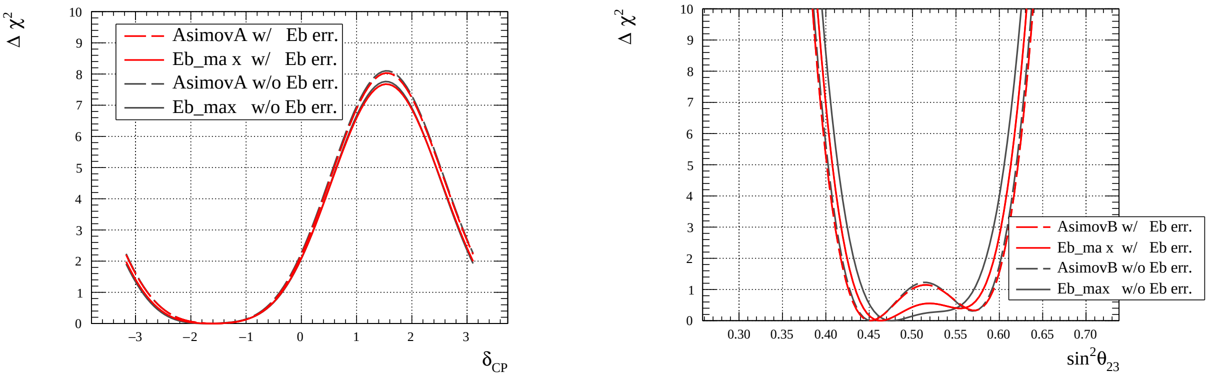

δ_{CP} $\sin^2\theta_{23}$ with alternative oscillation parameter

Figure 8.9: 1D contours of Δm^2_{32}, $\sin^2\theta_{23}$ and δ_{CP} with nominal (solid) and alternative modeling of the binding energy before (black) and after (red) adding the additional uncertainty of the binding energy (Eb). Oscillation parameters listed in Table 8.2 are used for the first three plots and that in Table 8.12 is used for the lower right plot.

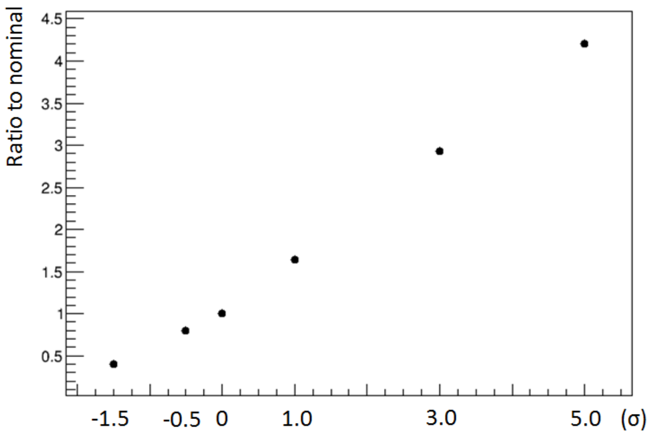

Figure 8.10: Spline for the new uncertainty from the binding energy. The nominal point of the y axis is taken by that at 0σ. The points at -1.5σ (3σ and 5σ) are linear extrapolation of the point of -0.5σ ($+1\sigma$). The points are fitted with three dimensional spline function to extrapolate between the points.

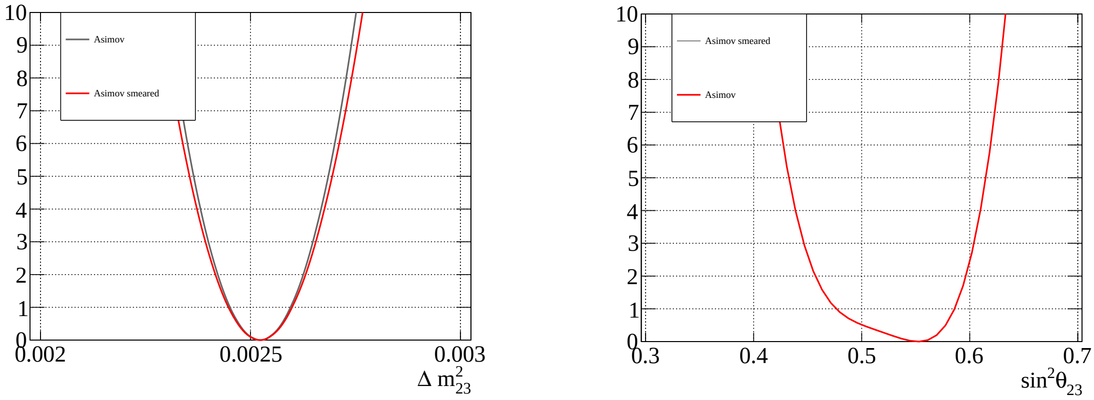

Δm^2_{32} $\sin^2\theta_{23}$

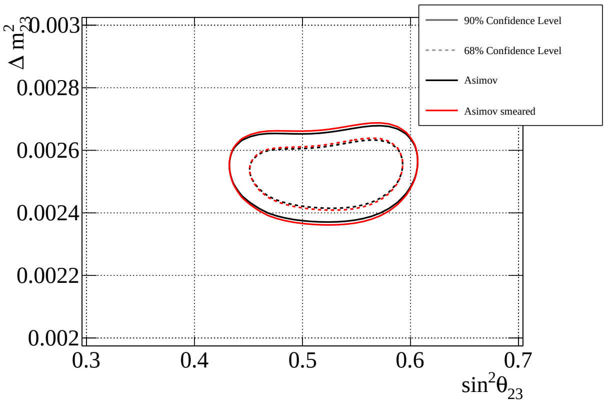

Δm^2_{32}-$\sin^2\theta_{23}$

Figure 8.11: Contours of Δm^2_{32} and $\sin^2\theta_{23}$ for nominal MC sample with the oscillation parameters listed in Table 8.2 with/without the smearing.

8.4.3 Expected sensitivity

Analysis is performed for MC simulation produced with the oscillation parameters listed in Table 8.2. Figure 8.12 (8.13) shows the contours of the oscillation parameters of θ_{23}, θ_{13}, Δm^2_{32} and δ_{CP} with (without) the constraint from the reactor. Table 8.14 shows the posterior probabilities with the normal and inverted hierarchies. For a comparison, expected sensitivities in the last T2K analysis performed in 2016 are shown in Fig. 8.14. Sensitivity study is also performed for other MC simulation with different set of the oscillation parameters for closure test, although they are not shown in this thesis.

Because the statistics of $\nu_\mu \to \nu_e$ and $\overline{\nu}_\mu \to \overline{\nu}_e$ are increased, the sensitivity of δ_{CP} is improved compared with the last analysis in 2016. With the constraint from the reactor, the $\delta_{CP} = 0$ is excluded with a significance of 2σ assuming the inverted hierarchy. This is the best sensitivity in the world. The sensitivity of θ_{13} without the reactor constraint is also improved since the last analysis. Although the accuracy is worse than the reactor experiment, this is the best sensitivity among the accelerator neutrino experiments. The size of the contours of Δm^2_{32} and θ_{23} are 10–20% smaller than that in the last analysis, mainly because the statistics of $\nu_\mu \to \nu_\mu$ is increased. These are the best sensitivity in the world. For the mass hierarchy, the normal hierarchy is preferred with Bayes factor of 2.7 corresponding to “substantial” evidence based on Jeffreys’s scale [129].

Table 8.14: Posterior probabilities of normal and inverted hierarchies with MC simulation with the reactor constraint.

Normal hierarchy	Inverted hierarchy	Ratio of Normal/Inverted
0.73	0.27	2.7

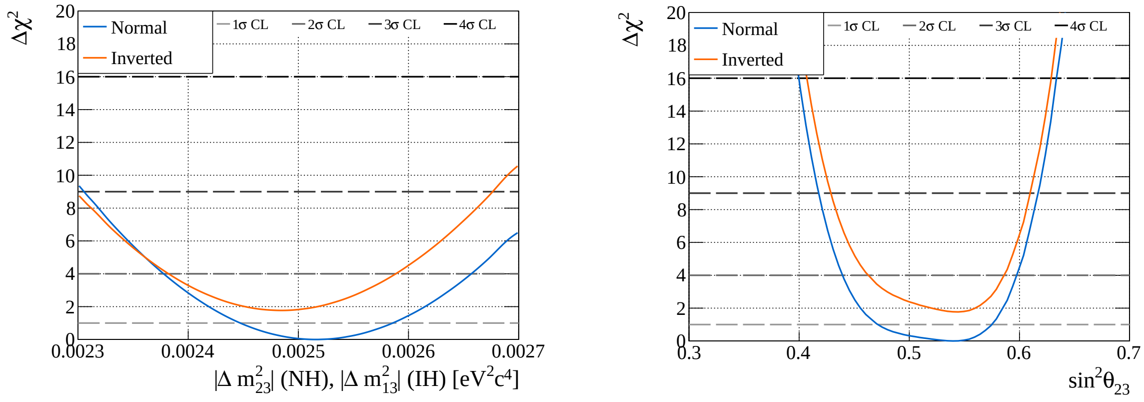

Δm^2_{32} $\sin^2\theta_{23}$

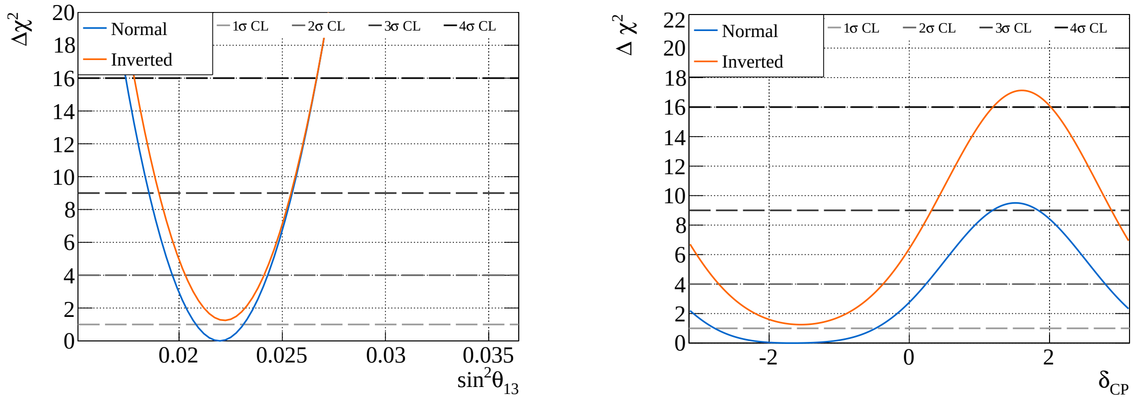

$\sin^2\theta_{13}$ δ_{CP}

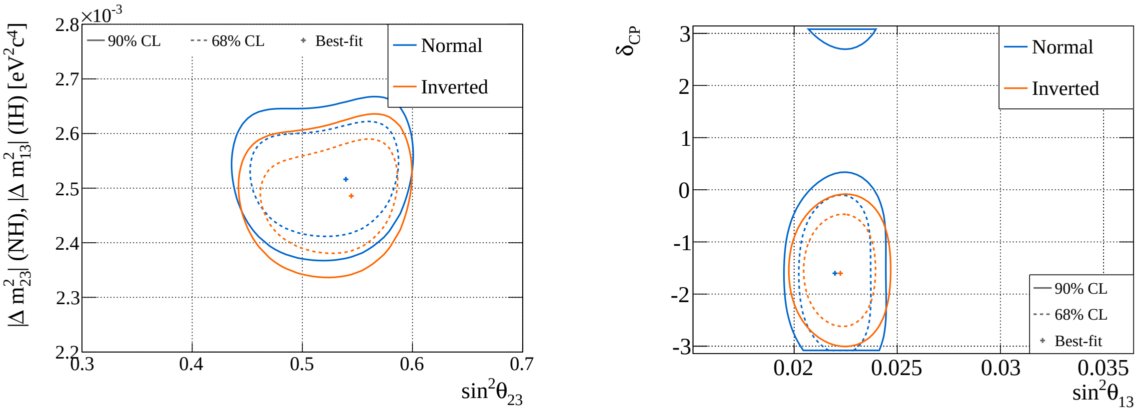

Δm^2_{32}-$\sin^2\theta_{23}$ δ_{CP}-$\sin^2\theta_{13}$

Figure 8.12: Expected contours of the oscillation parameters with MC simulation with reactor constraint.

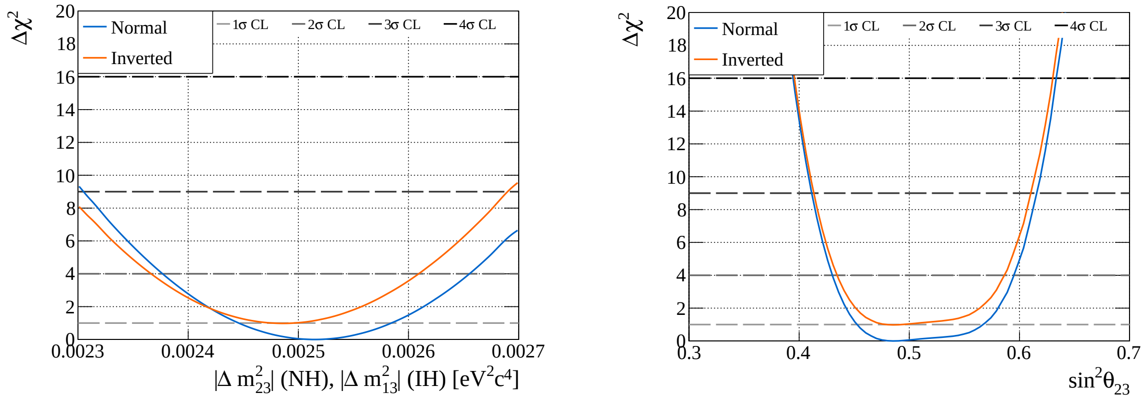

Δm^2_{32} $\sin^2\theta_{23}$

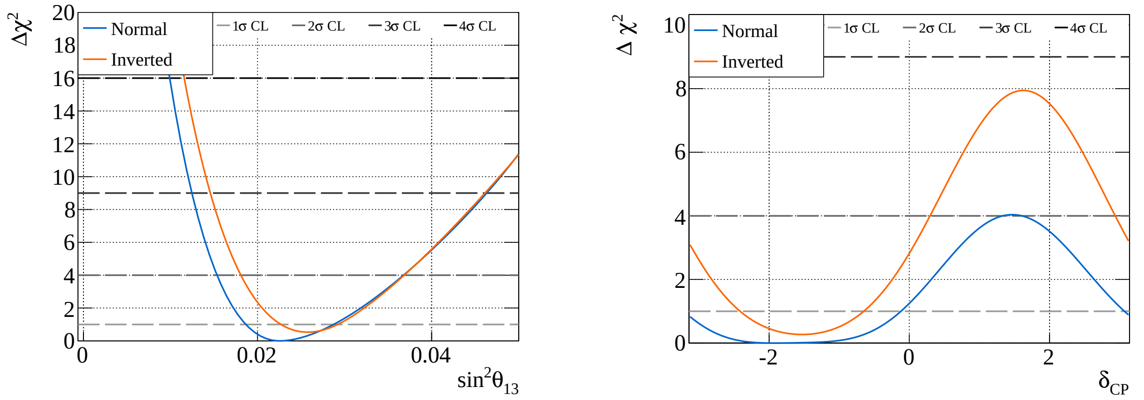

$\sin^2\theta_{13}$ δ_{CP}

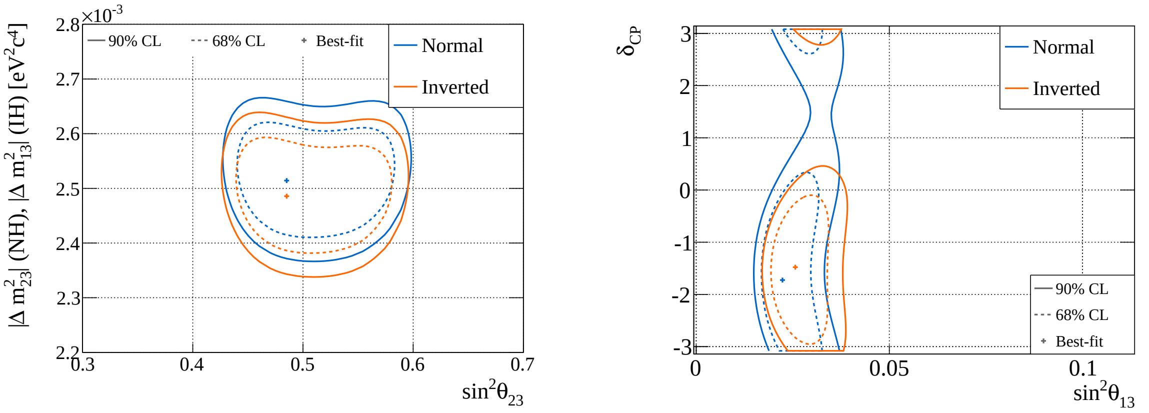

Δm^2_{32}-$\sin^2\theta_{23}$ δ_{CP}-$\sin^2\theta_{13}$

Figure 8.13: Expected contours of the oscillation parameters with MC simulation without reactor constraint.

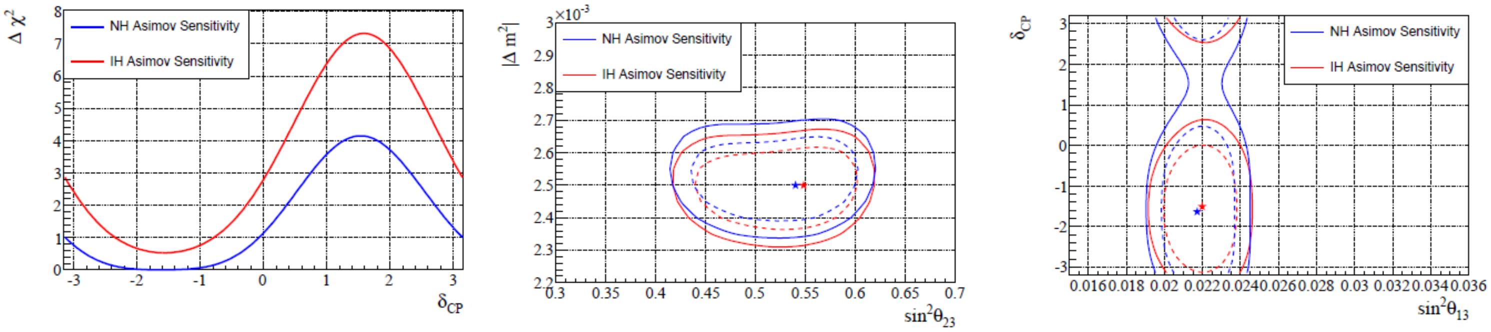

δ_{CP} Δm^2_{32}-$\sin^2\theta_{23}$ δ_{CP}-$\sin^2\theta_{13}$

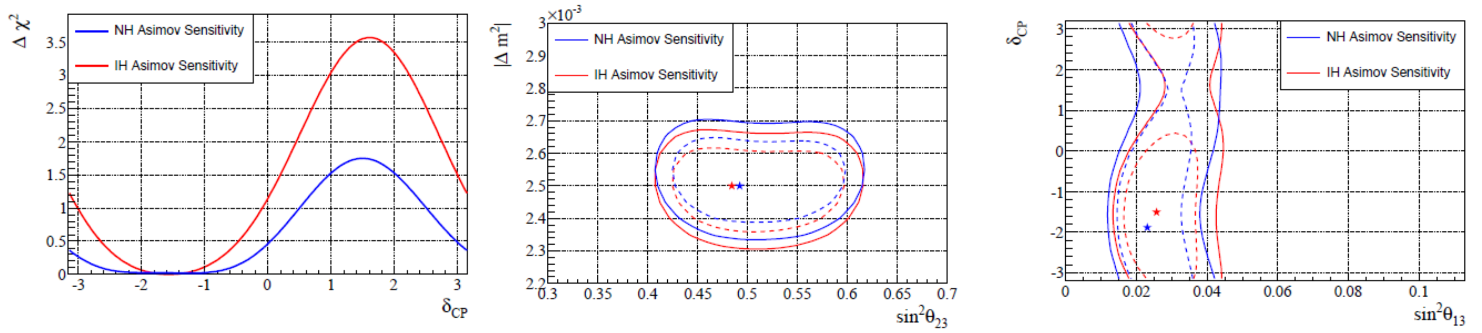

δ_{CP} Δm^2_{32}-$\sin^2\theta_{23}$ δ_{CP}-$\sin^2\theta_{13}$

Figure 8.14: Expected sensitivities with the last T2K analysis performed in 2016 with (top) and without (bottom) reactor constraint.

8.4.4 Results

Analysis is performed with data. Table 8.15 shows the best fit parameters (without the constraint from the reactor) and Fig. 8.15 (8.16) shows the contours of the oscillation parameters with (without) the constraint from the reactor. Table 8.16 shows the 1σ intervals of the 1D contours. The parameters of Δm^2_{32}, θ_{23} and δ_{CP} are measured with the best accuracy in the world. Figure 8.17 shows the 1D contours of the δ_{CP} with the Feldman Cousins method with the reactor constraint and Table 8.17 shows the 2σ interval of the δ_{CP}. Table 8.18 shows the posterior probabilities with the normal and inverted hierarchies.

Table 8.15: Best fit values of the oscillation parameters without the reactor constraint.

Parameters	Best fit	
	Normal hierarchy	Inverted hierarchy
$\sin^2 2\theta_{13}$	0.103	0.118
$\sin^2 \theta_{13}$	0.0027	0.0030
δ_{CP}	-1.85	-1.36
Δm^2_{32}	0.00246	0.00244
$\sin^2 \theta_{23}$	0.518	0.520

Table 8.16: 1σ (68.3%) credible intervals of the 1D contour of the oscillation parameters. Due to the marginalization, central value of each parameter is different from the best fit point in Table 8.15.

Parameters	1σ interval	
	Normal hierarchy	Inverted hierarchy
With reactor constraint		
$\sin^2 2\theta_{13}$	$0.0871^{+0.0045}_{-0.0043}$	0.0881 ± 0.0044
$\sin^2 \theta_{13}$	0.0223 ± 0.0011	0.0225 ± 0.0011
δ_{CP}	$-1.72^{+0.61}_{-0.58}$	-1.48 ± 0.50
Δm^2_{32}	$(2.450^{+0.068}_{-0.065}) \times 10^{-3}$ eV^2	$(2.415^{+0.065}_{-0.064}) \times 10^{-3}$ eV^2
$\sin^2 \theta_{23}$	$0.544^{+0.029}_{-0.046}$	$0.543^{+0.028}_{-0.043}$
Without reactor constraint		
$\sin^2 2\theta_{13}$	$0.103^{+0.021}_{-0.017}$	$0.118^{+0.022}_{-0.019}$
$\sin^2 \theta_{13}$	$0.0264^{+0.0053}_{-0.0043}$	$0.0300^{+0.0055}_{-0.0048}$
δ_{CP}	$-1.86^{+0.85}_{-0.80}$	$-1.36^{+0.66}_{-0.68}$
Δm^2_{32}	$(2.446^{+0.065}_{-0.063}) \times 10^{-3}$ eV^2	$(2.414^{+0.067}_{-0.065}) \times 10^{-3}$ eV^2
$\sin^2 \theta_{23}$	$0.487^{+0.067}_{-0.024}$	$0.488^{+0.061}_{-0.026}$

Table 8.17: 2σ credible intervals of the 1D contour of the δ_{CP} with the Feldman Cousins method.

Parameters	2σ interval	
	Normal hierarchy	Inverted hierarchy
With reactor constraint		
δ_{CP}	$[-2.739, -0.6078]$	nothing

Table 8.18: Posterior probabilities of normal and inverted hierarchies of data with and without the reactor constraint.

	Normal hierarchy	Inverted hierarchy	Ratio of Normal/Inverted
Without reactor	0.792	0.208	3.81
With reactor	0.913	0.087	10.49

8.4.5 Discussion

δ_{CP}

The data result prefers the maximal CP violation ($\delta_{CP} \sim -\pi/2$) and $\delta_{CP} = 0$ is excluded with 2σ as shown in Fig. 8.17. This is because the observed number of FHC ν_e events are larger and RHC ν_e events are smaller than the MC expectation with an assumption of $\delta_{CP} = 0$ and consistent with $\delta_{CP} = -\pi/2$ as shown in Fig. 8.6. This may indicate the CP asymmetry is larger than the expectation from the standard three flavor mixing structure alone, although it is not statistically significant. To conclude if the CP violation is coming from not only the J_{CP} defined in Eq. 2.22 but also other new physics behind the standard three flavor mixing model, further data are necessary. Figure 8.18 shows the future sensitivity to exclude $\delta_{CP} = 0$ with true $\delta_{CP} = -\pi/2$ assumed. T2K can reach the sensitivity of 3σ with 20×10^{21} POT.

Mass hierarchy

The data prefer the normal hierarchy than the inverted hierarchy as shown in Table 8.18. This is because the observed number of FHC ν_e events are larger and RHC ν_e events are smaller than the MC expectation with an assumption of inverted hierarchy and consistent with the normal hierarchy as shown in Fig. 8.6. The Bayes factor of NH/IH is 10.49 corresponds to near the boundary of "substantial"(3–10) and "strong"(10–32) evidence based on the Jeffreys's scale.

Comparison with external experiments

The measured values of the oscillation parameters are compared with the other oscillation experiments. The measured value of θ_{13} without the reactor shown in Table 8.16 is consistent with the reactor measurement of $\sin^2 2\theta_{13} = 0.0857 \pm 0.046$ and Fig. 2.6 around 1σ. The measured values of θ_{23} and Δm^2_{32} are consistent with atmospheric and accelerator experiments with 90% CL as shown in Figs. 8.19 and 2.9. The former figure includes the latest result from NOνA presented in a conference held in June 2018 [130]. It is interesting that NOνA prefer non-maximal mixing of θ_{23}, although T2K prefers the maximal mixing. Because the tensions are not statistically significant and difference of the treatment of systematics between T2K and NOνA is not clear, more improvement of statistics and systematics are needed. The value of δ_{CP} is measured by only NOνA and T2K at present and the result presented by NOνA in June 2018 is shown in Fig. 8.20. The best fit point of NOνA is $\delta_{CP} = 0.17\pi$ with the normal hierarchy and any region of δ_{CP} is not excluded with 2σ with the normal hierarchy. Although these tendency are not the same as the T2K and the best fit point of NOνA is excluded by T2K, the 2σ regions of T2K are not excluded by NOνA and they are consistent statistically. Further data are necessary to validate the standard three flavor mixing model. The mass hierarchy is measured by SK [131] and normal hierarchy is preferred around 90% and it is consistent with T2K. NOνA also prefers the hypothesis of normal hierarchy with 1.8σ [130].

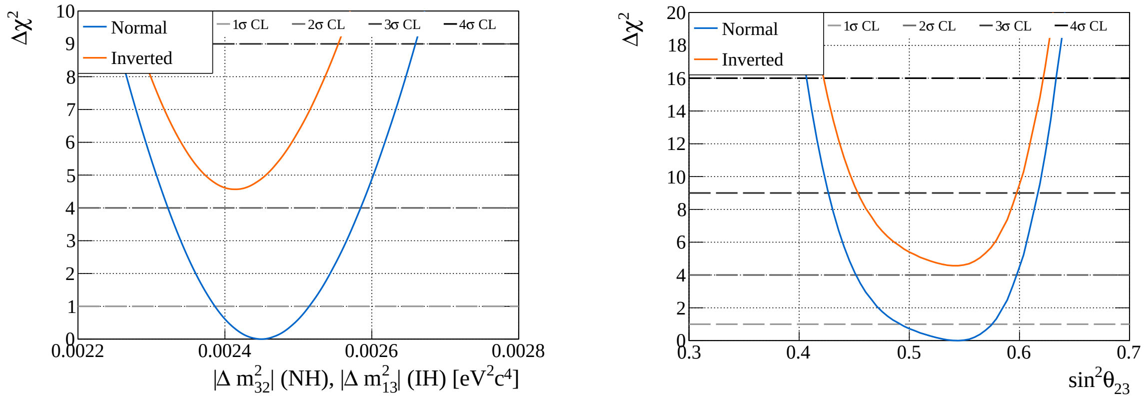

Δm^2_{32} $\sin^2\theta_{23}$

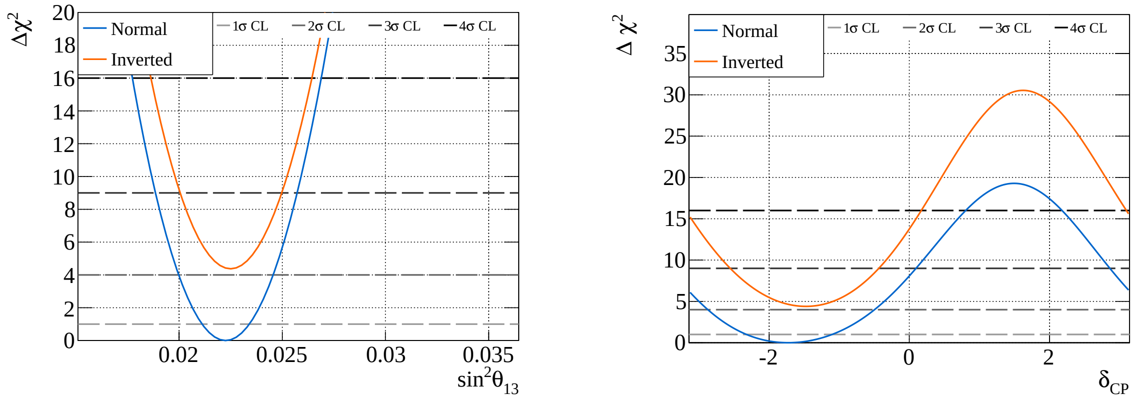

$\sin^2\theta_{13}$ δ_{CP}

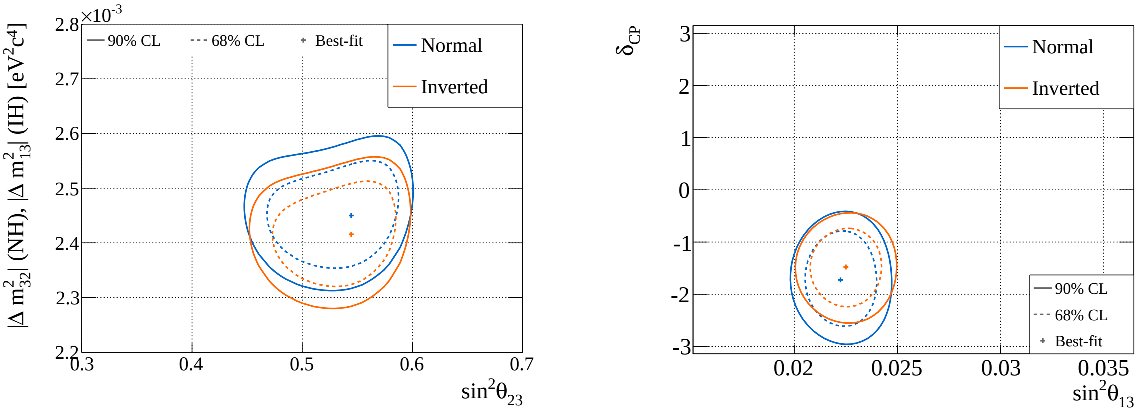

Δm^2_{32}-$\sin^2\theta_{23}$ δ_{CP}-$\sin^2\theta_{13}$

Figure 8.15: Contours of the oscillation parameters with data with reactor constraint.

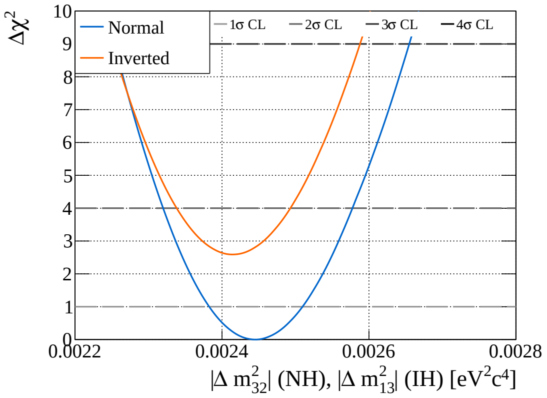

Δm^2_{32}

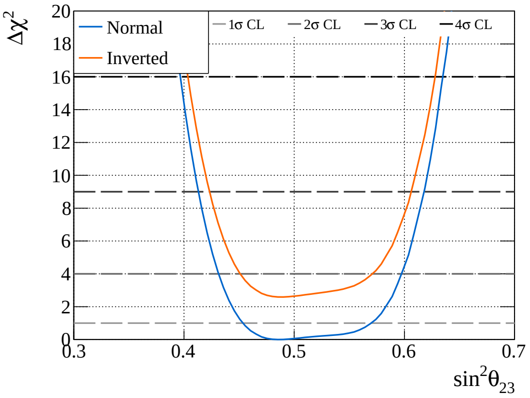

$\sin^2\theta_{23}$

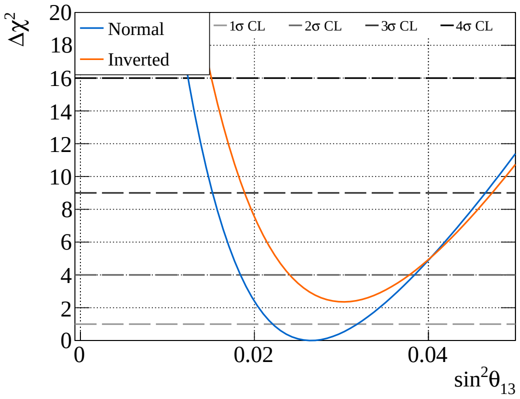

$\sin^2\theta_{13}$

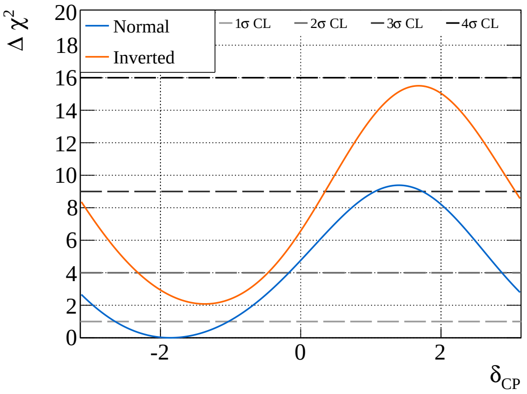

δ_{CP}

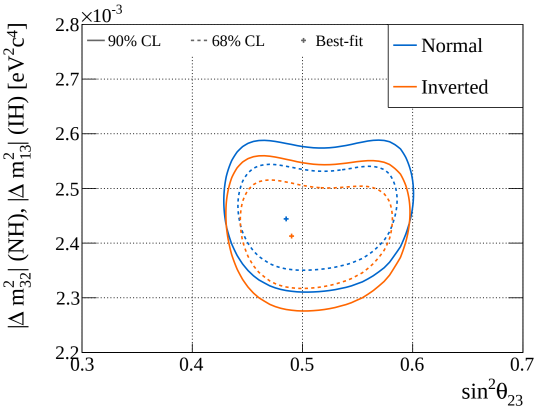

Δm^2_{32}-$\sin^2\theta_{23}$

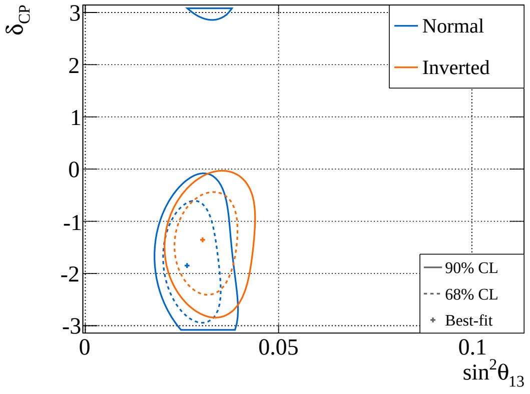

δ_{CP}-$\sin^2\theta_{13}$

Figure 8.16: Contours of the oscillation parameters with data without reactor constraint.

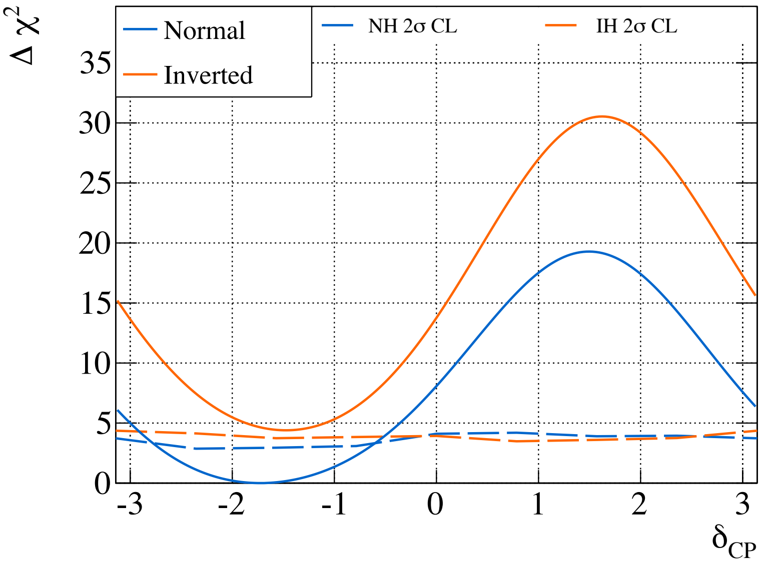

Figure 8.17: Contour of the δ_{CP} with critical $\Delta\chi^2$ values of 2σ obtained by the Feldman Cousins method.

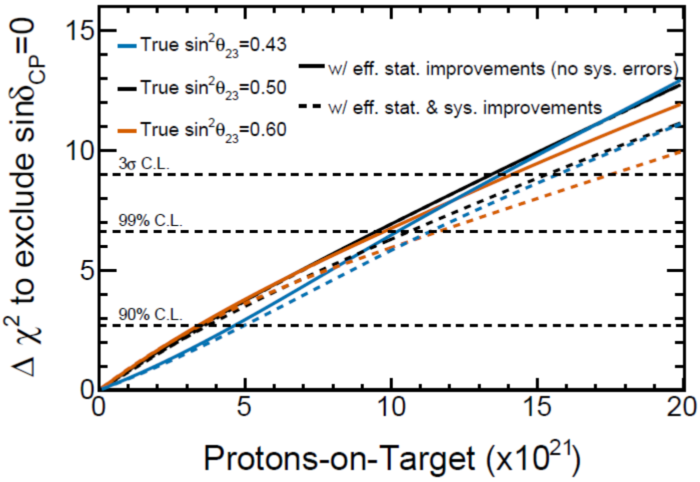

Figure 8.18: Sensitivity to exclude $\delta_{CP} = 0$ as a function of accumulated POT. True $\delta_{CP} = -\pi/2$, normal hierarchy and three cases of θ_{23} are assumed. Solid lines assume only statistical uncertainty and dashed lines assume statistical and systematic uncertainties. The size of the systematic uncertainties are assumed to be 2/3 of the values in 2016. [98]

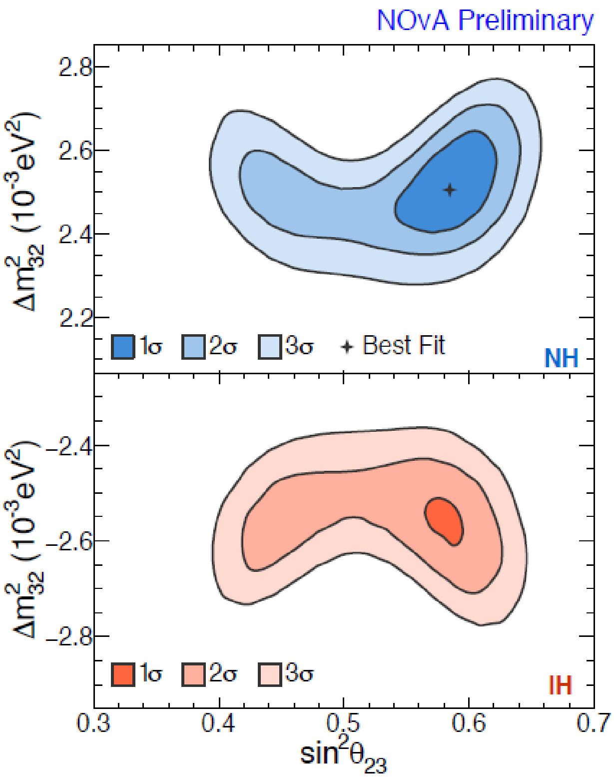

Figure 8.19: Contour of the $\sin^2\theta_{23}$ vs Δm^2_{32} by NOνA presented in June 2018 [130] with normal hierarchy (top) and inverted hierarchy(bottom).

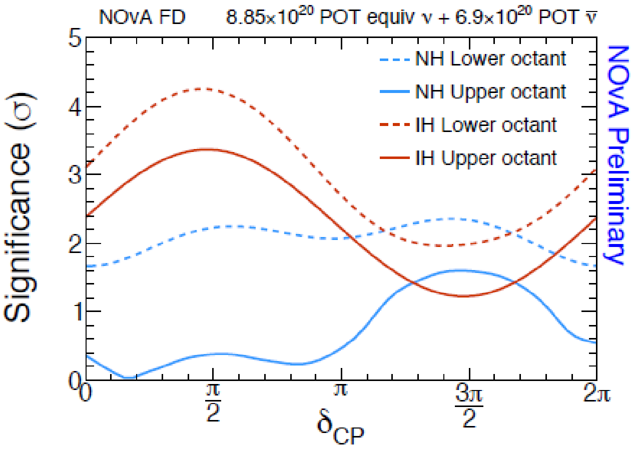

Figure 8.20: Contour of the δ_{CP} by NOνA presented in June 2018 [130] with the reactor constraint. $\frac{3\pi}{2}$ of NOνA corresponds to $\frac{-\pi}{2}$ of T2K.

8.5 Search for $\overline{\nu}_\mu \rightarrow \overline{\nu}_e$ appearance

In order to search for the $\overline{\nu}_\mu \rightarrow \overline{\nu}_e$ appearance, the hypotheses test is performed by using the RHC 1Rν_e sample at the SK. The p-values of hypotheses are calculated with two ways: rate only analysis and rate+shape analysis. For the rate only analysis, information of only the number of events of the RHC 1Rν_e sample is used. For the rate+shape analysis, both information of the number of events and p-θ information of leptons in the RHC 1Rν_e sample are used. In order to constrain the uncertainty of the oscillation parameters of the PMNS matrix, other four samples, FHC 1Rν_μ, FHC 1Rν_e, FHC $\nu_e 1\pi$ and RHC 1Rν_μ are jointly fitted in the same way as the measurement of oscillation parameters described in Sec. 8.4.

8.5.1 Analysis procedure

Definition of hypothesis

In this analysis, two hypotheses are tested statistically. One hypothesis is "no $\overline{\nu}_\mu \rightarrow \overline{\nu}_e$ appearance", i.e absence of $\overline{\nu}_\mu \rightarrow \overline{\nu}_e$ oscillation. The other hypothesis is "$\overline{\nu}_\mu \rightarrow \overline{\nu}_e$ appearance with the same probability that is predicted from the PMNS matrix parameters". In order to switch between these two hypotheses, a parameter β is introduced in the oscillation probability. It multiplies the $\overline{\nu}_\mu \rightarrow \overline{\nu}_e$ oscillation probability.

$$P(\overline{\nu}_\mu \rightarrow \overline{\nu}_e) = \beta \times P_{\mathrm{PMNS}}(\overline{\nu}_\mu \rightarrow \overline{\nu}_e) \tag{8.9}$$

where $P_{\mathrm{PMNS}}(\overline{\nu}_\mu \rightarrow \overline{\nu}_e)$ is the probability of $\overline{\nu}_\mu \rightarrow \overline{\nu}_e$ appearance predicted by the PMNS matrix, including both effect of the θ_{13} and θ_{12}. β is chosen to be either 0 or 1, respectively indicating the former or latter hypothesis. Both of the hypotheses are tested. When $\beta = 0$ hypothesis is tested, the $\beta = 0$ hypothesis is assumed as the null hypothesis and the $\beta = 1$ hypothesis is assumed as the alternative hypothesis. On the other hand, when $\beta = 1$ hypothesis is tested, the null and alternative hypothesis are reversed.

Definition of test statistics

The hypotheses are tested by two test statistics. For the rate only analysis, the number of RHC 1Rν_e events, N, is used as the test statistics:

$$N = N^{\mathrm{obs}}_{\mathrm{RHC1R}\nu_e} \tag{8.10}$$

For the rate+shape analysis, $\Delta\chi^2$ defined as follows is used as the test statistics:

$$\Delta\chi^2 \;\;=\;\; \chi^2(\beta = 0) - \chi^2(\beta = 1) \tag{8.11}$$

To calculate the $\Delta\chi^2$, we use the same binned likelihood L_s as Eq. 8.2 . In this analysis, all the systematic and oscillation parameters are marginalized (as well as the mass hierarchy) as nuisance parameters, except for the β parameter. For the marginalization, templates of the systematic and oscillation parameters are prepared based on the posterior with the constraint from the 4 samples other than RHC 1Rν_e. For the preparation, sets of the $\boldsymbol{o}$ and $\boldsymbol{f}$ are thrown based on their prior (Table 8.19 and constraint from the ND280) and constraint from the 4 sample other than RHC 1Rν_e is applied as a weight (W) for each set,

$$W(N^{\mathrm{obs}}_{\mathrm{data}}, \boldsymbol{x}^{\mathrm{obs}}_{\mathrm{data}}, \boldsymbol{o}_i,\; \boldsymbol{f}_i) = \prod_{s=1}^{4} L_s(N^{\mathrm{obs}}_{\mathrm{data}}, \boldsymbol{x}^{\mathrm{obs}}_{\mathrm{data}} | \boldsymbol{o}_i, \boldsymbol{f}_i, \beta = 1) \tag{8.12}$$

where $N^{\mathrm{obs}}_{\mathrm{data}}$ and $\boldsymbol{x}^{\mathrm{obs}}_{\mathrm{data}}$ are given by the data (Monte Carlo simulation for sensitivity study) of the 4 samples other than RHC 1Rν_e. $\boldsymbol{o}_i$ and $\boldsymbol{f}_i$ are i-th set of the nuisance parameters. By using the M sets of the nuisance parameters, marginalized likelihood, L_{marg}, is calculated as follows:

$$\begin{aligned} L_{\mathrm{marg}}(N^{\mathrm{obs}}, \boldsymbol{x}^{\mathrm{obs}}|\beta = l) &= \frac{1}{\sum_{i=1}^{M} W(N^{\mathrm{obs}}_{\mathrm{data}}, \boldsymbol{x}^{\mathrm{obs}}_{\mathrm{data}}, \boldsymbol{o}_i,\ \boldsymbol{f}_i)} \times \\ & \sum_{i=1}^{M} \left[\prod_{s=1}^{5} \left\{ L_s(N^{\mathrm{obs}}, \boldsymbol{x}^{\mathrm{obs}}, \boldsymbol{o}_i, \boldsymbol{f}_i|\beta = l) \right\} \times W(N^{\mathrm{obs}}_{\mathrm{data}}, \boldsymbol{x}^{\mathrm{obs}}_{\mathrm{data}}, \boldsymbol{o}_i,\ \boldsymbol{f}_i) \right] \quad (8.13) \end{aligned}$$

$\Delta\chi^2$ defined by Eq. 8.11 is calculated by using the L_{marg}:

$$\begin{aligned} \Delta\chi^2 &= \chi^2(\beta = 0) - \chi^2(\beta = 1) \\ &= 2 \times \left\{ -\ln L_{\mathrm{marg}} \left(N^{\mathrm{obs}}, \boldsymbol{x}^{\mathrm{obs}}|\beta = 0 \right) + \ln L_{\mathrm{marg}} \left(N^{\mathrm{obs}}, \boldsymbol{x}^{\mathrm{obs}}|\beta = 1 \right) \right\} \quad (8.14) \end{aligned}$$

Table 8.19: Prior of the oscillation parameters.

Parameter	Prior	Variation range
$\sin^2\theta_{12}$	fixed	0.304
$\sin^2 2\theta_{13}$	Gaussian	0.0857 ± 0.0046
$\sin^2\theta_{23}$	uniform	$[0.3, 0.7]$
Δm^2_{21}	fixed	7.53×10^{-5} eV^2
Δm^2_{32}	uniform	$[2, 3] \times 10^{-3}$ eV^2
δ_{CP}	uniform	$[-\pi, +\pi]$
Mass hierarchy	uniform	0.5 NH and 0.5 IH

Production of test statistics distributions

In this section, we describe the procedure for producing the test statistics distributions with the toy ensemble based on the real data (MC simulation for sensitivity study) of the 4 samples other than RHC 1Rν_e.

1. Parameter set for the marginalization

200k sets of the oscillation and systematic parameters are prepared for the marginalization in the calculation of the $\Delta\chi^2$. They are commonly used for all the toy ensembles.

2. Production of toy ensemble

Toy ensembles are produced by casting the systematic and oscillations parameters based on their prior (Table 8.19 and constraint from the ND280). In addition, for each throw of the nuisance parameters, statistical throws are generated by assuming the β equaled to that of the null hypothesis. For the rate only analysis, 100k throws of the nuisance parameters and 100k statistical throws are generated. For the rate+shape analysis, 2M throws of the nuisance parameters and one statistical throw are generated.

3. Calculation of test statistics

For the each toy experiment, test statistics defined in Eq. 8.10 and Eq. 8.11 are calculated. For the marginalization in the calculation of the $\Delta\chi^2$, templates prepared in step 1 are used.

4. Production of test statistics distributions

In order to produce the test statistics distribution, the test statistics of each toy experiment is stored with a weight of the constraint from the 4 samples other than RHC 1Rν_e, C. The weight is given as follows:

$$C(N^{\mathrm{obs}}_{\mathrm{data}}, \boldsymbol{x}^{\mathrm{obs}}_{\mathrm{data}}, \boldsymbol{o}_k,\ \boldsymbol{f}_k) = \prod_{s=1}^{4} L_s(N^{\mathrm{obs}}_{\mathrm{data}}, \boldsymbol{x}^{\mathrm{obs}}_{\mathrm{data}} | \boldsymbol{o}_k, \boldsymbol{f}_k, \beta = 1) \tag{8.15}$$

where $\boldsymbol{o}_k$ and $\boldsymbol{f}_k$ are oscillation and systematic parameters of k-th toy experiment. The test statistics distribution for each β is normalized and named $D_\beta(N^{\mathrm{obs}})$ for the rate only analysis and $D_\beta(\Delta\chi^2)$ for the rate+shape analysis.

Calculation of test statistics of data

The test statistics defined in Eq. 8.10 and Eq. 8.11 are calculated with data of all 5 samples at the SK. For the marginalization in the $\Delta\chi^2$, the set of the parameters prepared in Sec. 8.5.1 is used.

P-value calculation

For the rate only analysis, p-value of $\beta = 0$ hypothesis is calculated by integrating the right tail of the test statistics distribution as follows:

$$\mathrm{pvalue} = \int_{N^{\mathrm{obs}}=N^{\mathrm{obs}}_{\mathrm{data}}}^{+\infty} D_{\beta=0}(N^{\mathrm{obs}})dN^{\mathrm{obs}} \tag{8.16}$$

where $N^{\mathrm{obs}}_{\mathrm{data}}$ is the number of actual $\overline{\nu}_e$ like events in the input data set. On the other hand, p-value of $\beta = 1$ hypothesis is calculated by integrating the left tail of the test statistics as follows:

$$\mathrm{pvalue} = \int_{-\infty}^{N^{\mathrm{obs}}=N^{\mathrm{obs}}_{\mathrm{data}}} D_{\beta=1}\left(N^{\mathrm{obs}}\right) dN^{\mathrm{obs}} \tag{8.17}$$

For the rate+shape analysis, p-value of $\beta = 0$ hypothesis is calculated by integrating the right tail of the test statistics distribution because negative value of $\Delta\chi^2$ is preferred by $\beta = 0$ due to definition of $\Delta\chi^2$ (Eq. 8.11). The p-value is calculated as follows:

$$\mathrm{pvalue} = \int_{\Delta\chi^2\ =\ \Delta\chi^2{}_{\mathrm{data}}}^{+\infty} D_{\beta=0}(\Delta\chi^2)d\Delta\chi^2 \tag{8.18}$$

where $\Delta\chi^2_{data}$ is actual $\Delta\chi^2$ of the input data set. On the other hand, the p-value of $\beta = 1$ hypothesis is calculated by integrating the left tail of the test statistics distribution as follows:

$$\mathrm{pvalue} = \int_{-\infty}^{\Delta\chi^2\ =\ \Delta\chi^2{}_{\mathrm{data}}} D_{\beta=1}(\Delta\chi^2)d\Delta\chi^2 \tag{8.19}$$

8.5.2 Expected sensitivity

Sensitivity with a MC simulation

Sensitivity studies are performed for a MC simulation produced with the oscillation parameters listed in Table 8.2. P-value of both $\beta = 0$ and $\beta = 1$ hypotheses are calculated with the rate only

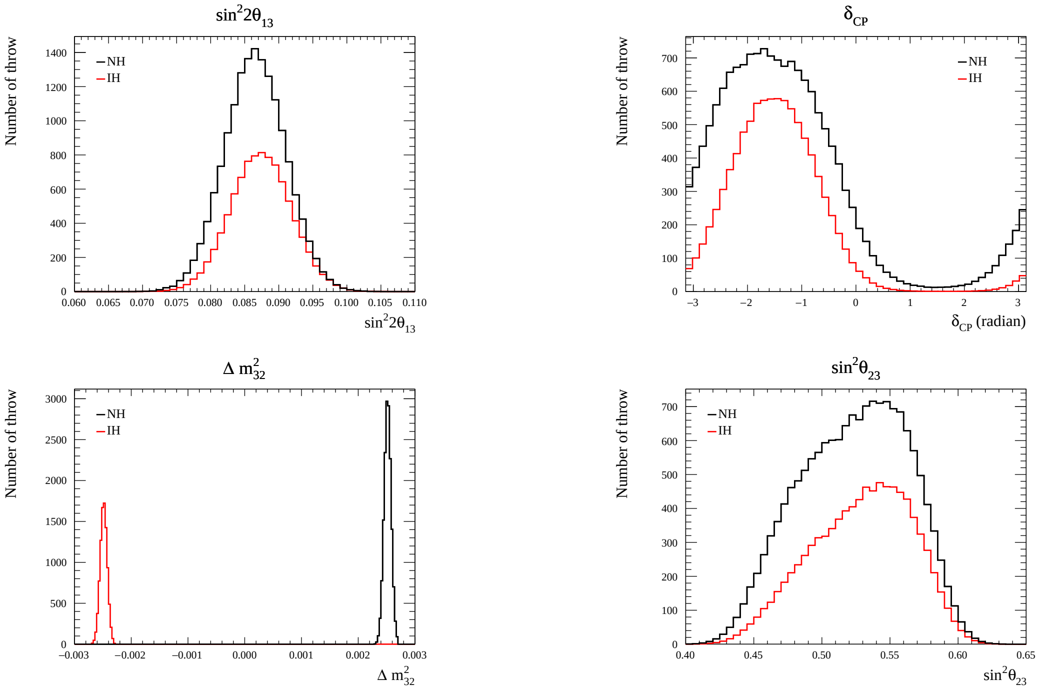

Figure 8.21: Posterior of the oscillation parameters with the normal (black line) and inverted (red line) hierarchy after the constraint from the 4 samples other than RHC 1Rν_e of the MC simulation.

and rate+shape analyses. Figure 8.21 shows prior of the oscillation parameters with constraint from the 4 samples other than RHC 1Rν_e based on Eq. 8.12.

Figure 8.22 shows the test statistics distributions for the rate only and rate+shape analysis with $\beta = 0$ and $\beta = 1$ hypotheses. For the rate-only analysis, the number of expected events with the MC is 11.765 events and p-value is 0.0383 with $\beta = 0$ and 0.373 with $\beta = 1$. For the rate+shape analysis, the $\Delta\chi^2$ with the MC is 4.278 and p-value is 0.0149 with $\beta = 0$ and 0.388 with $\beta = 1$. Table 8.22 shows a summary of the calculated p-values as well as corresponds values of σ by assuming Gaussian (pvalue $= 1 - \text{erf}(\text{N}\sigma/\text{sqrt}(2))$).

Table 8.20: P-values with the MC simulation for both rate only and rate+shape analyses. Values in parentheses are corresponds values of σ by assuming Gaussian.

Analysis	P-value for $\beta = 0$	P-value for $\beta = 1$
Rate only	0.0383 (2.07 σ)	0.373 (0.89 σ)
Rate+shape	0.0149 (2.43 σ)	0.388 (0.86 σ)

Toy experiments with constraint from 4 samples of data

In order to evaluate the sensitivity including the error of statistic, systematic and oscillation parameters, sensitivity study is done with 200k toy experiment. For each toy experiment, statistics, systematics, oscillations parameters of the RHC 1Rν_e sample are thrown based on the posterior after the constraint from the 4 samples other than RHC 1Rν_e of data. For each set, p-value is evaluated for both rate only and rate+shape analysis, as shown in Fig. 8.23 and 8.24. The number of toy experiments which exceed 3 σ and 2 σ are counted as shown in Table 8.21.

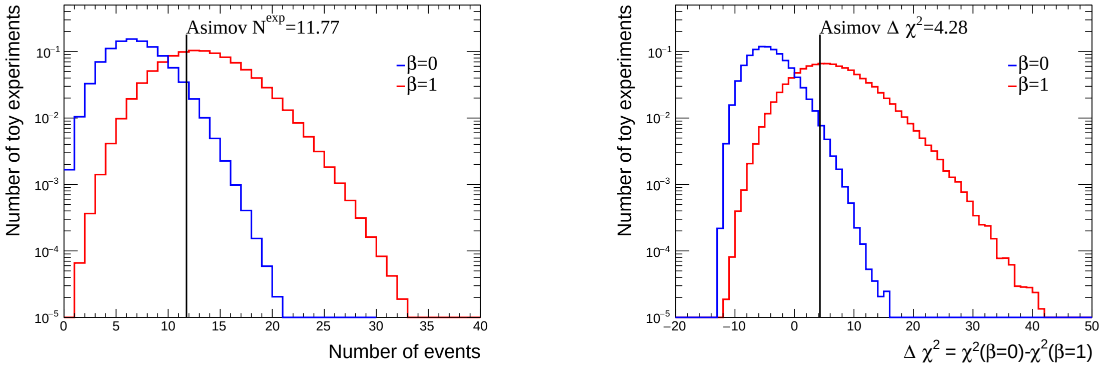

Figure 8.22: Sensitivity study with the MC simulation for the rate only analysis (left) and rate+shape analysis (right).

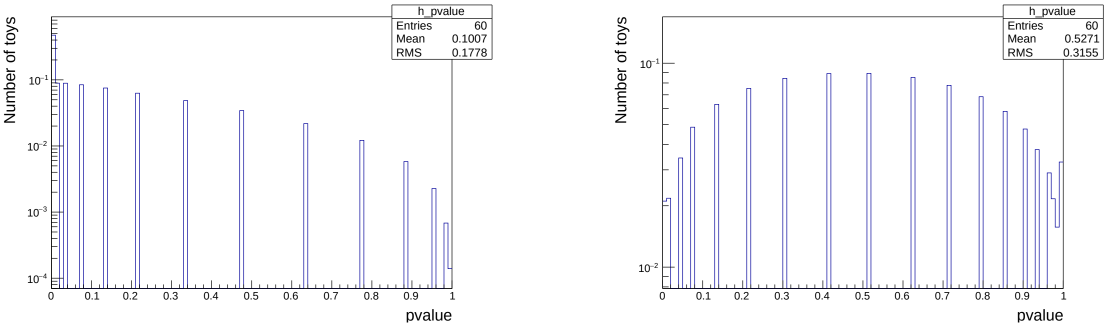

Figure 8.23: P-value of the set of toy experiments for the rate only analysis with $\beta = 0$(left) and $\beta = 1$(right).

Table 8.21: Fraction of toy experiments of p-value exceed 3 σ and 2 σ.

Analysis	Fraction of toys exceed 3 σ	Fraction of toys exceed 2 σ
Rate only ($\beta = 0$)	20.7%	58.8%
Rate only ($\beta = 1$)	0.7%	7.9%
Rate+shape ($\beta = 0$)	41.8%	74.0%
Rate+shape ($\beta = 1$)	0.3%	3.8%

8.5.3 Results

By using data, p-value of both $\beta = 0$ and $\beta = 1$ hypotheses are calculated with the rate only and rate+shape analysis. The number of observed RHC ν_e events is 9 and their p-θ distribution is shown in Fig. 8.25. Figure 8.26 shows that for each type of neutrinos predicted by MC simulation. Figure 8.27 shows prior of the oscillation parameters with constraint from the 4 samples other than RHC 1Rν_e based on Eq. 8.12.

Figure 8.28 shows the test statistics distribution for the rate only and rate+shape analyses with $\beta = 0$ and $\beta = 1$ hypotheses. For the rate only analysis, the number of observed events is 9 and p-value is 0.219 with $\beta = 0$ and 0.213 with $\beta = 1$. For the rate+shape analysis, the $\Delta\chi^2$ given by data is -1.67 and p-value is 0.233 with $\beta = 0$ and 0.0867 with $\beta = 1$. Table 8.22 shows a summary of the calculated p-values as well as corresponds values of σ by assuming Gaussian

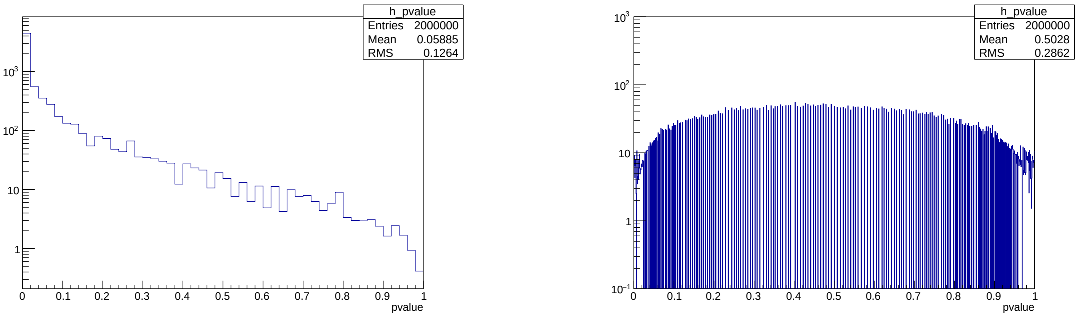

Figure 8.24: P-value of the set of toy experiments for the rate+shape analysis with $\beta = 0$(left) and $\beta = 1$(right).

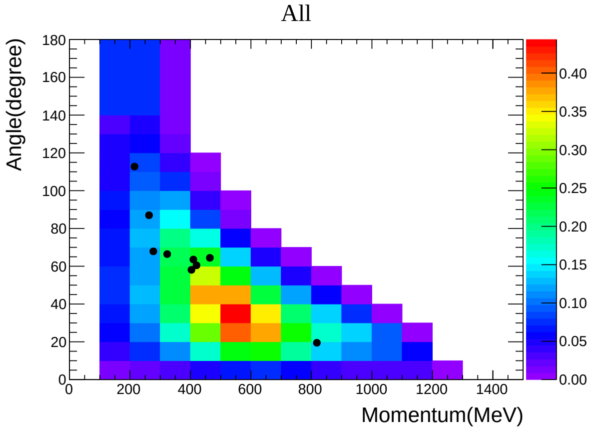

Figure 8.25: RHC ν_e p-θ distribution with data(black point) and MC prediction with $\beta = 1$, oscillation parameters listed in Table 8.2 and constraint from the ND280.

(pvalue $= 1 - \mathrm{erf}(\mathrm{N}\sigma/\mathrm{sqrt}(2))$).

Table 8.22: Result of p-values for both rate only and rate+shape analyses. Values in parentheses are corresponds values of σ by assuming Gaussian.

Analysis	P-value for $\beta = 0$	P-value for $\beta = 1$
Rate only	0.219 (1.23 σ)	0.213 (1.25 σ)
Rate+shape	0.233 (1.19 σ)	0.0867 (1.71 σ)

8.5.4 Discussion

As shown in Table 8.5, the number of expected background is 6.475 and signal is 5.290 by MC simulation. Because the number of observed event by data, 9, is between the expectation of background and signal+background, both of the hypotheses are not excluded for the rate only analysis. For the rate+shape analysis, the p-value with $\beta = 0$ ($\beta = 1$) hypothesis is larger (smaller) than that for the rate only analysis because the p-θ spectrum of observed events are far from that of $\overline{\nu}_\mu \to \overline{\nu}_e$ and close to $\nu_\mu \to \nu_e$, $\overline{\nu}_\mu \to \overline{\nu}_\mu$ and $\nu_\mu \to \nu_\mu$ as shown in Fig. 8.26. Especially, there is no observed events around the peak of $\overline{\nu}_\mu \to \overline{\nu}_e$, which can not be described

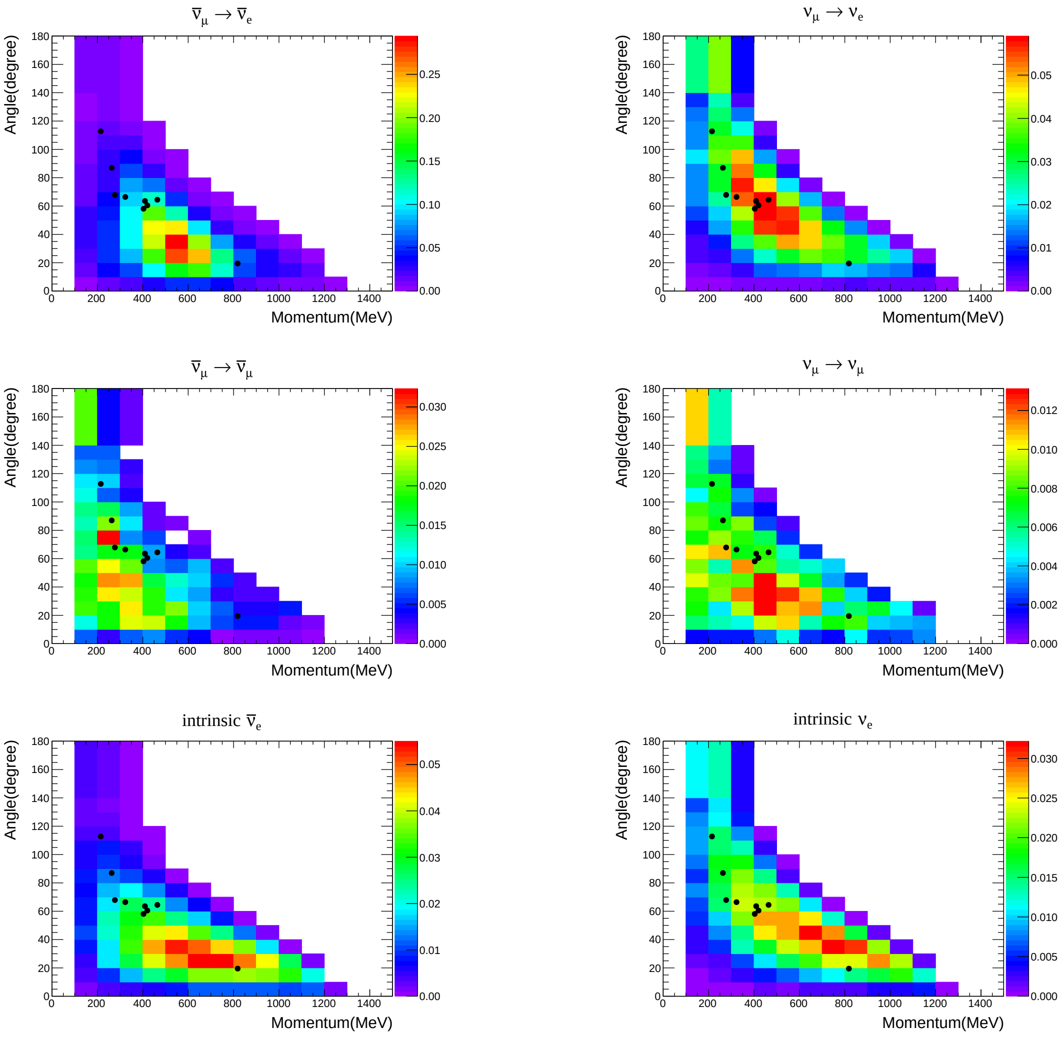

Figure 8.26: RHC ν_e p-θ distribution with data(black point) and MC prediction with each type of neutrinos with oscillation parameters listed in Table 8.2 and constraint from the ND280.

by any excess/shortage of the backgrounds. However, it is not statistically significant and further data are needed.

Figure 8.29 and 8.30 show expected sensitivities with the expected number of POT with RHC by the end of 2018 (1.56×10^{21}), 2019 (2.46×10^{21}) and 2020 (3.36×10^{21}). Figure 8.29 shows p-values of $\beta = 0$ hypothesis estimated by MC with the oscillation parameters listed in Table 8.2 and $\beta = 1$. Figure 8.30 shows p-values of $\beta = 1$ hypothesis estimated by MC with the oscillation parameters listed in Table 8.2 and $\beta = 0$. We have a chance to exclude either $\beta = 0$ or $\beta = 1$ hypothesis in a few years because the expected p-values are around or more than 3σ at the end of 2020.

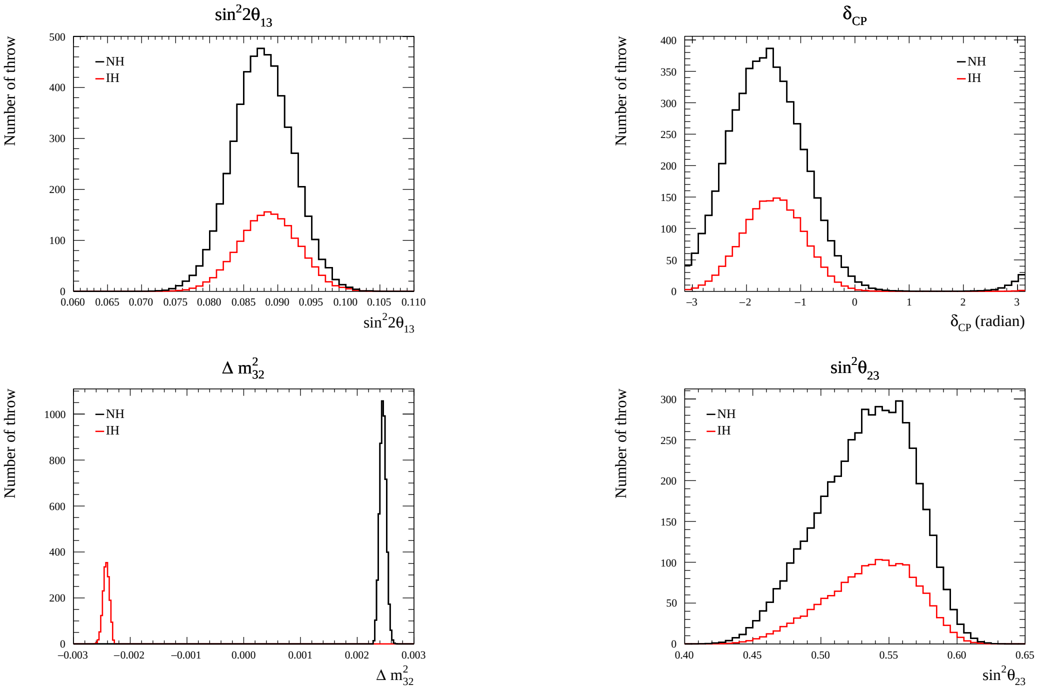

Figure 8.27: Posterior of the oscillation parameters after the constraint from the 4 samples of data.

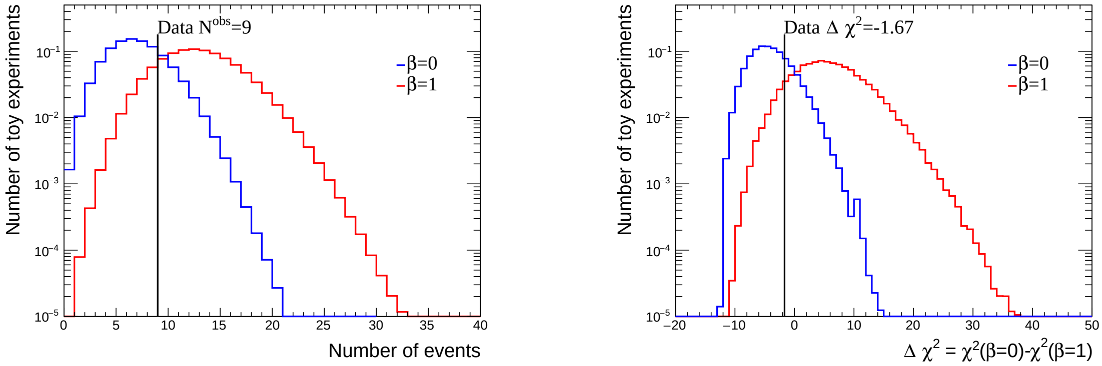

Figure 8.28: Results for rate only analysis (left) and rate+shape analysis (right).

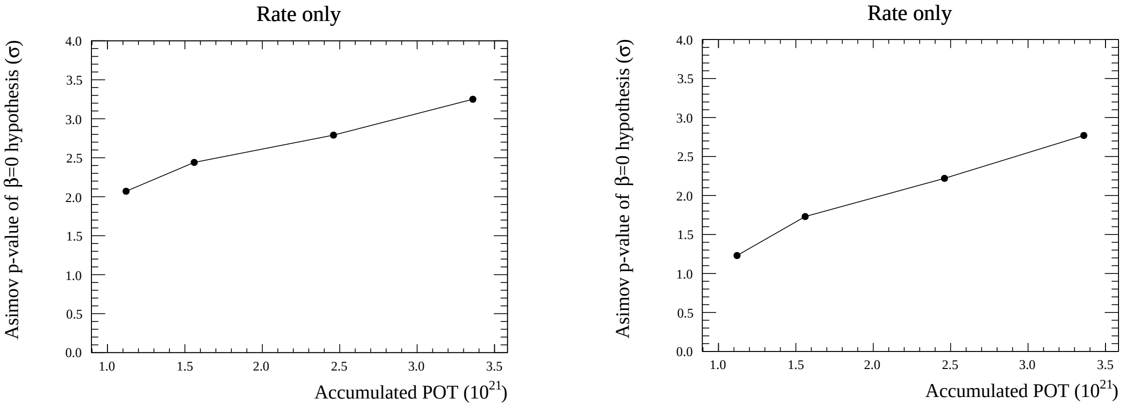

MC Data + MC

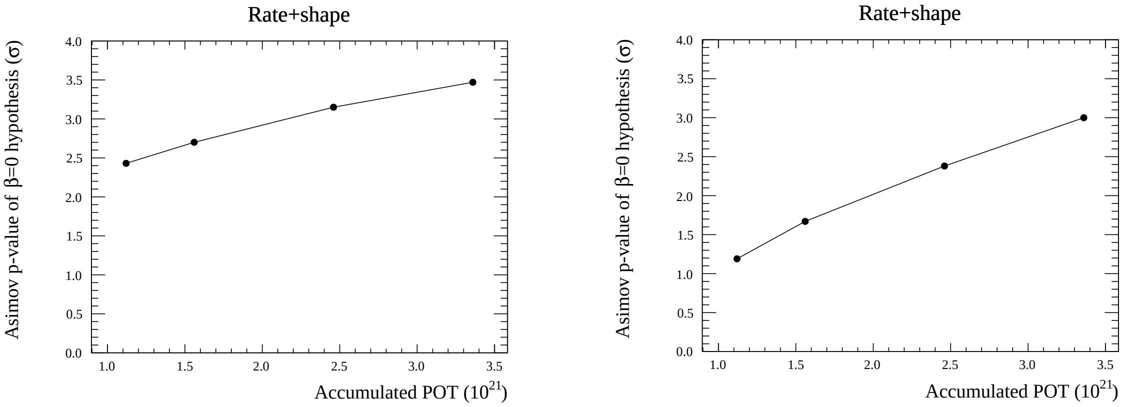

MC Data + MC

Figure 8.29: P-values of $\beta = 0$ hypothesis for the rate only (top) and rate+shape (bottom) analyses with expected POT by the end of 2017 (at present), 2018, 2019 and 2020. In the left figures, MC is produced with $\beta = 1$ and expected POT. In the right figures, MC is produced with $\beta = 1$ and increased amount of POT since the end of 2017 and it is added to the existed data by the end of 2017.

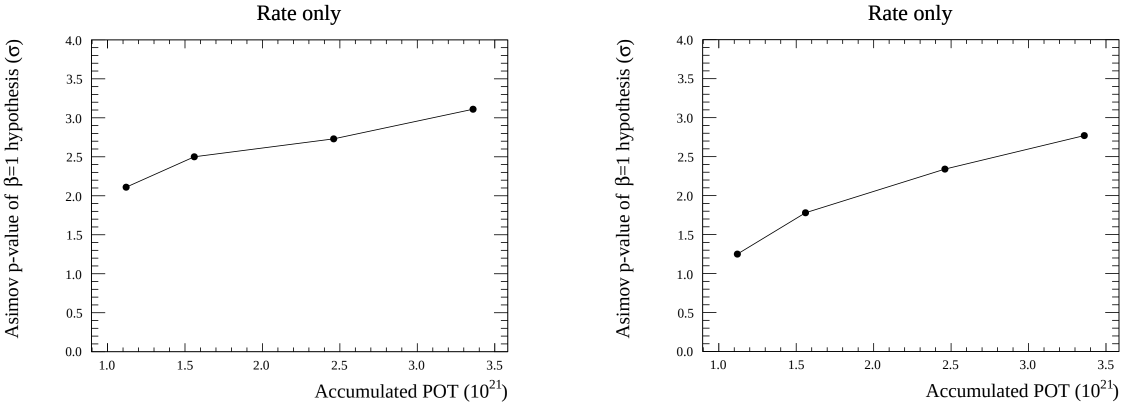

MC Data and MC

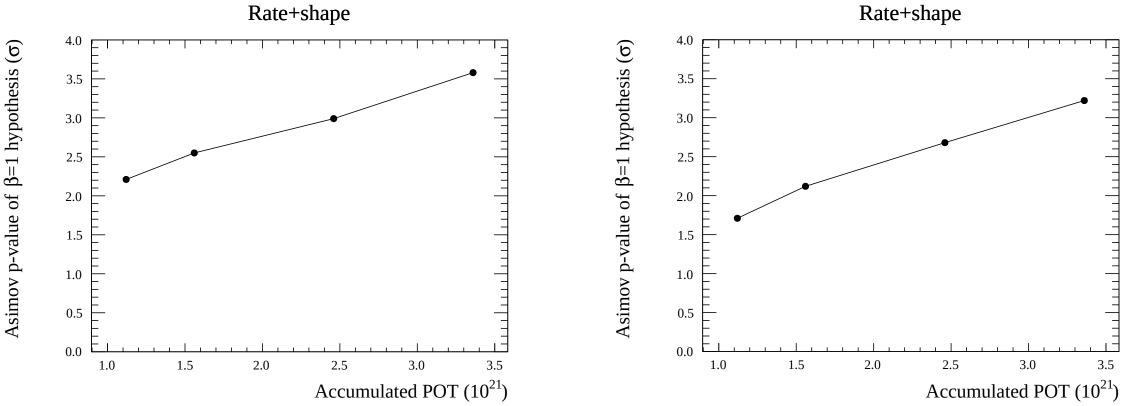

MC Data and MC

Figure 8.30: P-values of $\beta = 1$ hypothesis for the rate only (top) and rate+shape (bottom) analyses with expected POT by the end of 2017 (at present), 2018, 2019 and 2020. In the left figures, MC is produced with $\beta = 0$ and expected POT. In the right figures, MC is produced with $\beta = 0$ and increased amount of POT since the end of 2017 and added to the existed data by the end of 2017.

Chapter 9

Conclusions

T2K is a long baseline neutrino oscillation experiment, started from 2009. A muon neutrino beam produced by J-PARC accelerator is measured by the Super-Kamiokande detector to measure probabilities of neutrino oscillations. Main purposes of the T2K are the first observation of CP violation in lepton sector and an investigation of flavor mixing structure. In this thesis, three analyses are performed to achieve a precise neutrino oscillation measurement in the T2K experiment.

The first analysis is measurements of inclusive charged current muon neutrino cross sections with water, plastic, iron and their ratios. The purpose of the measurements is to understand difference of the neutrino-nucleus interactions between the plastic and water target that is one of systematic uncertainties in the T2K. The analysis is performed with a new water target detector, water module, one of the T2K near detectors located at on-axis. Main results of the measurements are $\sigma_{\mathrm{CC}}^{\mathrm{H_2O}} = (0.840 \pm 0.010(\mathrm{stat.})^{+0.10}_{-0.081}(\mathrm{syst.})) \times 10^{-38}$ cm^2/nucleon and $\frac{\sigma_{\mathrm{CC}}^{\mathrm{H_2O}}}{\sigma_{\mathrm{CC}}^{\mathrm{CH}}} = 1.028 \pm 0.016(\mathrm{stat.}) \pm 0.053(\mathrm{syst.})$ for muons whose angle is less than 45 degrees and momentum is more than 0.4 GeV with the mean neutrino energy of 1.5 GeV. These are the best measurement of the neutrino interaction with water target and the first measurement of the cross section ratio of water and plastic. Because there has been almost no data of the water target, this measurement ensures correctness of assumed systematic uncertainty of the difference of neutrino interaction between water and plastic target for the oscillation analysis with experimental data for the first time in the world and improves reliability of the oscillation analysis of the T2K.

The second analysis is a validation of the measurement of the T2K near detector, ND280. The ND280 measures neutrino flux and interactions and constrains their uncertainties for the T2K oscillation measurements. However, it is impossible to check if the constraint is correct or not at the far detector directly because not only the flux and interactions but also the neutrino oscillations affect the neutrino events at the Super-Kamiokande. In this analysis, observed neutrino event rates at other near detectors located at on-axis, water module and Proton Module, are compared with Monte Carlo prediction with the constraint from the ND280. This is the first trial to cross check the constraint from the near detector based on real data in any long baseline neutrino experiments. The measured event rates of the forward scattered muons at the water module and Proton Module are consistent with the prediction with a p-value of 0.303. This ensures the correctness of the constraint from the ND280. On the other hand, the measured event rates of large angle muons and protons, which are not included in the ND280 measurement, are not consistent with the prediction with a p-value of 4×10^{-4}. It indicates the over prediction of the number of emitted protons and gives a significant hint to improve a modeling of the neutrino interactions.

The third analysis is a measurement of the neutrino oscillations with doubled statistics compared with the last T2K analysis performed in 2016. The accumulated number of protons used for the analysis is 1.49×10^{21} with neutrino beam and 1.12×10^{21} with anti neutrino beam. Four types of the neutrino oscillations, $\nu_\mu \to \nu_\mu$, $\nu_\mu \to \nu_e$, $\overline{\nu}_\mu \to \overline{\nu}_\mu$ and $\overline{\nu}_\mu \to \overline{\nu}_e$, are measured by the Super-Kamiokande. The four oscillations are jointly fitted to extract the parameters of the unitary matrix in the standard three flavor mixing model (PMNS matrix): δ_{CP}, θ_{23}, Δm^2_{32} and θ_{13} as well as the mass hierarchy. The measured values with 1σ uncertainties are $\delta_{CP} = -1.72^{+0.58}_{-0.61}$($[-2.739, -0.6078]$ with 2σ intervals), $\sin^2\theta_{23} = 0.544^{+0.046}_{-0.029}$, $\Delta m^2_{32} = (2.450^{+0.065}_{-0.068}) \times 10^{-3}$ eV^2 and $\sin^2 2\theta_{13} = 0.0871^{+0.0043}_{-0.0045}$ with the normal hierarchy assumption and constraint from solar and reactor neutrino experiments. The δ_{CP}, θ_{23} and Δm^2_{32} are measured with the best accuracy in the world. $\delta_{CP} = 0$, corresponding to CP conservation, is excluded with a significance of 2σ for the first time in the world. Normal hierarchy is more preferred than inverted hierarchy with a Bayes factor of 10.49 with the reactor constraint. These results are consistent with other neutrino oscillation experiments. In addition, a search for $\overline{\nu}_\mu \to \overline{\nu}_e$ oscillation is performed. $\overline{\nu}_\mu \to \overline{\nu}_e$ oscillation is not observed so far although it is predicted by the standard oscillation framework. Two hypotheses are tested in this analysis. One hypothesis assumes a probability of $\overline{\nu}_\mu \to \overline{\nu}_e$ is zero and the other assumes the probability is the same as the prediction from the PMNS matrix parameters. P-value of the former (latter) hypothesis is calculated to be 0.219 (0.213) based on information of only the total number of observed event. With additional information of lepton kinematics, the p-value of the former (latter) hypothesis is calculated to be 0.233 (0.087). Both of the hypotheses are not excluded. This analysis is performed with the best sensitivity in the world

In this thesis, to answer the questions not described by the SM through the precise measurement of the neutrino oscillation, three physics analyses are performed. All of the three analyses are on the frontiers of the neutrino physics and give us important information of the neutrino properties and neutrino researches, which are still under the development. Based on the analyses results in this thesis, it is also expected that more precise measurement of the neutrino oscillation is achieved and properties of the neutrinos are understood more significantly in near future.

Appendix A

Detail formulas of neutrino-nucleus cross sections

A.1 Charged current quasi-elastic interaction with a nucleon

Differential cross section of the CCQE interaction is written as Eq. 3.1. The leptonic tensor $L_{\alpha\beta}$ and hadronic tensor $H^{\alpha\beta}$ are written as follows:

$$\begin{aligned} L_{\alpha\beta} &= k_\alpha k'_\beta + k'_\alpha k_\beta - g_{\alpha\beta} k \cdot k' \pm i\varepsilon_{\alpha\beta\sigma\delta} k'^\sigma k^\delta \qquad (A.1) \\ H^{\alpha\beta} &= Tr \left\{ (\not{p} + M)\gamma^0 (\Gamma^\alpha)^\dagger \gamma^0 (\not{p}' + M)\Gamma^\beta \right\} \qquad (A.2) \end{aligned}$$

where the $+(-)$ sign of the L is used for $\nu(\overline{\nu})$ interactions. The amputated amplitudes Γ^α enter the weak charged currents. The latter ones can be written with the vector and axial currents as follows:

$$\begin{aligned} J^\alpha &= \overline{u}(p')\Gamma^\alpha u(p) = V^\alpha - A^\alpha \qquad (A.3) \\ V^\alpha &= \overline{u}(p') \left\{ \gamma^\alpha F_1(q^2) + \frac{i}{2M}\sigma^{\alpha\beta} q_\beta F_2(q^2) \right\} u(p) \qquad (A.4) \\ A^\alpha &= \overline{u}(p') \left\{ \gamma^\alpha \gamma_5 F_A(q^2) + \gamma_5 \frac{q^\alpha}{M} F_P(q^2) \right\} u(p) \qquad (A.5) \end{aligned}$$

With vector-current conservation $q_\alpha V^\alpha = 0$ and isospin symmetry, vector form factors F_1 and F_2 are given by the electromagnetic form factors of neutrons, G_E^V and G_M^V:

$$\begin{aligned} G_E^V(q^2) &= \left(1 - \frac{q^2}{M_V^2}\right)^{-2} \qquad (A.6) \\ G_M^V(q^2) &= (1 + \mu_p - \mu_n)\left(1 - \frac{q^2}{M_V^2}\right)^{-2} \qquad (A.7) \end{aligned}$$

where μ_p and μ_n are magnetic moment of proton and neutron. M_V is a vector mass and its value is measured to be 0.84 GeV by electron scattering experiments. On the other hand, the axial form factor is usually parametrized with a dipole approximation:

$$F_A(q^2) = g_A \left(1 - \frac{q^2}{M_A^{QE\ 2}}\right)^{-2} \qquad (A.8)$$

which corresponds to an exponential shape for the axial charged density distribution. F_P can be related to the F_A [51]:

$$F_P(q^2) = \frac{2M^2 F_A(q^2)}{m_\pi^2 - q^2} \tag{A.9}$$

where m_π is mass of a pion.

A.2 Charged current quasi-elastic interaction with a nucleus

In general, differential cross section of the quasi elastic scattering with a nucleus per unit volume can be expressed as follows:

$$\frac{d}{dr^3}\left(\frac{d\sigma}{d\Omega(k')dk^{0\prime}}\right) = \frac{G^2 c_{CC}^2}{4\pi^2}\frac{|\vec{k}'|}{|\vec{k}|} L_{\alpha\beta} W^{\alpha\beta} \tag{A.10}$$

where $L_{\alpha\beta}$ is a leptonic tensor represented by Eq. A.1. Hadronic tensor $W^{\alpha\beta}$ is decomposed as

$$W^{\alpha\beta} = W_s^{\alpha\beta} + iW_a^{\alpha\beta} \tag{A.11}$$

where $W_s^{\alpha\beta}$ ($W_a^{\alpha\beta}$) is a real symmetric (asymmetric) tensor. It can be expressed in terms of the polarization propagator:

$$W_{(s,a)}^{\alpha\beta} = -\frac{1}{\pi} Im \Pi_{(s,a)}^{\alpha\beta} \tag{A.12}$$

This is a general expansion of the many body framework (MBF) of electroweak interactions with nucleus, which successfully describe the measurement of inclusive electron-nucleus scattering [56]. Figure 3.3 shows an example of possible diagrams of the polarization propagator. Because it is difficult to calculate all diagrams precisely, effect of a few models which are considered to have large effect have been estimated, by using a method established for the electron-nucleus scattering as a reference.

A.2.1 Random phase space approximation

Following the MBF, the polarization effects in 1p1h contribution corresponding to (a) of Fig. 3.3 is estimated by random phase space approximation (RPA). In this approximation, many body interaction is assumed as an interaction of a particle in an averaged potential and the correction is given by sum of the chain diagrams. An effective potential V [63] is written as follows:

$$V = c_0\left\{f_0(\rho) + f_0'\vec{\tau_1}\vec{\tau_2} + g_0(\rho)\vec{\sigma_1}\vec{\sigma_2} + g_0'(\rho)\vec{\sigma_1}\vec{\sigma_2}\vec{\tau_1}\vec{\tau_2}\right\} \tag{A.13}$$

$$f_i(\rho(r)) = \frac{\rho(r)}{\rho(0)} f_i^{in} + \left(1 - \frac{\rho(r)}{\rho(0)} f_i^{(ex)}\right) \tag{A.14}$$

$$g_i(\rho(r)) = \frac{\rho(r)}{\rho(0)} g_i^{in} + \left(1 - \frac{\rho(r)}{\rho(0)} g_i^{(ex)}\right) \tag{A.15}$$

where $\vec{\sigma}$ and $\vec{\tau}$ are Pauli matrices acting on the nucleon spin and isospin spaces, respectively. $\rho(r)$ is the nuclear density. The c, f and g are parameters determined from nuclear electric and magnetic moments calculated with a non-relativistic nuclear dynamics scheme.

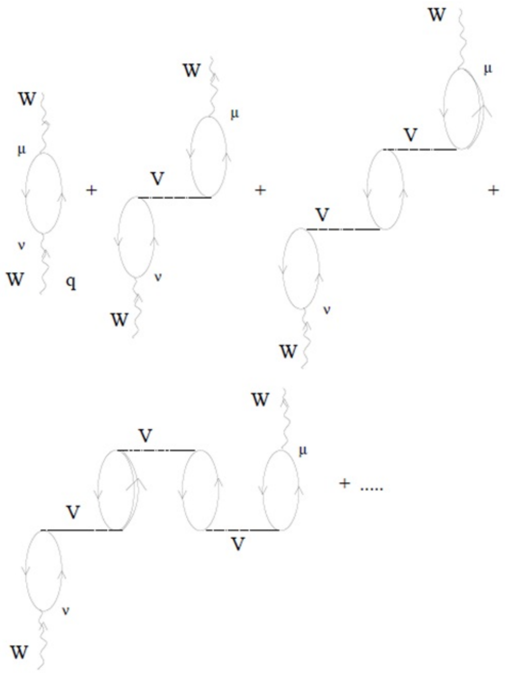

Figure A.1: Set of irreducible diagrams responsible for the polarization effects in the 1p1h contribution [64]

A.3 Charged current single pion production

Differential cross section of the CC1π interaction is calculated by assuming the process is composed of excitation of the Δ resonance ($\nu + N \rightarrow l + \Delta$) and decay of Δ ($\Delta \rightarrow N^{'}\pi$). It is written as follows [50]:

$$\frac{d\sigma}{dq^2} = \frac{1}{32\pi}\frac{1}{M^2 E_\nu^2}G^2 c_{CC}^2 L_{\alpha\beta}H^{\alpha\beta}_{RES} \tag{A.16}$$

This is the same equation as the CCQE with nucleon (Eq. 3.1) except for the $H^{\beta\alpha}_{RES}$ written as follows [70]:

$$H^{\alpha\beta}_{RES} = <\Delta|V^\alpha - A^\alpha|N><\Delta|V^\beta - A^\beta|N>^* \tag{A.17}$$

The cross section is dominated by the axial-vector contribution as follows:

$$\frac{d\sigma}{dq^2} = \frac{G_F^2 C_{cc}}{12\pi}\frac{2m_N E_\nu + m_N^2 - m_{\Delta^{++}}^2}{2m_N E_\nu}\left(\frac{m_\Delta + m_N}{m_\Delta}\right)^2 |C_5^A(q^2)|^2 \tag{A.18}$$

$$C_5^A(q^2) = \frac{C_5^A(0)}{\left(1 + \frac{Q^2}{M_A^{RES\ 2}}\right)^2} \tag{A.19}$$

where C_5^A is a form factor parameterized by $C_5^A(0)$ and M_A^{RES}.

A.4 Charged current deep inelastic scattering

The cross section of the DIS interaction can be approximated as an interaction with a quark as follows:

$$\frac{d^2\sigma}{dxdy} = \frac{G_F^2 m_N E_\nu}{\pi}\left[\left(1 - y + \frac{1}{2}y^2 + C_1\right)F_2(x) + y\left(1 - \frac{1}{2}y + C_2\right)xF_3(x)\right] \tag{A.20}$$

$$\begin{aligned}
C_1 &= \frac{m_l^2(y-2)}{4m_N E_\nu x} - \frac{m_N x y}{2E_\nu} - \frac{m_l^2}{4E_\nu^2} && \text{(A.21)}\\
C_2 &= -\frac{m_l^2}{4m_N E_\nu x} && \text{(A.22)}\\
x &= -\frac{q^2}{2m_N(E_\nu - E_\mu)} && \text{(A.23)}\\
y &= \frac{E_\nu - E_\mu}{E_\nu} && \text{(A.24)}
\end{aligned}$$

where F_2 and F_3 are composed of parton distribution functions $Q(x)$ and $\overline{Q}(x)$:

$$\begin{aligned}
F_2(x) &= 2x\left(Q(x) + \overline{Q}(x)\right) && \text{(A.25)}\\
xF_3(x) &= 2x\left(Q(x) - \overline{Q}(x)\right) && \text{(A.26)}
\end{aligned}$$

A.5 Charged current coherent interaction

The cross section is written by using the cross section of pion-nucleus scattering ($\pi^+ N \to \pi^+ N$) as follows: [83]

$$\frac{d\sigma}{dQ^2dydt} = \frac{G_F^2 c_{CC}^2 \theta_C f_\pi^2}{2\pi^2}\frac{E}{|q|}uv[(G_A - \frac{1}{2}\frac{Q^2_{min}}{Q^2 + m_\pi^2})^2 + \frac{y}{4}(Q^2 - Q^2_{min})\frac{Q^2_{min}}{(Q^2 + m_\pi^2)^2}] \times \frac{d\sigma(\pi^+ N \to \pi^+ N)}{dt} \tag{A.27}$$

where $Q^2 = q^2 - \nu^2$, $\nu = k^0 - k^{0}$’ is the energy transfer, $Q_{min} = m_l^2 y/(1-y)$ is the high energy approximation to the true minimal Q^2 and t is the modulus of the four-momentum transfer squared between incoming virtual boson and outgoing pion. The kinematical factors u and v are given by $u, v = (k^0 + k^{0}$’$\pm|q|)/2k^0$. f_π is a pion decay constant. The axial vector form factor is defined by

$$G_A = \frac{m_A^2}{Q^2 + m_A^2} \tag{A.28}$$

with a typical value for the axial vector meson mass m_A of 0.95 GeV.

Appendix B

Water module detector construction

The water module detector had been constructed from October 2015 to March 2016. Procedure of the construction is manualized for keeping sufficient mechanical and optical qualities of the detector. Figure B.1 shows a flow of the procedure.

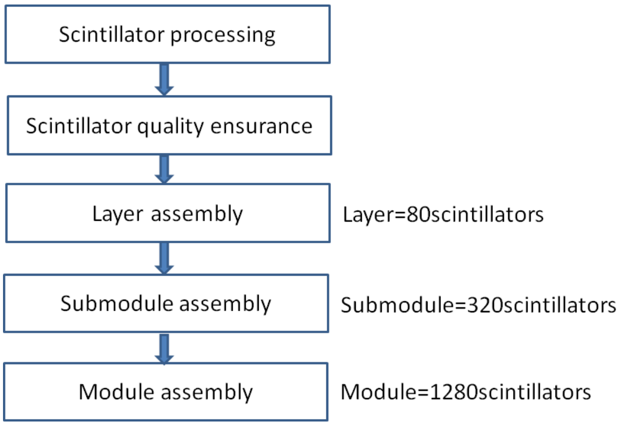

Figure B.1: A flow of the detector construction procedure.

First, the scintillators are produced in Fermi National Accelerator Laboratory. The groove on the scintillator to put the wavelength shifting fiber and reflectors around the scintillators are co-excluded. The scintillators are processed by G-tech company to make slits and adjust their length. The fiber is put in the groove of the processed scintillator and glued by the optical cement. In order to make this procedure efficient, a semi-automated gluing system is developed as shown in Fig. B.2. The system is on aluminum plate which has sufficient flatness. The scintillators and fibers are fixed on the plate by jigs with a position accuracy of 0.5 mm, as shown in Fig. B.2. Along with the fiber, optical cement is automatically injected by movable stages and a dispenser. For making the gluing smoothly, following parameters are optimized: speed of the movable stage, pressure of the dispenser, thickness of the needle of the syringe and softness of the cement. 20 scintillators are glued in a cycle for 30 minutes and three cycles are performed per day. To harden the cement, they are naturally dried for a day. After the drying, the reflector is pained on the optical cement by hand as shown in Fig. B.3.

Second, qualities of the scintillators are checked. Weights of scintillators are measured by weight, including the fibers, optical cements and reflectors as shown in Fig. B.4. Weight of all scintillators are measured because it is used for the physics analysis as the weight of non-water material in water target region. Weight of the fiber, optical cement and reflector are measured by sampling part of the scintillators to make sure composition of the scintillator material. Volume of the scintillators is also measured by sampling part of the scintillators by using Archimedese's method to calculate the weight of the water in the water target region, as shown in Fig. B.4. Next, before assembly, qualities of all scintillators are checked by eye. Checked items are as follows: if there is a crack of the fiber, if the fiber is floated from the scintillator and if the optical cement is enoughly covered by the reflector. In addition, light yield of part of the scintillator (10% of all) is measured by cosmic ray. If the mean light yield of a scintillator is less than threshold (15p.e.), the scintillator is removed and all of the scintillators in the same cycle as the problematic scintillator are checked by cosmic ray. After applying these criteria, 5% of the scintillators are removed. Totally 1400 scintillators are proceeded for six weeks from October to November 2015 with six human resources per day.

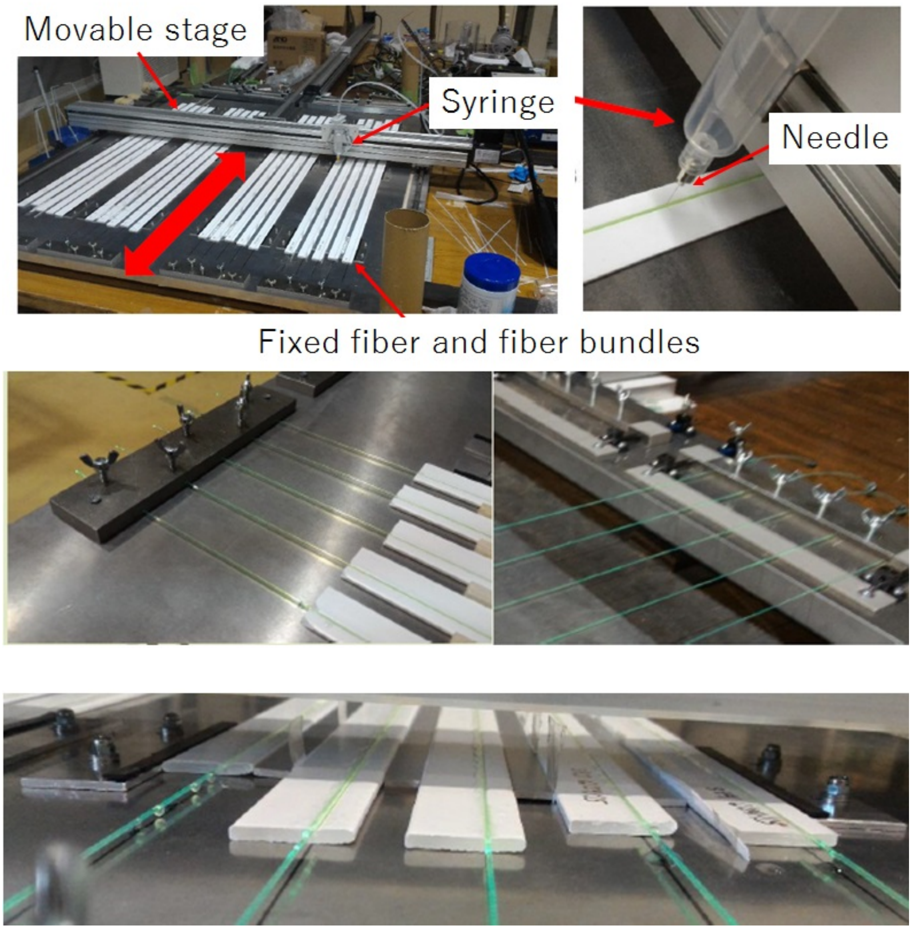

Figure B.2: View of the gluing system (top) and view of the jigs to fix the fibers and scintillators (bottom).

Third, the scintillators which pass the quality criteria are assembled. They are fixed with the abs resin frame as shown in Fig. B.5. First, the grid scintillators are eventually inserted into grooves of the frame. After setting a jig to fix curvature of the scintillator, light yield of all inserted scintillators is checked by LED and eye. If there is a dead channel, it is replaced. After that, the frame and edge of the scintillators are glued with silicon glue by a dispenser. To harden the glue, they are naturally dried in a night. After measuring position of each grid scintillator by metal scale as shown in Fig. B.6, parallel scintillators are set and glued on the grid scintillators in the same way as the grid scintillators. 80 scintillators are fixed with a frame

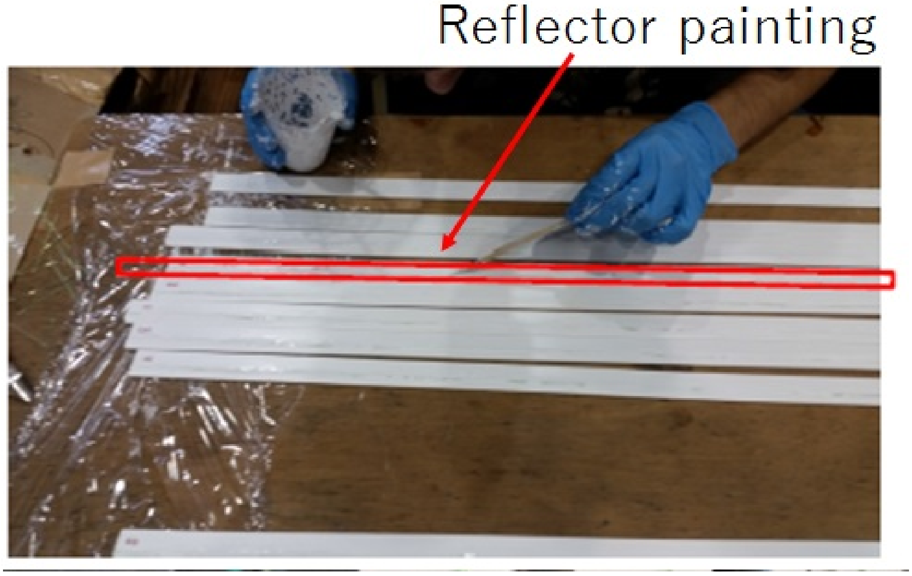

Figure B.3: View of the reflector painting work.

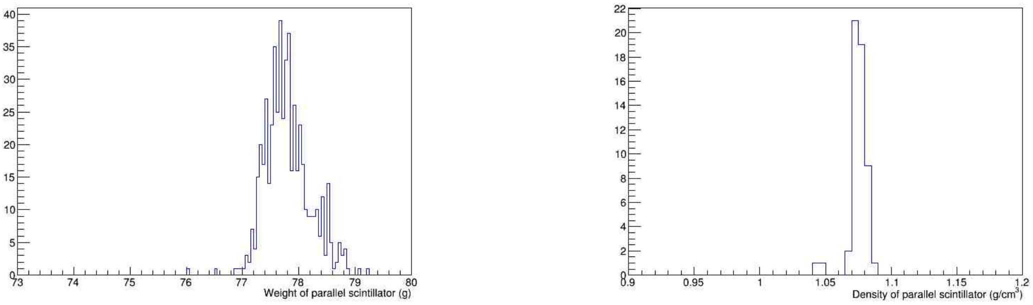

Figure B.4: Measured weight (left) of density (right) of the parallel scintillators

and called a “layer”. Totally 16 layers are assembled for six weeks from October to November 2015 with six human resources per day. Next, surface of the scintillator layer is painted by black silicon painting to reduce optical crosstalk between the scintillators from a few percents to less than one percent. The scintillators are painted from both top and bottom of the layers by spray. This procedure is added after testing the first sub module and done in January 2016.

The four layers are overlaid and called a “submodule”. The fibers from a submodule are collected and inserted together into the fiber bundles as shown in Fig. 5.5. 10 fiber bundles are used for a submodule to bundle 320 channels. In order to glue the fiber and fiber bundles with enough amount of the optical cement to prevent water leak, the optical cement is poured into the hole of the fiber bundle by gravity. After the gluing, submodules are shipped to Suzuno Giken company for polishing the surface of the fiber bundle by a diamond cutter to ensure sufficient and uniform amount of the light yield. Completed submodule is promptly tested by cosmic to check light yield of the scintillators and there was no dead channel in this stage.

In March 2016, all four submodules are jointed with a specific jig and called a “module”. After measuring the distance between layers and curvature of the layers, the module is installed into the water tank as shown in Fig. B.7. The module is once lifted above the tank and down along with a rail inside the tank for the installation. After landing, the layers are shifted by using screws to match the fiber bundles and holes of the tank. Finally, layers and bundles are

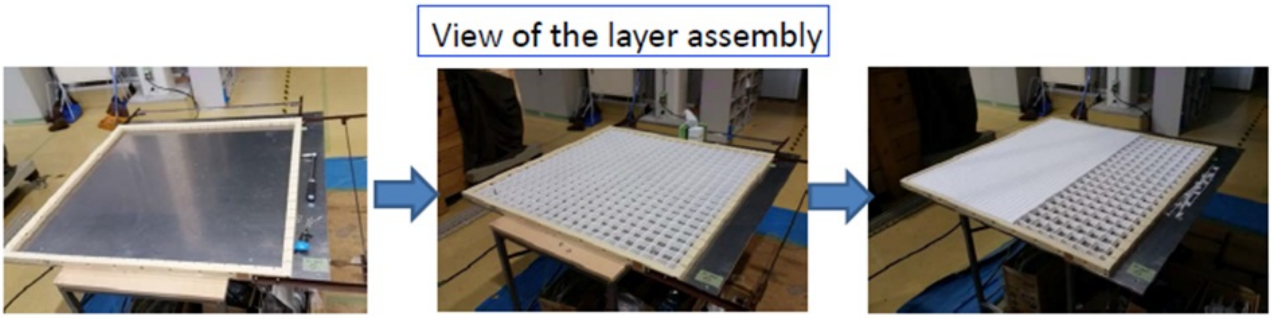

Figure B.5: View of the layer assembly.

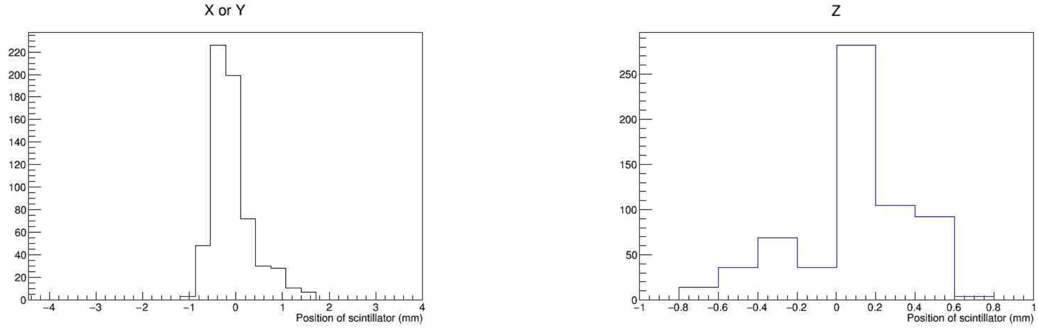

Figure B.6: Measured position of parallel scintillators along with xy-axis(left) and z-axis (right). Difference of the measured and designed values is shown.

fixed with the water tank by screws. After the confirmation of no water leak, the MPPCs and electronics are attached in the electronics boxes as shown in Fig. B.8 and detector is completed. The performance of the MPPCs and electronics has been evaluated channel by channel by a test measurement separately. The detector was installed at the experimental hall, SS floor of the neutrino monitor building in July 2016 as shown in Fig. B.9.

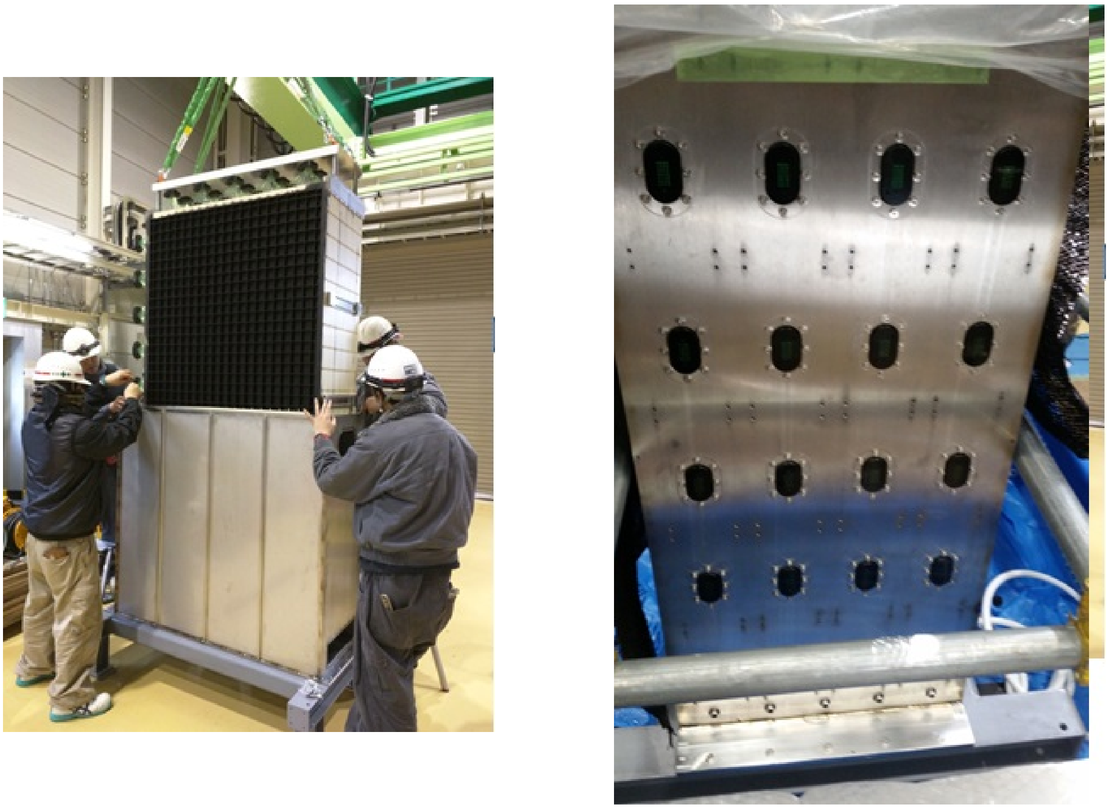

Figure B.7: View of the installation work (left) and installed fiber bundles(right).

Figure B.8: View of the MPPCs and TFBs set in the electronics hat.

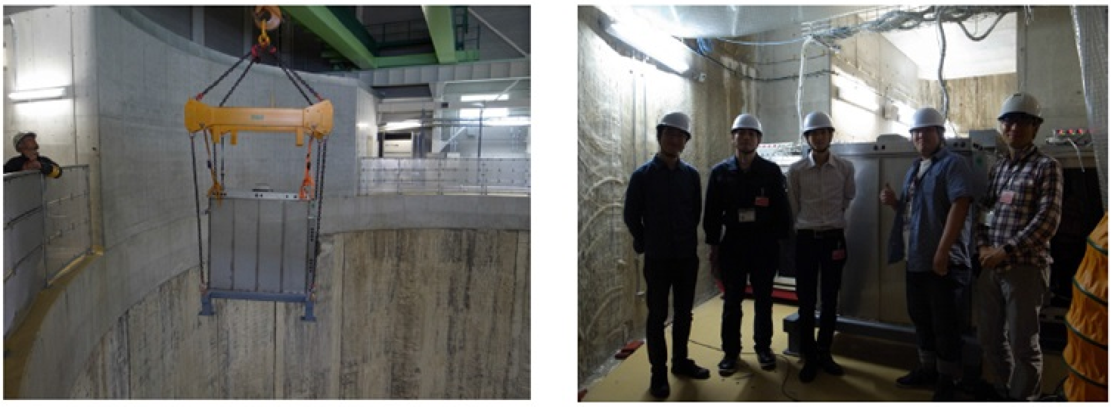

Figure B.9: View of the detector installation.

Appendix C

Details of event selection criteria for on-axis detectors

C.1 Two-dimensional track reconstruction algorithm

At the on-axis detectors, 2D track is reconstructed in x-z and y-z view independently based on the hit pattern of the scintillators. A track reconstruction algorithm, Cellular automaton, is used for all three detectors. For the INGRID and Proton Module, tracks with forward scattered angle is searched along with z-axis. For the water module, tracks are searched along with both z-axis and xy-axis to achieve large angular acceptance. The track reconstruction algorithm for the water module is as follows:

1. Long track search along z-axis
2. Long track search along xy-axis
3. Short track search along z-axis
4. Short track search along xy-axis
5. Joint broken tracks

Track search

The cellular automaton pairs two hits in the side-by-side planes as a cell and the cells are connected as a track based on a likelihood fitting with a linear function. Because the geometry of the scintillator of the water module is different from that of the INGRID and PM, used parameters for tracking are different as shown in Table C.1. When it is applied along z-axis (xy-axis), the scintillators are divided into plane as shown in a left(right) figure in Fig. C.1. First, based on the algorithm, long tracks which have more than 6 hits are reconstructed along z-axis. Only tracks with an angle of less than 60 degree with respect to the neutrino beam are reconstructed in this step. Because the grid scintillator planes do not always have hit when a charged particle go through the detector with small scattering angle respect to the beam, the number of allowed skipped layers is set to 5. This corresponds that the number of allowed skipped parallel scintillator layer is 1 because two grid scintillators are located per one parallel scintillator. Second, long tracks along xy-axis are reconstructed. Only tracks with an angle of more than 60 degree with respect to the neutrino beam are reconstructed. In this step, used hits in the first step are reused but they are not counted as the number of hits for the reconstructed track. The same procedure is repeated to search short tracks at step 3 and 4.

After each track search, non-used hits around the reconstructed track are searched. If a distance between the reconstructed track and non-used hit is less than 2.5 cm and the hit is not shared with any reconstructed track, the hit is merged with the track. The z position of the merged hits should be between the upstream and downstream or equal to downstream of the reconstructed track.

Joint broken tracks

Sometimes, secondary particle goes through a gap between scintillator layers and more than 2 tracks are reconstructed from one track, as shown in Fig. C.3. To solve this, a pair of the reconstructed 2D tracks is merged into one track based on following criteria:

- a distance of two reconstructed tracks at the middle point of them is less than 2.5 cm
- difference of angle between two tracks is less than 20 degrees

The former threshold of 2.5 cm is determined the size of the gap. The latter threshold of 20 degrees is determined based on the angle distribution of the broken tracks, as shown in Fig. C.2. Figure C.4 shows typical neutrino event display of the reconstructed 2D tracks.

In addition, the performance of the 2D track reconstruction is also evaluated by the detector Monte Carlo. Figure C.5 shows the 2D track reconstruction efficiency tested by the sample of single muons with momenta of 500 MeV injected from the central region of the water module detector. In this test, more than zero reconstructed track is required both or either of x-z and y-z view. The efficiency is more than 99% for all scattering angle region. The efficiency is low with the angle of muon with 0-20, 80-100 and 160-180 degrees respect to the beam is due to the geometry of the detector.

Table C.1: Used parameters for the cellular automaton

Parameter	WM	INGRID and PM
# of allowed skipped layers for making cell	5	1
limit χ^2 for making neighbours	3.0	3.0 for short cell 1.5 for long cell
# of required hit for tracking	6 for long track 3 for short track	3

C.2 Event selection criteria for Proton Module and INGRID

Because the geometry of the scintillator of the water module is different from that of the INGRID and PM, used parameters for event selection are different as shown in Table C.2. These are tuned to get similar detection efficiencies of the CC interactions among the detectors.

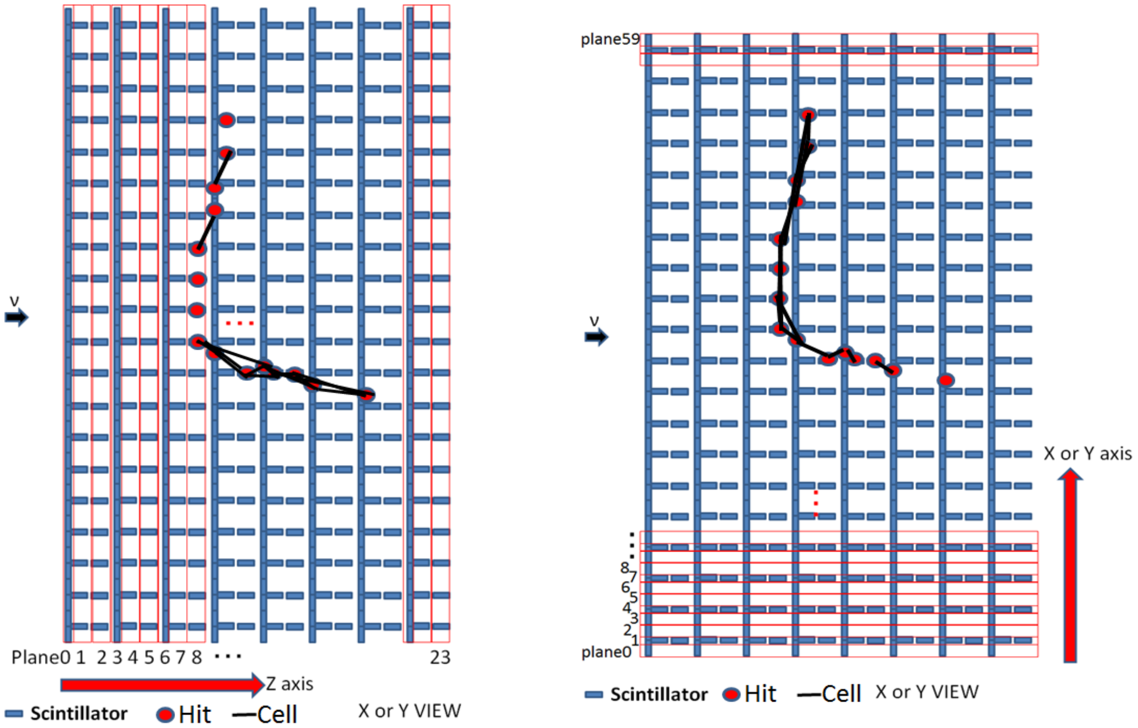

Figure C.1: Definition of plane for the cellular automaton along z-axis (left) and xy-axis (right). The black lines are cells which are pair of two hits in the next plane.

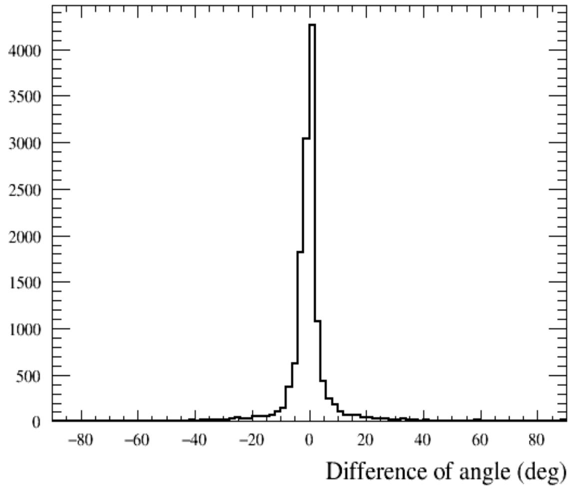

Figure C.2: Difference of the angle of the broken tracks

Figure C.3: Example of the broken track (left) and track after merging (right). Green bars are scintillators, red circles are observed hits and black lines are reconstructed 2D track.

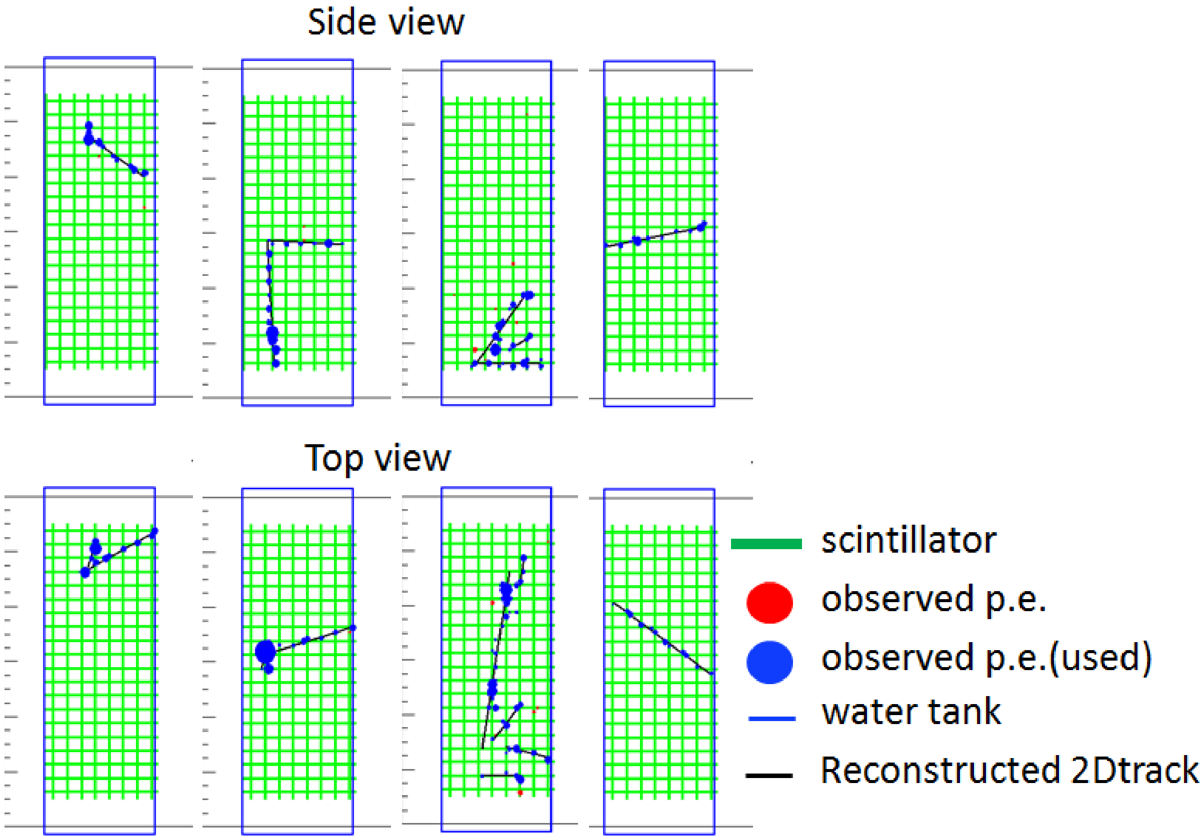

Figure C.4: Example of event display of reconstructed 2D tracks

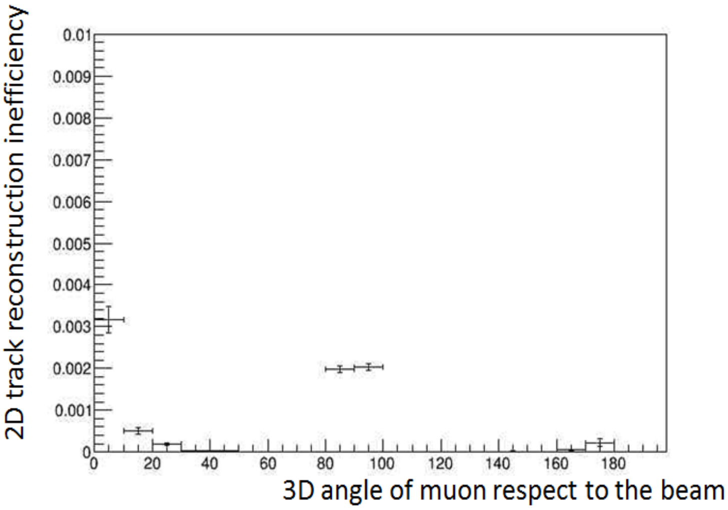

Figure C.5: 2D track reconstruction inefficiency estimated by detector Monte Carlo as a function of muon angle. It is checked using the sample of single muons with momenta of 500 MeV and with vertex inside the central region (20 cm× 20 cm × 10 cm) of the detector.

Table C.2: Parameters used for the event selection criteria for the on-axis detectors.

	WM	PM	INGRID
Time clustering	±50 nsec	±50 nsec	±50 nsec
2D track reconstruction	Table C.1	Table C.1	Table C.1
Track matching with INGRID	±35 deg	±35 deg	-
	±150 mm	±150 mm	-
3D track matching	<=1 parallel plane	<=1 plane	<=1 plane
Vertexing	<3 plane	<2 plane	<2 plane
	<150 mm	<150 mm	<150 mm
Beam timing	±100 nsec	±100 nsec	±100 nsec
Front-veto	>=second parallel plane	>=second plane	>=first plane
Fiducial	700 mm×700 mm	700 mm×700 mm	700 mm×700 mm
Reconstructed angle	<45 deg	<45 deg	<45 deg
Acceptance cut	-	-	○

Appendix D

Details of selected event distributions at on-axis

In this section, a few distributions of the selected events in Section 7 are summarized. Figures D.1–D.5 show the true neutrino energy, muon p-θ and proton p-θ distributions of the Proton Module. Figures D.6–D.9 show the reconstructed track angle of the water module and Proton Module.

True neutrino energy

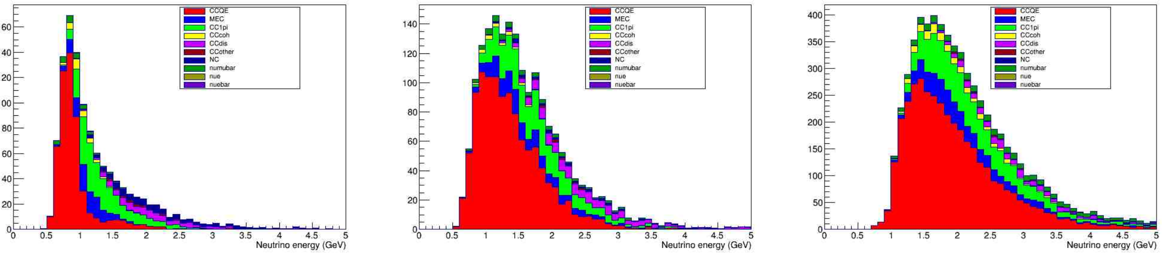

1 track,
μ stop

1 track,
μ escape

1 track,
μ penetrate

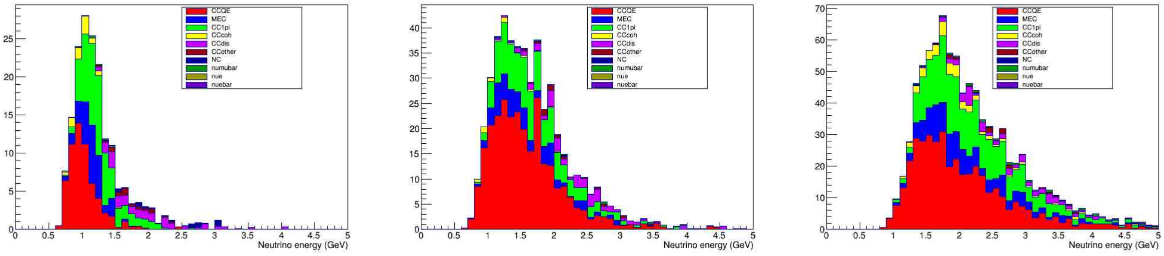

2 track,
μ stop, p stop

2 track,
μ escape, p stop

2 track,
μ penetrate, p stop

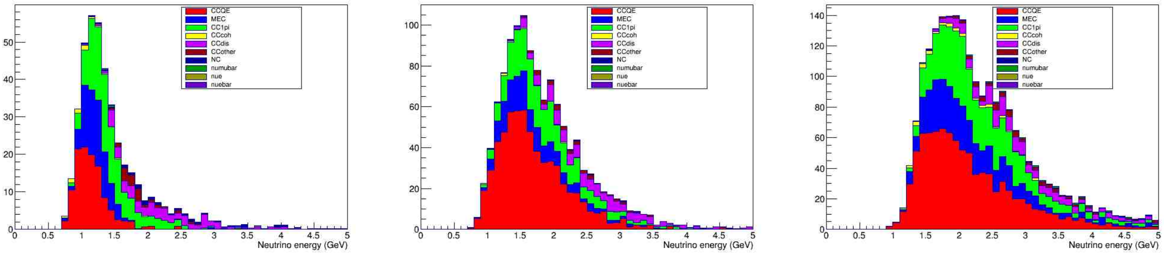

2 track,
μ stop, p escape

2 track,
μ escape, p escape

2 track,
μ penetrate, p escape

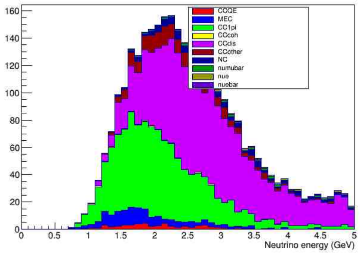

multi track

Figure D.1: True neutrino energy for each sample for the Proton Module predicted by MC with the parameters of the neutrino flux and interaction tuned with the best fit of the ND280 measurement.

True muon momentum

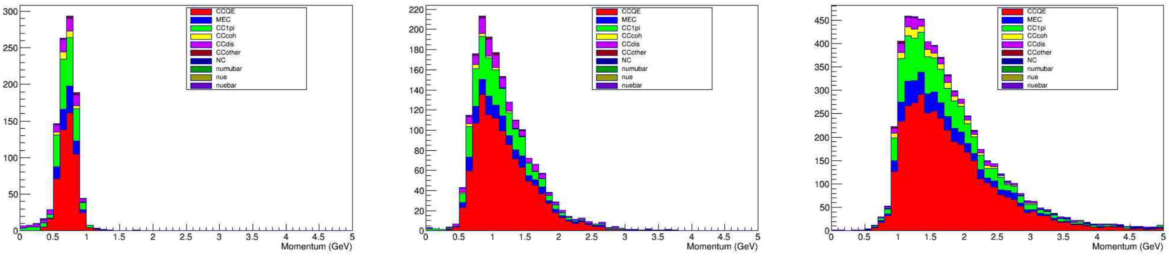

1 track,
μ stop

1 track,
μ escape

1 track,
μ penetrate

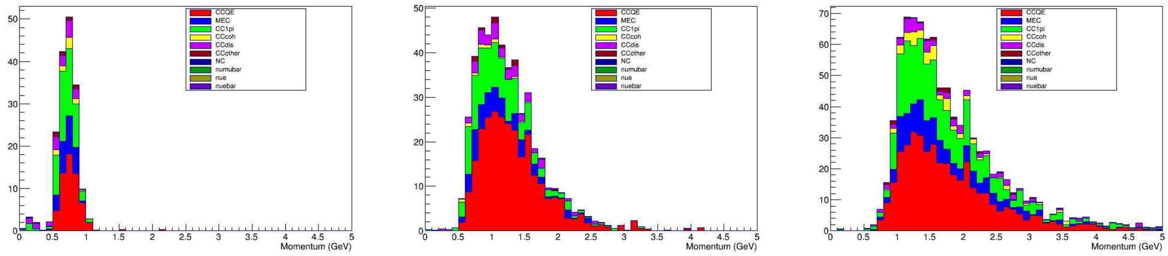

2 track,
μ stop, p stop

2 track,
μ escape, p stop

2 track,
μ penetrate, p stop

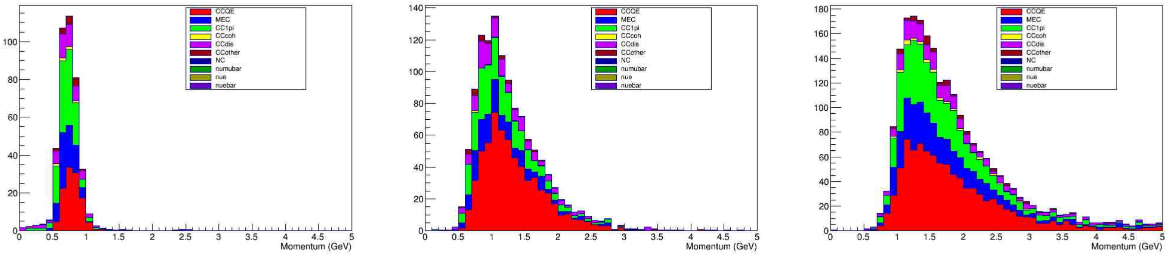

2 track,
μ stop, p escape

2 track,
μ escape, p escape

2 track,
μ penetrate, p escape

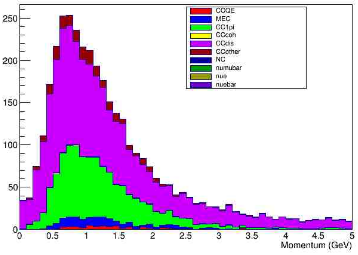

multi track

Figure D.2: True muon momentum for each sample for the Proton Module predicted by MC with the parameters of the neutrino flux and interaction tuned with the best fit of the ND280 measurement.

True muon angle

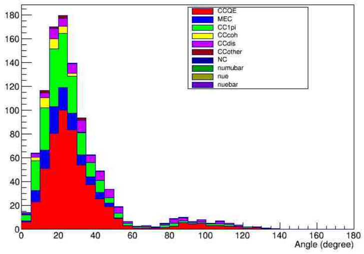

1 track,
μ stop

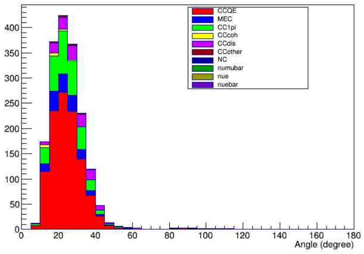

1 track,
μ escape

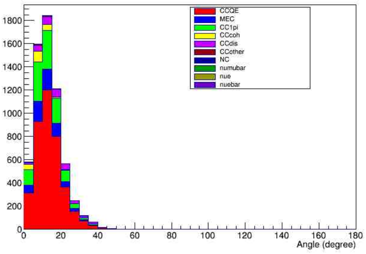

1 track,
μ penetrate

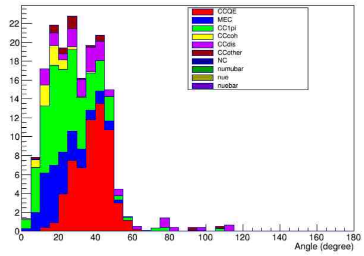

2 track,
μ stop, p stop

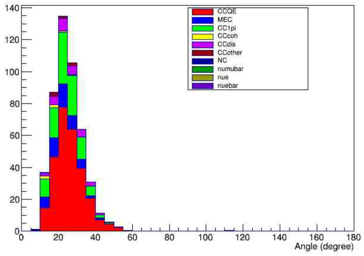

2 track,
μ escape, p stop

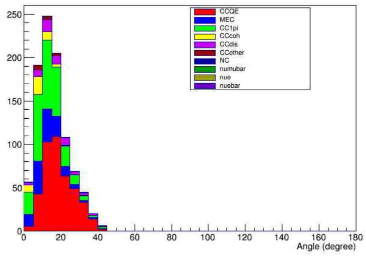

2 track,
μ penetrate, p stop

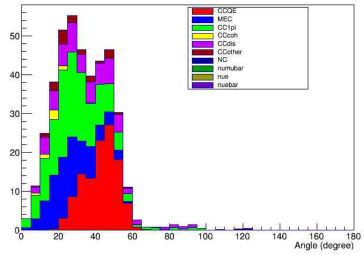

2 track,
μ stop, p escape

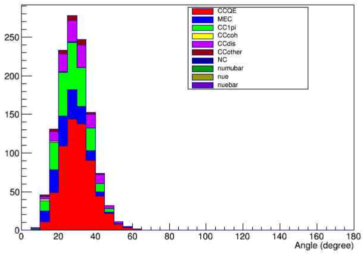

2 track,
μ escape, p escape

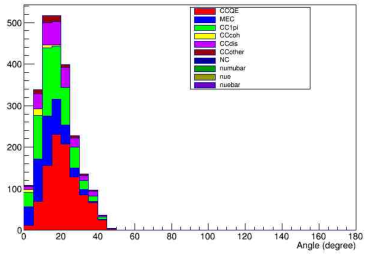

2 track,
μ penetrate, p escape

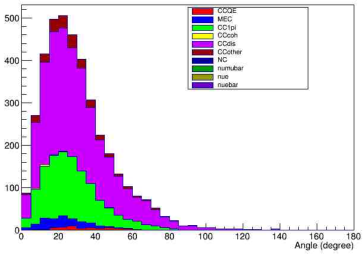

multi track

Figure D.3: True muon angle for each sample for the Proton Module predicted by MC with the parameters of the neutrino flux and interaction tuned with the best fit of the ND280 measurement.

True proton momentum

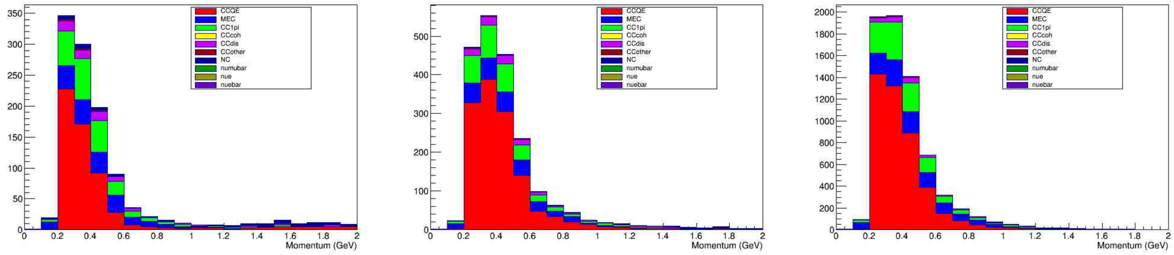

1 track,
μ stop

1 track,
μ escape

1 track,
μ penetrate

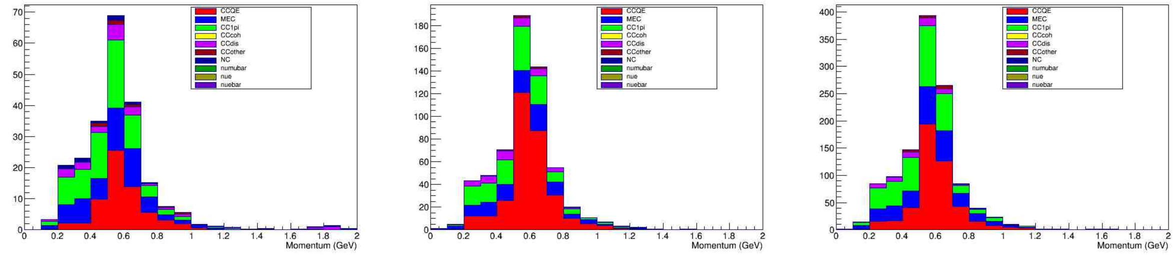

2 track,
μ stop, p stop

2 track,
μ escape, p stop

2 track,
μ penetrate, p stop

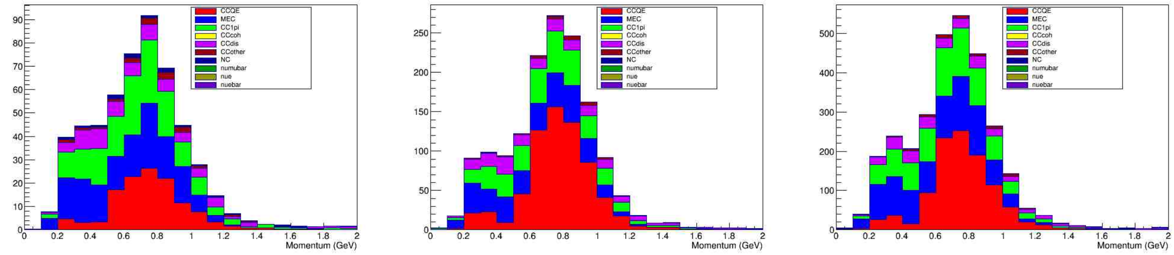

2 track,
μ stop, p escape

2 track,
μ escape, p escape

2 track,
μ penetrate, p escape

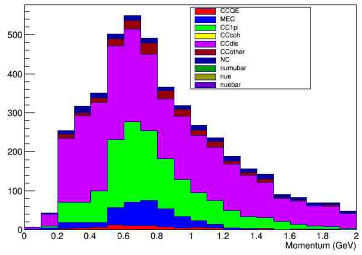

multi track

Figure D.4: True proton momentum for each sample for the Proton Module predicted by MC with the parameters of the neutrino flux and interaction tuned with the best fit of the ND280 measurement.

True proton angle

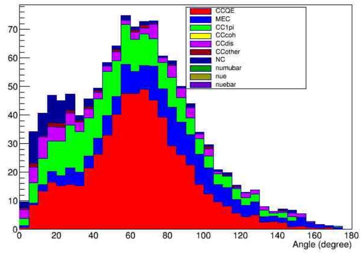

1 track,
μ stop

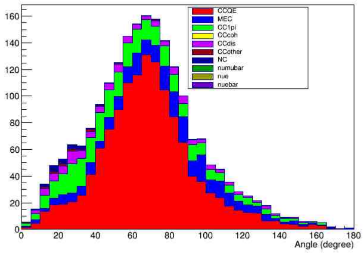

1 track,
μ escape

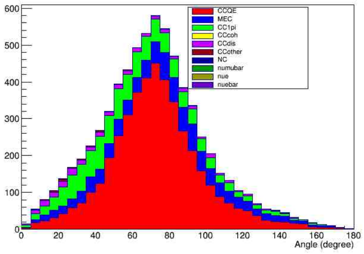

1 track,
μ penetrate

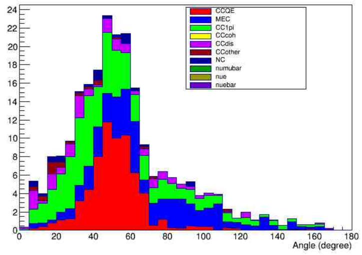

2 track,
μ stop, p stop

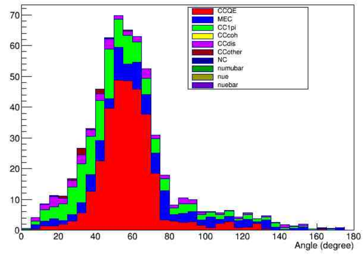

2 track,
μ escape, p stop

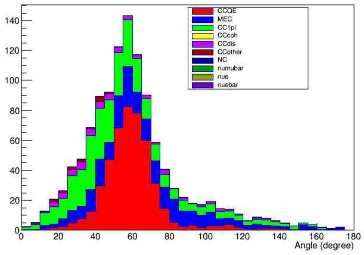

2 track,
μ penetrate, p stop

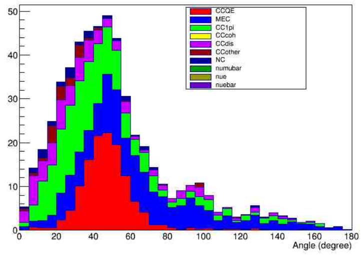

2 track,
μ stop, p escape

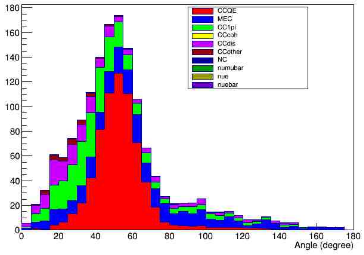

2 track,
μ escape, p escape

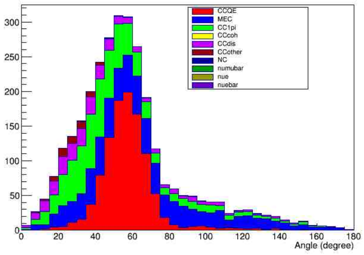

2 track,
μ penetrate, p escape

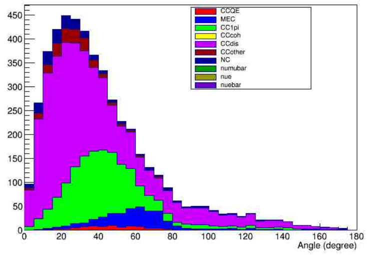

multi track

Figure D.5: True proton angle for each sample for the Proton Module predicted by MC with the parameters of the neutrino flux and interaction tuned with the best fit of the ND280 measurement.

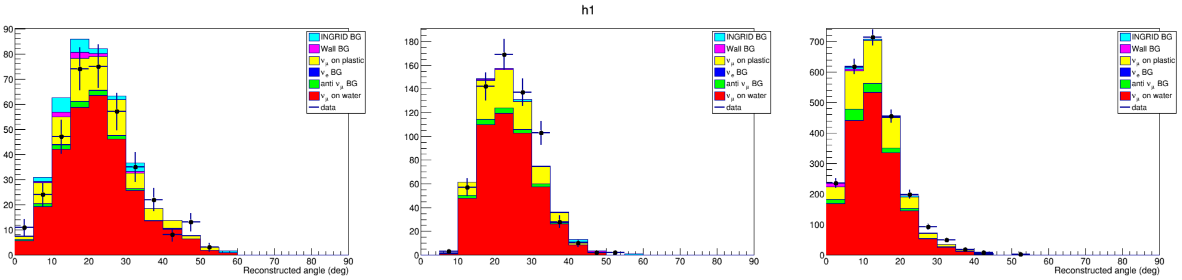

1 track,
μ stop

1 track,
μ escape

1 track,
μ penetrate

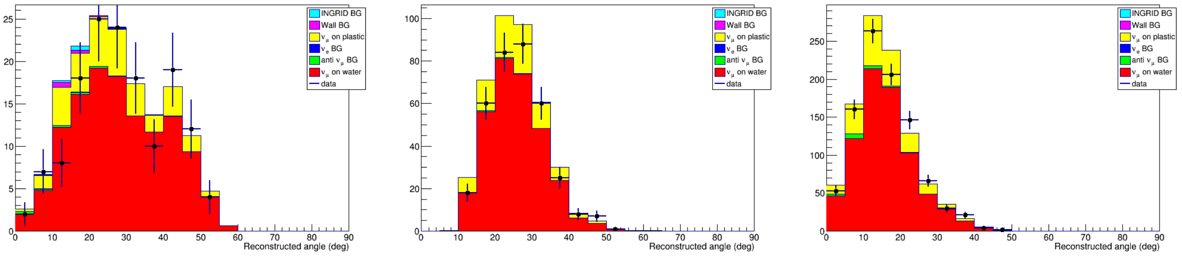

2 track,
μ stop, p stop

2 track,
μ escape, p stop

2 track,
μ penetrate, p stop

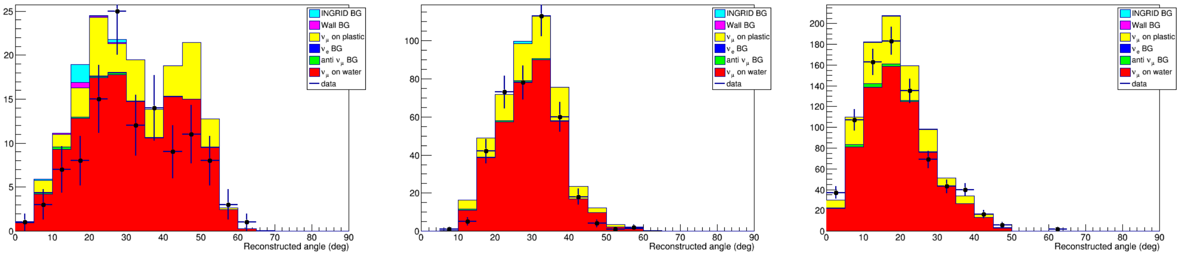

2 track,
μ stop, p escape

2 track,
μ escape, p escape

2 track,
μ penetrate, p escape

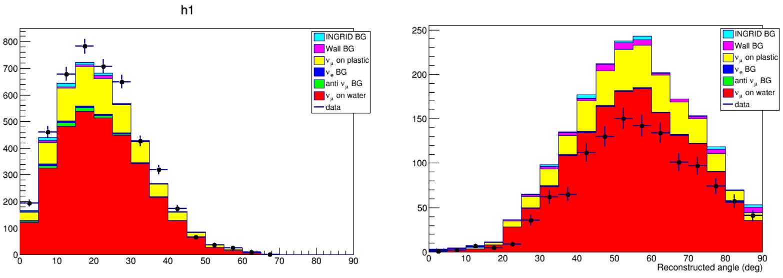

multi track

large angle

Figure D.6: Reconstructed angle of the muon like track among a vertex for each sample for the water module. Black lines show statistical uncertainties of Data. Histograms show MC prediction with the parameters of the neutrino flux and interaction tuned with the best fit of the ND280 measurement.

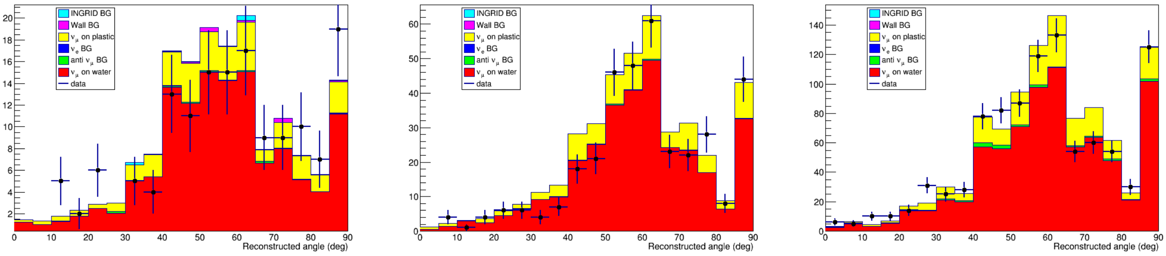

2 track,
μ stop, p stop

2 track,
μ escape, p stop

2 track,
μ penetrate, p stop

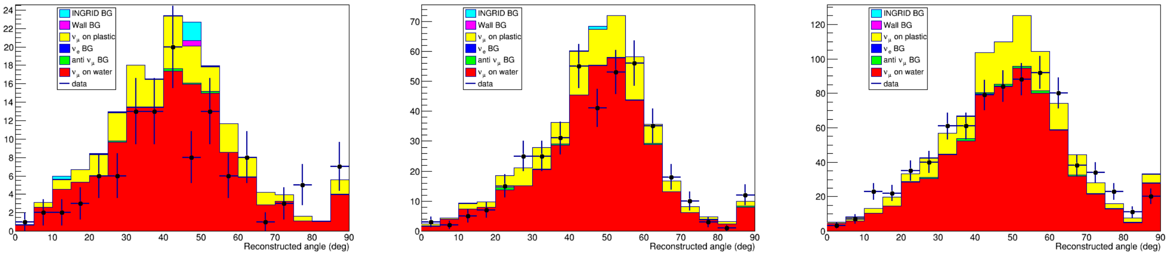

2 track,
μ stop, p escape

2 track,
μ escape, p escape

2 track,
μ penetrate, p escape

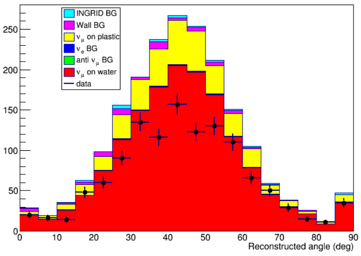

large angle

Figure D.7: Reconstructed angle of the proton like track among a vertex for each sample for the water module. Black lines show statistical uncertainties of Data. Histograms show MC prediction with the parameters of the neutrino flux and interaction tuned with the best fit of the ND280 measurement.

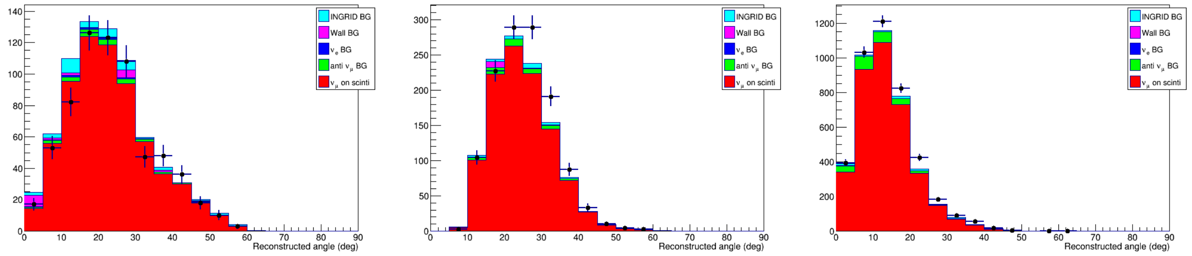

1 track,
μ stop

1 track,
μ escape

1 track,
μ penetrate

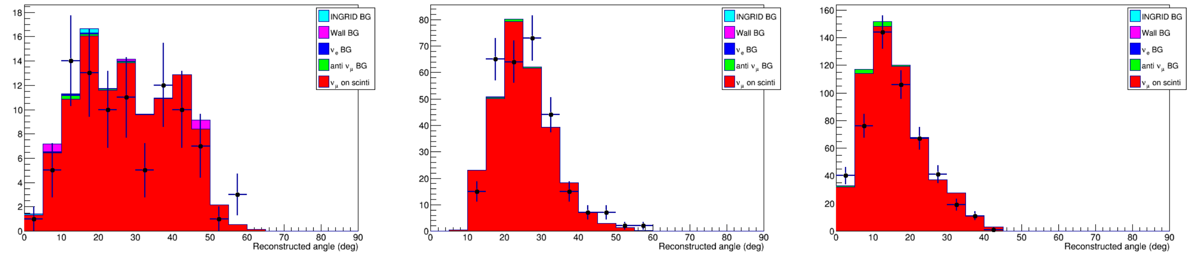

2 track,
μ stop, p stop

2 track,
μ escape, p stop

2 track,
μ penetrate, p stop

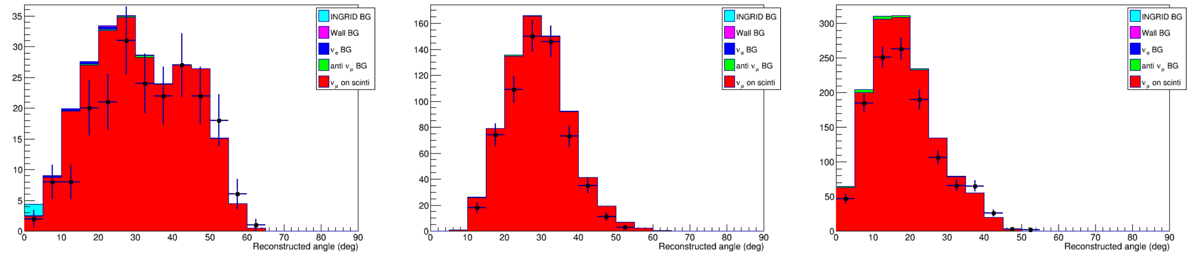

2 track,
μ stop, p escape

2 track,
μ escape, p escape

2 track,
μ penetrate, p escape

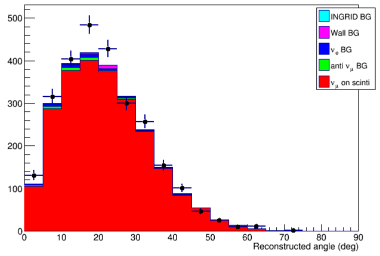

multitrack

Figure D.8: Reconstructed angle of the muon like track among a vertex for each sample for the Proton Module. Black lines show statistical uncertainties of Data. Histograms show MC prediction with the parameters of the neutrino flux and interaction tuned with the best fit of the ND280 measurement.

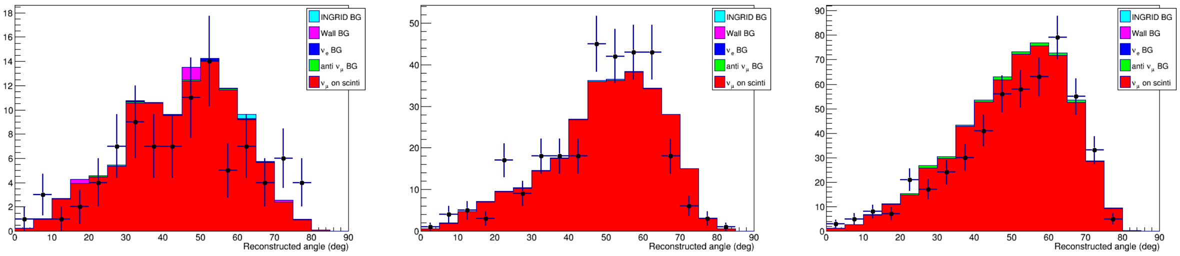

2 track,
μ stop, p stop

2 track,
μ escape, p stop

2 track,
μ penetrate, p stop

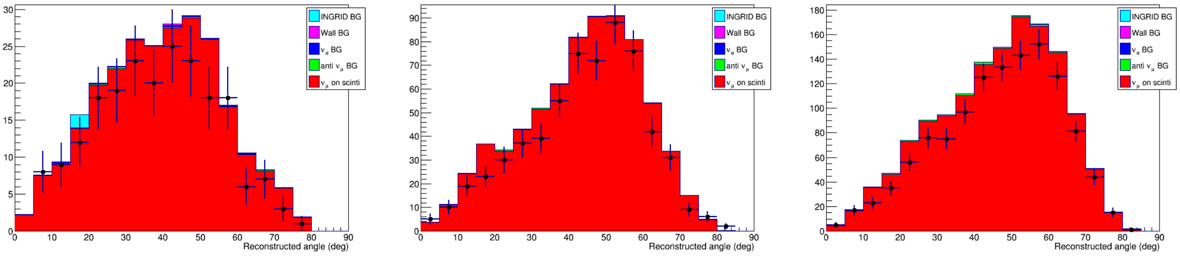

2 track,
μ stop, p escape

2 track,
μ escape, p escape

2 track,
μ penetrate, p escape

Figure D.9: Reconstructed angle of the proton like track among a vertex for each sample for the Proton Module. Black lines show statistical uncertainties of Data. Histograms show MC prediction with the parameters of the neutrino flux and interaction tuned with the best fit of the ND280 measurement.

Bibliography

[1] Y. Fukuda *et al.* [Super-Kamiokande Collaboration], Phys. Rev. Lett. **81**, 1562 (1998) [hep-ex/9807003].

[2] M. Fukugita and T. Yanagida, Phys. Lett. B **174**, 45 (1986). doi:10.1016/0370-2693(86)91126-3

[3] Z. Maki, M. Nakagawa and S. Sakata, Prog. Theor. Phys. **28**, 870 (1962).

[4] C.Patrignari *et al.* (Particle Data Group), Chin. Phys. C, 40, 100001 (2016).

[5] C. L. Cowan, F. Reines, F. B. Harrison, H. W. Kruse and A. D. McGuire, Science **124**, 103 (1956). doi:10.1126/science.124.3212.103

[6] R. Davis, Jr., Phys. Rev. **97**, 766 (1955). doi:10.1103/PhysRev.97.766

[7] G. Danby, J. M. Gaillard, K. A. Goulianos, L. M. Lederman, N. B. Mistry, M. Schwartz and J. Steinberger, Phys. Rev. Lett. **9**, 36 (1962). doi:10.1103/PhysRevLett.9.36

[8] S. Schael *et al.* [ALEPH and DELPHI and L3 and OPAL and SLD Collaborations and LEP Electroweak Working Group and SLD Electroweak Group and SLD Heavy Flavour Group], Phys. Rept. **427**, 257 (2006) doi:10.1016/j.physrep.2005.12.006 [hep-ex/0509008].

[9] R. Davis, Jr., D. S. Harmer and K. C. Hoffman, Phys. Rev. Lett. **20**, 1205 (1968). doi:10.1103/PhysRevLett.20.1205

[10] J. N. Abdurashitov *et al.* [SAGE Collaboration], J. Exp. Theor. Phys. **95**, 181 (2002) [Zh. Eksp. Teor. Fiz. **122**, 211 (2002)] doi:10.1134/1.1506424 [astro-ph/0204245].

[11] P. Anselmann *et al.* [GALLEX Collaboration], Phys. Lett. B **285**, 376 (1992). doi:10.1016/0370-2693(92)91521-A

[12] K. S. Hirata *et al.* [Kamiokande-II Collaboration], Phys. Rev. Lett. **65**, 1297 (1990). doi:10.1103/PhysRevLett.65.1297

[13] J. N. Bahcall, Phys. Scripta T **121**, 46 (2005) doi:10.1088/0031-8949/2005/T121/006 [hep-ph/0412068].

[14] L. Wolfenstein, Phys. Rev. D **17**, 2369 (1978). doi:10.1103/PhysRevD.17.2369

[15] K. S. Hirata *et al.* [Kamiokande-II Collaboration], Phys. Lett. B **205**, 416 (1988). doi:10.1016/0370-2693(88)91690-5

[16] C. Berger *et al.* [Frejus Collaboration], Phys. Lett. B **227**, 489 (1989). doi:10.1016/0370-2693(89)90968-4

[17] M. Aglietta *et al.* [NUSEX Collaboration], Europhys. Lett. **8**, 611 (1989). doi:10.1209/0295-5075/8/7/005

[18] M. C. Goodman [Soudan-2 Collaboration], Nucl. Phys. Proc. Suppl. **38**, 337 (1995). doi:10.1016/0920-5632(94)00766-O

[19] K. Eguchi *et al.* [KamLAND Collaboration], Phys. Rev. Lett. **90**, 021802 (2003) doi:10.1103/PhysRevLett.90.021802 [hep-ex/0212021].

[20] Q. R. Ahmad *et al.* [SNO Collaboration], Phys. Rev. Lett. **89**, 011301 (2002) doi:10.1103/PhysRevLett.89.011301 [nucl-ex/0204008].

[21] B. Richter, hep-ph/0008222.

[22] J. Arafune, M. Koike and J. Sato, Phys. Rev. D **56**, 3093 (1997) Erratum: [Phys. Rev. D **60**, 119905 (1999)] doi:10.1103/PhysRevD.60.119905, 10.1103/PhysRevD.56.3093 [hep-ph/9703351].

[23] S. Abe *et al.* [KamLAND Collaboration], Phys. Rev. C **84**, 035804 (2011) doi:10.1103/PhysRevC.84.035804 [arXiv:1106.0861 [hep-ex]].

[24] M. P. Decowski [KamLAND Collaboration], Nucl. Phys. B **908**, 52 (2016). doi:10.1016/j.nuclphysb.2016.04.014

[25] K. Abe *et al.* [Super-Kamiokande Collaboration], Phys. Rev. D **97**, no. 7, 072001 (2018) doi:10.1103/PhysRevD.97.072001 [arXiv:1710.09126 [hep-ex]].

[26] M. G. Aartsen *et al.* [IceCube Collaboration], Phys. Rev. Lett. **120**, no. 7, 071801 (2018) doi:10.1103/PhysRevLett.120.071801 [arXiv:1707.07081 [hep-ex]].

[27] P. Adamson *et al.* [MINOS Collaboration], Phys. Rev. Lett. **112**, 191801 (2014) [arXiv:1403.0867 [hep-ex]].

[28] K. Abe *et al.* [T2K Collaboration], Phys. Rev. Lett. **118**, no. 15, 151801 (2017) doi:10.1103/PhysRevLett.118.151801 [arXiv:1701.00432 [hep-ex]].

[29] P. Adamson *et al.* [NOνA Collaboration], Phys. Rev. Lett. **118**, no. 15, 151802 (2017) doi:10.1103/PhysRevLett.118.151802 [arXiv:1701.05891 [hep-ex]].

[30] F. P. An *et al.* [Daya Bay Collaboration], Phys. Rev. Lett. **118**, no. 25, 251801 (2017) doi:10.1103/PhysRevLett.118.251801 [arXiv:1704.01082 [hep-ex]].

[31] A. Minotti, Phys. Part. Nucl. **48**, no. 1, 47 (2017). doi:10.1134/S1063779616060162

[32] H. Seo, PoS EPS **-HEP2017**, 134 (2017). doi:10.22323/1.314.0134

[33] J. H. Christenson, J. W. Cronin, V. L. Fitch and R. Turlay, Phys. Rev. Lett. **13**, 138 (1964). doi:10.1103/PhysRevLett.13.138

[34] F. P. An *et al.* [Daya Bay Collaboration], Phys. Rev. D **95**, no. 7, 072006 (2017) doi:10.1103/PhysRevD.95.072006 [arXiv:1610.04802 [hep-ex]].

[35] P. I. Krastev and S. T. Petcov, Phys. Lett. B **205**, 84 (1988). doi:10.1016/0370-2693(88)90404-2

[36] P. F. Harrison, D. H. Perkins and W. G. Scott, Phys. Lett. B **530**, 167 (2002) doi:10.1016/S0370-2693(02)01336-9 [hep-ph/0202074].

[37] A. Gando *et al.* [KamLAND-Zen Collaboration], Phys. Rev. Lett. **117**, no. 8, 082503 (2016) Addendum: [Phys. Rev. Lett. **117**, no. 10, 109903 (2016)] doi:10.1103/PhysRevLett.117.109903, 10.1103/PhysRevLett.117.082503 [arXiv:1605.02889 [hep-ex]].

[38] K. Abe *et al.* [T2K Collaboration], Phys. Rev. Lett. **112**, 061802 (2014) [arXiv:1311.4750 [hep-ex]].

[39] E. Aliu *et al.* [K2K Collaboration], Phys. Rev. Lett. **94**, 081802 (2005) doi:10.1103/PhysRevLett.94.081802 [hep-ex/0411038].

[40] N. Agafonova *et al.* [OPERA Collaboration], Phys. Rev. Lett. **115**, no. 12, 121802 (2015) doi:10.1103/PhysRevLett.115.121802 [arXiv:1507.01417 [hep-ex]].

[41] F. P. An *et al.* [Daya Bay Collaboration], Phys. Rev. Lett. **108**, 171803 (2012) doi:10.1103/PhysRevLett.108.171803 [arXiv:1203.1669 [hep-ex]].

[42] M. H. Ahn *et al.* [K2K Collaboration], Phys. Rev. D **74**, 072003 (2006) doi:10.1103/PhysRevD.74.072003 [hep-ex/0606032].

[43] L. H. Whitehead [MINOS Collaboration], Nucl. Phys. B **908**, 130 (2016) doi:10.1016/j.nuclphysb.2016.03.004 [arXiv:1601.05233 [hep-ex]].

[44] K. Abe *et al.* [Hyper-Kamiokande Proto- Collaboration], PTEP **2015**, 053C02 (2015) doi:10.1093/ptep/ptv061 [arXiv:1502.05199 [hep-ex]].

[45] R. Acciarri *et al.* [DUNE Collaboration], arXiv:1601.05471 [physics.ins-det].

[46] K. Abe *et al.* [T2K Collaboration], Phys. Rev. Lett. **118**, no. 15, 151801 (2017) doi:10.1103/PhysRevLett.118.151801 [arXiv:1701.00432 [hep-ex]].

[47] K. Abe *et al.* [T2K Collaboration], Phys. Rev. D **96**, no. 9, 092006 (2017) doi:10.1103/PhysRevD.96.092006 [arXiv:1707.01048 [hep-ex]].

[48] K. Abe *et al.* [T2K Collaboration], Phys. Rev. D **88**, no. 3, 032002 (2013) [arXiv:1304.0841 [hep-ex]].

[49] Yoshinari Hayato,
Seminar of neutrino interaction with nucleus and their simulation,
http://www-he.scphys.kyoto-u.ac.jp/nufrontier/files/hayato-20140111.pdf

[50] L. Alvarez-Ruso, Y. Hayato and J. Nieves, New J. Phys. **16**, 075015 (2014) doi:10.1088/1367-2630/16/7/075015 [arXiv:1403.2673 [hep-ph]].

[51] J. Nieves, J. E. Amaro and M. Valverde, Phys. Rev. C **70**, 055503 (2004) Erratum: [Phys. Rev. C **72**, 019902 (2005)] doi:10.1103/PhysRevC.70.055503, 10.1103/PhysRevC.72.019902 [nucl-th/0408005].

[52] C. Adamuscin, E. Tomasi-Gustafsson, E. Santopinto and R. Bijker, Phys. Rev. C **78**, 035201 (2008) doi:10.1103/PhysRevC.78.035201 [arXiv:0706.3509 [nucl-th]].

[53] B. Bhattacharya, R. J. Hill and G. Paz, Phys. Rev. D **84**, 073006 (2011) doi:10.1103/PhysRevD.84.073006 [arXiv:1108.0423 [hep-ph]].

[54] A. Bodek, S. Avvakumov, R. Bradford and H. S. Budd, Eur. Phys. J. C **53**, 349 (2008) doi:10.1140/epjc/s10052-007-0491-4 [arXiv:0708.1946 [hep-ex]].

[55] A. A. Aguilar-Arevalo *et al.* [MiniBooNE Collaboration], Phys. Rev. D **81**, 092005 (2010) doi:10.1103/PhysRevD.81.092005 [arXiv:1002.2680 [hep-ex]].

[56] A.L.Fetter and J.D.Walecka, Dover books (2008)

[57] R. A. Smith and E. J. Moniz, Nucl. Phys. B **43**, 605 (1972) Erratum: [Nucl. Phys. B **101**, 547 (1975)]. doi:10.1016/0550-3213(75)90612-4, 10.1016/0550-3213(72)90040-5

[58] A. Bodek, arXiv:1801.07975 [nucl-th].

[59] J. Nieves, E. Oset and C. Garcia-Recio, Nucl. Phys. A **554**, 509 (1993). doi:10.1016/0375-9474(93)90245-S

[60] J. Nieves, I. Ruiz Simo and M. J. Vicente Vacas, Phys. Rev. C **83**, 045501 (2011) doi:10.1103/PhysRevC.83.045501 [arXiv:1102.2777 [hep-ph]].

[61] O. Benhar, A. Fabrocini, S. Fantoni and I. Sick, Nucl. Phys. A **579**, 493 (1994). doi:10.1016/0375-9474(94)90920-2

[62] A. Bodek, M. E. Christy and B. Coopersmith, Eur. Phys. J. C **74**, no. 10, 3091 (2014) doi:10.1140/epjc/s10052-014-3091-0 [arXiv:1405.0583 [hep-ph]].

[63] J. Speth, V. Klemt, J. Wambach and G. W. Brown, Nucl. Phys. A **343**, 382 (1980). doi:10.1016/0375-9474(80)90660-0

[64] J. Nieves, J. E. Amaro and M. Valverde, Phys. Rev. C **70**, 055503 (2004) Erratum: [Phys. Rev. C **72**, 019902 (2005)] doi:10.1103/PhysRevC.70.055503, 10.1103/PhysRevC.72.019902 [nucl-th/0408005].

[65] V. Pandey, N. Jachowicz, T. Van Cuyck, J. Ryckebusch and M. Martini, Phys. Rev. C **92**, no. 2, 024606 (2015) doi:10.1103/PhysRevC.92.024606 [arXiv:1412.4624 [nucl-th]].

[66] N. Van Dessel, N. Jachowicz, R. Gonzalez-Jimenez, V. Pandey and T. Van Cuyck, Phys. Rev. C **97**, no. 4, 044616 (2018) doi:10.1103/PhysRevC.97.044616 [arXiv:1704.07817 [nucl-th]].

[67] M. Martini, M. Ericson, G. Chanfray and J. Marteau, Phys. Rev. C **80**, 065501 (2009) doi:10.1103/PhysRevC.80.065501 [arXiv:0910.2622 [nucl-th]].

[68] J. Nieves, I. Ruiz Simo and M. J. Vicente Vacas, Phys. Rev. C **83**, 045501 (2011) doi:10.1103/PhysRevC.83.045501 [arXiv:1102.2777 [hep-ph]].

[69] S. Boyd, S. Dytman, E. Hernandez, J. Sobczyk and R. Tacik, AIP Conf. Proc. **1189**, 60 (2009). doi:10.1063/1.3274191

[70] K.Suzuki, Doctor thesis, Kyoto University, https://www-he.scphys.kyoto-u.ac.jp/theses/doctor/ (2014)

[71] D. Rein and L. M. Sehgal, Annals Phys. **133**, 79 (1981). doi:10.1016/0003-4916(81)90242-6

[72] G. M. Radecky *et al.*, Phys. Rev. D **25**, 1161 (1982) Erratum: [Phys. Rev. D **26**, 3297 (1982)]. doi:10.1103/PhysRevD.25.1161, 10.1103/PhysRevD.26.3297

[73] T. Kitagaki *et al.*, Phys. Rev. D **34**, 2554 (1986). doi:10.1103/PhysRevD.34.2554

[74] T. Kitagaki *et al.*, Phys. Rev. D **42**, 1331 (1990). doi:10.1103/PhysRevD.42.1331

[75] K. M. Graczyk and J. T. Sobczyk, Phys. Rev. D **77**, 053001 (2008) Erratum: [Phys. Rev. D **79**, 079903 (2009)] doi:10.1103/PhysRevD.79.079903, 10.1103/PhysRevD.77.053001 [arXiv:0707.3561 [hep-ph]].

[76] S. X. Nakamura, JPS Conf. Proc. **13**, 020038 (2017). doi:10.7566/JPSCP.13.020038

[77] M. Kabirnezhad, Phys. Rev. D **97**, no. 1, 013002 (2018)

[78] T. Sjostrand, S. Mrenna and P. Z. Skands, Comput. Phys. Commun. **178**, 852 (2008) doi:10.1016/j.cpc.2008.01.036 [arXiv:0710.3820 [hep-ph]].

[79] A. Bodek and U. k. Yang, arXiv:1011.6592 [hep-ph].

[80] J. Mousseau *et al.* [MINERvA Collaboration], Phys. Rev. D **93**, no. 7, 071101 (2016) doi:10.1103/PhysRevD.93.071101 [arXiv:1601.06313 [hep-ex]].

[81] P. Adamson *et al.* [MINOS Collaboration], Phys. Rev. D **81**, 072002 (2010) doi:10.1103/PhysRevD.81.072002 [arXiv:0910.2201 [hep-ex]].

[82] A. Mislivec *et al.* [MINERvA Collaboration], Phys. Rev. D **97**, no. 3, 032014 (2018) doi:10.1103/PhysRevD.97.032014 [arXiv:1711.01178 [hep-ex]].

[83] C. Berger and L. M. Sehgal, Phys. Rev. D **79**, 053003 (2009) doi:10.1103/PhysRevD.79.053003 [arXiv:0812.2653 [hep-ph]].

[84] Ieki Kei, Doctor thesis, Kyoto University, https://www-he.scphys.kyoto-u.ac.jp/theses/doctor/ (2013)

[85] D. Ashery, I. Navon, G. Azuelos, H. K. Walter, H. J. Pfeiffer and F. W. Schleputz, Phys. Rev. C **23**, 2173 (1981). doi:10.1103/PhysRevC.23.2173

[86] Y. Hayato, Acta Phys. Polon. B **40**, 2477 (2009).

[87] L. L. Salcedo, E. Oset, M. J. Vicente-Vacas and C. Garcia-Recio, Nucl. Phys. A **484**, 557 (1988). doi:10.1016/0375-9474(88)90310-7

[88] M. Day and K. S. McFarland, Phys. Rev. D **86**, 053003 (2012) doi:10.1103/PhysRevD.86.053003 [arXiv:1206.6745 [hep-ph]].

[89] K. Abe *et al.* [T2K Collaboration], Phys. Rev. D **90**, no. 5, 052010 (2014) doi:10.1103/PhysRevD.90.052010 [arXiv:1407.4256 [hep-ex]].

[90] B. G. Tice *et al.* [MINERvA Collaboration], Phys. Rev. Lett. **112**, no. 23, 231801 (2014) doi:10.1103/PhysRevLett.112.231801 [arXiv:1403.2103 [hep-ex]].

[91] A. A. Aguilar-Arevalo *et al.* [MiniBooNE Collaboration], Phys. Rev. D **88**, no. 3, 032001 (2013) doi:10.1103/PhysRevD.88.032001 [arXiv:1301.7067 [hep-ex]].

[92] K. Abe *et al.* [T2K Collaboration], Phys. Rev. Lett. **107**, 041801 (2011) [arXiv:1106.2822 [hep-ex]].

[93] K. Abe *et al.* [T2K Collaboration], Nucl. Instrum. Meth. A **659**, 106 (2011) [arXiv:1106.1238 [physics.ins-det]].

[94] K. Abe *et al.* [T2K Collaboration], Phys. Rev. D **90**, no. 5, 052010 (2014) [arXiv:1407.4256 [hep-ex]].

[95] K. Abe *et al.* [T2K Collaboration], Nucl. Instrum. Meth. A **659**, 106 (2011) doi:10.1016/j.nima.2011.06.067 [arXiv:1106.1238 [physics.ins-det]].

[96] Y. Fukuda *et al.* [Super-Kamiokande Collaboration], Nucl. Instrum. Meth. A **501**, 418 (2003).

[97] N. Antoniou *et al.* [NA49-future Collaboration], CERN-SPSC-2006-034, CERN-SPSC-P-330.

[98] K. Abe *et al.*, arXiv:1609.04111 [hep-ex].

[99] M. H. Ahn *et al.* [K2K Collaboration], Phys. Rev. Lett. **90**, 041801 (2003) doi:10.1103/PhysRevLett.90.041801 [hep-ex/0212007].

[100] A. Suzuki *et al.* [K2K Collaboration], Nucl. Instrum. Meth. A **453**, 165 (2000) doi:10.1016/S0168-9002(00)00624-0 [hep-ex/0004024].

[101] S. Takahashi, Master thesis, University of Kyoto, https://www-he.scphys.kyoto-u.ac.jp/theses/master/

[102] S. Assylbekov *et al.*, Nucl. Instrum. Meth. A **686**, 48 (2012) doi:10.1016/j.nima.2012.05.028 [arXiv:1111.5030 [physics.ins-det]].

[103] P. A. Amaudruz *et al.* [T2K ND280 FGD Collaboration], Nucl. Instrum. Meth. A **696**, 1 (2012) doi:10.1016/j.nima.2012.08.020 [arXiv:1204.3666 [physics.ins-det]].

[104] L. Aliaga *et al.* [MINERvA Collaboration], Nucl. Instrum. Meth. A **743**, 130 (2014) doi:10.1016/j.nima.2013.12.053 [arXiv:1305.5199 [physics.ins-det]].

[105] K. Abe *et al.* [T2K Collaboration], Phys. Rev. D **95**, no. 1, 012010 (2017) doi:10.1103/PhysRevD.95.012010 [arXiv:1605.07964 [hep-ex]].

[106] K. Abe *et al.* [T2K Collaboration], Phys. Rev. D **97**, no. 1, 012001 (2018) doi:10.1103/PhysRevD.97.012001 [arXiv:1708.06771 [hep-ex]].

[107] Taichiro Koga, Master thesis, University of Tokyo, http://hep.phys.s.u-tokyo.ac.jp/ (2015)

[108] T. Koga *et al.*, JPS Conf. Proc. **8**, 023003 (2015). doi:10.7566/JPSCP.8.023003

[109] Kuraray Co. Scintillator Fiber Products (1994)

[110] A. Vacheret, S. Greenwood, M. Noy, M. Raymond and A. Weber, doi:10.1109/NSSMIC.2007.4436543

[111] K. Abe *et al.* [T2K Collaboration], Phys. Rev. D **87**, no. 1, 012001 (2013) Addendum: [Phys. Rev. D **87**, no. 1, 019902 (2013)] doi:10.1103/PhysRevD.87.012001, 10.1103/PhysRevD.87.019902 [arXiv:1211.0469 [hep-ex]].

[112] Tatsuya Kikawa, Doctor thesis, Kyoto University, https://www-he.scphys.kyoto-u.ac.jp/theses/doctor/ (2013)

[113] G. D'Agostini, Nucl. Instrum. Meth. A **362**, 487 (1995). doi:10.1016/0168-9002(95)00274-X

[114] N. Abgrall *et al.* [NA61/SHINE Collaboration], Eur. Phys. J. C **76**, no. 2, 84 (2016) doi:10.1140/epjc/s10052-016-3898-y [arXiv:1510.02703 [hep-ex]].

[115] T. Abbott *et al.* [E-802 Collaboration], Phys. Rev. D **45**, 3906 (1992). doi:10.1103/PhysRevD.45.3906

[116] J. V. Allaby, F. G. Binon, A. N. Diddens, P. Duteil, A. Klovning and R. Meunier, CERN-70-12.

[117] M. Apollonio *et al.* [HARP Collaboration], Phys. Rev. C **80**, 035208 (2009) doi:10.1103/PhysRevC.80.035208 [arXiv:0907.3857 [hep-ex]].

[118] M. Bonesini, A. Marchionni, F. Pietropaolo and T. Tabarelli de Fatis, Eur. Phys. J. C **20**, 13 (2001) doi:10.1007/s100520100656 [hep-ph/0101163].

[119] G. Bellettini, G. Cocconi, A. N. Diddens, E. Lillethun, G. Matthiae, J. P. Scanlon and A. M. Wetherell, Nucl. Phys. **79**, 609 (1966). doi:10.1016/0029-5582(66)90267-7

[120] S. P. Denisov, S. V. Donskov, Y. P. Gorin, R. N. Krasnokutsky, A. I. Petrukhin, Y. D. Prokoshkin and D. A. Stoyanova, Nucl. Phys. B **61**, 62 (1973). doi:10.1016/0550-3213(73)90351-9

[121] M. J. Longo and B. J. Moyer, Phys. Rev. **125**, 701 (1962). doi:10.1103/PhysRev.125.701

[122] J. W. Cronin, R. Cool and A. Abashian, Phys. Rev. **107**, 1121 (1957). doi:10.1103/PhysRev.107.1121

[123] B. W. Allardyce *et al.*, Nucl. Phys. A **209**, 1 (1973). doi:10.1016/0375-9474(73)90049-3

[124] K. Abe *et al.* [T2K Collaboration], arXiv:1802.05078 [hep-ex].

[125] C. Adams *et al.* [MicroBooNE Collaboration], [arXiv:1805.06887 [hep-ex]].

[126] S.Tobayama, Doctor thesis, University of British Columbia (2016)

[127] G. J. Feldman and R. D. Cousins, Phys. Rev. D **57**, 3873 (1998) doi:10.1103/PhysRevD.57.3873 [physics/9711021 [physics.data-an]].

[128] Micheal D.Lee, Bayesian Congnitive Modeling: A practical Course (2014)

[129] Sir Harold Jeffreys, The Theory of Probability (1961)

[130] Neutrino 2018, international conference on Neutrino Physics and Astrophysics (June 2018)

[131] K. Abe *et al.* [Super-Kamiokande Collaboration], Phys. Rev. D **97**, no. 7, 072001 (2018) doi:10.1103/PhysRevD.97.072001 [arXiv:1710.09126 [hep-ex]].